Planar Opto-acoustic Microscopy Applied to the Metrology of Periodic Nanostructures

by

Thomas James Grimsley II
B.Sc., SUNY Buffalo 2004

Thesis
Submitted in partial fulfillment of the requirements for
The Degree of Doctor of Philosophy
In the department of Physics at Brown University

Providence, Rhode Island
May 2012

This dissertation by Thomas James Grimsley II is accepted in its present form by the Department of Physics as satisfying the dissertation requirement for the degree of Doctor of Philosophy

Date . . . . . .

. . . . . .
Professor Humphrey J. Maris

Recommended to the Graduate Council

Date . . . . . .

. . . . . .
Professor Arto V. Nurmikko

Date . . . . . .

. . . . . .
Professor Derek Stein

Approved by the Graduate Council

Date . . . . . .

. . . . . .
Dean Peter M. Weber

The vita of Thomas J Grimsley II

Thomas was born on January 24, 1982, in Rochester, New York. He received his B.Sc. in Engineering Physics from State University of New York at Buffalo in 2004, graduating magna cum laude. In the fall of that same year he was accepted into the Physics Department at Brown University, RI. The work for this thesis began in the spring of 2006.

Publications

T. J. Grimsley, F. Yang, S. Che, G. A. Antonelli, H. J. Maris and A. V. Nurmikko. "Ultrafast opto-acoustics applied to the study of material nanostructures." *Journal of Physics: Conference Series* **278**, 012037 (2011).

T. J. Grimsley, J. Ma, Q. Miao, A. V. Nurmikko, and H. J. Maris. "Picosecond Ultrasonic and Heat Flow Measurements with Enhanced Sensitivity," *Chinese Journal of Physics* **49** (1), 176 (2011).

T. J. Grimsley, F. Yang, G. A. Antonelli, H. J. Maris, and A. V. Nurmikko. "Experiments to Study the Propagation of Picosecond Sound Pulses in Water" *Chinese Journal of Physics* **49** (1), 151 (2011).

F. Yang, T. J. Grimsley, S. Che, G. A. Antonelli, H. J. Maris, and A. V. Nurmikko. "Picosecond ultrasonic experiments with water and its application to the measurement of nanostructures." *J. Appl. Phys.* **107**, 103537 (2010).

T.J. Grimsley, G. A. Antonelli, F. Yang, H.J. Maris, and A.V. Nurmikko. "Nanometer Metrology of Periodic Structures With Ultrafast Optoacoustics" in MRS Online Proceedings Library **1249**, 1249-F10-05 (2010).

T. J. Grimsley, F. Yang, C. H. Dang, S. Che, G. A. Antonelli, H. J. Maris, Q. Zhang, and A. V. Nurmikko. "Nanometer Metrology Using Ultrafast Optoacoustics," in *Conference on Lasers and Electro-Optics/International Quantum Electronics (CLEO/IQE 2009) Conference*, OSA Technical Digest (Optical Society of America, 2009), paper CTuAA6.

T.J. Grimsley, C.H. Dang, Q. Zhang, S. Che, F. Yang, G. A. Antonelli, A.V. Nurmikko, H.J. Maris. "Picosecond Ultrasonic Microscopy of Semiconductor Nanostructures," in Proceedings of the International Symposium on Laser Ultrasonics (2008).

F. Yang, T. Atay, C. H. Dang, T. J. Grimsley, S. Che, J. Ma, Q. Zhang, A. V. Nurmikko and H. J. Maris. "Study of Phonon Propagation in Water Using Picosecond Ultrasonics," in Proceedings of the International Conference Phonons 2007, *J. Phys. Conference Series* **92**, 012024 (2007).

F. Yang, T. J. Grimsley and H. J. Maris. "Enhancement of Picosecond Ultrasonic Signals Through the Use of an Optical Cavity," in Proceedings of the International Conference Phonons 2007, *J. Phys. Conference Series* **92**, 012023 (2007)

Acknowledgments

I would like to thank Professor Humphrey J Maris for being an excellent advisor. It has been a privilege working with him for the last several years. I have come to admire his unassuming demeanor and absolute emphasis on clarity in communication at all levels.

Professor Arto V. Nurmikko also offered much time, guidance and advice, all of which was greatly appreciated. Many thanks are given to both Prof. Nurmikko and Prof. Derek Stein for reading this dissertation.

The positioning requirements for the experiments described in this work were challenging. I wish to sincerely thank the scientists and engineers at Zygo, Inc., in particular Carl Zanoni, Peter de Groot, and Robert Stoner for their help. In March 2008, I journeyed to Zygo headquarters in Connecticut and my eyes were opened to the fascinating and challenging world of precision machine design. One half day spent with these professionals was invaluable in the completion of this work.

One of the perils of making a measurement system is the possibility of having no samples to measure once the system is completed. Thanks to Dr. G. Andrew Antonelli, of Novellus Systems Inc., this was not a danger. In addition to providing many high quality, state-of-the-art samples, including all the ones discussed in this work, Dr. Antonelli also provided advice, guidance, and encouragement.

I would like to thank the many professors, staff, and students that I have worked with in both the Physics Department and the Division of Engineering at Brown, especially the students in Humphrey`s research groups. I have been very fortunate to work with so many interesting and bright people. There were many people that helped successfully complete this project. Charlie Vickers and the machinists at JEPIS introduced me to the subtle art of machining and assisted with many of the more

demanding operations. Dr. Fan Yang spent many hours with me in the lab as we mulled over the results of early POAM experiments. Dr. Cuong Dang assisted with the fabrication of early test samples and optical cavities. Dr. Dafei Jin and Wanchun Wei lent tools and hardware on many occasions. Dr. Anthony McCormick helped with the sample preparations for the cross sectional SEM imaging.

I would like to thank Zygo, Inc. and the Department of Energy for funding this research.

Finally, my deepest gratitude goes to my family for their unflagging emotional support, and to my dear fiancée, Ruth Ophardt, for her patience during these years of work.

Table of Contents

List of Tables

List of Figures

Chapter 1
Introduction

Acoustic microscopy, an imaging technique that uses sound as opposed to light, has been used to study a variety of microstructures, material defects, and biological tissues[1]. One of the key limitations in pulsed acoustic microscopy is the duration of sound pulses that can be generated. An acoustic microscope usually has a piezo-electric transducer that is used to generate the sound. The electronic equipment used to generate the signals that drive the transducers play a large role in limiting the achievable resolution. The goal of this ongoing project is to develop an acoustic microscope that uses ultrashort laser pulses, with durations on the order of 100 fs, to generate short sound pulses, with durations on the order of 10 ps. These short sound pulses will then be used to form images of the sample being studied in a manner similar to a traditional acoustic microscope. This technique is referred to below as scanning opto-acoustic microscopy (SOAM).

As a proof of concept and first step towards the construction of a SOAM instrument, a system which contains all of the key components except for the acoustic lens and the sample scanning stages was constructed. The acoustic pulses generated by the ultrafast optical source, instead of being focused by an acoustic lens, were launched into the coupling fluid directly. This technique is referred to here as planar opto-acoustic microscopy (POAM). The spatial extent of the sound was determined by the spot size of

the focused laser beam, instead of the focusing properties of an acoustic lens. The first samples examined, as a test of the system's performance and capabilities, were periodic groups of nanostructures. With a repeat distance in the submicron regime, this meant that the acoustic pulse was probing anywhere from 20 – 100 nanostructures at once. By comparing experimental results with simulations, the average features of groups of nanostructures, such as height and spacing, could be measured with nanometer sensitivity. The dimensions inferred from the POAM data were compared to destructive measurements of the sample profiles using scanning electron microscopy.

The general outline of this work is as follows. Chapter 2 contains a brief review of picosecond ultrasonics and a summary of relevant aspects of acoustic microscopy, which is followed by a description of the POAM measurement principle. Chapter 3 presents an in depth description of the apparatus used for this work. Chapter 4 describes the development and characterization of the opto-acoustic transducer. In Chapter 5, details of the two simulation methods used to analyze the POAM data are given. Chapter 6 describes the results of POAM measurements of periodic arrays of nanostructures. Finally, Chapter 7 provides a summary of this work and suggestions for possible future work.

Bibliography

1. Briggs, A. Acoustic microscopy-a summary. *Rep. Prog. Phys.* **55**, 851-909 (1992).

Chapter 2

Picosecond Ultrasonics Applied to Acoustic Microscopy

2.1 Introduction

This chapter explores the use of the picosecond ultrasonics technique for acoustic microscopy. The picosecond ultrasonics technique is reviewed in section 2.2, with emphasis on the generation and detection of short longitudinal strain pulses. The field of acoustic microscopy is large and varied, with applications ranging from basic materials research to industrial nondestructive evaluation. Section 2.3 provides a brief summary of the development and principles of acoustic microscopy, with particular emphasis on the parameters which determine the spatial resolution. Section 2.4 discusses the main issues that arise when attempting to construct a scanning acoustic microscope which uses sound pulses generated by an ultrafast optoacoustic method. Section 2.5 introduces the concept of a planar opto-acoustic microscope, a stepping stone towards a full scanning version of an acoustic microscope based on the picosecond ultrasonics technique.

2.2 Picosecond Ultrasonics – A Review

With the introduction of ultrafast mode-locked lasers that produce stable pulses with durations less than 100 fs, a new range of measurement possibilities has opened up. These lasers have been used to probe fast chemical reactions and bond dynamics[1,2], semiconductors[3], and phonons in solids and solid-liquid interfaces[4,5]. The picosecond ultrasonics technique[6] is an example of an ultrafast pump-probe technique.

2.2.1 The basic pump probe technique

A schematic diagram of a basic picosecond ultrasonic experiment is shown in Figure 2.1. The output of an ultrafast laser is split into two beams, a pump beam and a probe beam. The pump beam is focused onto the sample being studied, and the energy absorbed increases the temperature by an amount typically of the order of 1 to 10 K. The increase in temperature, which occurs on a picosecond timescale, causes a thermal stress to be set up in the material. When this stress relaxes it launches an acoustic pulse into the material. When the acoustic pulse impinges upon an interface between two materials, a part of it is reflected and returns towards the surface. The returning stress perturbs the optical properties of the film, and the change in the optical reflectivity of the probe beam as a function of the probe delay time is monitored.

Figure 2.2 shows data taken on a sample consisting of a sputtered aluminum film on a silicon substrate. Zero probe time delay corresponds to the pump and probe pulses being incident on the sample at the same time. The jump in reflectivity near time zero is due to the change in reflectivity of the metal film that results from its increase in temperature (thermoreflectance). The slow decay in the change in reflectivity is a result of the Al film cooling by heat flow into the substrate. The echo near 27 ps is caused by a strain pulse that has propagated through the metal film, reflected off of the Al/Si interface, and returned to the sample. The echo arrival time t_{echo} corresponds to a round trip through the thickness of the Al film, *i.e.*, $t_{echo} = 2d_{Al}/v$, where v is the longitudinal sound velocity in the Al film, and d is the thickness of the film. The inset in Figure 2.2 shows an

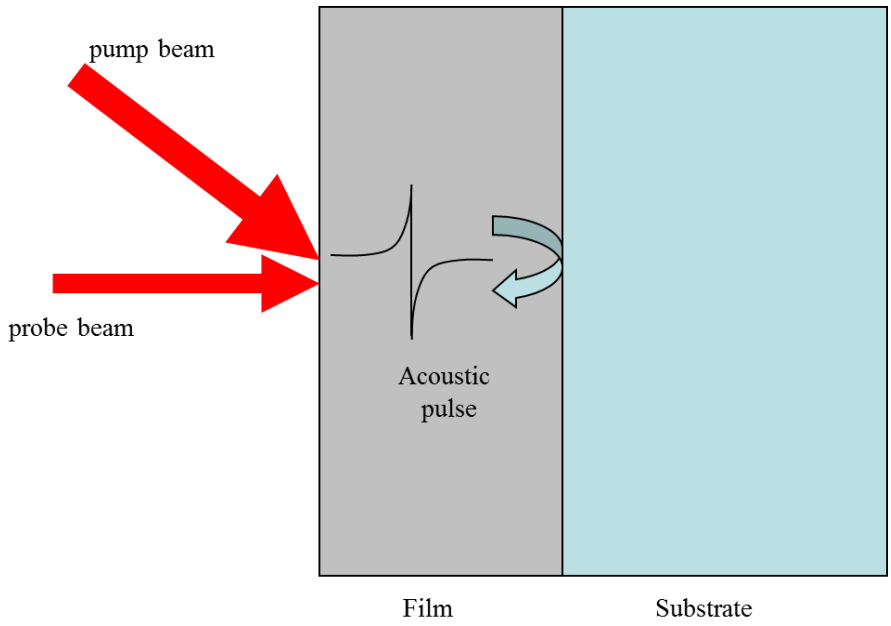

Figure 2.1: Schematic of the picosecond ultrasonics technique. The pump and probe beams are focused onto the same spot on the sample, and the changes in reflectivity are monitored by the time delayed probe beam.

expanded view of the first echo after subtraction of the background due to the thermoreflectance contribution to the signal. If the sound velocity in thin film aluminum is assumed to be same as that in the bulk material (v = 6.4 nm / ps), then one can estimate from the echo arrival time that this film has a thickness of 86 nm. The sound velocity may differ slightly from the bulk value, and vary according to the deposition method used. However, it is possible to determine the sound velocity for a particular deposition process by making measurements on a test sample whose thickness is determined by another (potentially destructive) technique such as scanning/transmission electron microscopy or x-ray reflectivity. It is reasonable to assume that the sound velocity remains the same for other samples made using the same process, and so the picosecond ultrasonics technique can be used to non-destructively measure the thickness of thin metal films with Angstrom precision.

2.2.2 Optical generation of sound

Suppose that a short pulse of light (duration $\tau < 1\text{ps}$) with energy Q is incident upon the free surface of the sample. Let $z = 0$ denote the free surface of the sample in the

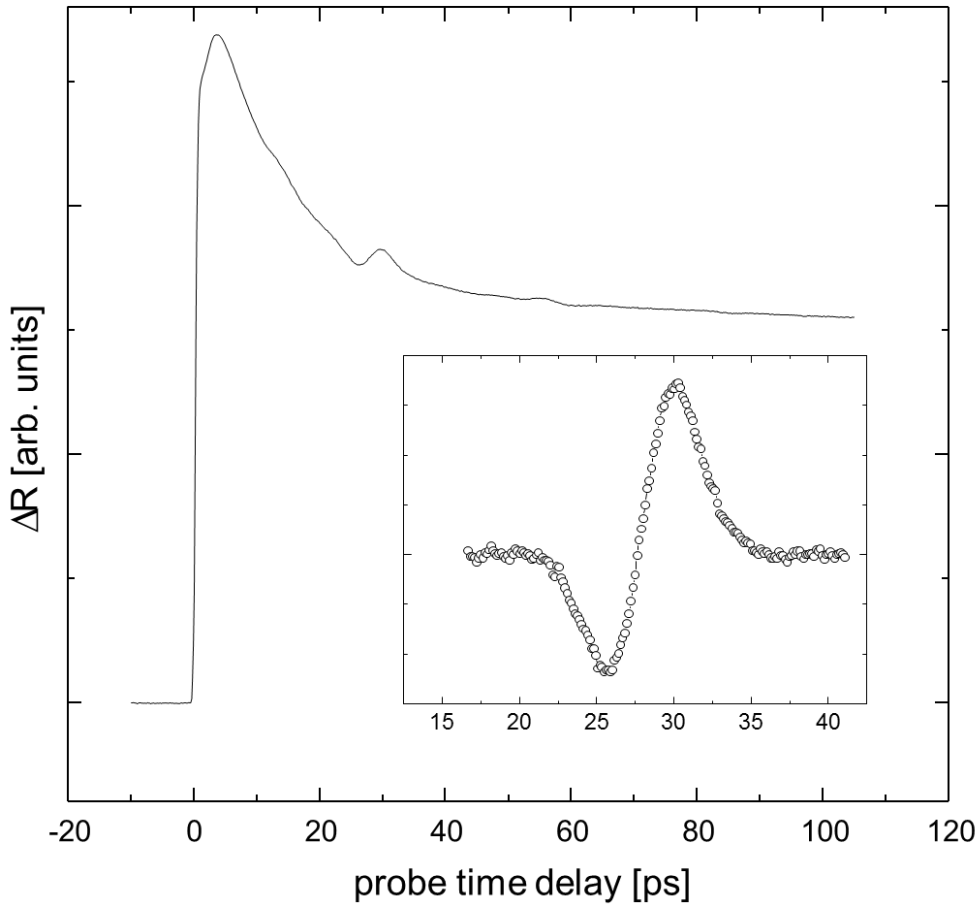

Figure 2.2: Change in reflectivity of an 86 nm aluminum film on a silicon substrate. Inset : close up of the first echo centered at 27 ps after the subtraction of the thermal background.

unstrained state, with the sample occupying the region $z > 0$. Let the penetration depth of the light into the sample be ξ and the optical reflectivity be *R*. The area of the spot illuminated by the pump pulse is *A*. We assume that this area is sufficiently large that the sound propagation can be treated as one dimensional, *i.e.*, the strain and displacement vary only with the distance *z* from the free surface. The energy per unit volume deposited into the material at position *z* is given by

$$W(z) = (1-R)\frac{Q}{A\xi}\exp\left[-\frac{z}{\xi}\right]. \qquad 2.1$$

The energy deposited by the pump pulse creates a rise in temperature

$$\Delta T(z) = \frac{W(z)}{C} = (1-R)\frac{Q}{CA\xi}\exp\left[-\frac{z}{\xi}\right], \qquad 2.2$$

where C is the specific heat per unit volume of the sample. In this treatment, this change in temperature is assumed to happen instantly. This change in temperature results in an isotropic thermal stress $-3B\beta\Delta T(z)$, where B is the bulk modulus and β is the linear thermal expansion coefficient of the metal film. Since the stress varies only in the z direction, all motion will be in the z direction and the only nonzero component of the strain tensor is η_{zz}.

The relevant equations of linear elasticity are then

$$\sigma_{zz} = 3\frac{1-\mu}{1+\mu}B\eta_{zz} - 3B\beta\Delta T(z), \qquad \rho\frac{\partial^2 u_z}{\partial t^2} = \frac{\partial \sigma_{zz}}{\partial z}, \qquad \frac{\partial u_z}{\partial z} = \eta_{zz}, \qquad 2.3$$

where u_z is the particle displacement in the z direction, ρ is the material density, and μ is the Poisson ratio of the metal film. The solution to the above equations that satisfies the initial condition of zero strain everywhere and the boundary condition of a stress free surface at $z = 0$ is

$$\eta_{zz}(z,t) = (1-R)\frac{Q\beta}{A\xi C}\frac{1+\mu}{1-\mu}\left[\exp\left(-\frac{z}{\xi}\right) - \frac{1}{2}\exp\left(-\frac{z+vt}{\xi}\right) - \frac{1}{2}\exp\left(-\frac{|z-vt|}{\xi}\right)\mathrm{sgn}(z-vt)\right] \qquad 2.4$$

where v is the longitudinal sound velocity in the material given by

$$v^2 = 3\frac{1-\mu}{1+\mu}\frac{B}{\rho}. \qquad 2.5$$

This solution for the strain can be broken down into propagating and non-propagating parts. After time zero the solid is no longer in its equilibrium configuration, but in a state of compressive strain. The propagating strain for small times takes the form of two counter propagating pulses. One of these pulses reflects off of the free surface and changes sign. The result is a bipolar pulse propagating into the film. The non-propagating part of the solution represents the thermal expansion that remains after the strain pulses

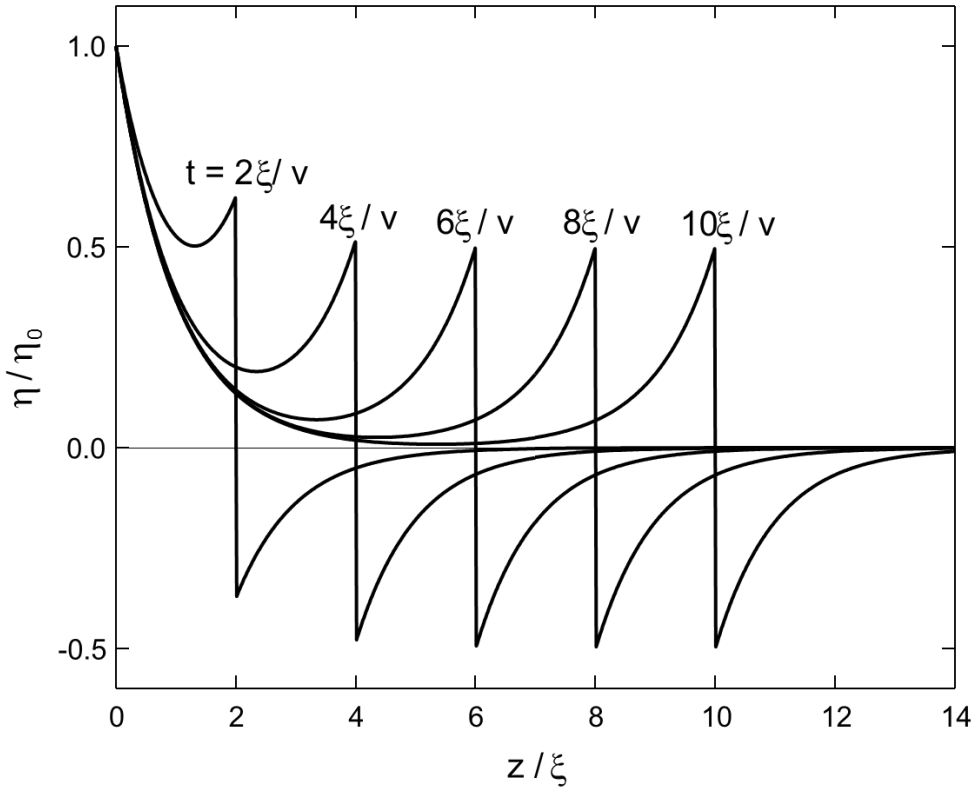

Figure 2.3: Spatial profile of the strain pulse at different delay times. At time delay t = 0 ps, the strain is zero everywhere.

have propagated away. Figure 2.3 shows the strain profile for several values of the time in multiples of ξ / v. The strain has been normalized by the factor

$$\eta_0 = (1-R)\frac{Q\beta}{A\xi C}\frac{1+\mu}{1-\mu}. \qquad 2.6$$

In the above description of the generation process, the thermal stress set up by the pump pulse was assumed to occur instantaneously. If the pump pulse has a finite duration τ_{pump}, then the strain generated during the pump pulse absorption will move a distance $v\tau_{pump}$. The finite duration of the pump pulse can be ignored if $\xi >> v\tau_{pump}$. Metals typically have a sound velocity on the order of 5 nm ps^{-1}, and a penetration depth of 10 –

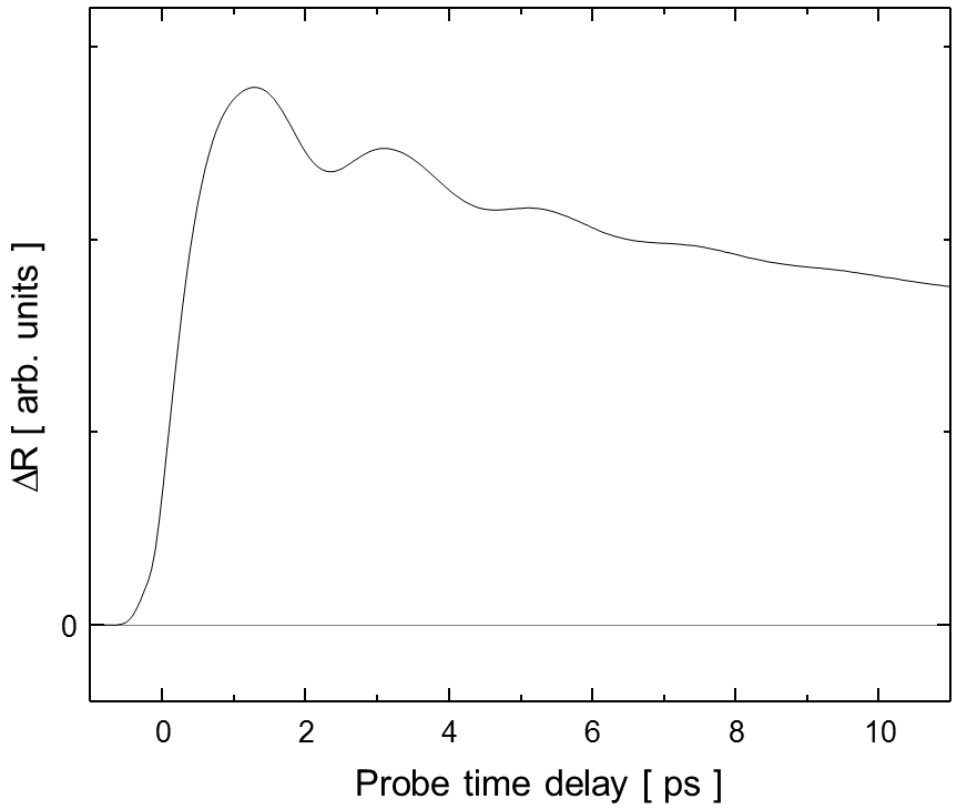

Figure 2.4: Change in reflectivity of a thin aluminum film (thickness ~6 nm) on a glass substrate. The measured period is 2.1 ps.

100 nm. In the experiments reported in this work, the pump pulse had a duration of approximately 200 fs, so the effect of the pulse width is small.

The generation is also affected by the diffusion of the electrons which are excited by the light pulse. These electrons can diffuse a significant distance before they give their energy to the lattice by electron- phonon coupling[7]. One can allow for this by replacing the optical penetration depth ξ by a larger effective penetration depth ξ^*. For high conductivity materials such as aluminum and copper ξ^* can be much larger than ξ, *e.g.*, 5 or 10 times larger. When the thickness of the film becomes comparable to the effective penetration depth, the initial strain will extend through the entire thickness of the film,

and the acoustic signature will change from distinct echoes to a damped oscillation. Figure 2.4 shows data taken on a 7 nm Al film on a glass substrate. The period of the oscillations, which corresponds to the lowest thickness mode of the thin film, is approximately 2.1 ps.

2.2.3 Optical detection of sound

The change in the optical reflectivity, as a function of probe delay time *t*, can be expressed in the form

$$\Delta R(t) = \int_0^\infty f(z)\eta_{zz}(z,t)dz \qquad 2.7$$

The function $f(z)$ is called the sensitivity function, and describes how a strain at depth z affects the reflectivity of the sample. Most of the change in reflectivity is caused by strain within a distance ξ of the sample surface. In a typical metal in the visible spectrum, $\xi = 10-100\text{nm}$ (*i.e.*, the imaginary part of the refractive index is 1 – 10). The fact that the probe beam only samples a small spatial slice of the sample will prove to be important in designing a thin film structure for the detection of sound pulses that have been significantly broadened, as discussed in section 2.4.

2.3 Acoustic Microscopy – A Brief Review

2.3.1 Historical overview and mode of operation

The key components of a reflection acoustic microscope are the transducer, the acoustic lens, and the coupling medium, as shown in Figure 2.5. The transducer is the device which generates the sound waves, which are then focused by the acoustic lens and transmitted through the coupling fluid to the sample. After reflecting and scattering off of the sample, the returning sound is collected by the acoustic lens, and the transducer converts the sound into an electrical signal. By mechanically scanning over the surface of the sample, an image is formed. Unlike optical microscopy, mechanical scanning is required for image formation, since typical acoustic lenses have poor off-axis imaging capabilities[8].

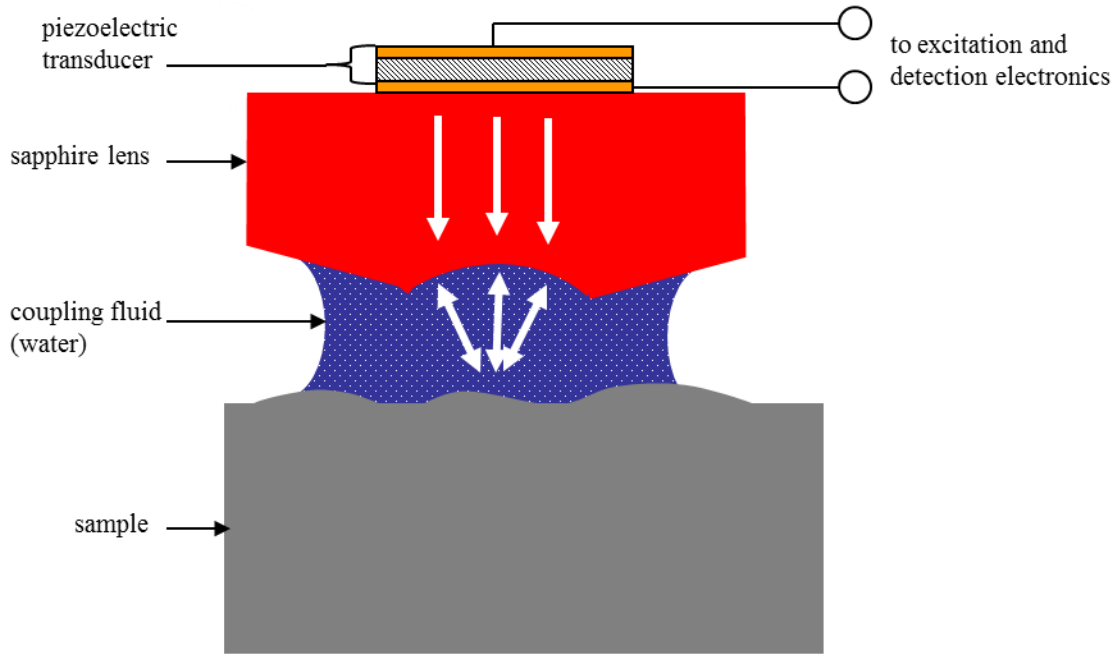

Figure 2.5: Schematic of the major components of a scanning reflection acoustic microscope. Sound waves generated by a piezoelectric transducer propagate through the sapphire rod, are focused by the acoustic lens, reflect off of the sample, and return to the piezoelectric transducer. The sample is scanned, and an image is formed point by point.

In commercially available acoustic microscopes, the transducer is often mounted or fabricated directly onto one end of a sapphire rod, and a concave spherical surface with a radius of curvature from 10 – 100 microns is ground into the other. Due to the difference in the sound velocities between the sapphire and the coupling fluid, this simple curved interface focuses planar wave fronts that impinge upon it. The ratio of the sound velocity of the sapphire to the velocity of the coupling fluid is analogous to the refractive index in optics.

Since the first demonstration of a scanning acoustic microscope by Lemons and Quate[9], many researchers have explored the possibilities of acoustic microscopy. One of the appeals of using sound for imaging is the possibility of detecting subsurface defects in materials that are opaque optically but relatively transparent (*i.e.*, non-attenuating) acoustically. In addition, an acoustic microscope can image systems where the optical

contrast is small but the acoustic contrast, or the difference in mechanical properties, is high [9]. Figure 2.6, taken from Lemons and Quate[10], shows a comparison of images taken with acoustic and optical microscopes. The object being imaged is a single high speed transistor. The optical microscope image, shown on the right, was taken using a Nomarski differential interference contrast technique. The acoustic image, shown on the left, was taken using continuous wave (cw) sound with a frequency of 600 MHz. At this frequency the wavelength of sound in the coupling fluid (water) is 2.5 μm, and the 2 μm wide fingers of the device are clearly resolved in the acoustic image .

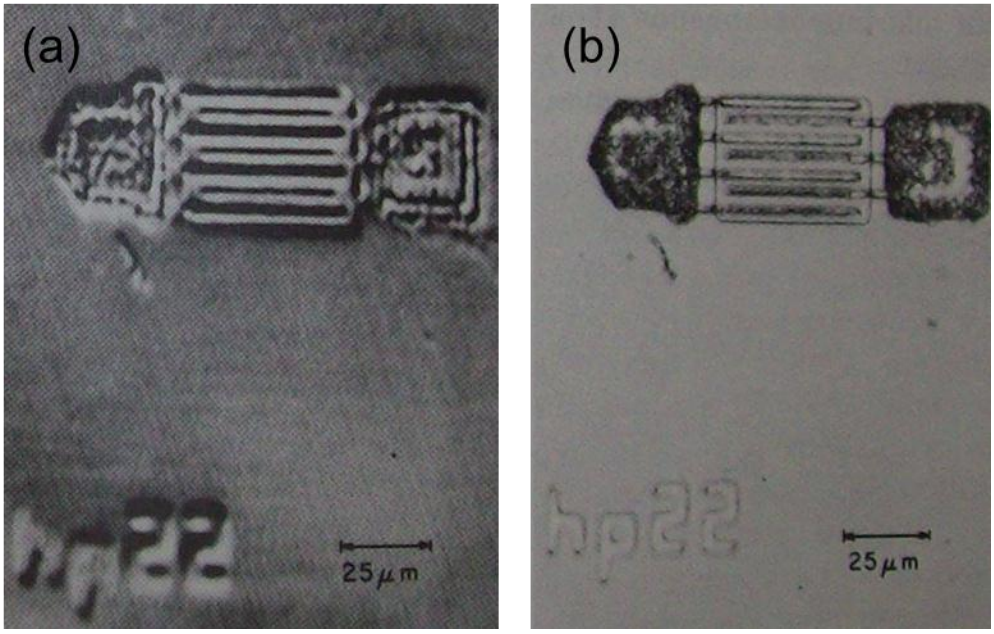

Figure 2.6: Acoustic (a) and optical (b) microscope images of a small bipolar transistor. The acoustic image was acquired using CW sound with a frequency of 600 MHz, which had a wavelength of 2 μm in the water coupling fluid. The optical image was taken using a Nomarski differential interferometer contrast (DIC) technique. Images taken from Lemons and Quate[10]

The first acoustic microscope[9] was operated in a cw mode, the sound waves had a frequency of 160 MHz, and the acoustic lens was a sapphire rod with a concave surface ground into it with a radius of curvature of 1.59 mm. At 160 MHz, the wavelength of sound in water is 9.4 microns, and this determines the resolution. The results published by Lemons and Quate in 1974 spurred a large interest in the field of acoustic microscopy, with research groups from around the world[11-18] developing in-house instruments. In

1986, Atalar and Hoppe reported on a commercial instrument, the ELSAM, that was a combination optical and acoustic microscope that operated in the 50 -2000 MHz frequency band[19]. The instrument, when operating at a frequency of 1.6 GHz in room temperature water (sound wavelength 0.94 microns), has a resolution on the order of 0.8 microns[19]. The best resolution for an instrument using water as a coupling fluid was reported by Hadimioglu and Quate[20] as 240 nm in the normal operating mode, and 200 nm in a nonlinear operating mode. In that work they used 3 ns rf pulses with a frequency of 4.4 GHz to excite a piezoelectric transducer. It is difficult to generate rf pulses much shorter than this.

There is an interwoven relationship between the radius of curvature of the lens, the attenuation of the coupling fluid, and the acoustic pulse length in determining the resolving power of a pulsed acoustic microscope. In a linear microscope (i.e., one with sufficiently low sound amplitude in the coupling fluid), the resolution[8] is $S = (F / D)\lambda$, where F is the lens focal length (approximately equal to the radius of curvature R), D is the lens opening diameter, and λ the wavelength of sound in the coupling fluid. To increase the resolution, higher frequency sound is required. However, for most fluids, the attenuation of sound increases as the frequency squared. To maintain a good signal to noise ratio, a shorter propagation path in the coupling fluid is required, which in turn requires an acoustic lens with a smaller radius of curvature. This places a limit on the pulse duration that is launched into the coupling fluid. When the pulse is launched by the transducer, there are two signals that are picked up; a reflection from the lens / fluid interface and the reflection from the fluid / sample interface. For these two signals to not overlap, the duration of the pulse should be less than the round trip travel time through the coupling fluid, which is approximately $2R/v$, where v is the sound velocity in the coupling fluid. Note also that the reflection from the lens / fluid interface is typically much larger than the signal from sound that has reflected off of the sample.

2.3.2 Choice of coupling fluid

The purpose of the coupling fluid in an acoustic microscope is to provide a medium that the sound can propagate through to reach the sample. There are several criteria that must

be considered when choosing a coupling fluid for acoustic microscopy. The two most pressing are the acoustic properties of the coupling fluid and the chemical compatibility with the sample.

Fluid	Formula	Temperature [K]	Velocity [nm / ps]	Impedance [10^6Rayl]	Attenuation constant [$10^{-17}s^2cm^{-1}$]
Water	H_2O	298	1.495	1.49	22.0
		333	1.551	1.525	9.9
Methanol	CH_3OH	303	1.088	0.866	30.1
Ethanol	C_2H_5OH	303	1.127	0.89	48.4
Acetone	$(CH_3)_2CO$	303	1.158	0.916	53.9
Carbon tetrachloride	CCl_4	298	0.93	1.482	537
Hydrogen peroxide	H_2O_2	298	1.545	2.26	10.0
Carbon disulphide	CS_2	298	1.31	1.65	10.0
Mercury	Hg	297	1.449	19.7	5.8
Gallium	Ga	303	2.87	17.5	1.6
Argon @ 4 Mpa	Ar	293	0.323	0.023	412
Argon @ 25 Mpa	Ar	293	0.323	0.145	82.9
Xenon @ 4 Mpa	Xe	293	0.178	0.042	952
Oxygen	O_2	90	0.9	1	9.89
Nitrogen	N_2	77	0.85	0.68	13.8
Hydrogen	H_2	20	1.19	0.08	5.64
Xenon	Xe	166	0.63	1.8	22.0
Argon	Ar	87	0.84	1.2	15.2
Neon	Ne	27	0.6	0.72	23.1
Helium	He	4.2	0.183	0.023	226
		1.95	0.227	0.033	70.2
		0.4	0.238	0.035	1.73
		0.1	0.238	0.345	0.0046

Table 2.1: Acoustic properties of liquids that have been used as coupling fluids in various implementations of acoustic microscopes. The characteristic acoustic impedance of a medium is given in units of Rayleigh (1 Rayl = 1 kg $m^{-2}s^{-1}$). Data for this table is taken from Attal and Quate[21] and references therein.

The relevant acoustic properties are the sound velocity, sound attenuation, and the acoustic impedance of the medium. The propagation of plane waves in an absorbing fluid is described by

$$p(z,t) = p_0 \exp(-\alpha z)\exp\left[ik(z - vt)\right], \qquad 2.8$$

where p is the excess pressure, α the amplitude attenuation per unit distance, and v the phase velocity. The attenuation of the intensity of the wave is given by 2α. For many fluids, the acoustic attenuation α is found to be proportional to the frequency squared

$$\alpha = Af^2, \qquad 2.9$$

where f is the frequency and A is a constant independent of frequency, and in what follows is referred to as the attenuation constant.

Shortly after the first report by Lemons and Quate[9] there was a substantial amount of work by various groups exploring the use of different fluids. Table 2.1 summarizes some of the pertinent properties of the various fluids that have been used as coupling fluids in acoustic microscopy. One of the hindrances to obtaining high signal to noise ratios is the large acoustic mismatch at a typical solid / fluid interface; most of the acoustic power incident on the interface is simply reflected and never makes it to the sample. Some groups worked with liquid metals, such as gallium[22] and mercury[23], but these present the distinct disadvantages of being poisonous. The experiments with gallium were difficult because gallium readily oxidizes and such experiments have not been repeated to date[24].

The other main fluid property that determines suitability for acoustic microscopy is the acoustic attenuation. Some work has been done with pressurized noble gasses, but the work was not continued[23]. Cryogenic liquids[23], in particular superfluid helium[25] at very low temperature, have an acoustic attenuation significantly smaller than that of water. By pressurizing liquid helium, the attenuation can be reduced even further, and the highest resolution was reported by Muha *et al*.[26] as 15 nm. In that work, the operating frequency was 15.3 GHz, and significant effort was required for the design of both the transmitting and receiving electronics and the transducer structure itself.

Biological samples limit the choice of coupling fluid to water, and even then the water must be at a reasonable temperature. While most microscopy of biological specimens is done on samples that have been fixed in some manner, investigating cells or tissues in situ provides unique imaging opportunities[24].

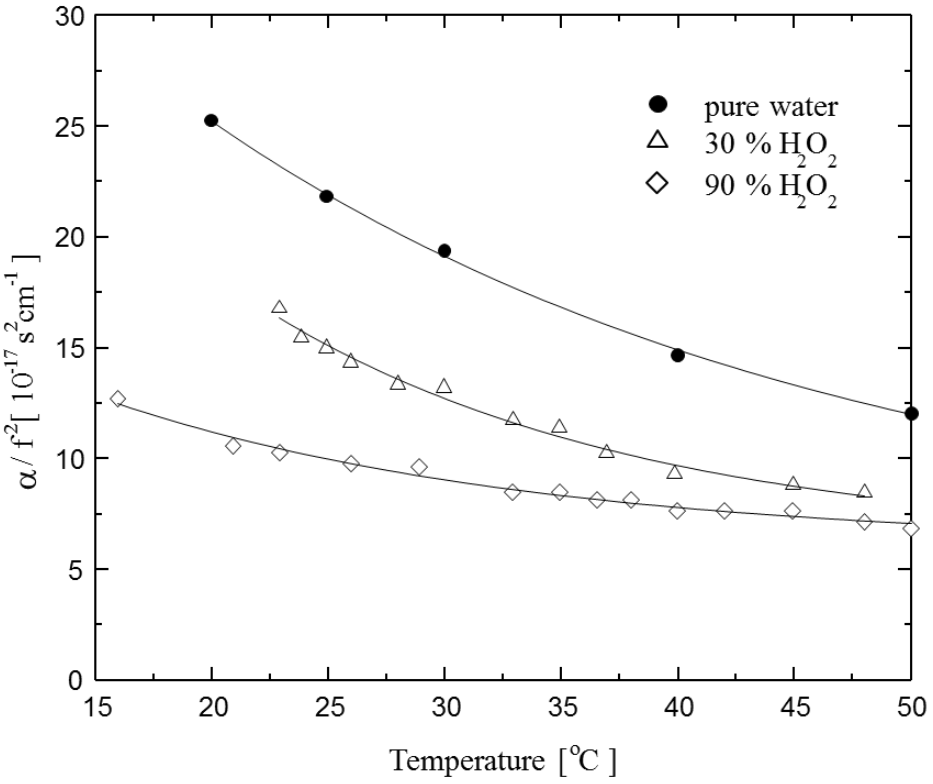

Figure 2.7: Attenuation of sound in 0% (pure water), 30%, and 90% hydrogen peroxide solutions versus temperature. Curves are to guide the eye. Data taken from Attal & Quate[21]

Usually, when substances are mixed with water the resulting ultrasonic attenuation of the solution is higher than that of pure water. Various association/dissociation reactions provide additional relaxation mechanisms which increase the attenuation[27] . However, some substances, when dissolved in water, serve to inhibit the structural relaxation between groups of water molecules that are responsible for the acoustic attenuation. This is referred to as anomalous attenuation and occurs, for example, in aqueous solutions of hydrogen peroxide and various group IA salts[21]. Figure 2.7 shows the acoustic attenuation for distilled water, 30%, and 90% solutions of hydrogen peroxide. A 90% solution of hydrogen peroxide at 25°C has the same acoustic attenuation as water at 90°C. Figure 2.8 shows the acoustic attenuation of solutions of various group IA salts versus concentrations. Significant reductions in the attenuation are possible, especially for solutions of KCN, but substantial concentrations of the salt are required. Breitschwerdt,

Kistenmacher, and Tamm[28] measured the acoustic attenuation for all combinations of group IA cations Li^+, Na^+, K^+, Cs^+, and group VIIA anions (F^-, Cl^-, Br^-, and I^-). They found that the reduction in attenuation was the largest for salts with K^+, and that the effect becomes more pronounced as the temperature approaches the freezing point of the solution.

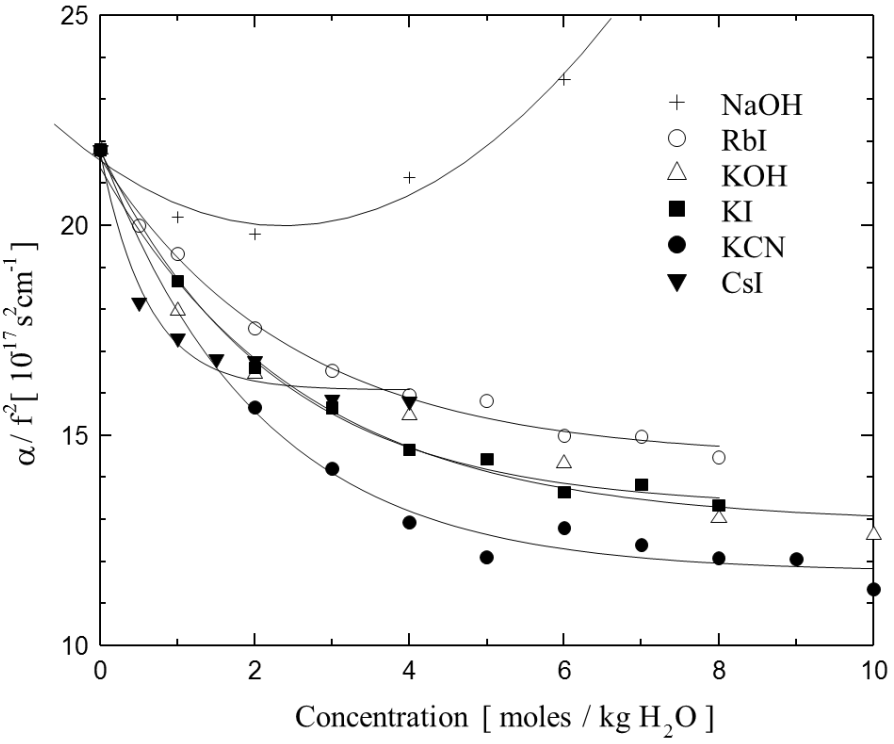

Figure 2.8: Attenuation of sound versus molality of the solution for various group IA salts. Curves are to guide the eye. Data taken from Attal & Quate[21]. The largest reduction in the attenuation takes place for solutions with K^+ ions, which was also observed in by Breitschwerdt, Kistenmacher, and Tamm[28]

There are several practical disadvantages to using a solute to inhibit relaxation mechanisms in the coupling fluid of an acoustic microscope. First, many of the most desirable substances are acutely toxic, like KCN. Second, the attenuation and sound velocity of the resulting solution depend on concentration, which must be accurately known and maintained during the course of the experiment in order to perform quantitative measurements. Finally, many of the resulting solutions will destroy the sample being studied.

2.4 Application of Picosecond Ultrasonics to Acoustic Microscopy

2.4.1 Sound velocity and attenuation in water

Of all liquids, water is the one whose sound velocity and attenuation have been measured the most. Table 2.2 summarizes some of the published data for the attenuation of sound in water. At all the temperatures at which measurements have been made, the attenuation has been found to be described by Eq. 2.9. Pinkerton[29] measured the attenuation at frequencies of 7.5 – 67.5 MHz using a pulse echo technique. Smith and Beyer[30] and Fox and Rock[31] measured the attenuation for frequencies in the 10-40 MHz range by using a balance technique, where the force on a submerged object due to radiation pressure as a function of distance away from a cw source was measured. Attal and Quate[21] measure the attenuation and sound velocity in a frequency range of 250 MHz to 4 GHz using a cw technique. Yang *et al.*[32] measured the attenuation using a pulse echo technique up to a frequency of 11 GHz.

For all frequencies at which the velocity of sound has been measured, no measurable dispersion has been detected. Barthel and Nolle[33] measured the velocity of sound at frequencies of 5, 15, and 25 MHz in water at temperatures of 25, 40, and 60 ^{o}C. The difference in the sound velocity at 5 and 25 MHz was smaller than 5 parts per 10,000, which is the limit of the sensitivity of their apparatus. Using a pulse-echo method, McSkimin[34] measured the velocity of sound in water at frequencies of 20, 60, and 100 MHz for water at 25 ^{o}C, and 20, 100, and 180 MHz for water at 74 ^{o}C (the temperature where the sound velocity reaches a maximum) and saw no evidence of dispersion. Carnevale *et al.* [35] measured the sound velocity in water at frequencies of 10, 30, and 70 MHz for water at temperatures 0 to 40 ^{o}C, and they also reported no evidence of dispersion. Yang *et al.*[32] report no evidence of dispersion for frequencies approaching 11 GHz for water at 25 – 80 ^{o}C.

T [^{o}C]	$A = \alpha f^{-2}$ $\left[10^{-17} \mathrm{s}^2 \cdot \mathrm{cm}^{-1}\right]$					
	Yang *et al.* (2010)	Attal and Quate (1976)	Kistenmacher and Breitschwerdt (1972)	Smith and Beyer (1948)	Fox and Rock (1946)	Pinkerton (1947)
0				69.5	68.5	56.9
4					50.5	
5			34.4	48.5	47.5	44.1
10			24	38.5	36.5	35.8
15		29.3			29	29.8
20		25.3	15.7	26.5	24	25.3
25	20.5	21.8			21.5	
30	15.9	19.4	11.8	20	20.5	19.10
33					20	
34	13					
40	12.5	14.7	8.7	16		14.61
50	10.6	12.1	6.6	13.5		11.99
60	8.5		5	11.5		10.15
70	8.1			9.5		8.71
80	8.8		3.4	8		7.89
90						7.24
100						6.87

Table 2.2: Summary of some of the measurements of the acoustic attenuation in water. Experiments have probed frequencies from 7.5 MHz to 11 GHz, and over this range water has obeyed a frequency square law.

2.4.2 Propagation of sound pulses in water

The above results show that for frequencies up to at least 11 GHz the attenuation in water obeys a frequency squared law, and there is no evidence of any dispersion. We now consider the effect of the attenuation on the propagation of a strain pulse in a fluid with specified initial shape.

First, consider an initial situation in which at time zero a right-going Dirac delta-function strain pulse has been launched at the origin. In the absence of attenuation the strain at later times would be given by

$$\eta(z,t) = \delta(z - vt). \qquad 2.12$$

As time develops each Fourier component making up this pulse will be attenuated at a rate proportional to the square of its frequency or, equivalently, the square of its wave number. As a result, the Fourier spectrum of the pulse changes from being a constant to become a Gaussian. The pulse shape then also becomes a Gaussian centered at $z = vt$. The profile of the pulse is given by

$$\eta(z,t) = \frac{1}{\sigma(t)\sqrt{\pi}} \exp\left[-\left(\frac{z - vt}{\sigma(t)} \right)^2 \right], \qquad 2.13$$

where the width parameter σ is given by

$$\sigma(t) = \frac{1}{\pi}\left(Av^3 t \right)^{1/2}. \qquad 2.14$$

The full width at half maximum (FWHM) of the strain pulse is $2(\ln 2)^{1/2}\sigma$. The width of the pulse is proportional to the square root of the distance that the pulse has propagated. In Figure 2.9 the FWHM of the pulse, calculated from Eq. 2.14, is plotted as a function of the propagation distance for water temperatures of 25 and 50 ^{o}C.

The results for the Dirac delta function initial condition can be used to calculate the change in shape for a pulse with any initial shape. If the initial shape of the pulse at time zero (again right-going) is $\eta_0(z)$, then the shape at time t will be

$$\eta(z,t) = \frac{1}{\sigma(t)\sqrt{\pi}} \int \eta_0(z') \exp\left[-\left(\frac{z - z' - vt}{\sigma(t)} \right)^2 \right] dz'. \qquad 2.15$$

As an example, consider an initial rectangular pulse

$$\eta_0 = \begin{cases} 1 & |z| \le L/2 \\ 0 & |z| > L/2 \end{cases} \qquad 2.16$$

The strain profile becomes

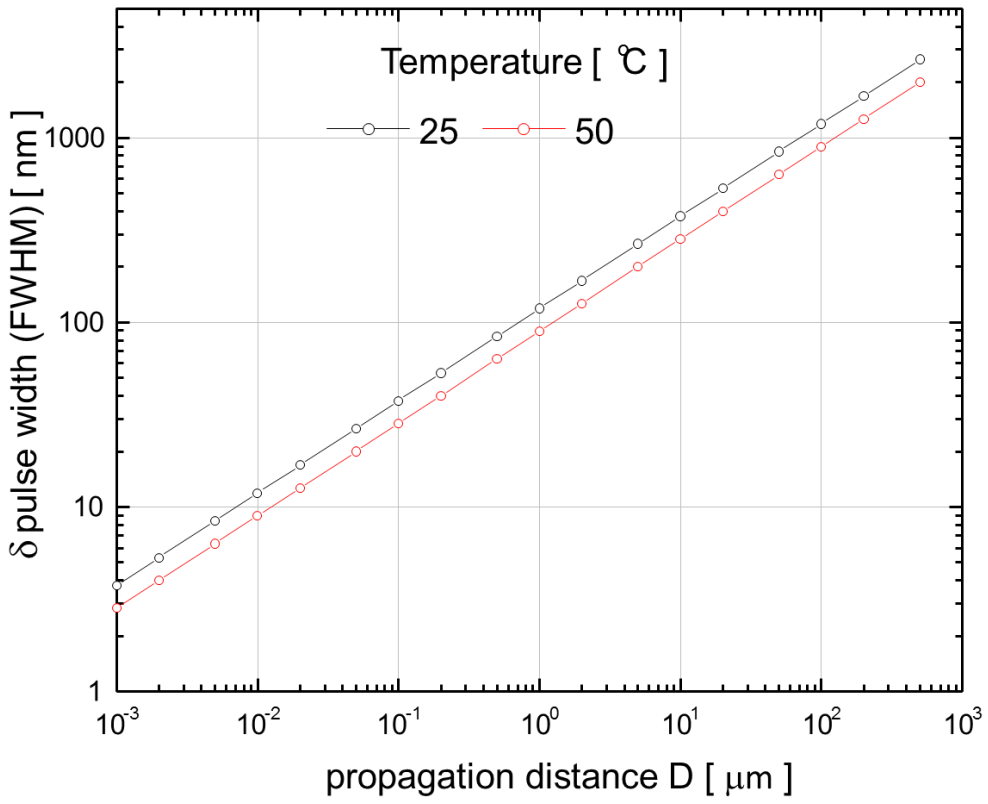

Figure 2.9: Full width half maximum (FWHM) of a pulse whose initial profile was a delta function versus propagation distance for water at 25 and 50 ^{o}C.

$$\eta(z,t)=\frac{1}{\sigma(t)\sqrt{\pi}}\int_{-L/2}^{L/2}\exp\left[-\left(\frac{z-z'-vt}{\sigma(t)}\right)^{2}\right]dz'. \qquad 2.17$$

By a suitable transformation of variables the strain can be expressed as

$$\eta(z,t)=\frac{1}{2}\left[\operatorname{erf}\left(\frac{z-vt}{\sigma}+\frac{L}{2\sigma}\right)-\operatorname{erf}\left(\frac{z-vt}{\sigma}-\frac{L}{2\sigma}\right)\right], \qquad 2.18$$

where the error function is defined as the value of the definite integral

$$\operatorname{erf}(x)=\frac{2}{\sqrt{\pi}}\int_{0}^{x}\exp\left[-\xi^{2}\right]d\xi. \qquad 2.19$$

For a strain pulse whose initial profile is described by Eq. 2.16 with L = 10 nm, the pulse profile after propagating through 50, 100, 200, 500, and 1000 nm of water at room temperature is plotted in Figure 2.10a. The difference between the FWHM of the pulses after propagation for a distance D compared to that for a delta pulse is shown in Figure

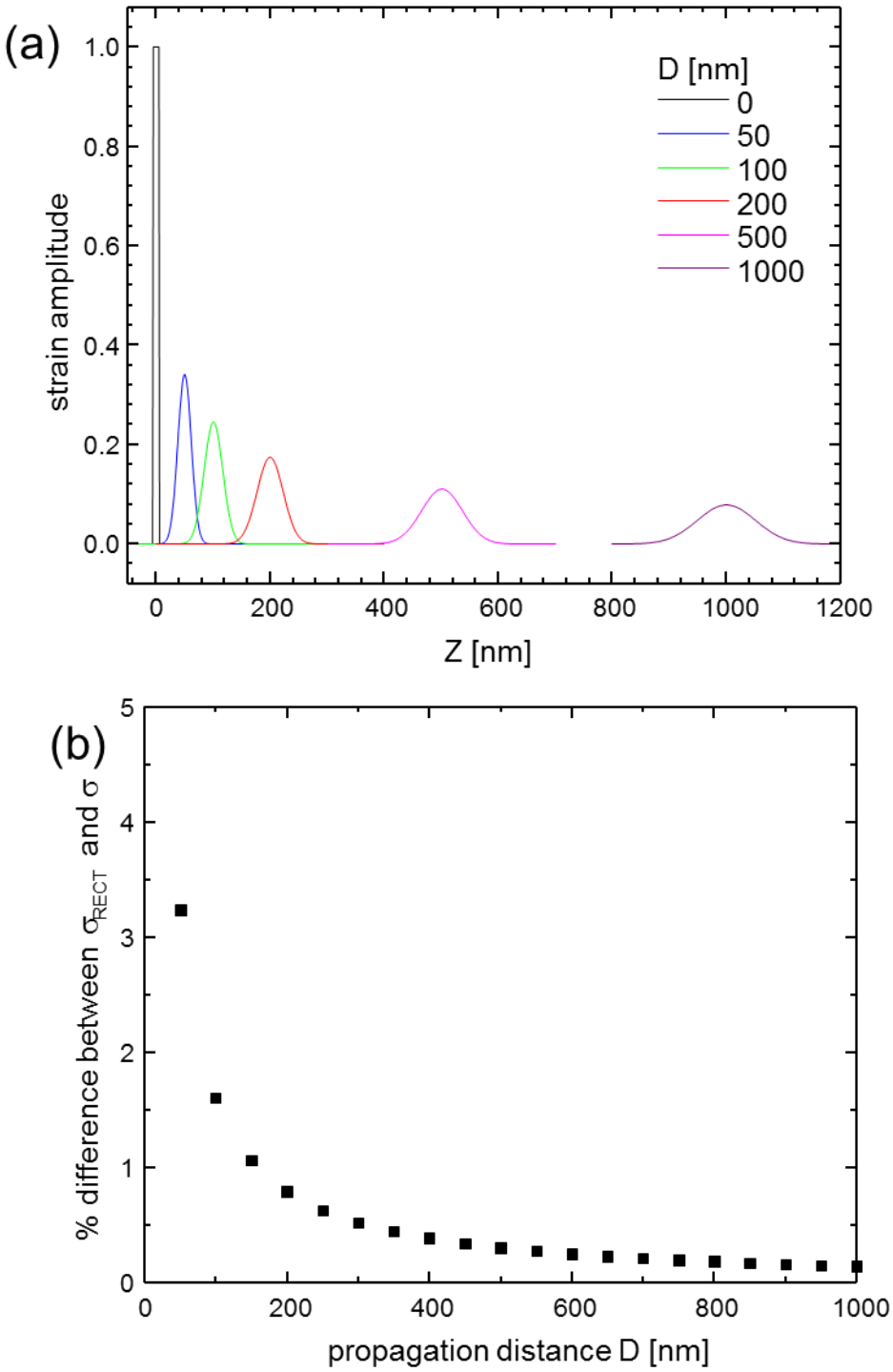

Figure 2.10: a) Strain profile in the water for selected propagation distances evaluated using Eq. 2.18. b) Percent difference in the FWHM of the plots on the left and the results for a pulse whose initial profile was a Dirac delta function.

2.10b. After propagating through 200 nm of water at room temperature, there is less than a 1% difference in the pulse FWHM obtained using 2.18 and using the result for the delta function initial condition.

2.4.3 Detecting attenuated pulses – a feasibility estimate

As discussed in section 2.3, the resolution of a reflection acoustic microscope is limited by the duration of the acoustic pulses that can be generated by the transducer device. Transducers based on piezoelectric materials and RF electronics can generate sound pulses and tone bursts with durations on the order of nanoseconds. The picosecond ultrasonics technique, however, can be used to generate acoustic pulses with durations on the order of picoseconds. Pulses this short remove the previous limits on the lens sizes, and a smaller lens can be used. Acoustic pulses with picosecond durations open up the opportunity to do acoustic microscopy with lenses whose radii of curvature are in the range of 0.5-2.5 μm.

To consider the feasibility of this approach, we imagine a simple experiment (Fig. 2.11) in which a short acoustic pulse is generated using the picosecond ultrasonics technique, propagates across a water layer, is reflected at the surface of a sample, and then returns to the Al layer to be detected. For simplicity, in this set up there is no acoustic lens. We would like to estimate the magnitude of the returning strain pulse and the resulting change in reflectivity.

For an interface between two materials, the reflection coefficient for a strain wave depends on the characteristic acoustic impedance of the media, $Z = \rho v$, where ρ is the density and v is the sound velocity. For a 1D strain wave propagating from medium a to medium b, the reflection and transmission coefficients for the strain are given by

$$T = \frac{v_a}{v_b}\frac{2Z_a}{Z_a + Z_b}, \qquad R = \frac{Z_b - Z_a}{Z_a + Z_b}\ . \tag{2.20}$$

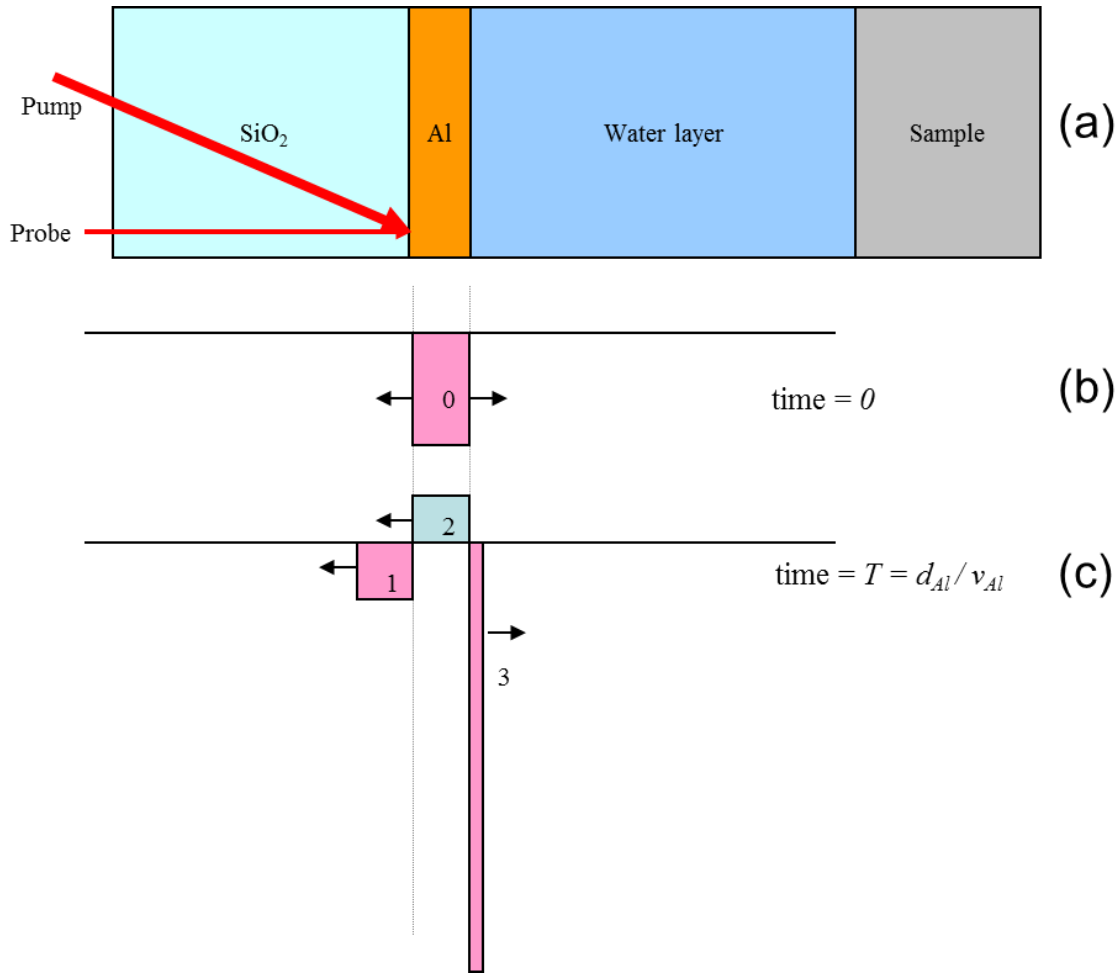

Figure 2.11: a) Schematic of the films. Strain pulses generated in the thin Al film propagate through the water, reflect off of the sample, and return to the thin Al film, where they are detected by a time delayed probe pulse. b) Initial strain generated by the pump pulse. The strain is assumed to be uniform throughout the film. c) Strain profile at a time *T*, which is the time it takes for the sound to propagate through the Al film once. For an Al film that is perfectly matched acoustically to the SiO_2 substrate, only three rectangular pulses are generated.

To simplify the analysis, we assume that the Al film and the SiO_2 substrate are matched acoustically, *i.e.*, their characteristic acoustic impedances are the same. Thus $R_{Al/SiO_2} = 0$. We consider the sample to be rigid so that $R_{Water/Sample} = 1$.

Assume that the aluminum film has a thickness d_{Al} and that after excitation by the pump pulse a uniform strain of η_0 is set up throughout the film. Figure 2.11b-c shows the strain pulses that are generated by the pump beam excitation. Rectangle 0 shows the

initial strain that is generated in the aluminum film. When this initial strain relaxes it will launch a strain pulse in each direction. Since the Al film is assumed to be perfectly matched with the substrate, the pulse propagating to the left will get transmitted into the substrate with no reflection at the Al/SiO_2 interface; this corresponds to rectangle 1. The pulse propagating to the right will encounter the Al/water interface, where a portion will be transmitted into the fluid (rectangle 3), and a portion will be reflected (rectangle 2). Since the acoustic impedance of the water is lower than that for the Al film, the strain that is reflected from the Al/water interface will change sign. This reflected pulse will then propagate into the SiO_2. Therefore, for an Al film that is perfectly matched to the SiO_2 substrate, only a single acoustic pulse will be launched into the water. The strain pulse that gets launched into the water will have a width of

$$d_{Water} = d_{Al}\left(\frac{v_{Water}}{v_{Al}}\right), \tag{2.21}$$

and a strain amplitude of

$$\eta_{Water} = \frac{1}{2}\eta_0 T_{Al/Water}\,. \tag{2.22}$$

The factor of ½ enters because only half of the strain in the Al moves in the direction towards the water. Using the results from section 2.4.3, this rectangular strain pulse will evolve into a shape that is well approximated by a Gaussian of the form

$$\eta(z,t) = \frac{\eta_{Water} d_{Water}}{\sigma(t)\sqrt{\pi}} \exp\left[-\left(\frac{z}{\sigma(t)}\right)^2\right], \tag{2.23}$$

where here the time *t* is the time of propagation <u>in the water</u> and *z* is the distance from the center of the propagating pulse. This expression is correct if the width $\sigma(t)$ is large compared to the width d_{Water} of the pulse when it enters the water.

When the returning pulse reenters the Al, the strain amplitude changes by a factor $T_{Water/Al}$ and the width of the pulse increases by a factor of v_{Al} / v_{Water}. The peak strain of the returning pulse, once it enters the Al film, is given by

$$\eta_{peak} = T_{Water/Al}\frac{\eta_{Water}d_{Water}}{\sigma(t)\sqrt{\pi}} = 2\frac{\eta_0 d_{Al}}{\sigma(t)\sqrt{\pi}}\left(\frac{v_{Water}}{v_{Al}}\right)\frac{Z_{Water}Z_{Al}}{\left(Z_{Water}+Z_{Al}\right)^2}. \qquad 2.24$$

Table 2.4 shows the peak strain that returns to the Al film for several propagation distances, taking v_{Water} = 1.5 nm ps^{-1}, v_{Al} = 6.4 nm ps^{-1}, and $Z_{Al}/Z_{Water} = 11.5$.

Propagation distance *D* [nm]	η_{peak}/η_0 [%]
100	3.4
200	2.2
500	1.5
1000	1.1

Table 2.4: Peak of the returning strain pulse in the aluminum film for different propagation distances, expressed as a percentage of the initial strain in the film.

Detecting strain pulses after they have been attenuated by the water layer presents two main difficulties. The first is that the amplitude of the strain pulse has been significantly decreased by acoustic attenuation in the water. The second is that the strain pulse, which was initially quite short, has now been extended so that its FWHM is on the order of hundreds of nm. The probe beam is only sensitive to perturbations in the optical properties that take place within a distance on the order of ξ, the optical penetration depth. For Al this will be approximately 10 nm, and the probe beam will only be sampling narrow parts of the returning strain pulse.

In an experiment like this, there are two efficiencies that need to be improved: the generation efficiency, which is measured by the magnitude of the initial strain generated, and the detection efficiency, which can be expressed as the change in reflectivity per unit strain. To improve the generation, the launched strain pulse can be made larger by increasing the power per unit area of the pump beam. However, a film of Al is only going to absorb perhaps 20% of the incident power, the rest of which is reflected. The detection efficiency is ultimately limited by the piezo-optic coefficients for the material.

Most materials have piezo-optic coefficients on the order of unity, which means that the change in reflectivity is going to be the same order of magnitude as the strain.

Since the returning sound pulse is extended in nature, the detection efficiency can be increased by replacing the single Al film with an extended thin film structure, with a total thickness comparable to the width of the returning strain pulse, and whose optical reflectivity is sensitive to the total strain within it. This structure, reffered to as an opto-acoustic transducer, takes the incoming light and turns it into a propagating strain pulse, and experiences significant changes in reflectivity when a returning sound pulse propagates through the structure. The design, fabrication, and characterization of such a structure are considered in chapter 4.

2.5 Planar Opto-acoustic Microscopy

In the proposed scanning opto-acoustic microscope (SOAM), shown in Figure 2.12a, the laser generated sound pulses are focused by an acoustic lens, and the sample is

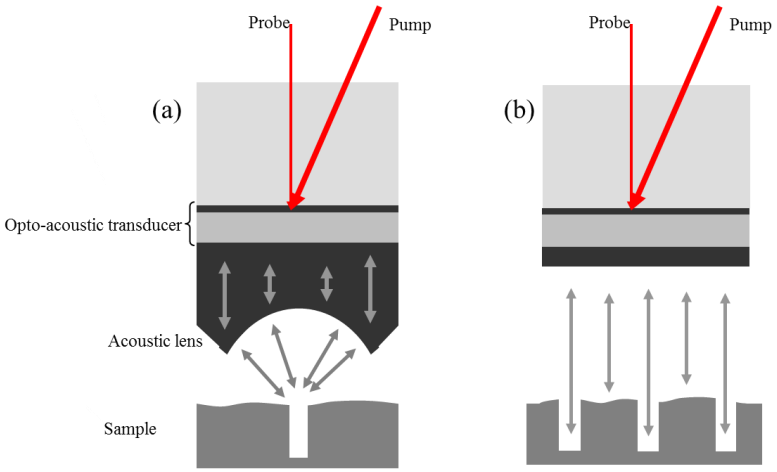

Figure 2.12: a) Scanning opto-acoustic microscope. Sound generated in the opto-acoustic transducer is focused by the acoustic lens onto individual features of a sample. Mechanical scanning of the sample is used to form an image. b) Planar opto-acoustic microscope. Sound generated in the transducer is launched directly into the coupling fluid, and groups of features on the sample are probed at once.

mechanically scanned to form an image point by point. The spherical lens takes the planar waves generated by the transducer and focuses them to an approximately spherically converging wave on the sample. In the planar opto-acoustic microscope

(POAM), shown in Figure 2.12b, the planar waves are launched into the coupling fluid directly. The spatial resolution of the SOAM is determined by the focusing properties of the acoustic lens, while the spatial resolution of the POAM is determined by the excitation area, *i.e.*, the focused spot size of the laser. However, by examining a periodic array of structures, average properties of the structures, such as height, can be measured.

Bibliography

1. Zewail, A.H. "Laser Femtochemistry." *Science* **242**, 1645 -1653 (1988).
2. Dantus, M., Bowman, R.M. & Zewail, A.H. "Femtosecond laser observations of molecular vibration and rotation." *Nature* **343**, 737-739 (1990).
3. Shah, J. *Ultrafast Spectroscopy of Semiconductors and Semiconductor Nanostructures*. (Springer Verlag: Berlin, 1999).
4. Min, C., Cahill, D.G. & Granick, S. "Time-resolved ellipsometry for studies of heat transfer at liquid/solid and gas/solid interfaces." *Rev. Sci. Instrum.* **81**, 074902 (2010).
5. Tas, G. & Maris, H.J. "Picosecond ultrasonic study of phonon reflection from solid-liquid interfaces." *Phys. Rev. B* **55**, 1852 (1997).
6. Thomsen, C., Grahn, H.T., Maris, H.J. & Tauc, J. "Surface generation and detection of phonons by picosecond light pulses." *Phys. Rev. B* **34**, 4129 (1986).
7. Tas, G. & Maris, H.J. "Electron diffusion in metals studied by picosecond ultrasonics." *Phys. Rev. B* **49**, 15046 (1994).
8. Lemons, R.A. & Quate, C.F. "Acoustic Microscopy" in *Physical Acoustics: Principles and Methods XIV*. (Academic Press: New York, 1979).
9. Lemons, R.A. "Acoustic microscope-scanning version." *Appl. Phys. Lett.* **24**, 163 (1974).
10. Lemons, R.A. "Integrated circuits as viewed with an acoustic microscope." *Appl. Phys. Lett.* **25**, 251 (1974).
11. Wilson, R.G. & Weglein, R.D. "Acoustic microscopy of materials and surface layers." *J. Appl. Phys.* **55**, 3261 (1984).
12. Hammer, R. "Enhancing micrographs obtained with a scanning acoustic microscope using false-color encoding." *Appl. Phys. Lett.* **40**, 678 (1982).
13. Poirier, M., Castonguay, M., Neron, C. & Cheeke, J.D.N. "Nonplanar surface characterization by acoustic microscopy." *J. Appl. Phys.* **55**, 89 (1984).
14. Guangqi, Y., Nikoonahad, M. & Ash, E. "Pulse-compression subsurface acoustic microscopy." *Electron. Lett.* **18**, 767-769 (1982).
15. Wang, J.K. & Tsai, C.S. "Reflection acoustic microscopy for thick specimens". *J. Appl. Phys.* **55**, 80 (1984).
16. Morozov, A. & Kulakov, M. "Single lens transmission scanning acoustic microscope." *Electron. Lett.* **16**, 596-597 (1980).
17. Kushibiki, J., Ohkubo, A. & Chubachi, N. "Theoretical analysis for *V(z)* curves obtained by acoustic microscope with line-focus beam." *Electron. Lett.* **18**, 663-664 (1982).
18. Nongaillard, B., Rouvaen, J.M., Bridoux, E., Torguet, R. & Bruneel, C. "Visualization of thick specimens using a reflection acoustic microscope. " *J. Appl. Phys.* **50**, 1245 (1979).
19. Atalar, A. & Hoppe, M. "High-performance acoustic microscope." *Rev. Sci. Instrum.* **57**, 2568 (1986).
20. Hadimioglu, B. "Water acoustic microscopy at suboptical wavelengths." *Appl. Phys. Lett.* **43**, 1006 (1983).
21. Attal, J. & Quate, C.F. "Investigation of some low ultrasonic absorption liquids". *J. Acoust. Soc. Am.* **59**, 69-73 (1976).

22. Jipson, V.B. "Acoustic microscopy of interior planes. "*Appl. Phys. Lett.* **35**, 385 (1979).
23. *Scanned Image Microscopy*. (Academic Press: London, 1980).
24. Briggs, A. "Acoustic microscopy-a summary." *Rep. Prog. Phys.* **55**, 851-909 (1992).
25. Foster, J.S. "High resolution acoustic microscopy in superfluid helium." *Appl. Phys. Lett.* **42**, 869 (1983).
26. Muha, M.S., Moulthrop, A.A., Kozlowski, G.C. & Hadimioglu, B. "Acoustic microscopy at 15.3 GHz in pressurized superfluid helium." *Appl. Phys. Lett.* **56**, 1019 (1990).
27. Blandamer, M.J. *Introduction to Chemical Ultrasonics*. (Academic Press: London, 1973).
28. Breitschwerdt, K., Kistenmacher, H. & Tamm, K. "Ultrasonic absorption and structure of ionic solutions." *Physics Letters A* **24**, 550-551 (1967).
29. Pinkerton, J.M.M. "A Pulse Method for the Measurement of Ultrasonic Absorption in Liquids: Results for Water." *Nature* **160**, 128 (1947).
30. Smith, M.C. & Beyer, R.T. "Ultrasonic Absorption in Water in the Temperature Range 0-80^{o}C." *J. Acoust. Soc. Am.* **20**, 608-610 (1948).
31. Fox, F.E. & Rock, G.D. "Compressional Viscosity and Sound Absorption in Water at Different Temperatures." *Phys. Rev.* **70**, 68 (1946).
32. Yang, F. et al. "Picosecond ultrasonic experiments with water and its application to the measurement of nanostructures." *J. Appl. Phys.* **107**, 103537 (2010).
33. Barthel, R. & Nolle, A.W. "A Precise Recording Ultrasonic Interferometer and Its Application to Dispersion Tests in Liquids." *J. Acoust. Soc. Am.* **24**, 8-15 (1952).
34. McSkimin, H.J. "Ultrasonic Pulse Technique for Measuring Acoustic Losses and Velocities of Propagation in Liquids as a Function of Temperature and Hydrostatic Pressure." *J. Acoust. Soc. Am.* **29**, 1185-1192 (1957).
35. Carnvale, A., Bowen, P., Basileo, M. & Sprenke, J. "Absolute Sound-Velocity Measurement in Distilled Water." *J. Acoust. Soc. Am.* **44**, 1098-1102 (1968).

Chapter 3
Experimental Apparatus

3.1 Introduction

This chapter contains a detailed examination of the apparatus used. Section 3.2 presents the pump probe setup at the component level. In chapter 2, the concept of planar opto-acoustic microscopy (POAM) was introduced. After a discussion of the stability requirements, section 3.3 presents the design, construction, and testing of a sample positioning stage suitable for POAM measurements.

3.2 The pump probe setup

In section 2.2, a brief sketch of the picosecond ultrasonics technique was presented. In this section more details about the apparatus used for this work are presented, along with results of some pump-probe measurements that are used to demonstrate the performance of the apparatus.

3.2.1 General comments

Figure 3.1 shows a schematic of the pump-probe setup used in this work. The output of the laser is split into a pump beam and a probe beam by a combination of a half-wave plate and polarizing beam splitter. The laser is a mode-locked Ti:Sapphire laser with repetition rate of 80 MHz and transform limited pulses with durations of approximately 200 fs. The center wavelength of the laser was tunable over a range of 780 – 830 nm, but for most of the experiments presented in this work, the wavelength was not modified during the course of a measurement.

Since the magnitude of the changes in reflectivity is small, lock-in detection was used. The pump beam was modulated by an electro-optic modulator (EOM) at a frequency of 1 MHz, and the modulation depth, defined as $\left(P_{MAX} - P_{MIN}\right) / P_{MAX}$, was measured to be 0.95. This modulation of the amplitude of the pump beam caused a modulation of the reflectivity of the sample, and therefore caused a small modulation in the amplitude of the reflected probe beam. The 1 MHz component of the signal coming from the probe photo-detector was recorded by the lock-in amplifier.

To vary the time delay of the probe relative to the pump, the probe beam was directed onto a corner cube retro-reflector mounted onto a translation stage such that the direction of travel of the stage was parallel to that of the beam. By using two corner cubes on the translation stage, moving the stage a distance *d* delayed the arrival time of the probe beam by *4d / c*, where *c* is the velocity of light in vacuum. The maximum probe delay available in the current configuration was around 7 ns, but in the experiments described

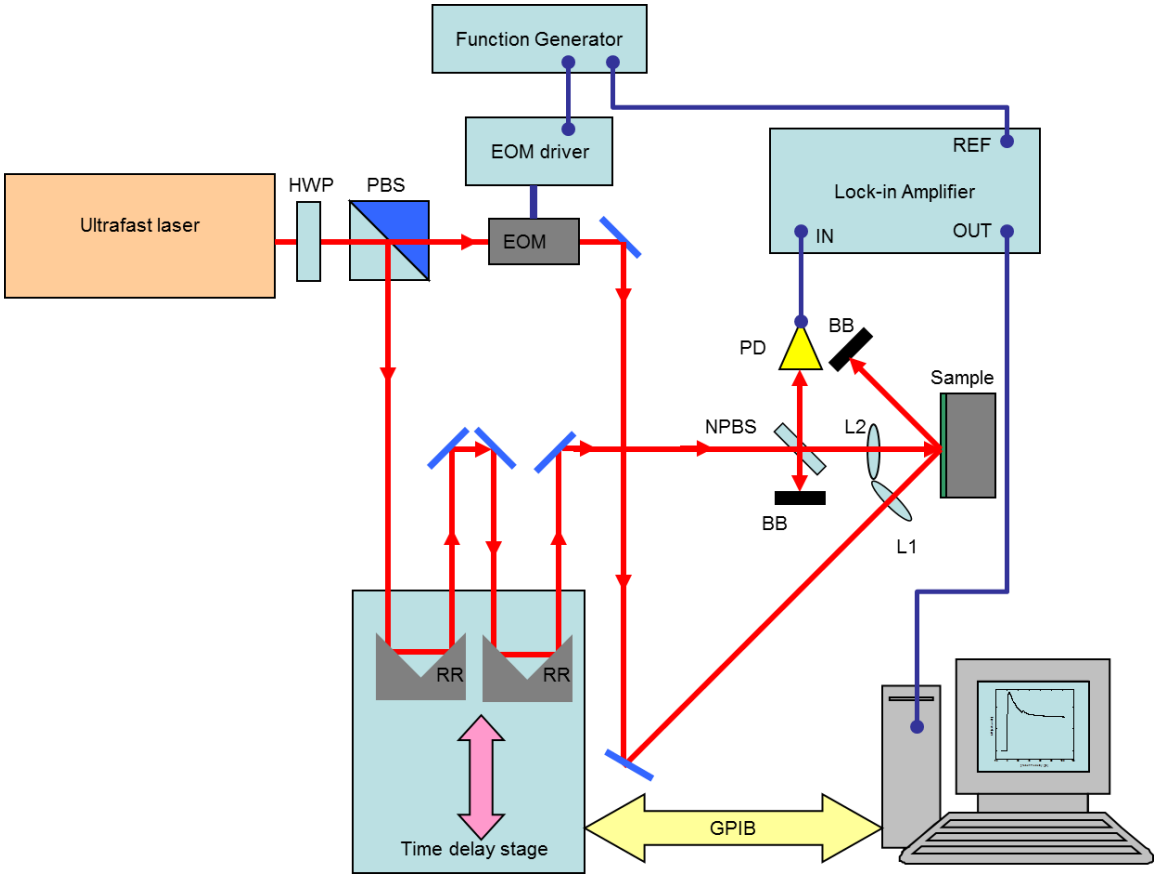

Figure 3.1: Diagram of the basic pump probe setup used to perform picosecond ultrasonics measurements. HWP – half wave plate, PBS- polarizing beam splitter cube, EOM – electro-optic modulator, NPBS – non-polarizing beam splitter, BB – beam block, L1 – pump lens, L2 – probe lens, PD – photodetector, RR – corner cube retro-reflector.

in this work the probe time delay was kept below 2 ns. For delays longer than this, beam walk and beam divergence effects became apparent[1].

The pump and probe beam were focused onto the sample with anti-reflective coated plano-convex lenses with focal lengths of either 5 or 10 cm. With 10 cm focal length lenses, the spatial distribution of the intensity of the focused pump and probe beams was measured to have a FWHM of 18 μm. The reflected probe light was collected and focused onto a photodetector. The output of the photodetector was directed to a high frequency lock-in amplifier, whose reference frequency input was derived from the same signal that was driving the EOM. The output signal of the lock-in amplifier was proportional to the change in reflectivity of the sample, and by scanning the mechanical

stage, the change in reflectivity versus probe delay time was collected. To further improve the signal to noise ratio, multiple scans were taken and averaged.

3.2.2 Estimate of the smallest fractional change in reflectivity that can be detected

Figure 3.2 shows data taken on a sample consisting of a 30 nm film of gold on a sapphire substrate. The incident probe power was set such that the dc voltage output of the photodetector was 8 V, and the lock-in time constant was set to 1 ms. The solid curve is the average of 116 scans, while the other data set is a single scan. For each scan, 1000 points were acquired in 5 s, *i.e.*, there were 5 lock-in time constants between data points. This acquisition rate was slower that what was usually done; in all the other experiments reported here there were only 1 – 3 lock-in time constants between the data points. For the single scan data, the rms of the points before zero time delay is 0.93 μV, while for the average of 116 scans the rms is 0.07 μV.

Using this, a limit can be placed on the smallest fractional change in reflectivity that can be detected when using this technique both with and without averaging. The fractional change in reflectivity is the quantity $\Delta R / R_0$, where R_0 is the static optical reflectivity, *i.e.*, the intensity reflectivity of the sample when it is not subjected to the pump beam, and ΔR is the change in reflectivity induced by the pump beam. In the pump-probe apparatus described above, an approximation to the fractional change in reflectivity is given by

$$\frac{\Delta R}{R_0} = 2\frac{V_{out}}{V_{dc}}, \qquad 3.1$$

where V_{out} is the output of the lock-in amplifier and V_{dc} is the dc voltage of the photodetector. The factor of 2 in Eq. 3.1 is to account for the voltage divider that is formed by the 50 Ω output impedance of the photodetector and the 50 Ω input impedance of the lock-in amplifier. Equation 3.1 is based on the assumption that the dc responsivity of the detector, *i.e.*, the output voltage of the photodetector per optical power incident on the detector's active area, is the same as that at 1 MHz. To estimate the smallest

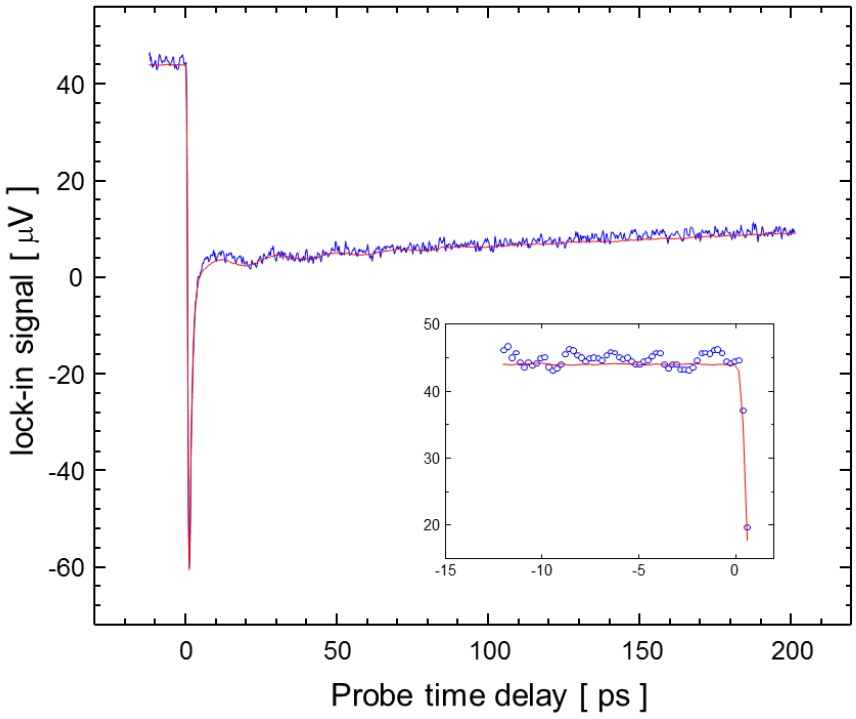

Figure 3.2: Change in reflectivity of a 30 nm gold film on a sapphire substrate. The solid red line is the average of 116 scans, while the blue dots are a single scan. The inset shows the fluctuations in the lock-in output signal before time delay $t = 0$ ps.

fractional change in reflectivity that can be detected, substitute the rms of the data points before zero time delay into Eq. 3.1,

$$\left(\frac{\Delta R}{R_0}\right)_{\min} = 2\frac{V_{rms}}{V_{DC}}. \qquad 3.2$$

For the single scan, $\left(\frac{\Delta R}{R_0}\right)_{\min} = 2\times10^{-7}$, whereas after averaging 116 traces,

$\left(\frac{\Delta R}{R_0}\right)_{\min} = 2\times10^{-8}$.

3.3 Design, Construction, and Testing of a Precision Z-tip-tilt stage

The stability and positioning requirements for POAM are markedly different from the requirements for most other scanning microscopy measurements. After summarizing the

stability and precision requirements for the POAM measurements, the relevant details of the construction and characterization of the positioning system are presented

3.3.1 Stability requirements for POAM measurements

In a POAM measurement there are three critical degrees of freedom between the optoacoustic transducer and the sample: the gap *d* and the tip/ tilt angles θ_X and θ_Y, as shown in Figure 3.3. The most critical requirement for the POAM measurement is that the gap remains fixed; the primary purpose of the stage is to maintain the gap during the course of a measurement. In what follows, the term Z-drift refers to slow changes in the gap *d* that take place on the time scale of minutes, whereas Z-fluctuation refers to changes that take place on the time scale of milliseconds to seconds. Z-drift and Z-fluctuation both need to be minimized.

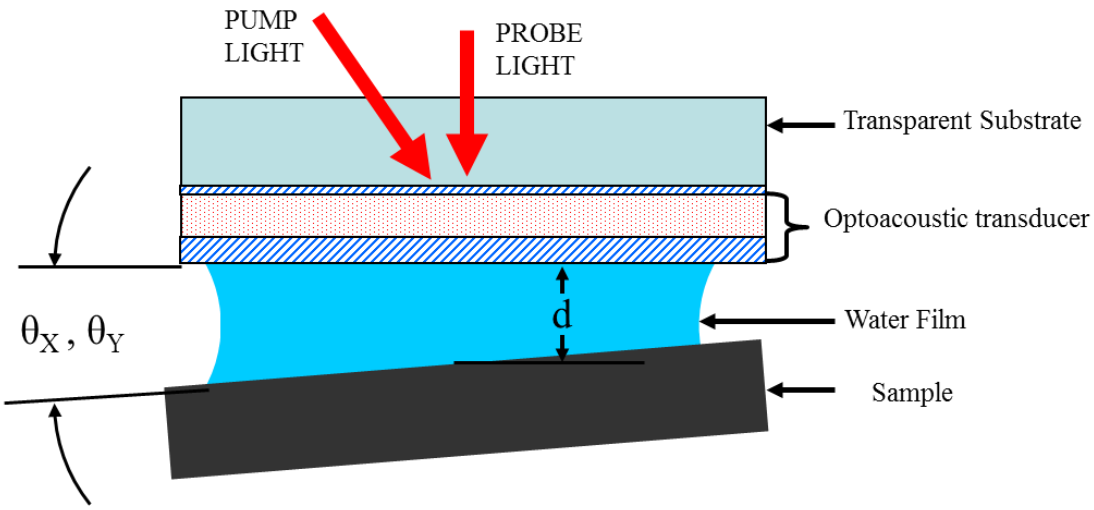

Figure 3.3: The critical degrees of freedom in a POAM measurement are the gap between the sample and the optoacoustic transducer, *d*, and the tip-tilt angles θ_X and θ_Y.

To estimate the allowable amounts of Z-drift and Z-fluctuation, consider a sample which is a planar piece of rigid material. The sound pulse launched by the optoacoustic transducer into the water reflects off of this sample and returns to the transducer. The change in the reflectivity of the probe light is assumed to be proportional to the pressure in the fluid at the transducer/water interface. The justifications for this assumption are explained in detail in Chapter 4, but for now the transducer is treated as a structure whose

change in reflectivity is proportional to the excess pressure at the transducer/water interface.

For the estimates of the allowable Z-drift, the measurement time is taken to be 5 minutes, and the gap between the sample and the optoacoustic transducer is assumed to be 500 nm. Using the results of section 2.4, for a sound pulse that travels through 1 μm of water, the width of the returning pulse will be approximately 80 ps. For a pulse of this width the arrival time can typically be detected with an accuracy of 2 ps. This uncertainty in the round trip time is equivalent to a change in the gap of 1.5 nm. This means that the allowable drift for the gap is 0.3 nm min^{-1} for a 5 minute measurement. Five minutes is a typical measurement time when measurements of the reflectivity are made over a full range of probe delay times. For measurements scanning over only a short probe delay time, the measurement time can be reduced and a higher drift rate can be accommodated.

A tip/tilt misalignment will cause a variation in the gap across the focused pump and probe beams. The beams are focused through the glass substrate of the opto-acoustic transducer, and the diameter of the focused spot is typically 30 μm. If the desired variation of the gap across the spot is 1.5 nm (which corresponds to a 2 ps variation in arrival time for an acoustic echo), then the tip/tilt between the transducer and the sample should be adjusted so that the transducer is parallel to the sample with an accuracy better than 50 μrad.

3.3.2 Overview of the main components

The optoacoustic transducer disc is held stationary, with the optics positioned and focused from above and with the sample below. The optoacoustic transducer is held in place by an invar frame. The sample is positioned by three piezo-electric actuators, and the position of the sample relative to the invar frame is measured with three capacitive displacement sensors. During operation, the actuators are constantly adjusted by a controller such that the readings of the capacitive displacements sensors are held constant. Some of the key components are reviewed below.

Figure 3.4 shows a picture of the completely assembled stage, and Figure 3.5 shows the stage with the cavity plate off. Figure 3.6 shows a cross sectional view of the assembled stage. The assembly that holds the optoacoustic transducer is bolted to an invar plate **A**. Three tungsten carbide balls **B** are seated into three hardened 440 stainless steel v-blocks **C** in a type II Kelvin clamp structure[2]. Piezoelectric actuators **H** adjust the sample, mounted on sample plate **K**, with respect to the optoacoustic transducer disc which is held fixed. Capacitive sensors (**L1**) are mounted onto the sample plate, and their corresponding tops (**L2**) are on the cavity plate **A**. The feedback from the capacitive sensors is used to maintain the relative separation between the sample plate **K** and plate **A**.

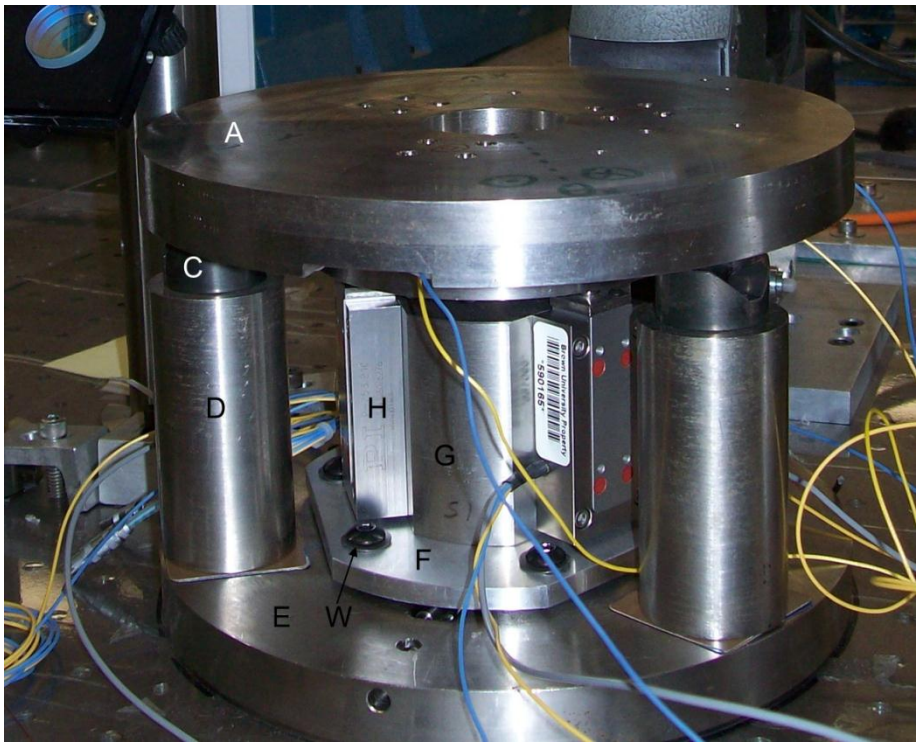

Figure 3.4: Side view of the assembled stage.

The sample plate **K** is coupled to the actuators **H** by three stainless steel balls **I** seated in three small hardened stainless steel v-blocks **J** bolted to the sample plate. The ball-block combination **I-J** is currently only loaded by the dead weight of the sample plate itself. The relative stiffness of the actuator – sample plate coupling can be greatly increased by

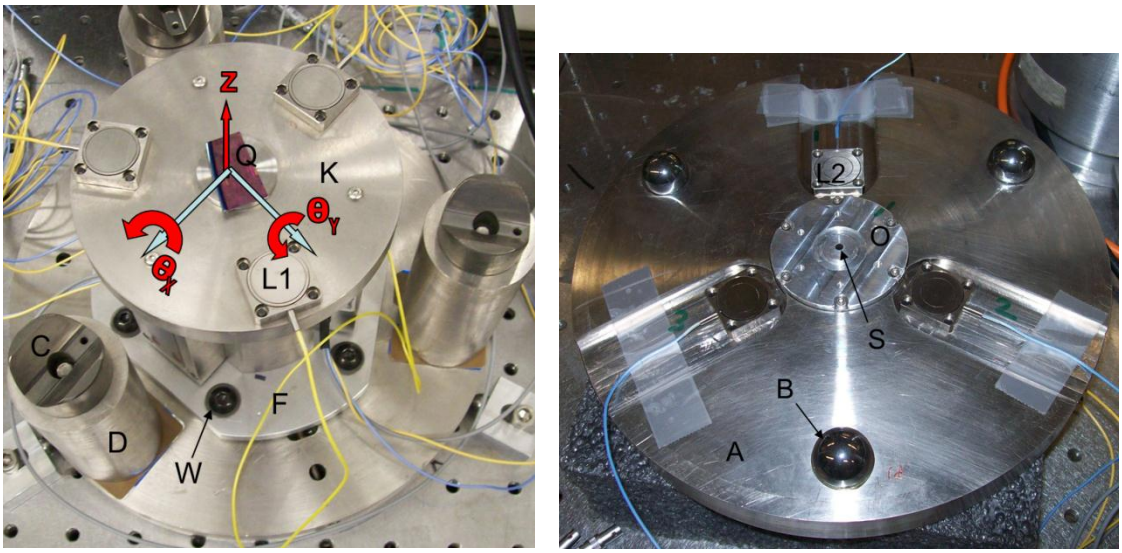

Figure 3.5: Partially disassembled view of the stage. (a) View of the sample and sample plate, with coordinate system labeled. (b) View of the cavity disc S mounted into the fully assembled cavity plate A. The relative position of the sample plate K and the cavity plate A is measured with three capacitive sensors L1-L2.

increasing the loading of the ball – v-block contact. The performance of the unloaded joint was satisfactory for the work reported herein.

Figures 3.7 and 3.8 show enlarged cross-sectional views of the apparatus near the sample. The optoacoustic transducer disc **S** is mounted onto a recess in the disc holder **N**, which is in turn held fixed by a flange **M** bolted to the cavity chuck **O**. The sample is mounted to the sample chuck **P**, which is in turn bolted to the sample plate **K**. Small pieces of aluminum foil (~20 microns thick), or stainless steel shim stock (thickness 2 – 5 mils) are placed between the edge of the sample chuck **P** and the sample plate **K** to provide coarse adjustments of the gap and relative angle between the cavity and the sample. Once the alignment procedure is complete, a drop of the acoustic coupling fluid **R** is placed on the sample **Q**, the plate **A** is placed such that the tungsten carbide balls **B** seat into the v-blocks **C**. After some fine adjustments, the measurement can then begin.

(a) Invar frame

The major components for the frame (**A**, **D**, and **E**) were constructed out of invar. Invar is a low thermal expansion alloy composed of nickel and iron whose properties were first

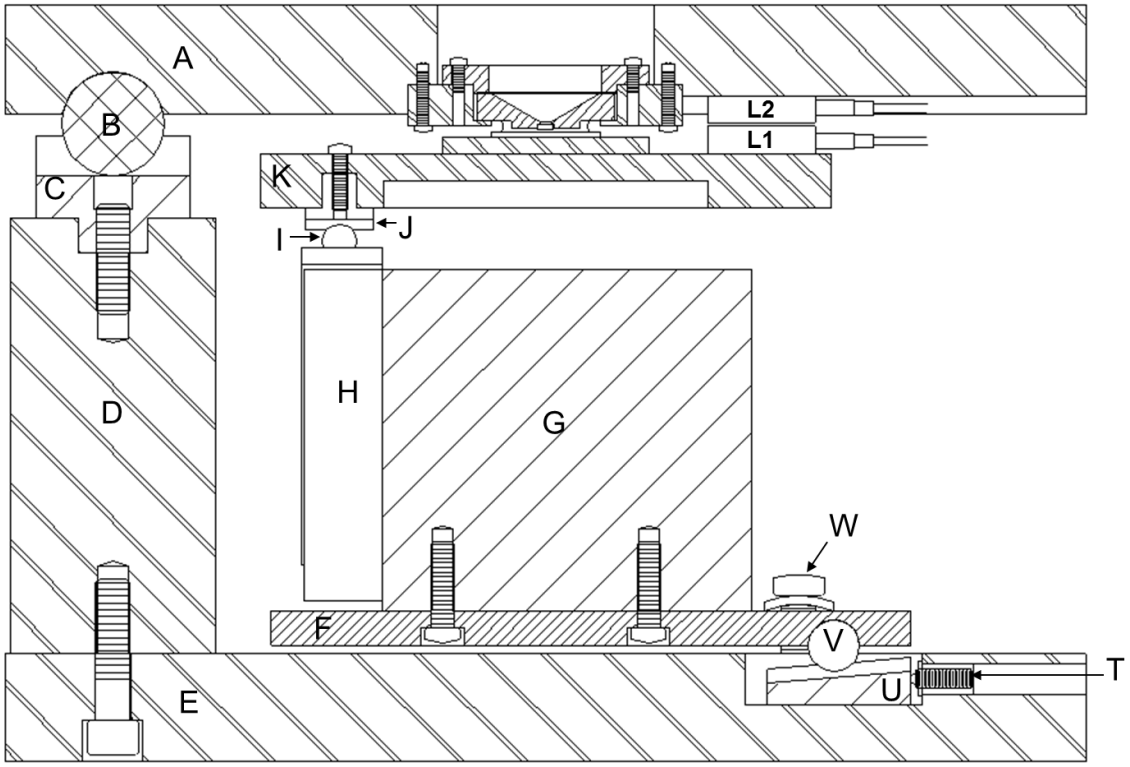

Figure 3.6: Cross sectional view of the assembled stage

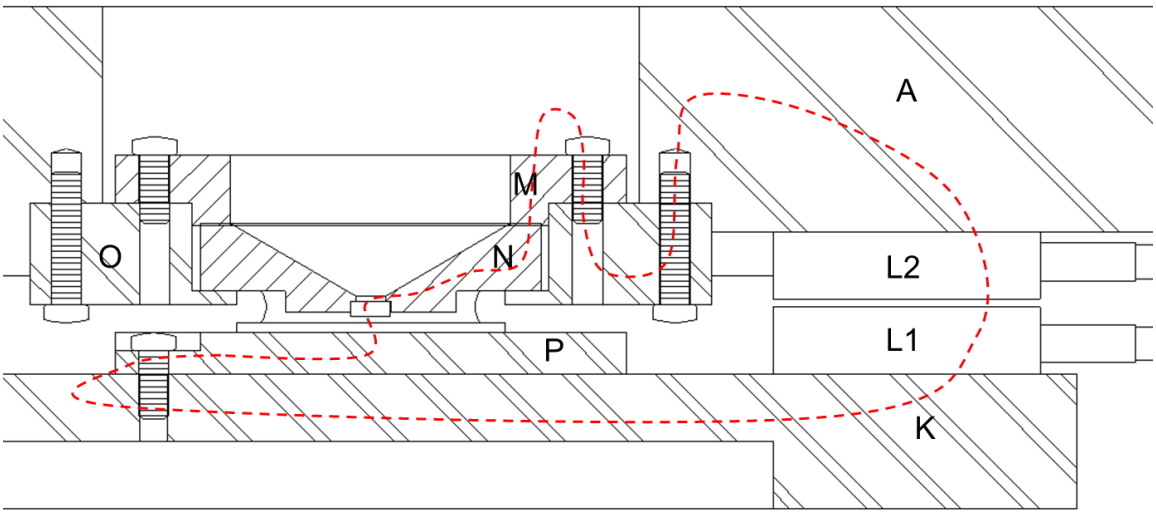

Figure 3.7: Expanded cross sectional view of the assembled stage. The metrology loop is shown as the dotted red line.

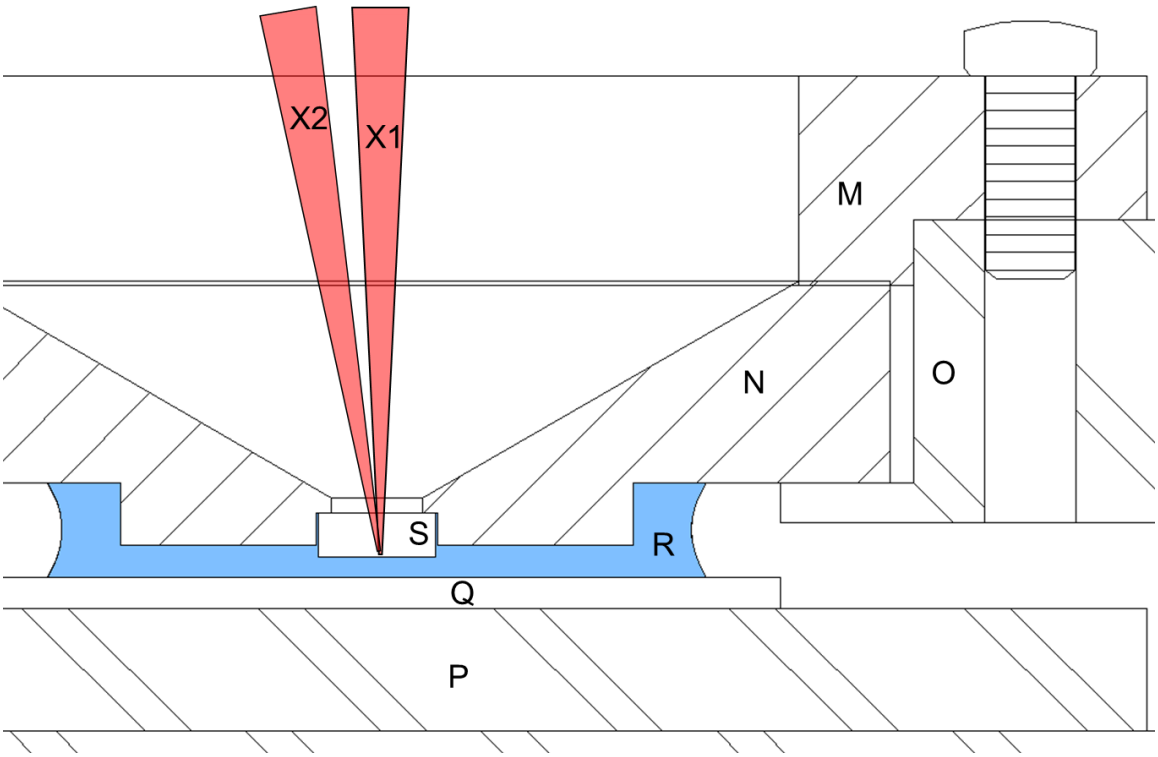

Figure 3.8: Expanded cross sectional view of the disc-sample assembly. The pump beam X2 has an angle of incidence of approximately 8°, while the probe beam is at normal incidence. In the figure, the gap between the optoacoustic transducer disc S and the sample Q has been expanded for clarity; during the POAM measurements the gap is maintained at 0.1 – 2 μm.

studied by Guillaume[3]. Invar is an austenitic material which is ferromagnetic at room temperature with a Curie temperature ~ 260 °C. One of the most common Fe-Ni alloys is Invar 36, where the alloy is 36% Ni, with the balance being Fe and small amounts of other metals. The thermal expansion coefficient of invar is very sensitive to the presence of certain impurities, in particular carbon and magnesium. Lament *et al.*[4], through a series of x-ray studies, were able to show that the solubility of carbon in invar is 0.18 % by weight at 830 °C, and is vanishingly small at room temperatures. Excess carbon present in the alloy will precipitate into graphite islands upon cooling, which significantly raise the thermal expansion. A procedure known as the "MIT triple treatment" has been developed to help avoid the formation of graphite inclusions. The steps of the treatment are:

(1) Heat to 830 °C for 30 minutes, then water quench.
(2) Heat to 315 °C for 60 minutes, then air cool.

(3) Heat to 95 ^{o}C in air for 48 hours, then air cool to room temperature.

The alloy is heated to 830 ^{o}C to dissolve the carbon present, and then quenched quickly (usually a water quench) to suppress the precipitation of graphite inclusions. This rapid cooling introduces some residual stress, which is then relieved with two steps of heating and air cooling. This procedure results in a good balance of low thermal expansion and long term dimensional stability. For our application, long term dimensional stability (measured in ppm/year)[5] is of no concern, since a series of measurements is made over the course of an hour.

Modern invar alloys are available with very low concentrations of carbon. The invar that we used contained 0.037 % carbon by weight for the cavity plate **A** and the base plate **E**, and 0.004% by weight for the main posts D and all the other smaller components (**K**, **O**, and **P**)[6]. All of the invar pieces (**A**, **D**, **E**, **K**, **O**, and **P**), after being machined, were subjected to steps 2 and 3 of the triple treatment to relieve any residual stress from the machining. As received, the thermal expansion coefficient of the invar stock was specified at 2.7 ppm K^{-1} by the supplier[6], however, it should be noted that the thermal expansion coefficient of invar is highly dependent on the history of the specimen. Measurements of the thermal drift of the assembled frame, not discussed herein, were consistent with the thermal expansion being lower than 2 ppm K^{-1}.

(b) Capacitive displacement sensors & piezoelectric actuators

The capacitive sensors, bottom halves **L1** and top halves **L2**, measure the separation between the sample plate **K** and the cavity plate **A**. The capacitive sensors[7] were custom pieces machined from invar. Any thermal expansion of the capacitive sensor itself will be read as an erroneous change in the gap.

The actuators[8] had a range of motion of 25 microns. The bodies of the actuators themselves are 300 series stainless steel. The actuators are bolted to the actuator base **G**. The base material was chosen to be stainless steel so that the base would be matched to the actuator bodies in terms of their thermal expansion coefficient. Any thermal

expansion in the individual actuators will change the gap of the capacitive sensors, and can be corrected.

(c) Coarse adjustment manual stage

The actuators **H** are bolted to the actuator base **G**, which is in turn bolted to base plate **F**. Three small balls **V** are seated on three movable v-blocks **U**. The movable v-blocks are slightly angled, and turning the three screws **T** provides a coarse adjustment of the gaps between the top and bottom halves of each of the capacitive sensors **L1** and **L2**. The ball-block combination is loaded by a set of six screws and spring washers **W**.

The screw **T** has a pitch of 80 threads per inch, so one rotation advances the wedge 318 microns. The wedges have an angle of inclination of 5 degrees, and one rotation of screw **T** will result in approximately 25 microns of vertical elevation. Any slow drift due to thermal effects or slow relaxation of various components (the sides of the wedges are coated with Teflon) will cause a change in the spacings of the capacitive sensors, which can be corrected for by the actuators.

3.3.3 Measuring the stability and performance of the stage

When designing and analyzing a structure with demanding stability requirements, the concept of a metrology loop proves useful. The metrology loop refers to a contour that runs through every part where a drift in the dimensions or relevant properties of that part will cause a change that cannot be distinguished from the quantity that is being measured[2]. The metrology loop is shown in Figure 3.7 as a dashed red line. Any drift of a component within the metrology loop will not be able to be corrected by the sensor-actuator feedback system. Consider, for example, a uniform expansion of the sample chuck **P**. This will cause the gap between the optoacoustic transducer disc **S** and the sample **Q** to decrease, while the gap between the capacitive sensor halves **L1** and **L2** will remain the same. The expansion of the sample chuck, therefore, contributes directly to the drift of the system since it is not picked up by the capacitive sensors. Thermal expansion errors in the metrology loop can be partially compensated by choosing materials with similar expansions for as many parts in the loop as possible[9]. Estimating

the performance of the metrology loop for the sample positioning system described here is difficult due to the bolted joints between pieces **O** and **A** and pieces **O** and **M**. The nanometer scale relaxations of a screw after being tightened and the deformations of bolted joints are problems that are fraught with unknowns. The pieces **M** and **N** were designed such that when flange **M** was bolted to cavity chuck **O**, the disc holder **N** was securely pressed against the lip of cavity chuck **O**. Any relaxation in the joint will mostly expand upward in a line above the cavity disc **S** and not affect the gap between the cavity disc **S** and the sample **Q**. While such a design is not perfect, it represents a compromise between convenience and performance. Given the tests that have been performed, as described below, it is not clear if the observed drift in the metrology loop is due to mismatched thermal expansions, bolted joint relaxation, or slow thermal expansions of the sample itself due to heating by the pump beam.

In what follows, the results of a series of tests are presented that demonstrate the performance of the various stage components. Only tests that are direct measures of the Z-drift and the Z-fluctuation are included.

(a) Optical Z-drift measurements

A distributed Bragg reflector (DBR) was placed in proximity to the sample using the apparatus. The DBR – air gap – sample configuration formed a Fabry-Perot cavity, whose reflectivity was highly dependent on the air gap spacing. One way to monitor the quality of the optical resonance of the DBR - air gap - sample optical cavity is to measure the optical reflectivity of the structure as a function of the air gap spacing. A schematic of the setup is shown in Figure 3.9. The probe beam was passed through a laser line filter[10] with a pass bandwidth of 3 nm and was focused by the lens onto the optical cavity. The DBR was custom fabricated by Rudolph Technologies to have a reflectivity of 0.84 for light with a wavelength of 800 nm at normal incidence. Over a wavelength range of 750 – 850 nm, the reflectivity of the DBR varied by less than 0.04. Part of the reflected probe was collected by a non-polarizing beam splitter and focused onto a photodetector. The stage was scanned in the Z direction (vertical) at a speed of 1 $\mu m\ s^{-1}$, and the voltage

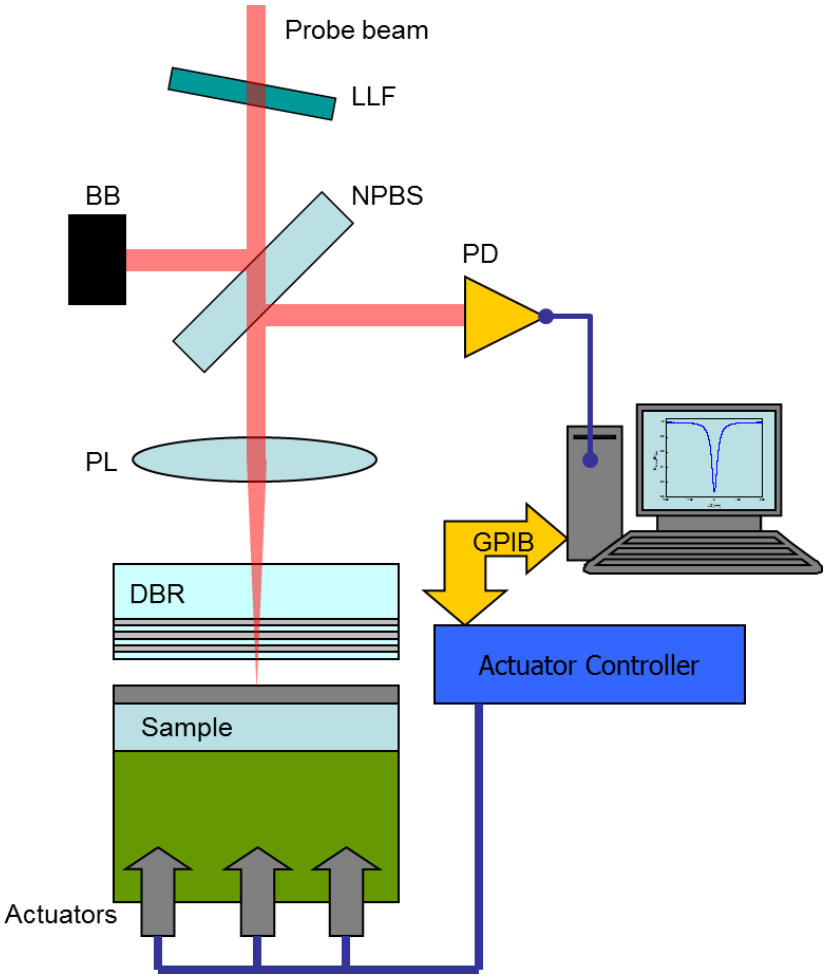

Figure 3.9: Diagram of the set-up used to monitor the resonances of the optical cavity consisting of the DBR – air gap – sample complex. BB – beam block, NPBS – non-polarizing beam splitter, PL – probe lens, PD – photodetector, DBR – distributed Bragg reflector (mirror). The photodetector voltage was recorded as a function of the Z position of the sample, which was controlled by the actuators.

of the photodetector was sampled at a frequency of 10 kHz (*i.e.*, each data point was separated by 0.1 nm). Figure 3.10 shows a typical scan for both filtered and unfiltered probe light. Due to the narrower bandwidth of the filtered probe beam, the resonances are much deeper over a larger range of air gap spacing.

By taking z-scans at one point on the DBR-air gap-sample structure, the Z-drift can be monitored. Figure 3.11 shows change in the location of the resonance measured every fifteen minutes over the course of five hours. Initially the observed drift was 1.0± 0.25 nm min^{-1}, but after four hours it settled down to approximately -0.1 ± 0.25 nm min^{-1}. In

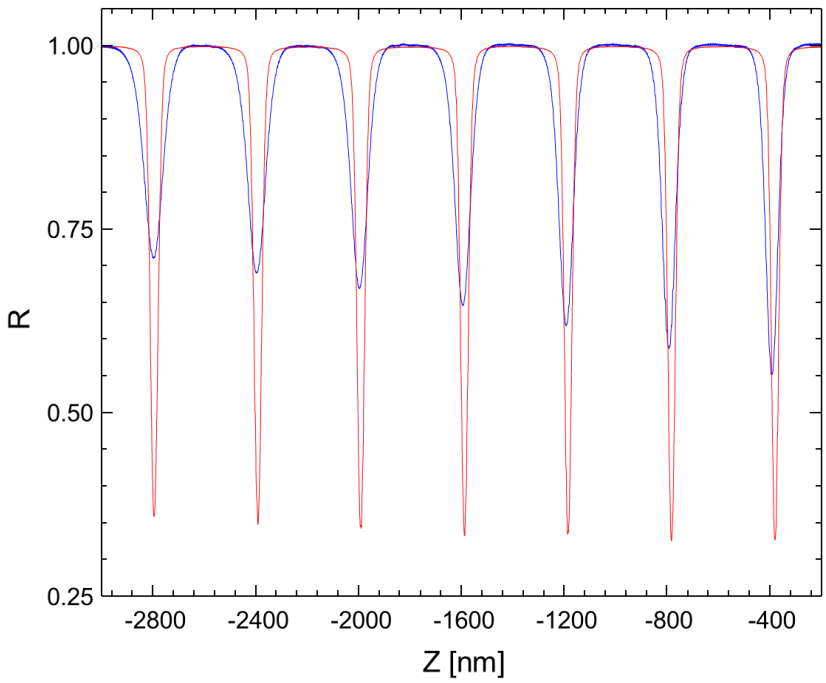

Figure 3.10: Optical resonances of the Fabry-Perot cavity formed by the DBR-air gap-sample, where the sample is a 150 nm Cu film on a Si substrate . Blue line : resonances for the unfiltered probe beam. Red line : resonances for the spectrally filtered probe beam.

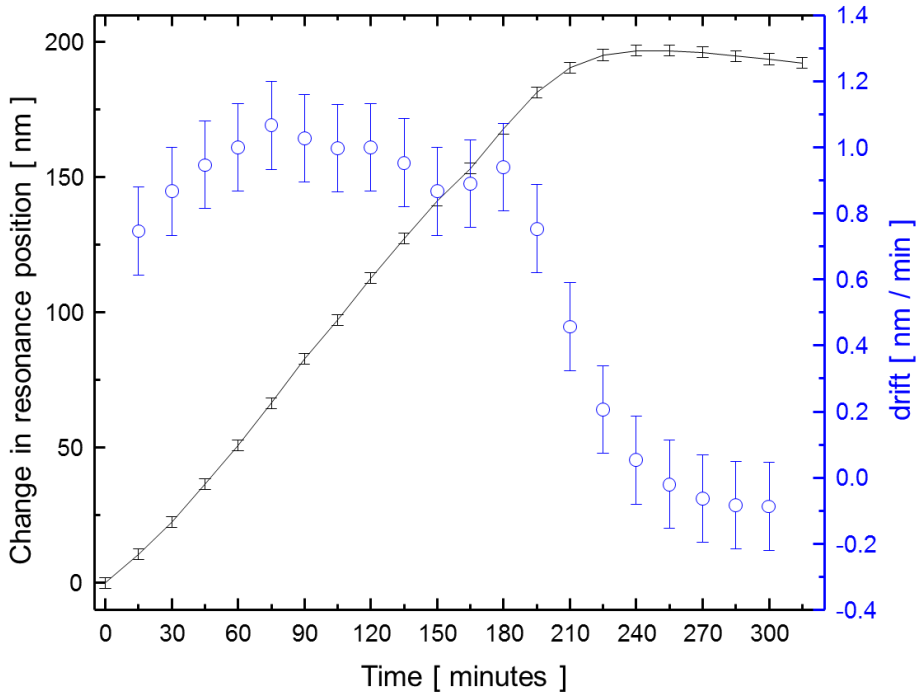

Figure 3.11: Black line : Position of the resonance versus time. Blue circles : estimated Z-drift by taking the numerical derivative of the black line.

general, it was observed that the drift rate was highly dependent on the slow temperature changes in the room that took place throughout the day. Typical drift rates were ± 0.3 – 1.0 nm min^{-1}, although when the building heat turned on, drift rates approaching 5 nm min^{-1} were observed, even with the servo-actuator control loop on. Enclosing the apparatus helped to alleviate the problem.

(b) Optical Z-fluctuation measurements

Using the same setup as discussed above and shown in Figure 3.9, the fluctuations in the gap spacing can be probed. By setting up a Fabry-Perot resonance and maintaining the air gap spacing so that the resulting structure is slightly off resonance, fluctuations in the gap spacing will be read as fluctuations in the output of the photodetector. A sample consisting of an aluminum film on silicon was mounted to the sample chuck, and Figure 3.12a shows the reflectivity of the DBR – sample optical cavity vs. Z position of the stage. The probe beam was filtered with the same laser line filter as in the previous section. At point A in Figure 3.12a, the reflectivity of the structure is quite sensitive to perturbations in the gap. By taking the derivative of the signal, the sensitivity as a change in reflectivity per change in the gap can be estimated. Figure 3.12b shows the numerical derivative of the data in Figure 3.12a. The sensitivity of the optical cavity to small changes in the gap was estimated to be, in terms of change in the photodetector voltage per nm change in the sample gap, 120 ± 20 mV nm^{-1}.

The Z position of the stage was set to the point where the derivative of the signal was at a maximum, and then the servos were turned off and the voltage of the photodetector was recorded for 10 seconds, with 100,000 points sampled at a rate of 10 kHz. The resulting data, shown in Figure 3.13a consists of a slow change in the voltage, attributed to the slow drift in the gap, and fast oscillations at the various mechanical resonance frequencies of the system. Figure 3.13b shows an expanded view in a 100 ms interval, where the oscillations are clearly apparent. The various frequencies that are present are attributed to the mechanical modes of the assembled stage. The data, $V(t)$, was fit to a

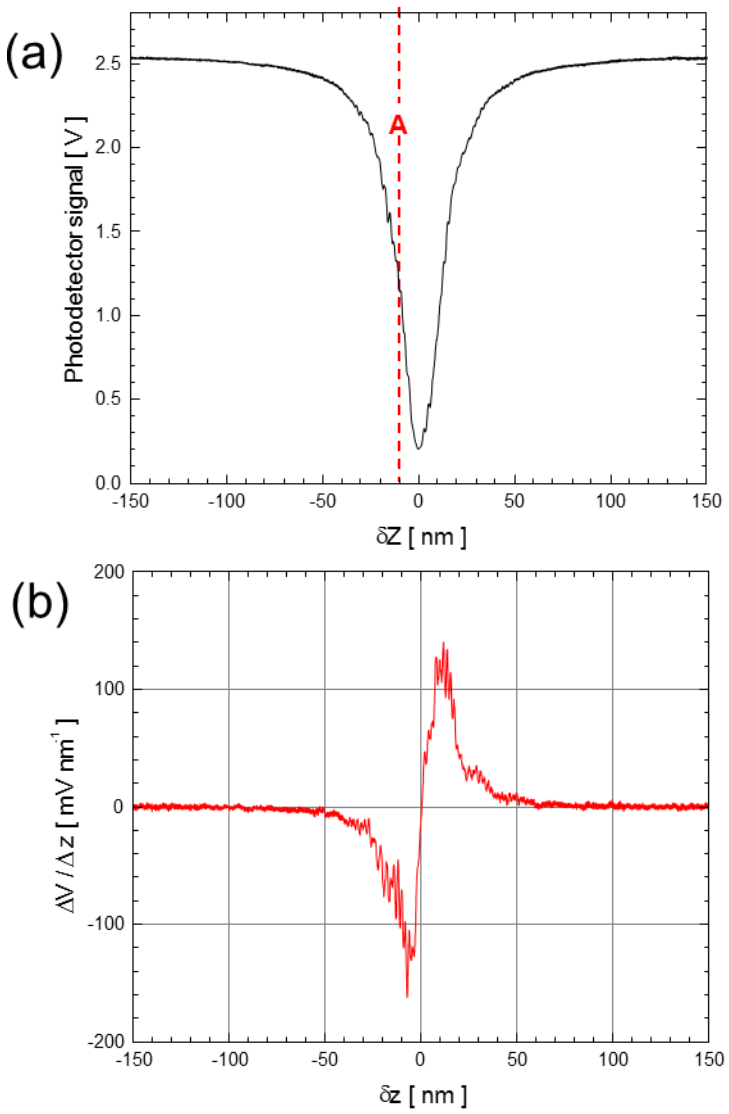

Figure 3.12: (a) Optical resonance used to measure the z stability of the assembled stage. The position δz = 0 corresponds to where the reflectivity is at a minimum. The point labeled A, at δz = – 10 nm corresponds to where the change in reflectivity per change in Z, shown in (b), was a maximum. (b) Numerical derivative of (a), where the maximum sensitivity has a magnitude of 120 ± 20 mV nm^{-1}

line $a + bt$, where a = 1.275 V and b = 2.20 mV s^{-1}, and then the linear fit was subtracted from the data to form

$$\Delta V(t) = V(t) - a - bt, \qquad 3.3$$

which is plotted as the histogram shown in Figure 3.14a. The cumulative probability is plotted in Figure 3.14b, and 90% of the time the quantity $|\Delta V|$ is less than 80 mV. Using

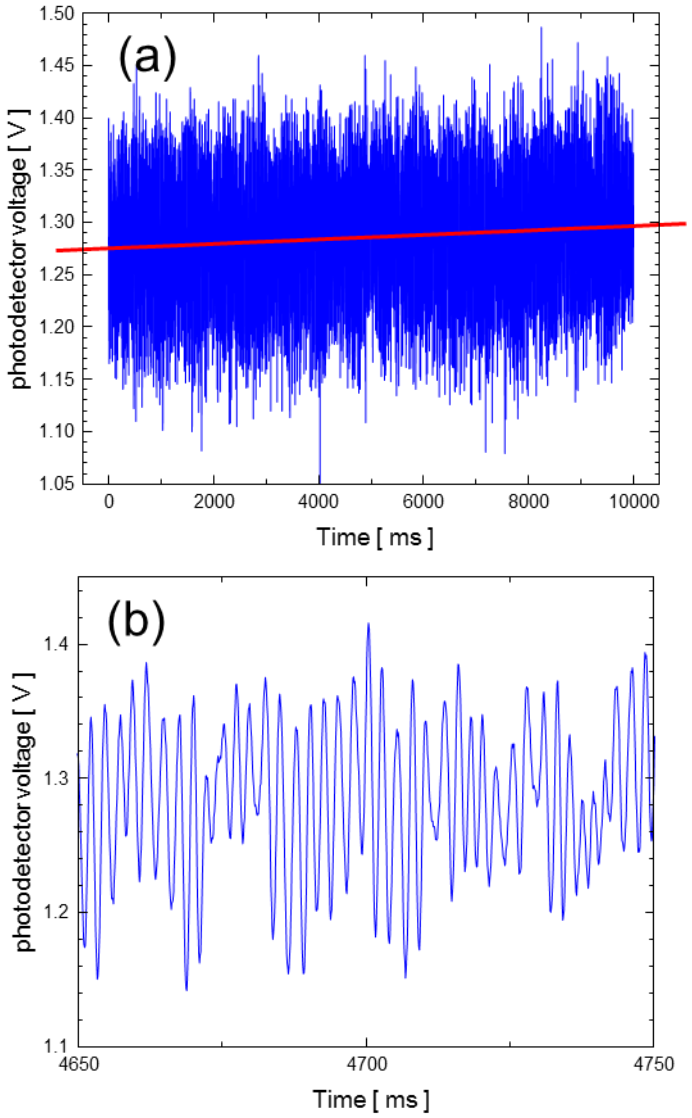

Figure 3.13: (a) Photodetector signal versus time. The solid red line is a linear fit to the data, and has a slope of 2.20 ± 0.05 mV s^{-1} (b) A expanded view of a 100 ms window in time. The dominant high frequency oscillations visible have a frequency of about 400 Hz and is attributed to a mechanical resonance of the stage

the sensitivity figure above, the DBR-sample spacing is oscillating about its equilibrium position, and 90% of the time it is within 0.7 nm of that position. The slow drift of 220 mV ms^{-1}, using the sensitivity figure of 120 ± 20 mV nm^{-1}, corresponds to a drift in the sample gap of approximately 1.1 ± 0.2 nm min^{-1}. The above was repeated except that the servo-actuator loop was turned on, and similar results for the Z fluctuations and Z drift were obtained.

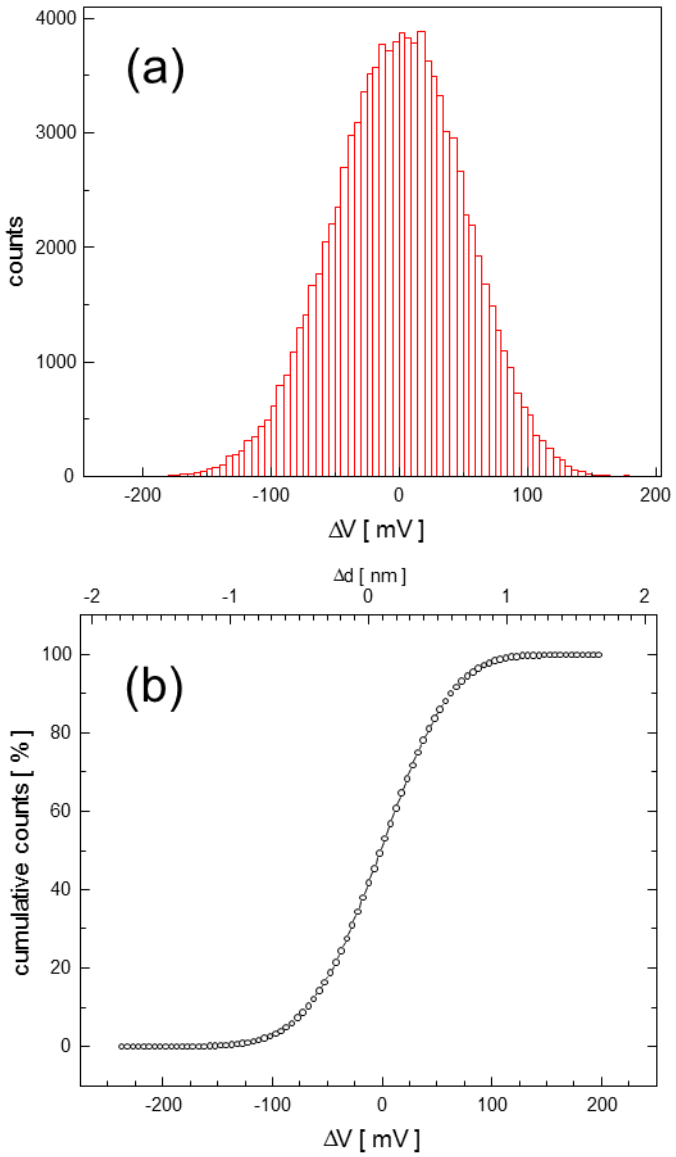

Figure 3.14: (a) Histogram of the data shown in Fig. 3.13a after subtracting the line shown in Fig. 3.13a (b) Cumulative counts as a percentage versus ΔV. The upper x axis converts the change in voltage to a change in airgap spacing assuming a sensitivity of 120 mV nm^{-1}.

(c) Acoustic pulse – echo measurement of the Z-drift

The results of a basic POAM measurement provide an additional way to monitor the Z-drift of the stage. An optoacoustic transceiver was held above a Si sample by the stage, and water was used as the coupling fluid. Upon excitation by the pump pulse, the

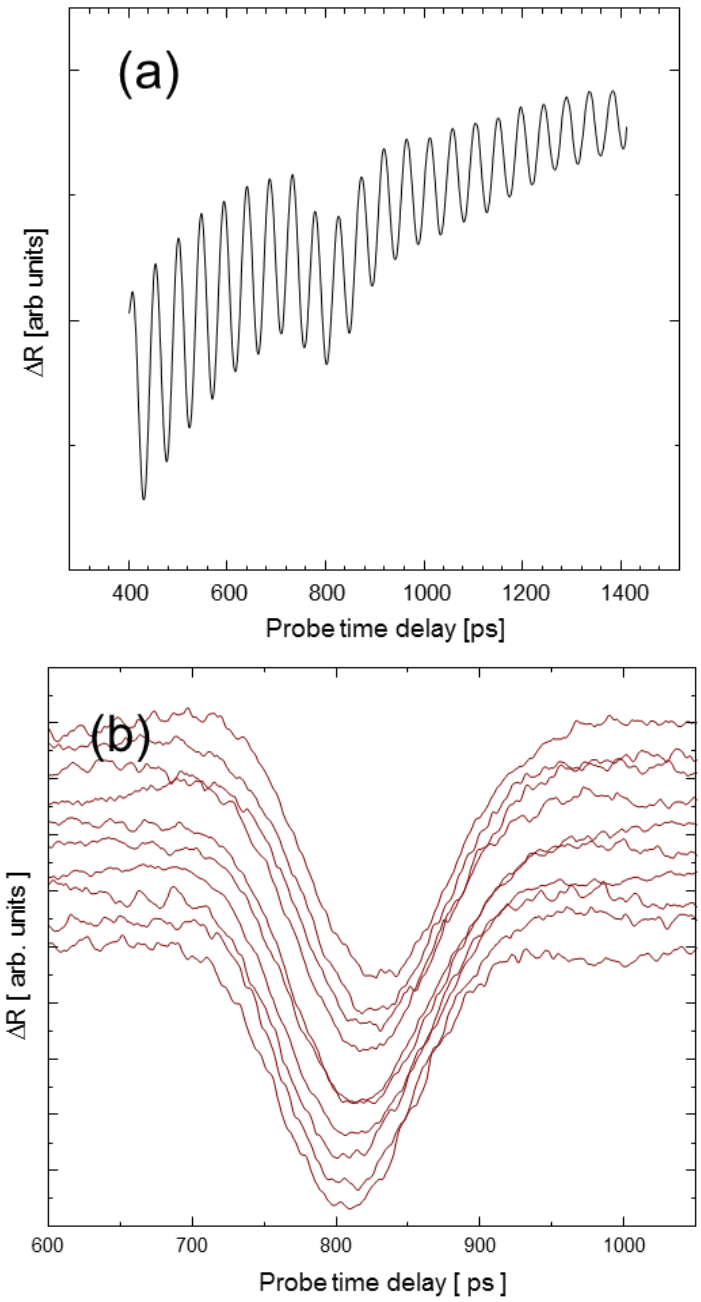

Figure 3.15: (a) Change in reflectivity versus probe delay time. The data consists of Brillouin oscillations with a period of 46 ps from sound propagating through the glass substrate of the opto-acoustic transducer, and an echo at around 800 ps from sound that has made one round trip through the water film (b) Data sets after filtering out the Brillouin oscillations in the glass substrate and subtraction of a low order polynomial to remove the thermal background. The same background was subtracted from each data set. One data set was taken every two minutes, and the curves have been translated vertically for clarity.

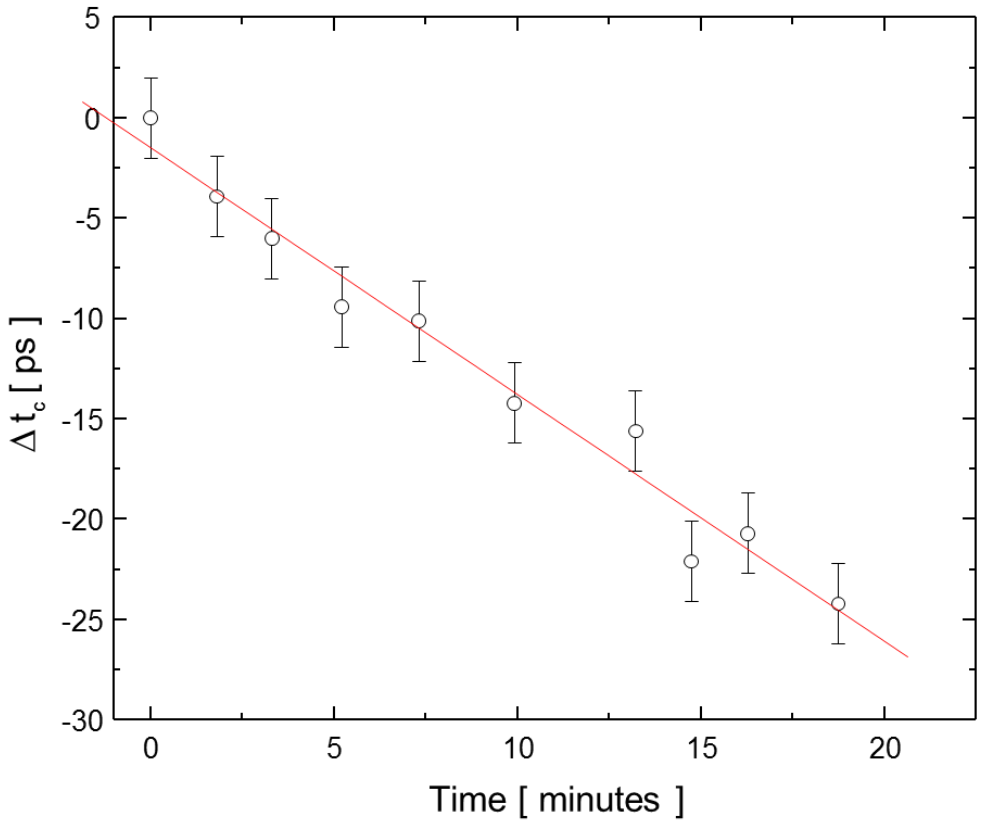

Figure 3.16: Circles: Change in the echo arrival time for the echoes in Figure 3.15b versus time. The linear fit to the data has a slope of 1.2 ± 0.3 ps min^{-1}, which corresponds to a Z-drift of 0.9 ± 0.2 nm min^{-1}.

optoacoustic transceiver launched an acoustic pulse into the water. The acoustic pulse traveled through the water, reflected off of the Si-water interface, and returned to the optoacoustic transceiver. A time delayed probe pulse monitored changes in reflectivity due to the returning acoustic echo.

The probe time delay was scanned from 400 – 1400 ps in 5 s, and each data set was an average of 15 scans. Figure 3.15a shows a typical data set, which consists of a set of oscillations with a period of 46 ps, an echo at approximately 800 ps, and a slowly changing background attributed to the various films in the opto-acoustic transducer cooling down after the excitation by the pump pulse. The origin of the oscillations, known as Brillouin oscillations, is deferred to Section 4.3. Figure 3.15b shows the data after numerically filtering out the Brillouin oscillations and then subtracting a low order

polynomial (the same polynomial was subtracted from each data set). A fuller description of the treatment of this kind of data is deferred until chapter 4; now we focus solely on the variation in the arrival time of the acoustic echo. The uncertainty of the echo arrival time was estimated to be ±2 ps. Each data set shown in Figure 3.15b was fitted to a Gaussian of the form

$$A\exp\left[-\left(\frac{t-t_c}{\sigma}\right)^2\right], \qquad 3.4$$

where t is the probe delay time and t_c the echo arrival time. A change in the echo arrival time Δt was attributed solely to a change in the thickness in the water film,

$$\Delta d = (v/2)\Delta t, \qquad 3.5$$

where v is the sound velocity in water. Figure 3.16 shows the change in the echo arrival time t_c for the data shown in Figure 3.15b over a twenty minute time period. From the slope of the linear fit, the estimated drift in the gap is 0.9 ± 0.2 nm min^{-1}.

3.4 Conclusions

In this chapter, a closer look was taken at all of the major equipment used in the work reported here. An estimate the smallest fractional change in reflectivity that could be detected was presented. A special stage was constructed for the POAM measurements, and its performance was verified with a series of tests. The measured performance of the stage is summarized in Table 3.1.

Parameter	Value
Z fluctuations	±1.0 nm
Z drift	0.3 – 1.0 nm/min
Z incremental move	1.0 nm
Z range of motion	25 μm
θ_x & θ_y incremental move	0.1 μrad
θ_x & θ_y range of motion	±1.0 mrad

Table 3.1: A summary of the stability and performance of the constructed positioning system used for the POAM measurements.

Bibliography

1. Capinski, W.S. & Maris, H.J. "Improved apparatus for picosecond pump-and-probe optical measurements." *Rev. Sci. Instrum.* **67**, 2720 (1996).
2. Smith, S.T. & Chetwynd, D.G. *Foundations of ultraprecision mechanism design.* (Gordon and Breach Science Publishers: 1992).
3. Guillaume, C.-E. *Les applications des aciers au nickel.* (Gauthier-Villars: Paris, 1904).
4. Lament, B.S., Averbach, B.L. & Green, M. "The Dimensional Behavior of Invar." *Trans. Am. Soc. Met.* **43**, 1072-1093 (1951).
5. Jacobs, S.F. "Dimensional Stability of Materials Useful in Optical Engineering." *Optica Acta* **33**, 1377 (1986).
6. Scientific Alloys, Westerly RI
7. PI part number D-100.00.
8. PI part number P-753.21C.
9. Jones, R.V. *Instruments and Experiences: Papers on Measurement and Instrument Design.* (John Wiley & Sons Inc: 1988).
10. SEMROCK Laser line filter LL01-808.

Chapter 4

Design, Fabrication, and Characterization of Optical Fabry-Perot Cavities for use in Picosecond Ultrasonics

4.1 Introduction

The details of the opto-acoustic transducer are presented in this chapter. In picosecond ultrasonics experiments, the energy of the pump pulse is incident upon an absorbing material, usually a single thin metal film. It has been discussed previously how this arrangement would not be adequate for a POAM or SOAM measurement. Consequently, we have used a thin film Fabry-Perot interferometer as an effective opto-acoustic transducer, *i.e.*, a structure in which incident light is converted into sound and where incident sound is translated into a change in optical reflectivity. The optical characterization of the cavity is presented, followed by the results of a POAM measurement on a simple planar sample. Comments on the response function of the cavity are presented. These will be necessary for interpreting POAM measurements on more complicated samples.

4.2 Optical cavities for POAM and SOAM measurements

In section 2.4, the feasibility of using a single metal film for detecting acoustic pulses that have propagated through 100 – 1000 nm of water was investigated. Several factors rendered optical detection of the attenuated sound pulses impractical. After propagating through the water and being transmitted back into the solid, the strain pulse returns with an amplitude that is 1-3% of the initial strain generated in the metal film by the pump pulse. The pulse is also significantly broadened so that its spatial width within the solid is 400-500 nm. For a structure like that shown in Fig. 4.1a, the probe beam is only sensitive to perturbations in the metal film within a depth on the order of the optical absorption length, which for a typical metal is about 10 nm. This means that the probe beam will only be sampling small slices of the returning strain. Finally, the actual magnitude of the change in optical reflectivity of the metal film is directly proportional to the piezo-optic constants, *i.e.*, the change in the real and imaginary parts of the refractive index of the metal per unit strain, $\partial n / \partial \eta$ and $\partial \kappa / \partial \eta$. These constants are typically on the order of unity, and consequently the strain and the change in optical reflectivity will be of approximately the same order of magnitude.

In this section, the design of a thin film structure optimized for the generation and detection of sound pulses is considered. The structures are Fabry-Perot interferometers, and their general form is shown in Fig. 4.1b. Two mirrors are separated by a gap whose thickness, combined with the optical properties of the mirrors, determine the resonance condition of the structure. The cap layer serves to protect the structure from the coupling fluid (water). The optical reflectivity of such a structure can be made highly sensitive to perturbations in the optical thickness of the spacer layer. In what follows, we refer to the structure as a Fabry Perot cavity, or simply cavity.

4.2.1 Detection of ultrasound with a Fabry-Perot cavity

The sensitivity of a Fabry-Perot cavity has resulted in its use in a variety of detection instruments. Thomson *et al.*[1] were the first to use a Fabry-Perot cavity for the purpose of

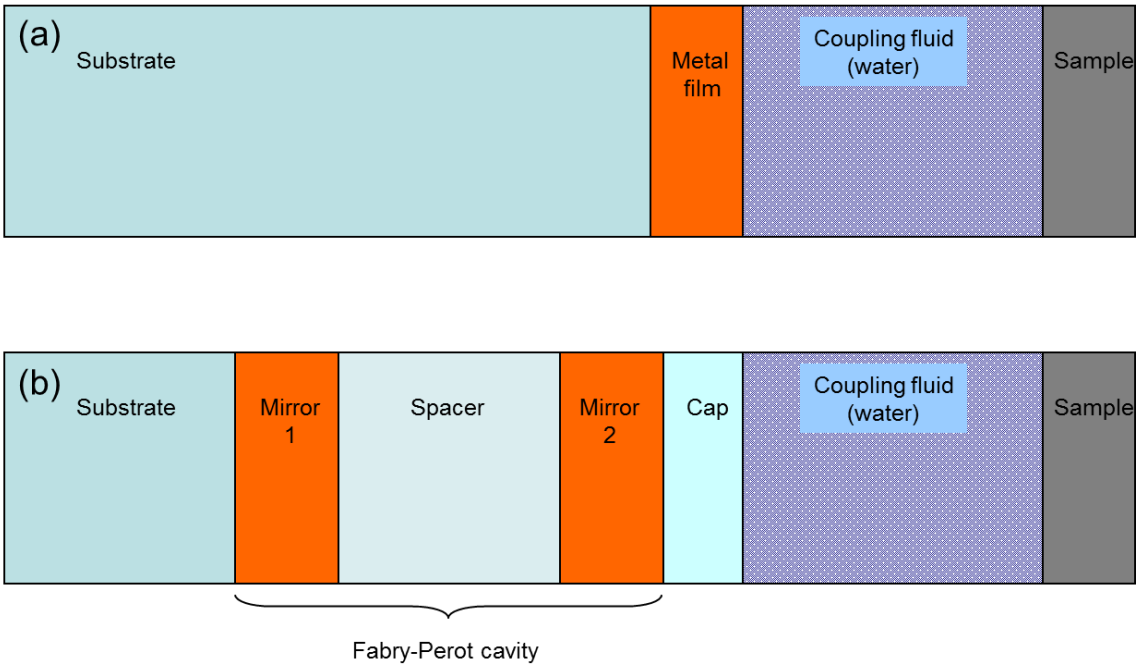

Figure 4.1: (a) The arrangement considered in section 2.4. The pump beam excites the thin metal film and launches a sound pulse into the coupling fluid. The returning sound pulse will have a width significantly larger than the thickness of the thin metal film. (b) The basic thin film cavity structure. A strain pulse in the spacer layer will perturb the optical thickness of the cavity structure, causing a change in the optical reflectivity. The thickness of the spacer layer is comparable to the width of the returning sound pulse.

detecting ultrasound. In their experiment, the cavity consisted of the sample surface being studied, an air gap of approximately 0.5 mm, and a mirror held in place near the sample. By scanning the interrogating probe beam across the mirror-sample area, an image of the displacement of a vibrating sample surface could be formed. The use of Fabry-Perot cavities as an optical pickup for ultrasound has also been demonstrated by Hamilton *et al.*[2]. In their work, the Fabry-Perot cavity consisted of two distributed Bragg reflectors (DBR) fabricated on either side of a 4 mm thick piece of fused silica. Ashkenazi *et al.*[3] continued along this line with a Fabry-Perot cavity consisting of two thin films of gold with a 10 µm layer of photoresist in between. In this work, the goal was to detect ultrasound that had been generated by an external transducer, and to develop a medical ultrasound detection system for frequencies in the MHz range. In the work of Li *et al.*[4], a Fabry-Perot cavity with an air gap spacer was used to enhance picosecond ultrasonics measurements on difficult to measure samples. In what follows,

we describe the use of a Fabry-Perot cavity for both the generation and detection of sound pulses.

First, consider a Fabry-Perot cavity that consists of two mirrors separated by a distance *w*. The reflection coefficients for the electric field amplitude for the mirrors are denoted by r_1 and r_2 and are complex quantities. The region between the reflectors is assumed to be transparent with refractive index *n*. When the structure is illuminated with monochromatic light with wavelength λ_0 at an angle of incidence θ_0, the intensity reflection coefficient for the structure can be shown to be[4]

$$R = \frac{\left(|r_1| - |r_2|\right)^2 + 4|r_1||r_2|\sin^2\left(\gamma/2\right)}{\left(1 - |r_1||r_2|\right)^2 + 4|r_1||r_2|\sin^2\left(\gamma/2\right)}, \qquad 4.1$$

where the parameter

$$\gamma = 2k_z w + \phi, \qquad 4.2$$

is the phase delay for a ray that has reflected once off of each mirror and traversed the spacer film twice, and

$$k_z = \frac{2\pi}{\lambda_0}\sqrt{n^2 - \sin^2\theta_0}\,. \qquad 4.3$$

All information about the phase change that the field suffers upon reflection from each mirror is contained in the constant ϕ. While ϕ affects the values of *w* at which the cavity has an optical resonance, it does not affect the spacing between the resonances and it does not affect the sensitivity of the cavity to perturbations. In what follows, it is convenient to express Eq. 4.1 as

$$R = \frac{R_{\min} + \left(\frac{2f}{\pi}\right)^2 \sin^2\left(\gamma/2\right)}{1 + \left(\frac{2f}{\pi}\right)^2 \sin^2\left(\gamma/2\right)}, \qquad 4.4$$

where the minimum reflectivity, $R_{\min}$, is

$$R_{\min} = \frac{\left(|r_1| - |r_2|\right)^2}{\left(1 - |r_1||r_2|\right)^2}, \qquad 4.5$$

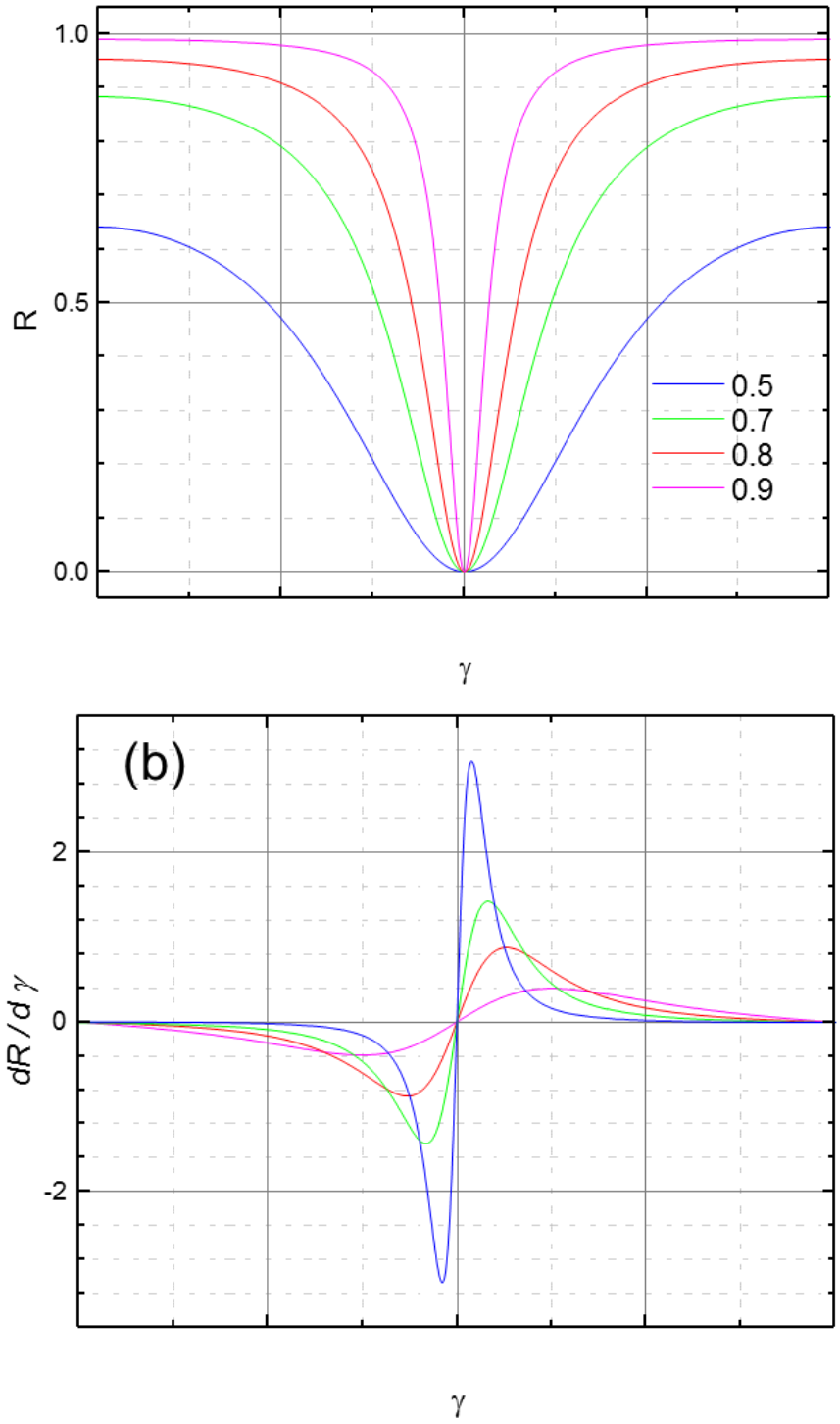

Figure 4.2: (a) Reflectivity versus the parameter γ, using equation Eq. 4.2, for several magnitudes of the mirror reflectance $|r|$. Both mirrors are assumed to have the same value of $|r|$. (b) Derivative of the plots in (a). The value of the derivative is a measure of how sensitive the cavity is to perturbations in its structure.

and the parameter f, which is referred to as the finesse of the interferometer, is

$$f = \frac{\pi\sqrt{|r_1||r_2|}}{\left(1-|r_1||r_2|\right)}. \qquad 4.6$$

A higher finesse results in a sharper resonance. Figure 4.2a shows plots of the optical reflectivity of the cavity structure for several choices of $|r| = |r_2| = |r_1|$. A cavity whose effective spacing is such that the structure is slightly off resonance is particularly sensitive to perturbations. Figure 4.2b shows plots of the quantity $dR/d\gamma$. Figure 4.3 plots the maximum value of the quantity $dR/d\gamma$ as a function of the finesse of the structure for cavities with $|r_2| = |r_1|$. As the finesse of the structure is increased, the

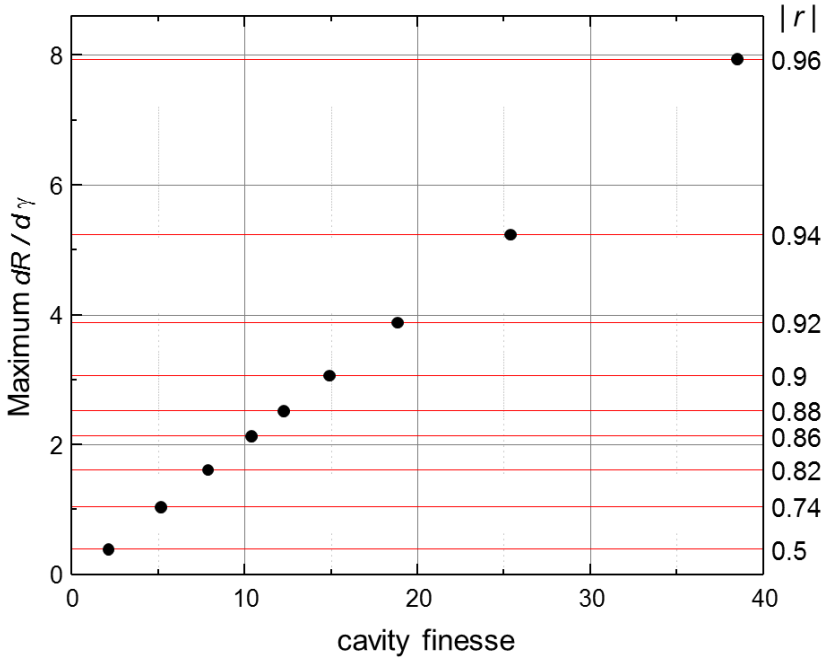

Figure 4.3: A plot of the maximum value of the quantity versus finesse of the cavity is approximately linear. Both of the mirrors are assumed to have the same reflectivity.

sensitivity increases, but the range of γ over which the sensitivity is high decreases. Thus, there is a tradeoff between sensitivity and range. In picosecond ultrasonics experiments, the strains and resulting displacements generated are very small, and their magnitude will not be what limits the finesse that can be used. The two factors that will limit the finesse

are the surface roughness of the substrate (and the subsequent films deposited) and the spectral width of the ultrafast laser. These will be discussed further below, but now we turn to the selection of the materials for the various films in the structure.

4.2.2 Cavity design considerations

Figure 4.1b shows the basic layout of the cavity structure. The cavity itself is formed by two mirror layers and the spacer layer. Each of the layers shown in the figure can consist of more than one film, for example, one of the mirrors could be a DBR. In designing a Fabry-Perot cavity structure for use in POAM and SOAM measurements, the substrate, mirrors, and spacer materials need to be chosen carefully. Since the structure is also going to be used to generate the sound as well, at least one of the films in the structure must be optically absorbing, such as a metal. The Fabry-Perot cavities that have been used in the past to detect ultrasound either use solid for a spacer layer or use air. In a solid spacer cavity, the two mirrors are separated by a transparent solid dielectric film whose thickness determines the resonance condition of the structure. We have decided to use a cavity with a solid spacer between two metal films. The design of the structure is complicated by its performance being dependent on both optical and mechanical properties of each of the films. Below, some of the primary considerations for each layer are stated and mention is made of some of the potential advantages and disadvantages of an air gap cavity.

A. Spacer layer

For a cavity with a solid spacer layer the fine tuning of the resonance condition has to be accomplished by small adjustments in the wavelength of the light interrogating the structure. Because of the solid layer, the cavity is highly stable. For an air cavity it is much easier to adjust the resonance condition, but it is harder to maintain the air gap spacing. As the finesse, and therefore sensitivity of the cavity to perturbations, increases, the stability requirements become more exacting. The use of a cavity with an air gap spacer in a POAM or SOAM measurement presents the considerable challenge of maintaining both the air gap spacing in the optical cavity and the spacing between the

cavity structure and the sample being investigated. It might be possible to construct a MEMS assembly to maintain one or both of these gaps, as has been done for tunable miniature lasers[5].

B. Mirrors

As stated above, one of the mirrors must be an optically absorbing film, and we have chosen to use a metal film as the absorber. For a cavity with a solid spacer, sound that is generated in the structure can propagate through the spacer and into the other mirror, and this can complicate both the generation and detection of sound. The air cavity with a single metal film has the advantage that sound generated in the film enters and returns from the sample and does not affect the other mirror. This makes the analysis of the measured reflectivity change easier.

At this point, it is necessary to distinguish between the primary modes of operation of a POAM versus a SOAM measurement. In a POAM measurement, the probe time delay is scanned in order to detect acoustic echoes from different depths which return at different probe time delays. In order to distinguish between the different echoes, it is desirable for the response of the cavity to sound to be as simple as possible. Each interface with a substantial acoustic impedance mismatch will result in multiple echoes as sound bounces around in the cavity structure. These echoes within the cavity complicate the interpretation of the POAM data. In a SOAM measurement, several modes of operation are possible. In what is referred to as a C-scan, an image is formed by scanning the sample at a fixed probe time delay. For a C-scan mode of operation, simplicity in the response of the cavity structure to returning sound can be sacrificed for increased sensitivity and magnitude of the returning echoes.

To make a cavity with a high finesse one needs to use mirrors of high reflectivity. This can be achieved using a multi-layer distributed Bragg reflector (DBR). However, it is difficult to make a DBR which does not result in large acoustic reflections originating from the differences in the acoustic properties of the different layers. These internal

acoustic reflections cause the response of the cavity to an incoming acoustic pulse to be complex, and this is a disadvantage for POAM measurements.

C. Substrate

The surface roughness of the substrate will affect the deposition of the subsequent films that make up the cavity; this will result in variations in the spacer layer thickness (assuming a cavity with a solid spacer), which will cause an effective reduction in the finesse, and therefore sensitivity, of the cavity. This is further discussed below.

The thermal conductivity of the substrate places an upper limit on the energy that can be deposited into the films by the pump beam. In terms of high thermal conductivity and a low surface roughness, sapphire is one of the more desirable materials. Diamond, while having a very high thermal conductivity, is quite difficult to polish, and its surface roughness will be at least 10 nm. The optical implications of surface roughness in terms of the performance of the cavity will be discussed further below.

D. Detection mechanism

From Eq. 4.1, it can be seen that the optical reflectivity of a Fabry Perot cavity is sensitive to perturbations in the parameter γ. In what follows, it is assumed that the spacer layer is a solid film, and so sound can propagate through the cavity. There are three mechanisms by which a sound pulse impinging upon the cavity can perturb γ. First, the strain pulse causes a small change in the distance between the two mirrors. A second change in γ comes about because the strain causes a change in the refractive index of the spacer medium. These two effects both change the optical thickness of the spacer layer. The unperturbed optical thickness is given by

$$t_0 = \int_0^{d_0} n_0 \, dz, \qquad 4.7$$

where d_0 and n_0 are the unperturbed thickness and refractive index, respectively. The change in *d* is

$$\int_0^{d_0} \eta(z) dz, \qquad 4.8$$

and the change in the refractive index at z is

$$\eta(z)\frac{\partial n}{\partial \eta}. \qquad 4.9$$

Hence, to lowest order in the strain the change in the optical thickness is

$$\Delta t = \int_0^{d_0} \eta(z)\, d_0 \left(n_0 + \frac{\partial n}{\partial \eta} \right) dz. \qquad 4.10$$

For most transparent materials, the piezo-optic coefficient is negative, and so the two effects have opposite sign. The third contribution is the strain-induced change in the phase of light reflected by the mirrors. This gives a change in the parameter ϕ in Eq. 4.2. This change can be calculated in terms of the piezo-optic constants $\partial n / \partial \eta$ and $\partial \kappa / \partial \eta$.

4.2.3 Comments on the factors that limit cavity performance

There are several factors which limit the sensitivity that a Fabry-Perot cavity can attain. The two most relevant ones for this application are the spectral width of the probe light and the surface roughness of the constituent films. The effects of surface roughness and spectral width of the light source can be estimated by considering an ensemble of ideal Fabry-Perot interferometers, and then finding the effective property of interest, for example, the reflection coefficient, by forming the average

$$R_{eff} = \int f(x) R(x) dx, \qquad 4.11$$

where x is the quantity that is being varied and the function $f(x)dx$ is the probability that the quantity x is between x and $x + dx$. For example, consider a light source that has a Gaussian distribution of wavelengths with standard deviation σ_λ centered at λ_c so that

$$f(\lambda) = \frac{1}{\sigma_\lambda \sqrt{2\pi}} \exp\left[-\frac{1}{2} \left(\frac{\lambda - \lambda_c}{\sigma_\lambda} \right)^2 \right], \qquad 4.12$$

where the full width half maximum (FWHM) of f is $2\sqrt{2\ln 2}\sigma_\lambda$. The effective reflection coefficient is then

$$R_{eff} = \frac{\int \exp\left[-(\lambda - \lambda_c)^2 / 2\sigma_\lambda^2 \right] R(\lambda)\, d\lambda}{\int \exp\left[-(\lambda - \lambda_c)^2 / 2\sigma_\lambda^2 \right] d\lambda}, \qquad 4.13$$

where $R(\lambda)$ is the reflection coefficient for light with wavelength λ (Eq. 4.1).

The roughness of the interfaces on either side of the cavity results in variations in the width of the spacer layer. Suppose that each interface has an rms roughness σ_i and there is no correlation between the fluctuations of the two interfaces. Then the width of the cavity will have an rms variation of $\sigma_i\sqrt{2}$. We assume that these fluctuations can be treated by considering an ensemble of cavities with perfectly smooth interfaces with a distribution of spacer thicknesses *u* given by

$$f(u) = \frac{1}{2\sigma_i\sqrt{\pi}} \exp\left[-\frac{1}{4}\left(\frac{u-w}{\sigma_i} \right)^2 \right]. \qquad 4.14$$

where *w* is the average width of the spacer layer.

From Eq. 4.2, variations in the phase γ are related to variations in the wavelength and width of the spacer layer by

$$\delta\gamma = \frac{4\pi n}{\lambda_0}\delta w - \frac{4\pi n w}{\lambda_0^2}\delta\lambda_0 , \qquad 4.15$$

where *w* is the average spacer layer thickness and *n* is the refractive index of the spacer layer. From the above, it is apparent that for a light source with a given spectral width, a thicker cavity spacer amplifies the variations in phase caused by variations in wavelength and lowers the sensitivity. If the laser light has a spectral distribution that can be described by Eq. 4.12, then the rms variations in the phase γ, using Eq. 4.15, will be

$$\sigma_\gamma = \frac{4\pi n w}{\lambda_0^2}\sigma_\lambda , \qquad 4.16$$

while the variation in the thickness of the cavity spacer layer gives

$$\sigma_\gamma = \frac{4\pi n}{\lambda_0}\sqrt{2}\sigma_i . \qquad 4.17$$

As an example, consider a cavity with spacer thickness 250 nm and refractive index 1.5, operating at a central wavelength of 800 nm. Suppose that the rms roughness of the

interfaces is 5 nm. This would result in rms phase variation across the cavity of 0.17. From Eq. 4.16, this is comparable to the effect of a light source with a spectral FWHM of 54 nm.

4.2.4 Chosen design for POAM measurements

For the cavities used in this work, the two mirrors of the Fabry-Perot cavity were a thin (<10 nm) and thick film of aluminum, and the solid spacer layer was silicon dioxide. These materials were chosen primarily because they are well matched acoustically; the ratio of the acoustic impedances of silicon dioxide to that of aluminum is $Z_{SiO_2} / Z_{Al} = 1.2$. For an interface between these two materials, using Eq. 2.20, the reflection coefficient for strain is 0.1.

4.3 Proof of concept experiment

In the last section, the various considerations that went into choosing the Al-SiO_2 material system for a Fabry Perot cavity were explored. Below, the results of a proof of concept experiment are presented, where the suitability of the cavity structure for both generating and detecting sound is demonstrated for different thicknesses of the spacer layer.

For testing purposes a cavity was fabricated with a spacer layer with thickness varying continuously along the substrate. A 7 nm film of aluminum (mirror 1) was sputtered onto a 50 x 25 mm substrate of Corning C1737 glass. Then a film of SiO_2 was deposited by plasma enhanced chemical vapor deposition (PECVD) with a process that used a tetraethyl orthosilicate (TEOS) precursor. By positioning the substrate slightly off center in the deposition system's chamber and modifying some of the deposition parameters, the thickness of the SiO_2 film was made to vary across the substrate. The process was tried several times with silicon test wafers, and the thickness and refractive index of the resulting films were characterized with a multi-wavelength multi-angle ellipsometer[6]. The results of the ellipsometry measurements indicated that across the Si test wafer, the refractive index of the SiO_2 film was constant at 1.46 for a wavelength of 800 nm, whereas the thickness varied smoothly from 430 to 660 nm along the length of the

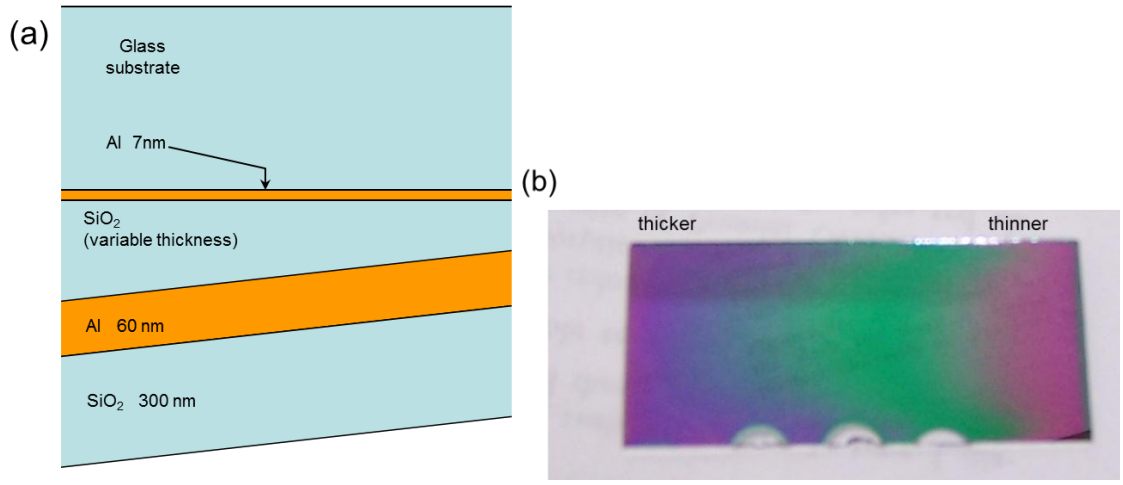

Figure 4.4: (a) Schematic of the films used for the proof of concept cavity. (b) Photograph of the finished cavity with variable spacer layer thickness. The spacer layer thickness increases from right to left.

substrate. This thickness variation was verified by the picosecond ultrasonics measurement discussed below. A 70 nm film of Al (mirror 2) was then sputtered on top of the variable thickness SiO_2 film. These first three films formed the Fabry-Perot cavity. Another film of SiO_2 was then deposited on top of the thick Al film as a test layer, so that sound pulses generated in the cavity propagated through the test SiO_2 film, reflected off the free surface, and returned to the cavity. A photograph of the completed structure, when viewed through the glass substrate, is shown in Fig. 4.4b. The variation in the color of the cavity is due to the variation of the thickness of the cavity SiO_2 layer.

Figures 4.5 and 4.6 show pump-probe data taken at different positions on the cavity sample. There are three features that change noticeably as the thickness of the spacer layer is increased: (1) the magnitude and sign of the change in reflectivity at probe time delay t = 0 ps, (2) the oscillations in the signal that, while obscured by other features at early time delays, are clearly visible after 300 ps, and (3) the steps in the signal, for example at around 90 ps. We now analyze these three features.

The jump in the reflectivity at time delay t = 0 ps is caused by the electronic response of the Al films. The excitation of the electrons in the metal causes a large change in the

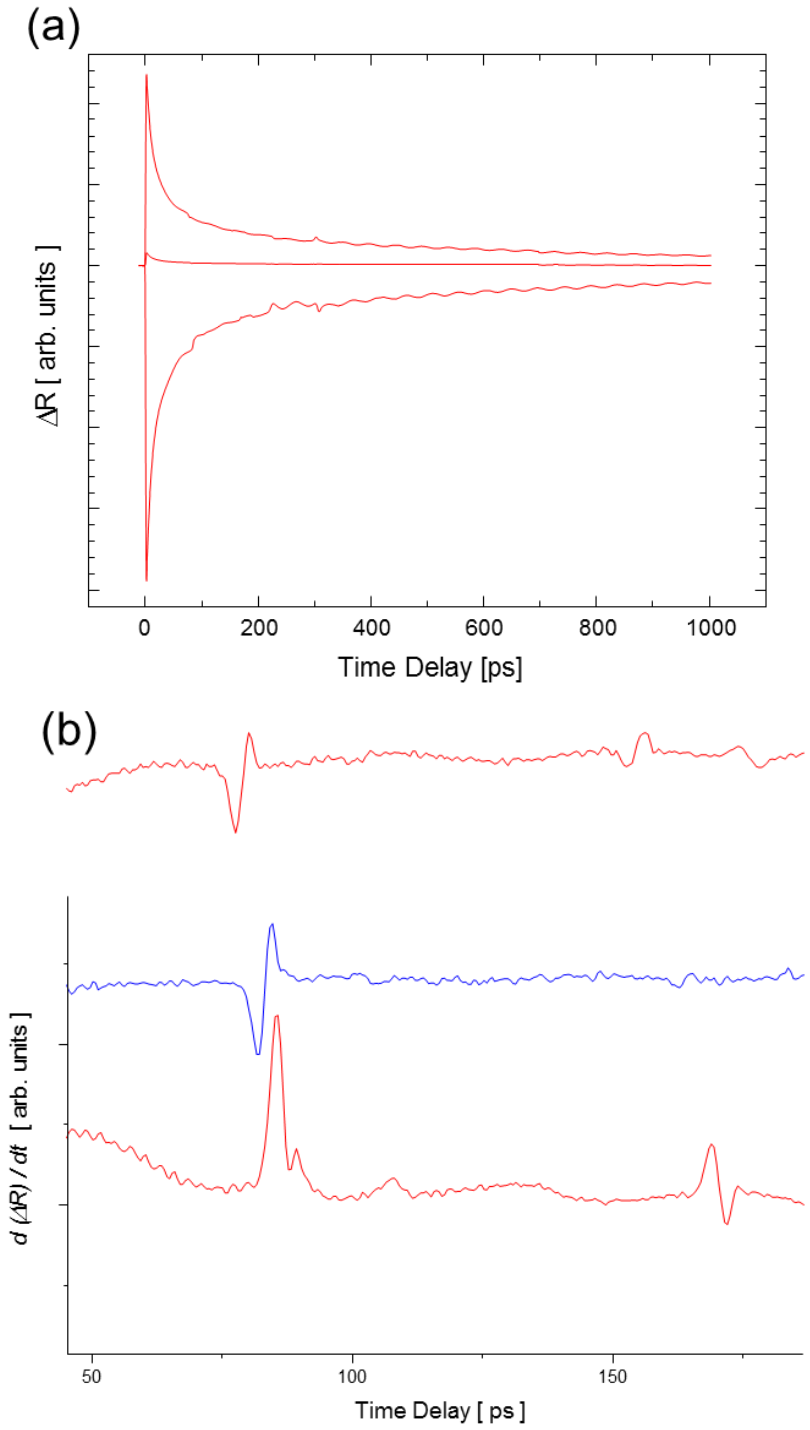

Figure 4.5: (a) Pump probe data taken at three different points on the cavity sample with a variable thickness spacer. (b) Derivative of the curves in (a), spaced vertically for clarity. From the top curve to the bottom, the arrival time of the first step increases by approximately 4 ps, which corresponds to an increase in the thickness of the spacer layer by about 25 nm. The scale of the middle curve has been multiplied by a factor of 5.

optical properties of the Al films. The effect on the overall change in the reflectivity of the cavity structure due to this depends on the resonance condition of the cavity.

The oscillations in the experimental data are known as Brillouin oscillations[7], and their origin is as follows. Consider a sample that consists of a film of metal on a transparent substrate, as illustrated in Figure 4.6. The pump and probe beams are focused onto the metal film through the transparent substrate. Upon excitation by the pump pulse, a strain

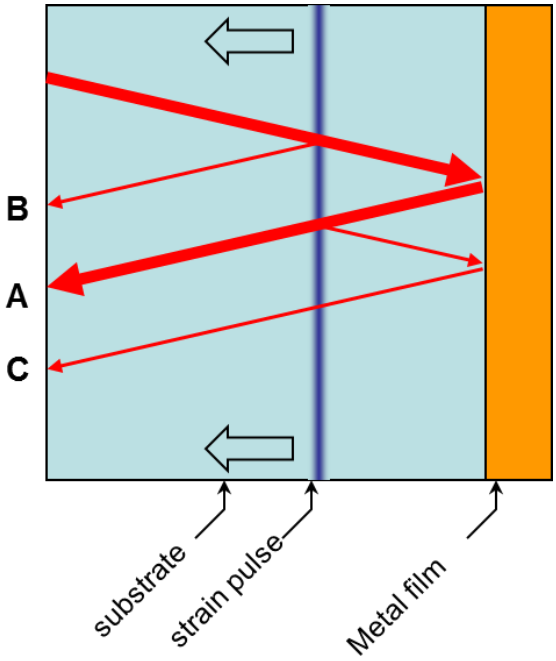

Figure 4.6: The origin of the Brillouin oscillations in the data. The probe light reflects from the metal film (ray A) and from the perturbation in the refractive index due to the strain pulse in the transparent material (rays B and C). The relative phase difference between ray A and rays B and C depends on the distance the strain pulse has propagated, and the interference condition oscillates between constructive and destructive as the pulse travels through the substrate.

pulse is launched into the substrate. The probe light reflects off of the thin Al-substrate interface; this is denoted by the ray labeled A in Fig. 4.6. Some of the probe light will also reflect off of the small perturbation in the refractive index of the substrate caused by the strain pulse; this is denoted by rays B and C in Fig. 4.6. Only light that has reflected once off of the strain pulse is considered. Depending on how far the strain pulse has propagated, rays B and C will interfere either constructively or destructively with ray A,

and it can be shown[7] that the period of the resulting oscillations in the reflection coefficient of the sample is given by

$$T = \frac{\lambda_0}{2v\sqrt{n^2 - \sin^2\theta}}, \qquad 4.18$$

where λ_0 is the wavelength of the probe light in vacuum, *n* the refractive index of the substrate, θ the angle of incidence of the probe light, and *v* the sound velocity in the substrate.

The steps are caused by the small change in the reflectivity of the cavity that occurs when a strain pulse enters or leaves the cavity structure. Each time a strain pulse encounters one of the metal films, a feature is added to the data. Taking the derivative of the data highlighted these features. The first sharp feature in the data, referred to below as feature A, occurs when strain generated in one Al film traverses the spacer and then encounters the other Al film. The thickness of the spacer layer can be estimated from the time at which feature A occurs. For the data sets shown in Fig. 4.5a, the arrival time of feature A ranged from 78 – 86 ps. Taking the sound velocity in the spacer layer to be 6.2 nm ps^{-1}, the spacer layer thickness ranged from 484 to 533 nm. Figure 4.5b shows the derivative of the curves in Fig. 4.5a. The difference in the cavity spacing between adjacent curves was about 25 nm. Figure 4.7a shows the curves spaced closer together in the region of the sample where feature A was the largest, and Fig. 4.7b shows the derivative of the curves in Fig. 4.7a The difference in the arrival time of feature A between adjacent curves was about 1 ps, which corresponds to a 6 nm change in the spacer layer thickness.

The cavity had two metal films, and energy deposited into them by the pump pulse launched four strain pulses, as illustrated in Figure 4.8. Pulse 1L contributed to the picosecond ultrasonics data only in the form of Brillouin oscillations. Figure 4.9 shows the signal and its derivative for the trace from Fig. 4.7a with the largest feature A. The features A-J each occur when pulses 1R, 2R, 2L, or one of their reflections, either enter or leave the cavity spacer layer. The time delay at which each feature occurs can be expressed as a sum of integer multiples of the transit time through each of the constituent

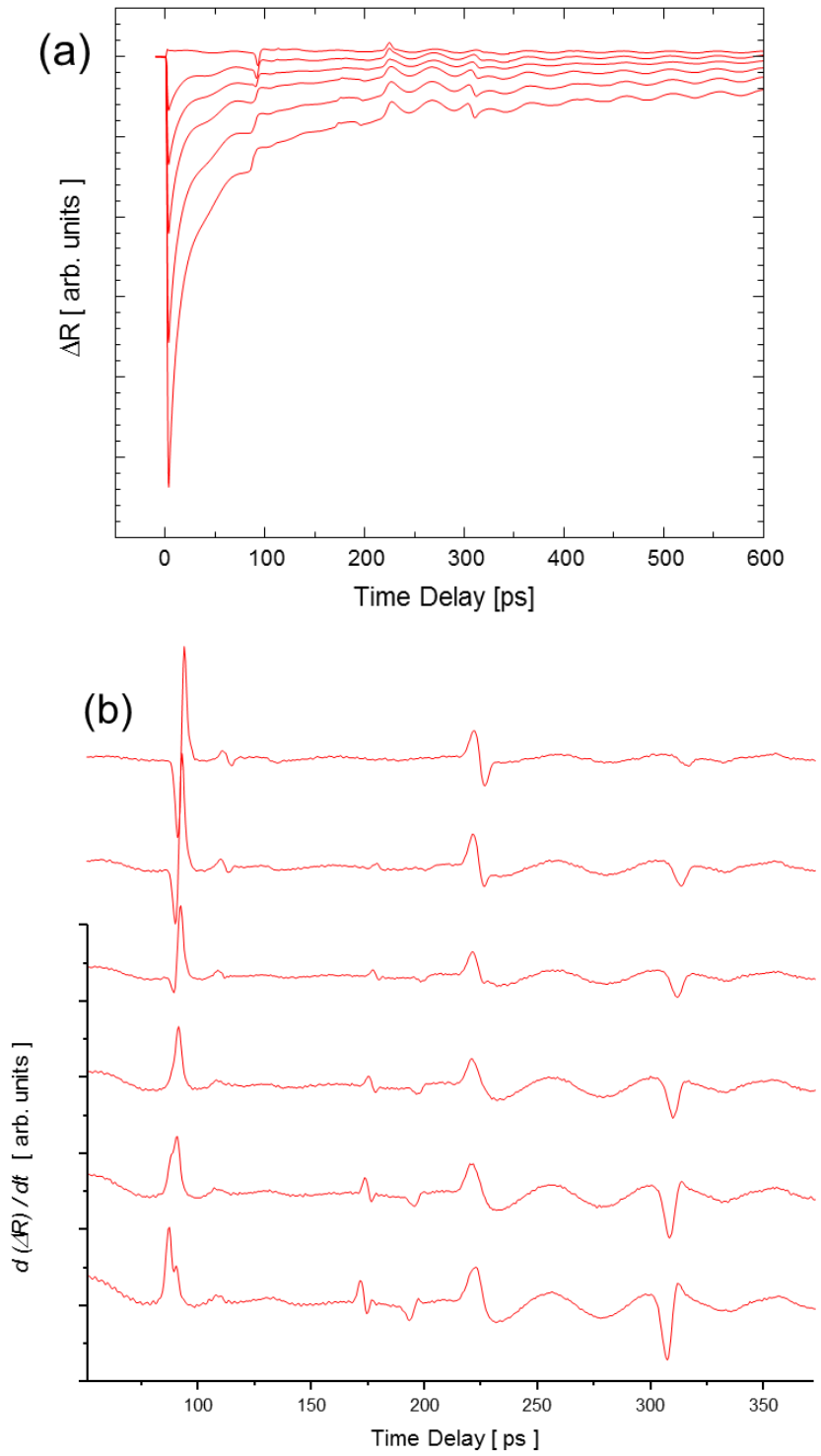

Figure 4.7: (a) Pump probe data taken at six different points on the cavity with a variable thickness spacer. (b) Derivative of the curves shown in (c), displaced vertically for clarity. From the bottom curve to the top, the arrival time of the first step increases by approximately 1 ps, which corresponds to an increase in the thickness of the spacer of about 6 nm.

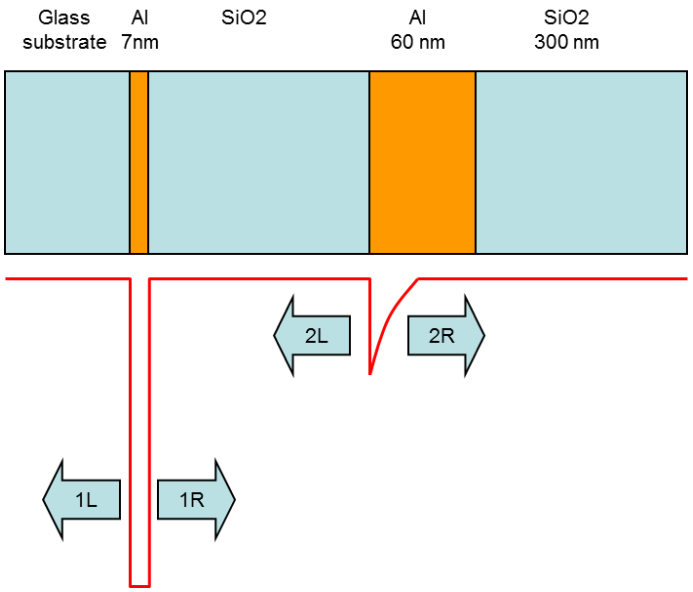

Figure 4.8 Schematic of the strain generated in a cavity with two metal films. Upon excitation, the strain generated in the two aluminum films launched 4 strain pulses.

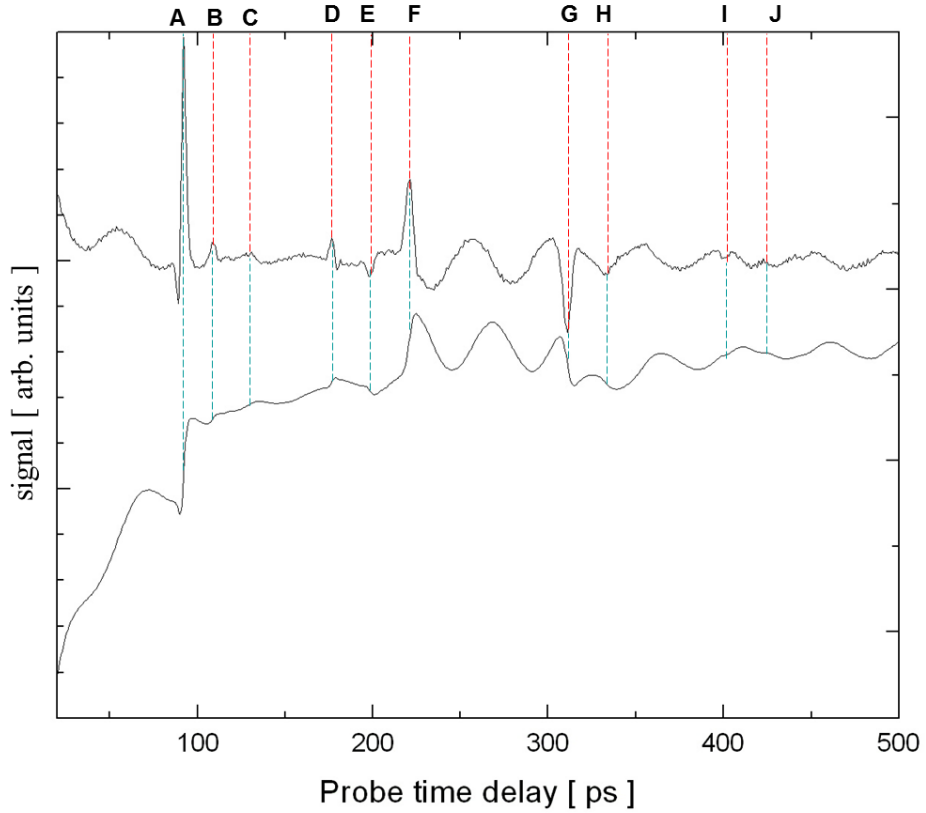

Figure 4.9: A closer view of the curve with the largest step at 90 ps (feature A) from Figure 4.6c, along with its derivative (upper curve). The features labeled A-J are due to strain pulses 1R, 2L, and 2R (or their subsequent reflections) either entering or leaving the cavity. Using Figure 4.8, it is possible to determine which strain pulses are responsible for a particular feature. In addition to features A-J, Brillouin oscillations, with a period of 46 ps, are also present in the data.

films. For the data shown in Fig. 4.9, the transit time through the spacer layer is 90 ps, the thick aluminum layer 10 ps, and the test film 55 ps. Figure 4.10 depicts the paths that the strain pulses 1R, 2R, 2L, and their subsequent reflections take. The thicker rays, referred to below as primary rays, are ones that have not reflected off of any of the Al-SiO_2 interfaces present. The thinner rays, referred to as secondary rays, are ones that have been reflected off an Al-SiO_2 interface once. It was assumed that the Al and SiO_2 had acoustic impedances such that sound which had reflected twice off of an Al-SiO2 interface could be ignored.

As shown in Fig. 4.10, each feature in the data can be connected to the strain pulses that generated that feature. For example, the step feature A is due to both strain pulses 1R and 2L leaving the spacer layer traveling in opposite directions. By comparing the magnitudes of features, it appears that the majority of the strain was generated in the thin Al film. There are two observations to support this conclusion. First, consider feature C. This feature is caused solely by the primary 2R ray after it reflects off of the SiO_2-air interface. The time at which feature C occurs is independent of the thickness of the spacer layer. For all of the sites on the sample that were measured, feature C occurs at 130 ps (2 x 10 ps + 2 x 55 ps; a round trip through the thick Al and test SiO_2 films), although in some data sets feature C was too small to accurately determine its arrival time. If a substantial amount of strain were generated in the thick Al film, then there would be a large step in the signal shown in Fig. 4.9 at around 130 ps; however, the step is significantly smaller than the step that occurs at F-G. Second, compare the magnitude of feature E to that of feature C. The magnitude of feature E, which is caused solely by a secondary ray from pulse 1R, is larger than that of feature C, which is caused by a primary ray from pulse 2R. These two observations suggest that upon excitation by the optical pump pulse the majority of the strain is generated in the thin Al film.

The size of the steps at A and at F-G is an indication of how sensitive the cavity is to perturbations in the optical thickness caused by strain. Feature A is large only over a

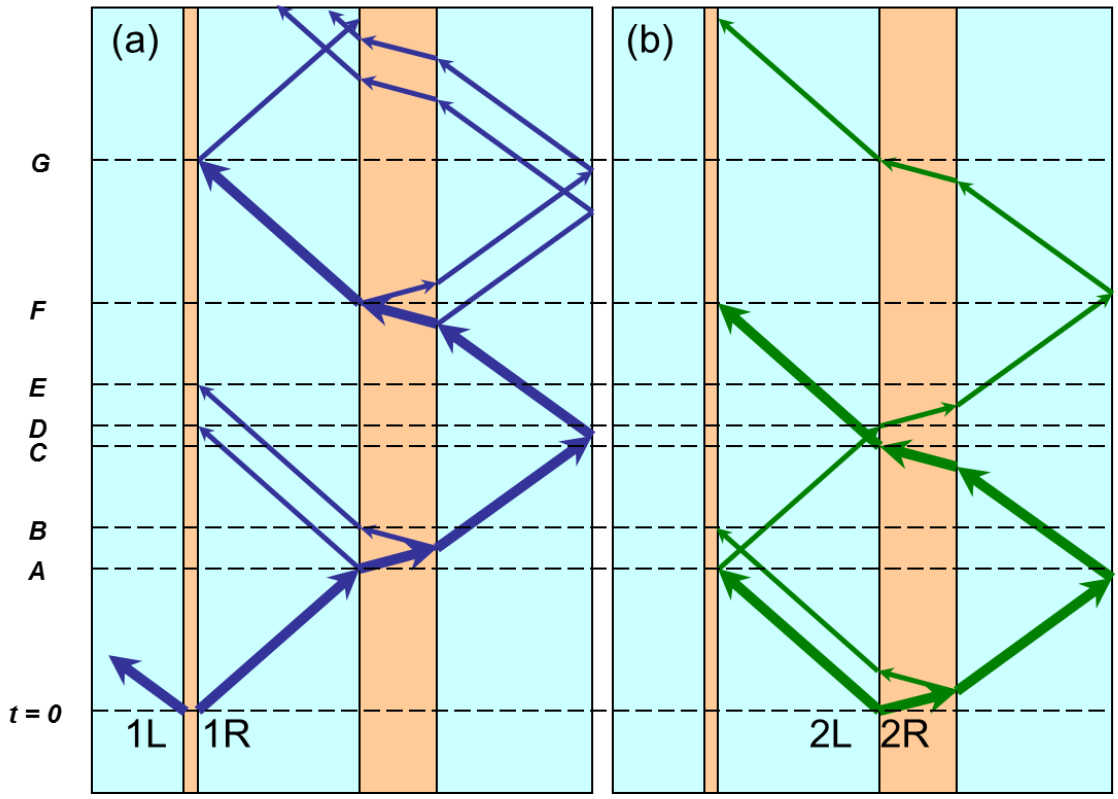

Figure 4.10: The paths that the launched strain pulses and their subsequent reflections take. The vertical axis is time, and the horizontal axis is distance normal to the sample surface. The vertical stripes represent the cavity films, from left to right: substrate, thin Al, spacer SiO2, thick Al, and test SiO2 layer. Rays that have suffered 2 or more reflections from an Al-SiO_2 interface are ignored. (a) Strain launched from the thin Al film (1L and 1R). Pulse 1L only contributes Brillouin oscillations to the signal. (b) Strain launched from the thick Al film (2L and 2R).

narrow range of cavity thickness. From the arrival time of feature A, the data with the largest steps at A and F-G occur when feature A is between 84 and 90 ps, which corresponds to a 36 nm variation in the cavity layer thickness. In order to make cavity structures with optimal sensitivities to strain, nanometer scale control of the thickness of the spacer SiO_2 layer is required. In addition, some wavelength tuning capability is also quite useful in getting the most out of a particular cavity structure once it has been fabricated. This is discussed more fully in the next section.

4.4 Characterization of thin film optical cavities

The cavity described in the last section had a spacer layer with varying thickness, and the optical resonance condition could be changed by translating the pump and probe beams

along the cavity. This provided an opportunity to take picosecond ultrasonics data at different resonance conditions of the cavity. However, there are three practical disadvantages in using a variable spacer cavity for a POAM measurement. First, more usable area is obtained when a cavity is fabricated with a single spacer thickness over the entire substrate. The cavity can be cut into small pieces. For example, during the course of this work one single 25 mm x 25 mm substrate provided enough cavity pieces for over 200 hours of measuring time. Second, the use of a variable thickness spacer would add another degree of freedom to the experimental setup, since the beams would have to be positioned on both the area of interest on the sample and on the proper site of the cavity structure. Finally, for the cavity structure that was discussed in the last section, different deposition systems were used to deposit the different layers, and the vacuum was broken between films. The performance of the cavity structure is sensitive to the thickness and optical properties of the thin Al film, and allowing the Al film to oxidize during the transition from one deposition system to the other added an element of uncertainty. To avoid these difficulties, a single deposition system was used to fabricate the cavities with a spacer layer whose thickness was uniform. With the thickness of the spacer layer fixed, it was critical to verify that the spacer thickness was near its optimal value.

After stating some of the details of the cavity fabrication, a series of tests to verify the performance of the cavity structure are presented. These tests progress from measurements of the optical intensity reflectivity to picosecond ultrasonics measurements. Two sets of picosecond ultrasonics experiments were performed to verify the performance of the cavity: measurements of just the cavity structure without any coupling fluid (‘dry’ tests), and POAM measurements of the cavity with water and an unpatterned sample (‘wet’ tests). As will be shown below, the ‘dry’ tests provide a quick way to choose the optimal center wavelength without going through the whole alignment procedure needed for a POAM measurement.

4.4.1 Fabrication and Structure Details

The cavity substrate was a square slide of Corning C1737 glass, 25 mm square by 1.1 mm thick. The C1737 glass is a boro-aluminosilicate glass that is made using the fusion

draw process[8], and the surface roughness of these substrates is less than 20 nm peak to peak over a 5 mm distance across the surface[9]. A multi-source sputtering system was used, and all the films were deposited without breaking vacuum. The sputtering system had a base pressure of 1.0×10^{-6} mbar. Typical deposition rates were 0.06 nm s^{-1} for Al, and 0.04 nm s^{-1} for SiO_2. The thickness of the thin aluminum film was about 10 nm, and the thick Al film 100 nm. The thickness of the SiO_2 spacer layer was around 250 nm; determination of the optimal thickness for the spacer layer is described below. A 15-20 nm thick cap layer of SiO_2 was deposited to protect the thick aluminum film from the water. It was observed, during the course of the measurements, that the cavity structures had a measurement life of 20 – 50 hours in de-ionized water, after which the thick Al film was observed to have been corroded.

4.4.2 Optical characterization

One way to characterize the thin film cavity structures is to measure their optical intensity reflectivity versus wavelength. Figure 4.11 shows the measured optical reflectivity versus wavelength using a reflection spectrometer for two different cavities. The kink near 800 nm is the result of a detector changeover that takes place during the measurement process. For cavities A and B, all of the deposition parameters were kept the same except for the thickness of the SiO_2 spacer layer. For cavity A, the thickness of the cavity SiO_2 layer was 246 nm, and for cavity B, 250 nm. A change in the thickness of the cavity spacer layer Δd is related to the shift in the wavelength of the first resonance $\Delta\lambda$ by

$$\Delta\lambda = 2n\Delta d, \qquad 4.19$$

where n is the refractive index of the spacer SiO_2 layer. In order to fabricate a cavity with a resonance within the 60 nm tuning range of the ultrafast laser, the thickness of the spacer needs to be within a 20 nm window centered on the target thickness. From Fig. 4.11, it is clear that these cavities had a low finesse, *i.e.*, their resonances were not particularly sharp. This was attributed to the fact that the thin Al film was not a very reflective mirror, with an estimated intensity reflectivity of 0.5.

The wavelength at which the cavity will perform best in a POAM measurement can be estimated from the optical reflectivity versus wavelength data. To optimize the

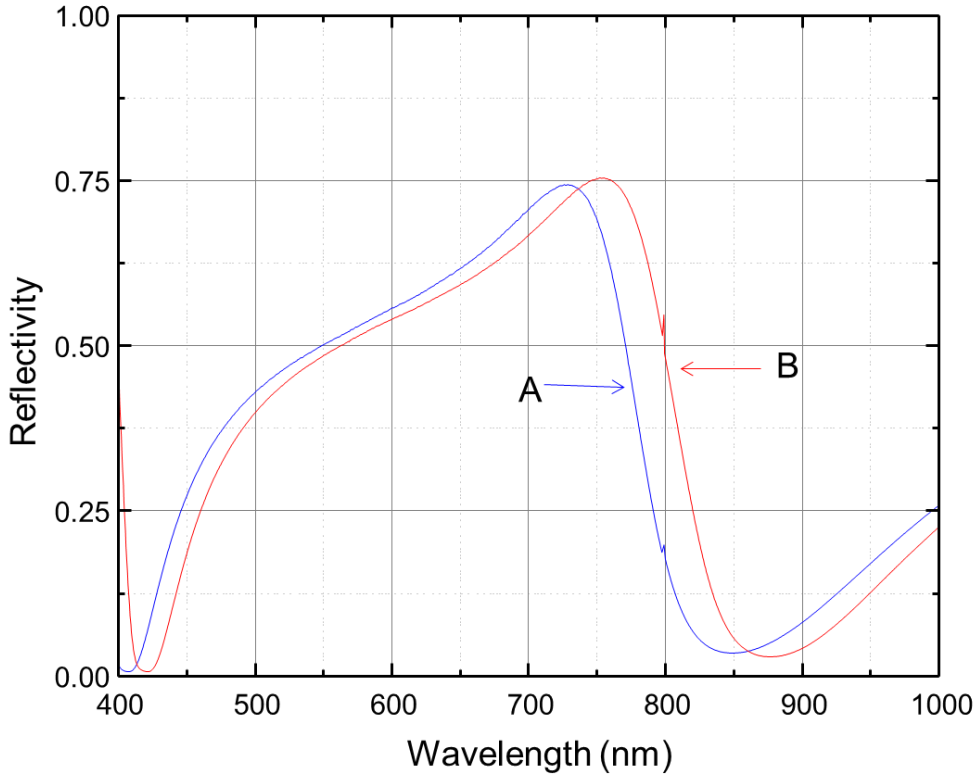

Figure 4.11: The measured optical intensity reflection coefficient for two cavity structures, A and B, versus wavelength.

performance of a cavity in a POAM measurement, both the strain generated by the cavity and the sensitivity of the cavity to perturbations need to be maximized. Thus, we could take the figure of merit for the cavity to be

$$M = \left(\left| \frac{dR_{probe}}{d\eta} \right| \frac{1}{R_{probe}} \right) \left(1 - R_{pump} \right), \qquad 4.20$$

where R_{pump} (R_{probe}) refers to the optical intensity reflectivity of the pump (probe) light. The first term is the fractional change in reflectivity of the probe light per unit strain, and the second term is the fraction of pump light that is absorbed by the cavity.

The derivative with respect to η in Eq. 4.29 is not precisely defined since the strain is a function of both time and position. However, the strain pulses that are to be detected are

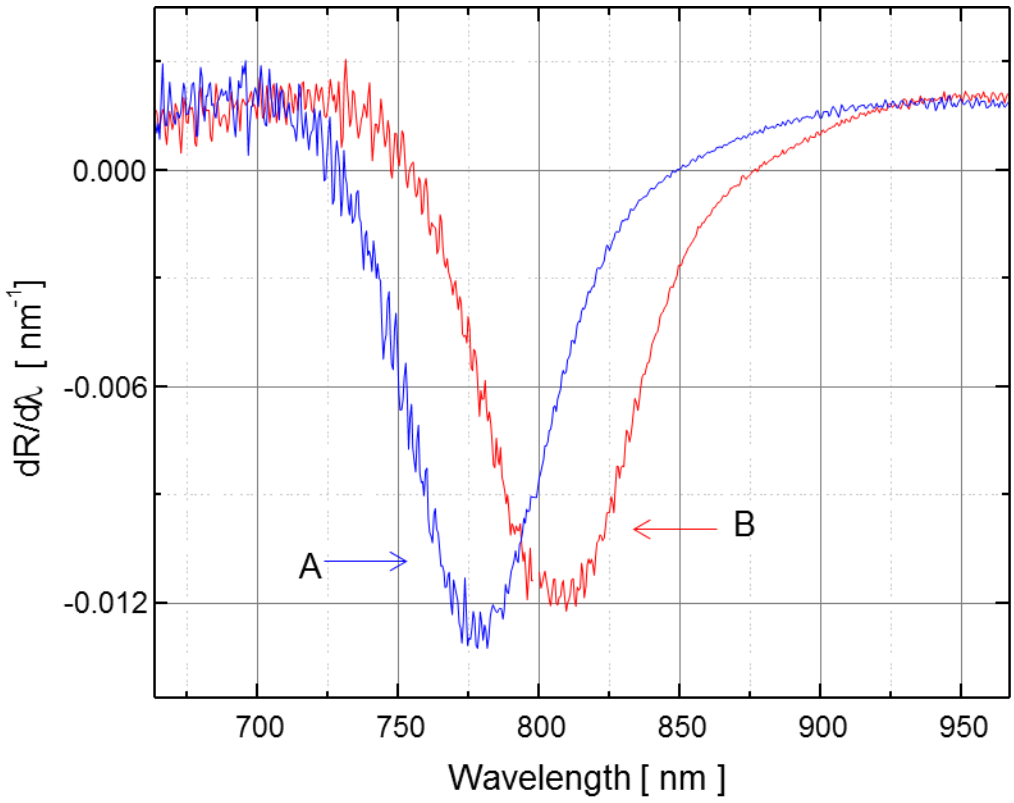

Figure 4.12: Numerical derivative of the data in Fig. 4.11 for cavity structures A and B.

pulses with a width comparable to the dimensions of the cavity spacer layer. We therefore assume that the main contribution to the change in reflectivity comes from the change in the optical thickness of the cavity spacer layer that takes place. Then the change in the optical thickness of the cavity is connected to the strain present in the spacer layer by Eq. 4.10, and the figure of merit *M* can be replaced by

$$M = \left(t \left| \frac{dR_{probe}}{dt} \right| \frac{1}{R_{probe}} \right) \left(1 - R_{pump} \right), \tag{4.21}$$

where *t* is the optical thickness of the cavity spacer layer given by

$$t = n_{cav} d_{cav}, \tag{4.22}$$

n_{cav} is the refractive index of the spacer layer, and d_{cav} is the thickness of the spacer layer. If we further assume that R_{probe} is just a function of t / λ_0 and also ignore the variation of the refractive index with wavelength, we then have

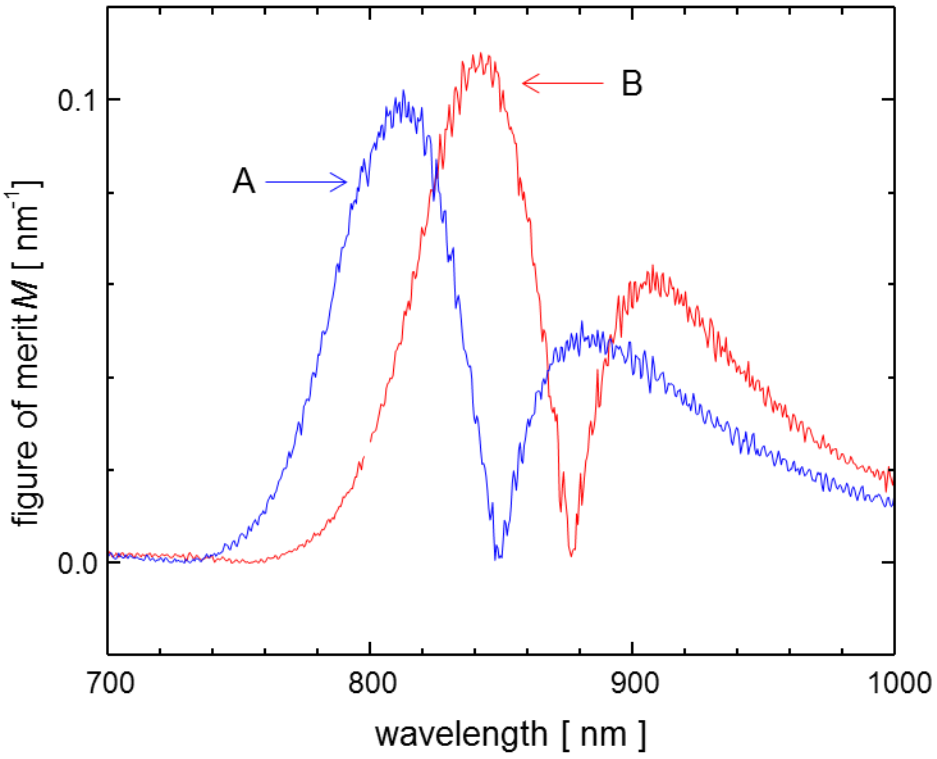

Figure 4.13: The proposed optical figure of merit, defined by Eq. 4.21, computed using the reflectivity versus wavelength data shown in Fig. 4.11.

$$M = \left(\lambda_0 \left| \frac{dR_{probe}}{d\lambda_0} \right| \frac{1}{R_{probe}} \right) \left(1 - R_{pump} \right), \qquad 4.25$$

where λ_0 is the center wavelength of the probe light. For the experiments reported here, the angle of incidence of the pump is 8 degrees, the probe is at normal incidence, and both the pump and the probe beam have the same wavelength. For this experimental configuration, the reflectivity of the pump beam will be close to that of the probe beam, and the reflectivity data shown in Fig. 4.11 can be used to evaluate both the pump and probe terms in Eq. 4.21. Figure 4.12 shows $dR/d\lambda_0$ for cavities A and B computed from the data shown in Fig. 4.11. The refractive index in the neighborhood of 800 nm of the cavity layer is approximately 1.46. Using the data shown in Figs. 4.11 and 4.12, the figure of merit M can be evaluated; this is shown in Fig. 4.13. The figure of merit provides a guide for evaluating the suitability of a particular cavity structure for POAM

experiments, and the ideal structure will have a peak figure of merit at a wavelength within the tuning range of the laser.

The cavity performance could be further improved by tuning the angle of incidence for the pump and the probe beams. For the best performance, the pump beam should have as low a reflection coefficient as possible, while the probe beam should have a reflection coefficient that is the most sensitive to perturbations. As discussed by Li et al.[4], this strategy is straightforward to implement for a cavity with a sharp resonance, since small changes in angle (less than 10 degrees) is enough to change the resonance condition from maximum absorption to maximum sensitivity. Angle tuning was not used in this work, since the spatial restrictions of the positioning system limited the angle of incidence to a maximum of 25 degrees, and for the low finesse cavities used in this work, that was not enough to significantly improve the performance of the cavity.

4.4.3 Picosecond ultrasonic characterization of the cavities – 'dry' tests

The reflection spectrometer that was used for the optical characterization described above sampled an area of about 4 mm x 8 mm, and significant variations in the cavity response can occur over this large an area. During the picosecond ultrasonics experiments, a small area of the structure is probed. Described below is a pump-probe measurement that can be done to determine which operating wavelength should be used for optimal cavity performance. A picosecond ultrasonics experiment was done at a series of center wavelengths of the ultrafast laser. A feature has been identified in the signal that correlates well with the performance of the cavity in a POAM measurement, but does not require the presence of a coupling fluid, sample, and sample positioning system.

Figure 4.14a shows picosecond ultrasonics data taken on a finished cavity structure at a series of different wavelengths. Both the pump and the probe beam had the same wavelength. Using the same notation as in Figures 4.9 and 4.10, feature A is from pulses 1R and 2L both leaving the cavity at the same time. The size of the step in the reflectivity at feature A is a good indication of the performance of the cavity in both

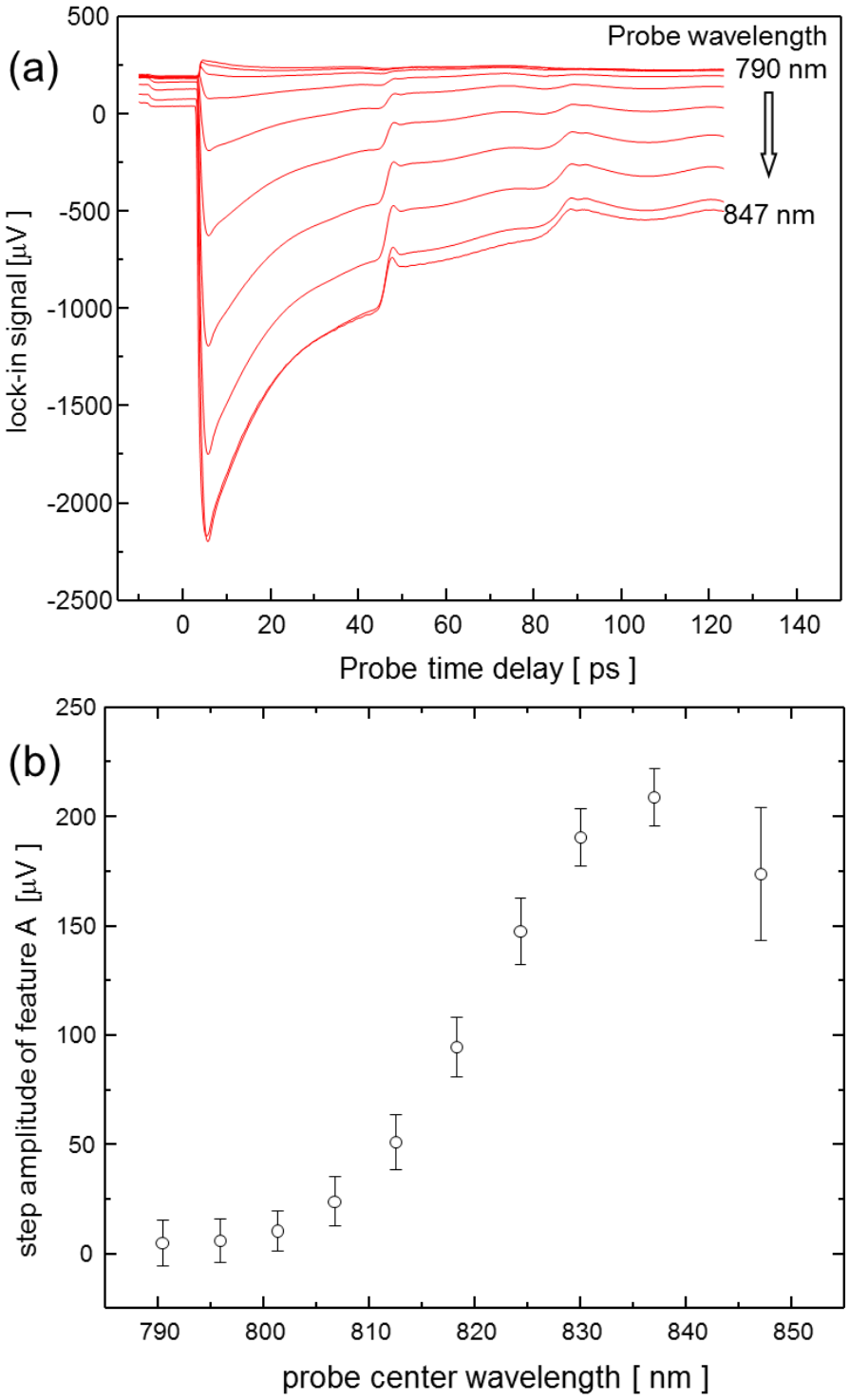

Figure 4.14: (a) Pump probe data taken on the cavity structure when it was dry (no coupling fluid). The step in the signal at a time delay of 45 ps is due to strain leaving the spacer SiO_2 layer. The magnitude of this step is an indicator of both the magnitude of strain generated by the pump pulse, and the sensitivity of the cavity to strain induced perturbations. (b) The size of the step at 45 ps versus the center wavelength of the laser. The step has a peak at around 840 nm.

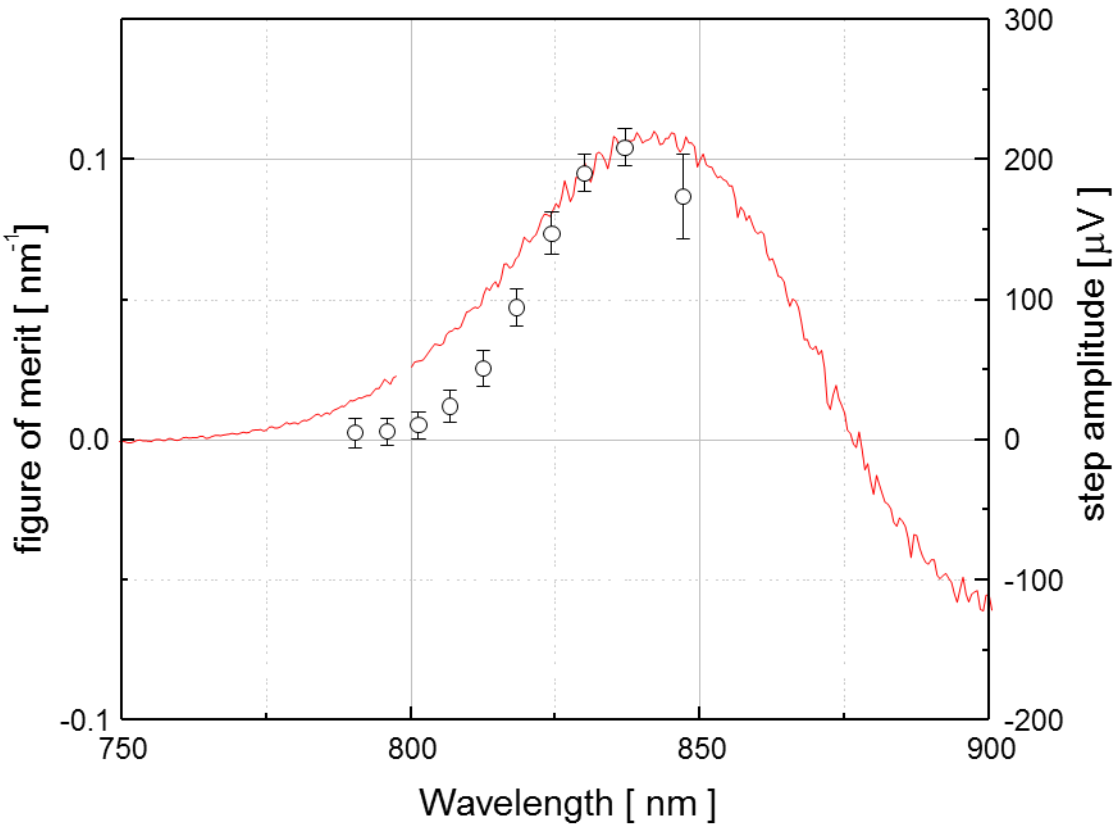

Figure 4.15: The solid curve is the calculated optical figure of merit for cavity B, and the points are the step amplitude taken from Fig. 4.14b. The optical figure of merit and the size of feature A both peak in at a probe wavelength of around 835 – 840 nm.

generating and detecting strain pulses. Figure 4.14b shows the size of the step of feature A as a function of the center wavelength. For this particular spot of the cavity structure, the optimal center wavelength of operation appears to be about 835 nm, although from Fig. 4.14b reasonable performance can be achieved in a 10 nm window around this value. The cavity used for the measurements shown in Figure 4.14 was cavity B from Figure 4.11. Figure 4.15 shows the figure of merit *M* for cavity B, from Figure 4.13, plotted with the data from Figure 4.14b such that their respective maxima have the same height on the plot. There is a clear correlation between the figure of merit *M* and the size of the step feature at 45 ps. However, it remains to be demonstrated that there is a correlation between size of the step feature at 45 ps and the performance of the cavity in an actual POAM measurement. This is discussed in the next section.

4.5 Characterization of the cavities – 'wet' tests

In this section, details as to the performance of the cavities in a POAM measurement are presented. Apart from the use of the sample positioning system described in Chapter 3, the experiment described below is identical to that reported by Yang *et al*.[10]. In that work, the decay of the various frequency components versus water film thickness was studied, and the attenuation of sound as a function of frequency, for frequencies approaching 11 GHz, was determined (results are summarized in Table 2.2.)

After a description of the experiment and the background subtraction procedure, two sets of measurements are presented below. First, the amplitude of a single acoustic echo was measured for different probe center wavelengths. The amplitude of the acoustic echo is a true measure of how well the cavity is performing, and it is shown below that the size of step feature A from the dry tests discussed above is correlated to the performance of the cavity. Second, by using the cavity to probe a simple, planar surface, information about the combined sound generation and detection processes of the cavity was obtained.

4.5.1 Planar reflector measurements

The sample was a piece of silicon wafer (orientation <100>), whose rms surface roughness was measured to be less than 0.3 nm by atomic force microscopy over a 20 μm x 20 μm area. The cavity was fabricated according to the procedure described in Section 4.4. After the cavity films were deposited onto the glass substrate, discs with a diameter of 3 mm were cut with an ultrasonic coring drill. The cavity disc and sample were then mounted into the sample positioning system described in Chapter 3. The cavity and sample were positioned such that their parallelism was better than 0.5 mrad. One drop (0.2-0.5 mL) of de-ionized water was placed between the sample and the cavity. The z position of the stage was increased until acoustic echoes were observed in the picosecond ultrasonics data. Once echoes were seen, further adjustments were made until the parallelism was better than 0.1 mrads. This was done by taking POAM data at three points on the sample, and then adjusting the tip and tilt until the arrival times of the echoes were the same.

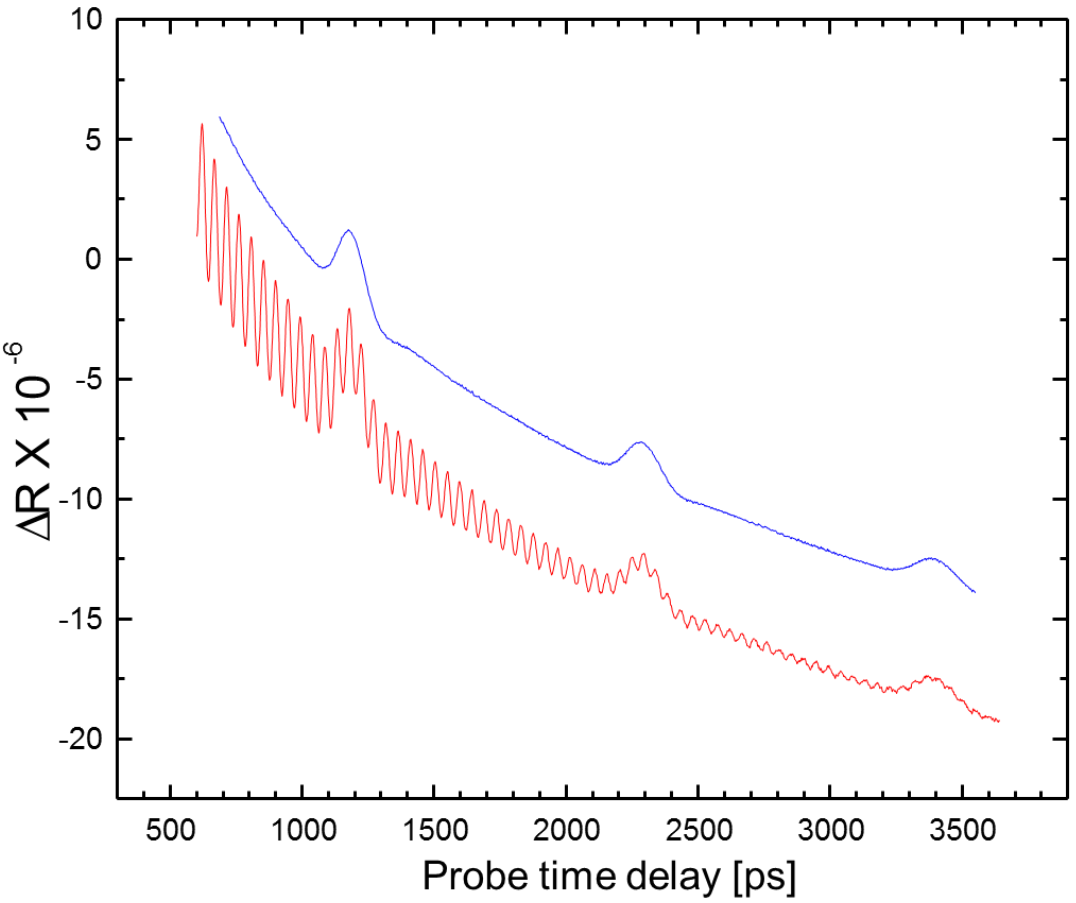

Figure 4.16: Measured change in optical reflectivity versus probe time delay. From the spacing between the echoes, the water thickness is 830 nm. The lower trace is the data as recorded; the upper trace shows the data after applying the numerical filter Eq. 4.23 (displaced vertically for clarity).

Figure 4.16 shows the change in reflectivity versus probe delay time. The data consisted of a slowly varying background, Brillouin oscillations with a period of 46 ps, and the acoustic echoes with widths on the order of 50 – 100 ps. The slowly varying background was attributed to the films in the cavity layer slowly cooling down after the excitation by the pump pulse.

To isolate the acoustic echoes, the Brillouin oscillations and the slowly changing background both needed to be removed from the data. The Brillouin oscillations were filtered out of the data by applying the transform

$$s(t) = \frac{1}{4}\Delta R(t + T/2) + \frac{1}{2}\Delta R(t) + \frac{1}{4}\Delta R(t - T/2), \qquad 4.26$$

where T is the measured period of the oscillations, and $\Delta R(t)$ is the measured change in reflectivity of the probe beam at probe time delay t. The period of the Brillouin oscillations was 46.6 ps. The filtered signal is shown as the blue curve in Fig. 4.16, and has been translated vertically for clarity. The slowly varying background can be removed by a two-step process. Once the data were taken at the desired water thickness, the stage was lowered, and another data set was taken with the water gap at a thickness on the order of 5-15 μm. In Fig. 4.17a, the water film thickness for the upper data set is approximately 750 nm. For the lower data set, the water film thickness was then increased by 4 microns. By subtracting the two data sets, it was hoped that their common, non-acoustic background would cancel, leaving only the acoustic signal. Unfortunately, there was a difference in the slowly changing background between the two data sets; in Figure 4.17a, the two curves are both plotted on the same scale. It is not clear what caused the background to be a function of the water film thickness. The background data set was smoothed, and then subtracted from the echo data set. Upon subtracting the background data from the echo data, a small residual background still remained. Figure 4.17b shows the data near the first echo after the subtraction of the background data. The points around the echo were then fitted, using a linear least squares procedure, to a low order polynomial of the form

$$p(t) = \sum_{n=0}^{N} a_n t^n , \qquad 4.27$$

where N was usually 2. The resulting polynomial was then subtracted from the data.

Figure 4.18a shows the amplitude of the acoustic echo taken at two probe center wavelengths, 795 and 824 nm. The size of the echo is a true measure of how well the cavity is performing, but it is time consuming to find the optimal wavelength by performing a POAM measurement at multiple wavelengths. As stated above, the size of feature A in the data served as a good indicator of the cavity's performance. Figure 4.18b shows the size of the step feature A from Figure 4.14b plotted on the same graph as the size of the acoustic echo versus probe center wavelength. The spot on the cavity used to

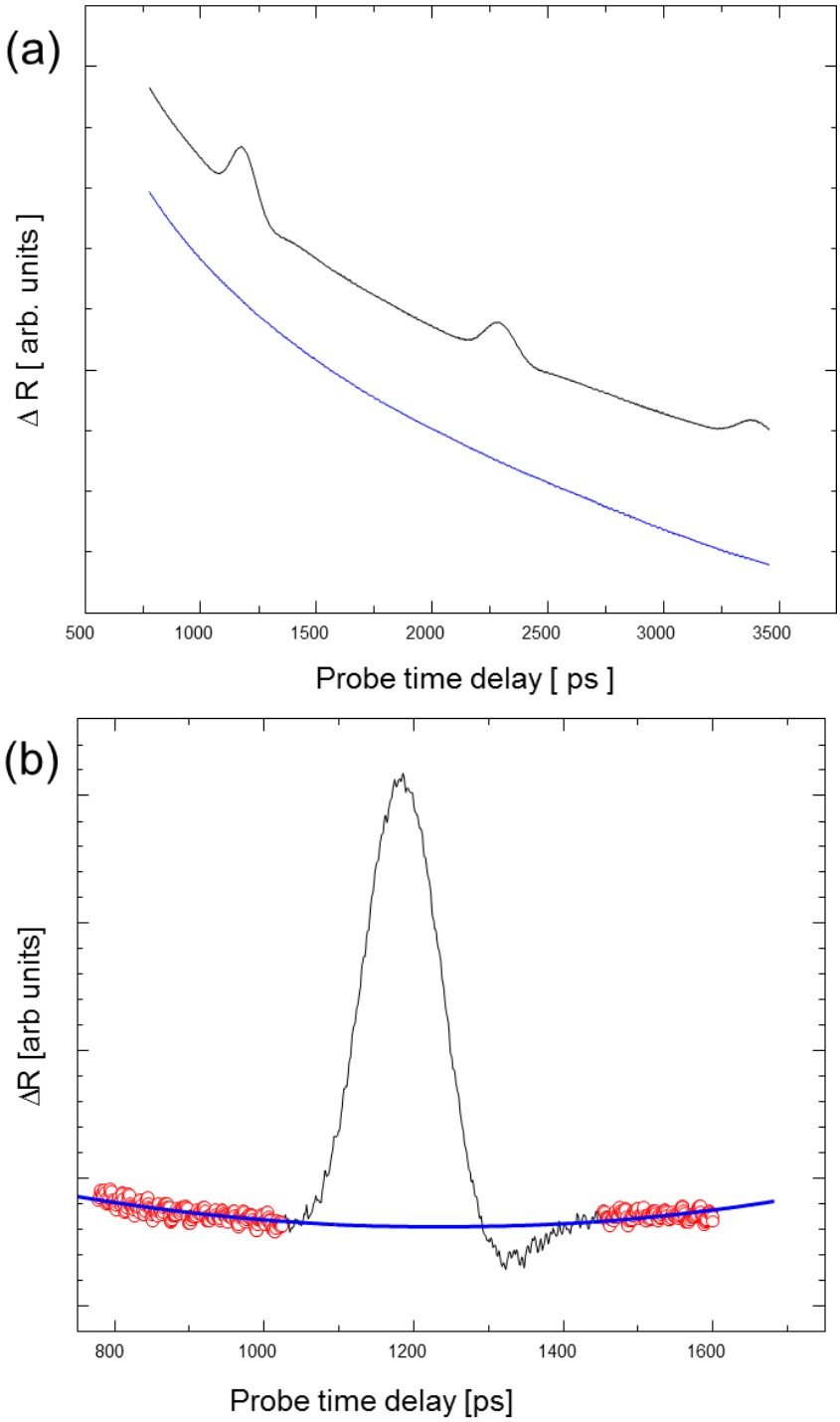

Figure 4.17: (a) Upper curve – data taken with a water film thickness of 750 nm after applying the filter Eq. 4.23. Lower curve – data taken with a water film thickness of approximately 5 μm. Both curves are plotted on the same scale (b) After subtracting the two curves in Fig. 4.17a, the remaining background was removed by fitting the points around the echo to a low order polynomial as described in text.

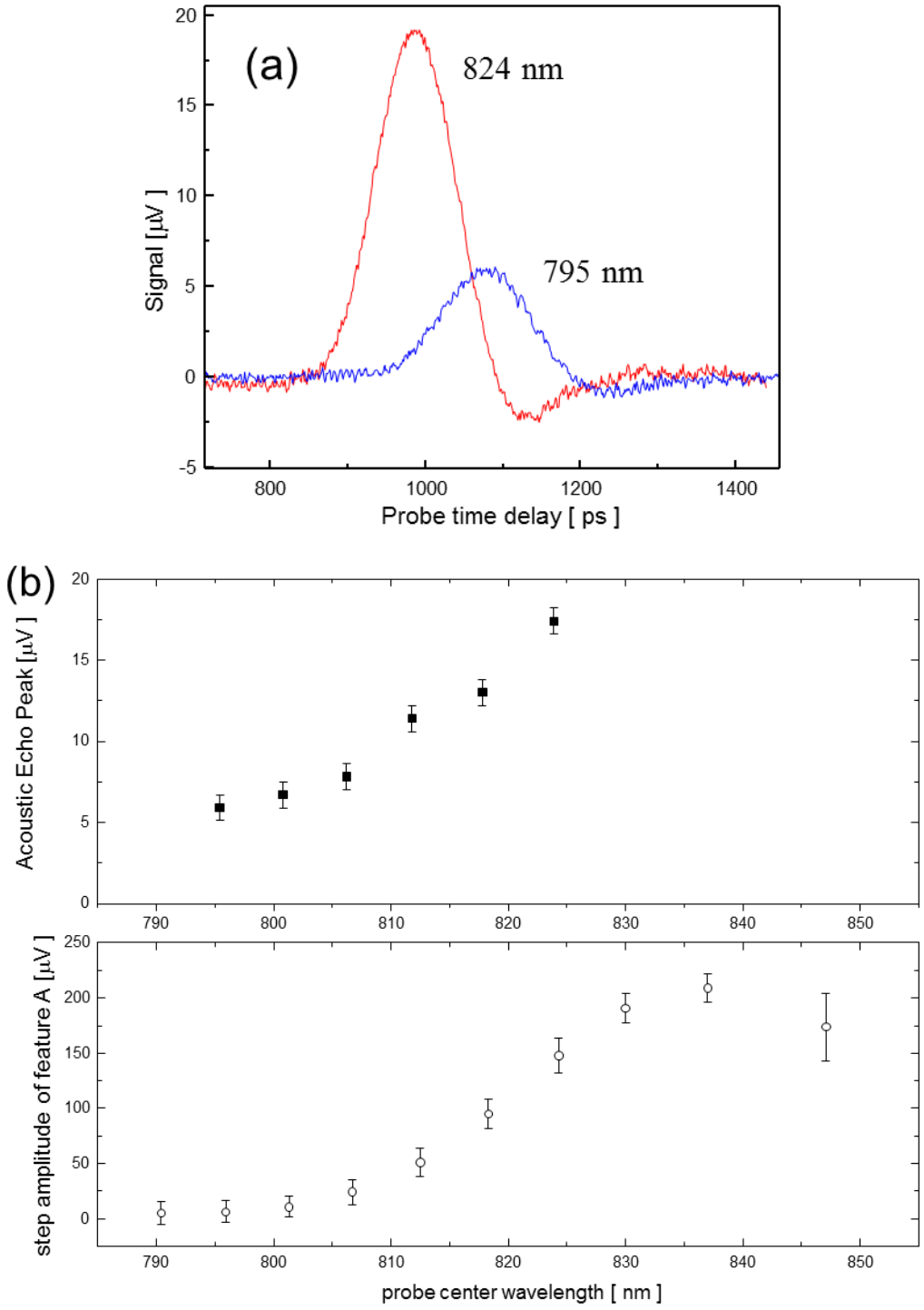

Figure 4.18: (a) Acoustic echoes taken with a probe center wavelength of 795 and 824 nm. The size of the echo is the best indicator of the cavity's performance. (b) The top plot shows echo amplitudes from a simple POAM measurement versus probe center wavelength, and the bottom plot the step amplitude taken from Fig. 4.14b.

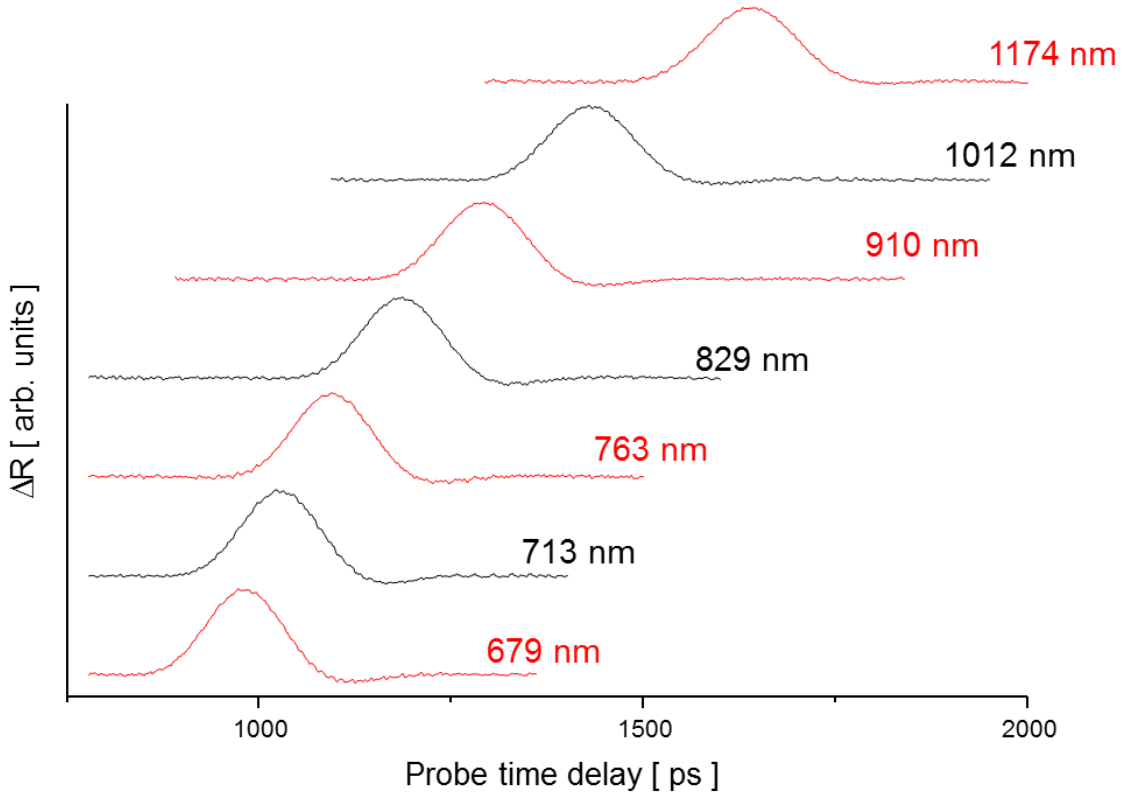

Figure 4.19: Echoes at several different water gap thicknesses. Data was treated in the manner described in the text.

collect this data was near the end of its measurement life, and acoustic echo data sets could not be taken at probe wavelengths larger than 824 nm. This makes it difficult to quantitatively compare the data in the two plots of Fig. 4.18b. It is clear, however, that there is at least a rough correlation between the magnitudes of step feature A and the amplitudes of the acoustic echo. By tuning the laser such that the step feature A is a maximum, the cavity will be near its optimal wavelength for POAM measurements. This proved invaluable in extending the useful measurement life of the cavity discs.

Figure 4.19 shows data taken at different water film thicknesses, where each data set has been treated using the method described above. In all of the echoes, there is a clear tail after the primary peak; an explanation as to its origin is presented below.

4.5.2 A simple model for sound generation and detection by the cavity

Based on the results described above, we present a model of the sound generation and detection processes of the cavity. The two following assumptions were made. First, it was assumed that all of the strain generated comes from the thin Al film. This assumption was based on the results of section 4.3, combined with results of a similar analysis of the cavities fabricated as described in section 4.4. Second, it was assumed that all the films have acoustic impedances such that the only two interfaces with significant reflection coefficients for the strain are the water – cavity interface and the cavity – substrate interface.

Using the above assumptions, the sound generated by the cavity structure after excitation by the pump beam will consist of two short pulses, with durations less than 2 ps, which originated from the thin Al film. If the sound takes a time T_1 to travel through the spacer layer of SiO_2, and a time T_2 to travel through the combined thickness of the Al film and cap SiO_2 layer, then the two pulses will be separated by a time of $2T_1 + 2T_2$; this is illustrated in Fig. 4.20. For the structures used in this work, T_1 is 45 ps, and T_2 is about 20 ps, so the two pulses generated by the cavity are separated by approximately 130 ps. The relative amplitude of the two pulses will be determined by the strain reflection coefficients for the cavity – substrate interface (r_{sub}), and the water – cavity interface (r_{water}). Since the acoustic impedance of the films is higher than that of water, the strain will suffer a sign change upon reflection from the water – cap layer interface $(r_{water} < 0)$. The strain generated by the cavity and launched into the fluid can be treated as having the following form

$$f(t,z) = \delta(t - z/v_w) - r_{sub}|r_{water}|\delta(t - z/v_w - \Delta t), \qquad 4.28$$

where Δt is $2T_1 + 2T_2$. Strain pulses that have reflected off of the cavity – substrate interface more than once have been neglected. The above description neglects any excitation of a thickness mode, or 'ringing', in the thin Al film. The thickness mode of

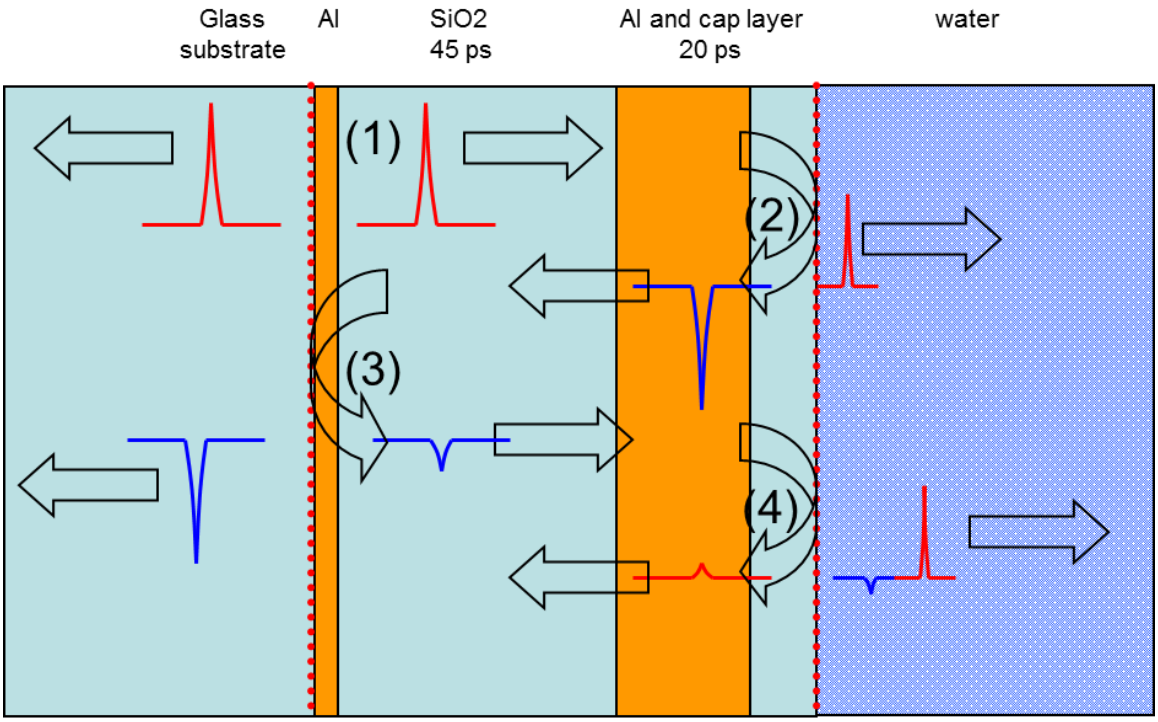

Figure 4.20: Model of the sound generated by the cavity. The cavity films are assumed to be perfectly matched, and the only acoustic reflections that take place are at the cavity-substrate interface and the cavity-water interfaces (marked by dotted lines). (1) Initial strain generated in the thin Al film relaxes and launches two pulses. (2) Strain reflects from cavity-water interface and changes sign – primary pulse transmitted into water. (3) Strain reflects from the cavity-substrate interface. (4) Strain reflects from cavity water interface and changes sign – secondary pulse transmitted into the water.

the thin Al film will have a period of less than 2 ps, and since these high frequencies will be rapidly attenuated by the water, they can be ignored. After propagating through several hundred nanometers of the coupling fluid, the initially sharp pulses will evolve into Gaussian shaped pulses as described in section 2.4.

Using the above assumptions, a simplified model for the cavity's response to incoming sound can be constructed. In a picosecond ultrasonics experiment, the change in reflectivity versus probe time delay can be expressed as

$$\Delta R(t) = \int f(z)\eta(z,t)dz\,, \qquad 4.29$$

where $\eta(z,t)$ is the strain in the sample at position z and time t. The function $f(z)$, called the sensitivity function, describes the effect of a strain at position z on the optical reflectivity of the structure. Using a perturbation technique as described by Thomsen *et*

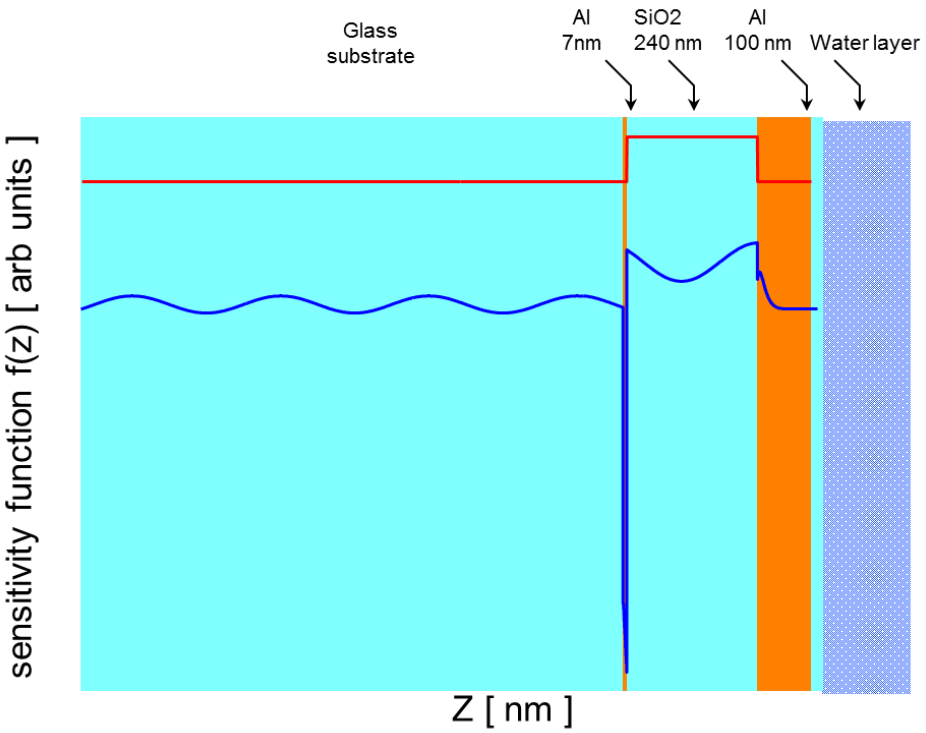

Figure 4.21: Computed (a) and simplified (b) sensitivity function *f(z)* of the cavity structure. Z axis, with layers, drawn to scale.

al.[11], the sensitivity functions for simple samples, such as optically opaque films on substrates, have been worked out to first order in the strain. A closed form expression for the sensitivity function of the cavity will be quite complicated, since it has many films and many piezo-optic constants. The sensitivity function of a multilayer sample can be numerically constructed based on a matrix method for computing the optical reflectivity of layered structures similar to that first employed by Abeles[12]. Each film is split into many bins, each of which has an optical transfer matrix. To find the value of the sensitivity function at a position z, a significant strain (10%) is placed into a single bin at position z, and the altered transfer matrix for the bin is computed. The effects of the change in the thickness of the bin and the change in its optical properties are both included. The sensitivity function for a cavity structure is shown in Fig. 4.21a. The properties used for the various materials in the calculation are summarized in Table 4.1.

Material	n	k	$\partial n / \partial \eta$	$\partial \kappa / \partial \eta$
Al	1.17*	4.15*	–0.8†	4.5†
SiO_2	1.45	0	–0.6‡	0

Table 4.1: Summary of the properties used for the calculation of the sensitivity function of the cavity shown in Fig. 4.21a. *From ellipsometry measurements performed on an Al film deposited with the same system used to deposit the cavity films. † taken from Ref. 4 ‡this value is from a calculation based on the results Waxler *et al.*[13] for a wavelength of 633 nm.

As a strain pulse propagates through the substrate, the oscillations in the sensitivity function will manifest themselves as Brillouin oscillations in the signal $\Delta R(t)$. Strain present in the thin and thick Al films will result in changes in reflectivity due to a combination of a change in the magnitude and phase of the optical reflection coefficients for the electric field at each film. These effects are difficult to characterize since they depend not only on the complex refractive index of the Al films, but also on their piezo-optic properties as well. When there is strain in the spacer layer, there are two contributions to the sensitivity function; approximately 1 period of Brillouin oscillations, and a step in the reflectivity due to the change in the optical thickness of the spacer layer caused by the strain. The complicated sensitivity function shown in Fig. 4.21a can be replaced by a simplified step function Fig. 4.21b, since after propagating through the coupling fluid, the strain pulses will have widths larger than the time it takes to propagate through the cavity films. This will serve to wash out the oscillations and sharp features in the sensitivity function shown in Fig. 4.21a.

The response function of the cavity is defined here as the change in reflectivity caused by an incoming Dirac delta function strain pulse propagating into the cavity structure from the water side. A simple model is proposed for the response function of the cavity. This model uses the simplified sensitivity function shown in Fig. 4.22b, along with the above assumptions of the films being perfectly matched except at the cavity – substrate and cavity – water interfaces. When the incoming strain pulse enters the cavity, it will suffer two reflections, as shown in Figure 4.22a; one reflection from the cavity – substrate

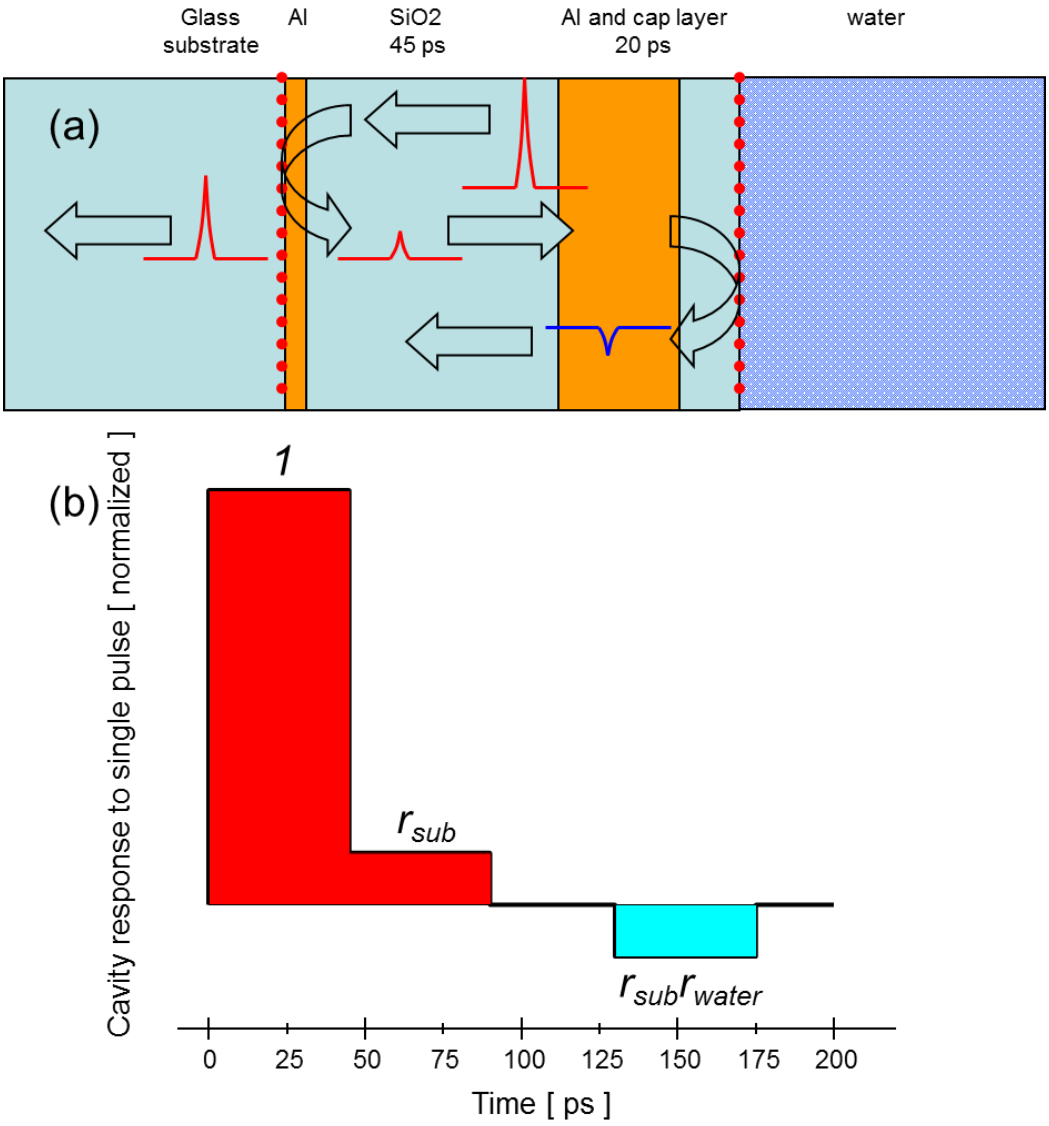

Figure 4.22: (a) The response of the cavity to a Dirac-delta pulse incident from the water side of the cavity. Assuming that the only substantial reflections take place at the thin cavity-substrate interface and the cavity-water interface (marked by dotted lines), an incoming pulse will generate a trailing pulse, with opposite sign. (b) The approximate change in optical reflectivity using the simplified sensitivity function of Fig. 4.19b. Time t = 0 ps is taken to as the time when the pulse enters the SiO_2 spacer layer

interface and one from the cavity – water interface. The response function of the cavity, using the simplified sensitivity function, is shown in Figure 4.22b.

The response of the cavity to an arbitrary incoming strain pulse can be modeled by taking the convolution of the incoming strain profile with the cavity response function. In the planar reflector experiments, the cavity launched a strain of the form of Eq. 4.28 into the

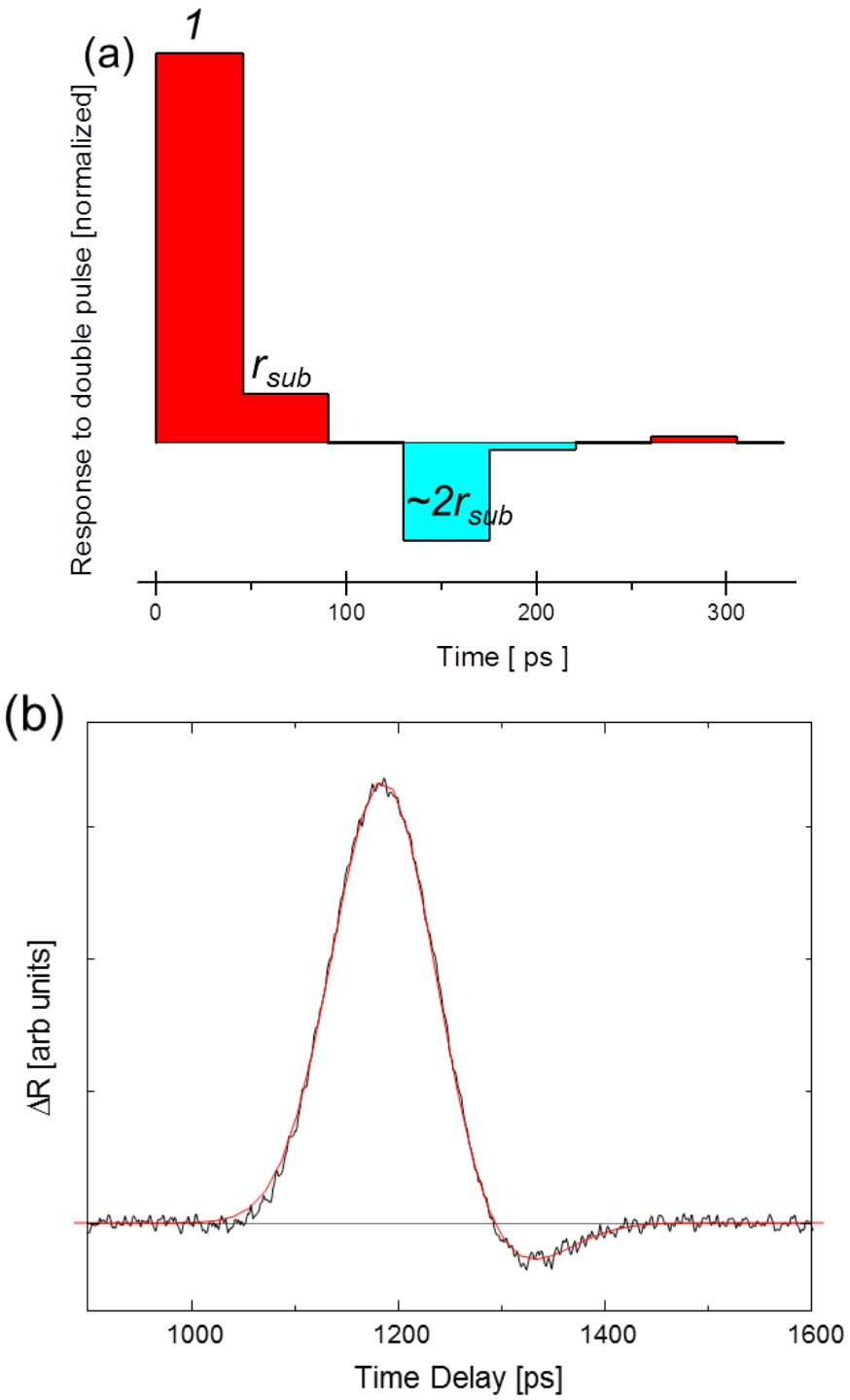

Figure 4.23: (a) The combined effects of the cavity generation and detection, without the effects of acoustic attenuation in the water. Time $t = 0$ corresponds to the time when the leading strain pulse enters the cavity spacer film. (b) Experimental data taken on a planar sample. The data was fitted to a function of the form in Eq. 4.27 with Δt =128 ps and $a = 0.1$.

water film. The strain reflected off of the water – silicon interface and then returned to the cavity. The convolution of the strain in Eq. 4.28 with the cavity response function shown in Fig. 4.22b is shown in Fig. 4.23a. Due to the acoustic attenuation of the water film, each rectangular strain profile will degenerate into a Gaussian profile. Figure 4.23b is a plot of a water echo, after going through the background subtraction process described above. Also plotted is a function of the form

$$C\left\{\exp\left[-\left(\frac{t-t_e}{\sigma_t}\right)^2\right]-a\exp\left[-\left(\frac{t-t_e-\Delta t}{\sigma_t}\right)^2\right]\right\} \qquad 4.30$$

where C is a constant, and t_e is the first echo arrival time. The first echo arrival time is related to the thickness of the water film, d, by $t_e = 2d/v$, where v is the sound velocity in the water. Each of the echoes shown in Fig. 4.19 was fitted to a function of the form Eq. 4.30. The value of Δt for the fits ranged from 120 – 140 ps, and the value of a ranged from 0.08 – 0.15, which implies that r_{sub} is in the range of 0.04 – 0.08. These values are consistent with the above discussion.

4.6 Conclusions

The fabrication, characterization, and testing of Fabry-Perot thin film cavities for use in picosecond ultrasonics measurements were presented. The design problem is certainly an involved one since the optical and mechanical/acoustic properties are interrelated. For cavities that were used in the POAM measurements, two main features need to be addressed; the magnitude and simplicity (*i.e.*, minimal acoustic 'ring down' time) of the cavity's response to an incoming strain pulse. This was accomplished by using films in the Al – SiO_2 material space. These materials were sufficiently well matched acoustically that the response function of the cavity only had a small tail whose magnitude was less than 15% of the main peak.

Bibliography

1. Thomson, J.K., Wickramasinghe, H.K. & Ash, E.A. "A Fabry-Perot acoustic surface vibration detector - application to acoustic holography". *J. Phys. D: Appl. Phys.* **6**, 677-687 (1973).
2. Hamilton, J.D., Buma, T., Spisar, M. & O'Donnell, M. "High frequency optoacoustic arrays using etalon detection." *Ultrasonics, Ferroelectrics and Frequency Control, IEEE Transactions on* **47**, 160-169 (2000).
3. Ashkenazi, S., Hou, Y., Buma, T. & O'Donnell, M. "Optoacoustic imaging using thin polymer étalon." *Appl. Phys. Lett.* **86**, 134102 (2005).
4. Li, Y., Miao, Q., Nurmikko, A.V. & Maris, H.J. "Picosecond ultrasonic measurements using an optical cavity." *J. Appl. Phys.* **105**, 083516 (2009).
5. Chang-Hasnain, C.J. "Tunable VCSEL." *Selected Topics in Quantum Electronics, IEEE Journal of* **6**, 978-987 (2000).
6. This sample was fabricated and characterized at the Semiconductor & Microsystems Fabrication Laboratory at the Rochester Institute of Technology with the assistance of Thomas J Grimsley Sr.
7. Lin, H.-N., Stoner, R.J., Maris, H.J. & Tauc, J. "Phonon attenuation and velocity measurements in transparent materials by picosecond acoustic interferometry." *J. Appl. Phys.* **69**, 3816 (1991).
8. http://www.corning.com/displaytechnologies/en/about_us/process.aspx.
9. http://www.delta-technologies.com/products.asp?C=1.
10. Yang, F. et al. "Picosecond ultrasonic experiments with water and its application to the measurement of nanostructures." *J. Appl. Phys.* **107**, 103537 (2010).
11. Thomsen, C., Grahn, H.T., Maris, H.J. & Tauc, J. "Surface generation and detection of phonons by picosecond light pulses." *Phys. Rev. B* **34**, 4129 (1986).
12. Born, M. *Principles of Optics: Electromagnetic Theory of Propagation, Interference and Diffraction of Light.* (Pergamon Press: Oxford, 1989).
13. Waxler, R.M., Horowitz, D. & Feldman, A. "Precision interferometer for measuring photoelastic constants." *Appl. Opt.* **16**, 20-22 (1977).

Chapter 5

Simulation of sound propagation in confined nanostructures

5.1 Introduction

In this chapter, two simulation methods for modeling the behavior of sound waves in a viscid and compressible fluid are presented. In section 5.2, a finite difference time domain (FDTD) method for modeling the scattering of sound from rigid nanostructures is demonstrated. In section 5.3, a frequency domain treatment of the problem of a fluid in an infinite channel waveguide is presented, and a numerical technique for determining the phase velocity and attenuation of the propagating modes is demonstrated. Both of these simulation methods, especially the FDTD program discussed in section 5.2, were used to interpret the POAM experimental results.

5.2 Simulation of the scattering of sound from periodic nanostructures

In a POAM measurement, the lateral extent of the sound launched into the coupling fluid is determined by the excitation area, *i.e.*, the focused spot size of the laser. For the optical setup used in this work, the excitation area was a circle with a radius of 10 – 15 μm. The large excitation area rules out the possibility of resolving individual nanostructures without further focusing of the sound. However, by examining a periodic array of structures with submicron features, average properties of the structures can be measured. Figure 5.1a shows a cross sectional scanning electron microscope (SEM)

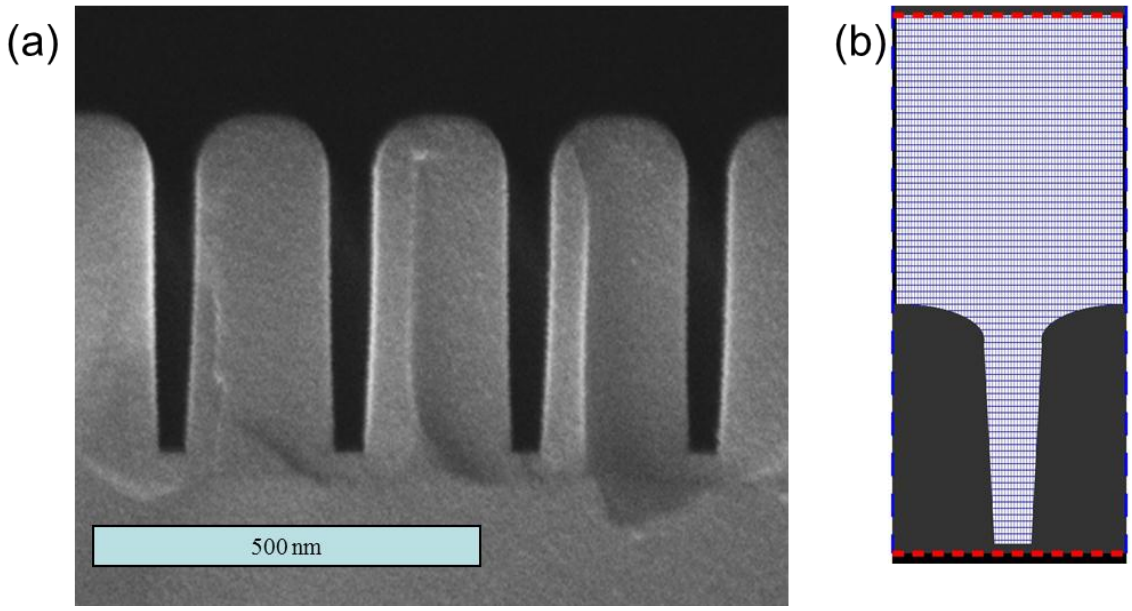

Figure 5.1: (a) Cross sectional SEM image of a typical sample studied in this work. Scale bar is 500 nm (b) Schematic of the computational domain. Zero displacement boundary conditions were enforced on the top and bottom faces (red dashed lines), and periodic boundary conditions were enforced on the lateral boundaries (blue dashed lines). The solid (gray) was taken to be a fluid with a density 10^6 times larger than that of water.

image of one of the samples studied. The samples were periodic in 1 dimension, and the spatial repeat distance, or period, of the sample was between 250 – 500 nm. Given the size of the excitation area, approximately 20 – 40 nanostructures were probed during a single measurement. More details about the sample fabrication will be given in Chapter

6. In what follows, some facts are stated about the FDTD method used to simulate the scattering of a sound pulse from rigid structures with profiles like that shown in Fig. 5.1a.

5.2.1 Equations of motion

The linearized partial differential equations describing the motion of the fluid are the continuity equation

$$\frac{1}{\rho_0}\frac{\partial \rho}{\partial t} + \vec{\nabla}\cdot\mathbf{v} = 0\,, \tag{5.1}$$

where ρ_0 is the density of the fluid in the absence of any sound and $\mathbf{v}$ is the velocity field, and Newton's second law applied to a fluid element

$$\rho_0 \frac{\partial \mathbf{v}}{\partial t} = \vec{\nabla}\cdot\mathbf{P}\,. \tag{5.2}$$

The connection between the density and the pressure is

$$B_s = \left(\rho\frac{\partial P}{\partial \rho}\right)_s, \tag{5.3}$$

where B_s is the bulk isentropic compressibility and is taken to be a constant. The divergence of the stress tensor can be written as[1]

$$\vec{\nabla}\cdot\mathbf{P} = -\nabla P + \vec{\nabla}\cdot\left(\mathbf{P}' + \mathbf{P}''\right), \tag{5.4}$$

where P is the hydrostatic pressure, and

$$P_{ij}' = \eta\left(\frac{\partial v_i}{\partial x_j} + \frac{\partial v_j}{\partial x_i}\right); P_{ii}' = 2\eta\left(\frac{\partial v_i}{\partial x_i} - \frac{\vec{\nabla}\cdot\mathbf{v}}{3}\right), \tag{5.5}$$

and

$$P_{ij}'' = 0; P_{ii}'' = \zeta\left(\vec{\nabla}\cdot\mathbf{v}\right). \tag{5.6}$$

The quantities η and ζ are the shear and volume coefficients of viscosity of the fluid. The second coefficient of viscosity can be deduced from measurements of the acoustic attenuation. It is straightforward to show, that for plane acoustic waves of the form

$$p(z,t) = p_0\exp(-\alpha z)\exp\left[i\left(kz-\omega t\right)\right], \tag{5.7}$$

where p is the excess pressure, that

$$\alpha = \frac{\omega^2}{2c_0^3\rho_0}\left(\frac{4}{3}\eta + \zeta\right), \qquad \omega = kc_0, \tag{5.8}$$

provided that $\alpha << k$, where $c_0 = \left(B_s / \rho_0\right)^{1/2}$ is the low frequency sound velocity. From the measured acoustic attenuation the volume coefficient of viscosity can be calculated. The relevant properties of water at 22 ^{o}C needed for the simulations are summarized in Table 5.1.

ρ_0 $\left(g \cdot cm^{-3}\right)$	c_0 $\left(cm \cdot s^{-1}\right)$	A $\left(s^2 \cdot cm^{-1}\right)$	η $\left(g \cdot s^{-1} \cdot cm^{-1}\right)$	$\left(\zeta / \eta\right)$
0.9977	1.4876 x 10^{5}	2.39 x 10^{-17}	9.62 x 10^{-3}	2.81

Table 5.1: Density, sound velocity, shear viscosity, and the ratio of bulk to shear viscosity for water at a temperature of 22 Celsius.

5.2.2 Finite difference time domain simulations in 2D

The equations of motion for the fluid in two dimensions, say *x* and *y*, can be written as

$$\frac{1}{\rho_0 c_0^2}\frac{\partial P}{\partial t} + \frac{\partial v_x}{\partial x} + \frac{\partial v_y}{\partial y} = 0 \tag{5.9a}$$

$$\rho_0 \frac{\partial v_x}{\partial t} = -\frac{\partial P}{\partial x} + \left(\zeta + \frac{\eta}{3}\right)\frac{\partial}{\partial x}\left(\frac{\partial v_x}{\partial x} + \frac{\partial v_y}{\partial y}\right) + \eta\left(\frac{\partial^2 v_x}{\partial x^2} + \frac{\partial^2 v_x}{\partial y^2}\right), \tag{5.9b}$$

$$\rho_0 \frac{\partial v_y}{\partial t} = -\frac{\partial P}{\partial y} + \left(\zeta + \frac{\eta}{3}\right)\frac{\partial}{\partial y}\left(\frac{\partial v_x}{\partial x} + \frac{\partial v_y}{\partial y}\right) + \eta\left(\frac{\partial^2 v_y}{\partial x^2} + \frac{\partial^2 v_y}{\partial y^2}\right). \tag{5.9c}$$

A finite difference time domain (FDTD) method was used to simulate the scattering of a sound pulse off of a periodic rigid structure. Figure 5.1b shows a schematic of the computational domain. The domain was split into a grid. The particle acceleration, velocity, and displacement were calculated on the grid points, while the strain and stress were computed in the center of the square formed by four grid points. Periodic boundary conditions were applied in the *x* direction, and the top and bottom faces were held fixed.

To simulate the incoming pulse generated by the cavity, the top face was displaced by a distance of 10% of the grid spacing, and was then held at that position for subsequent

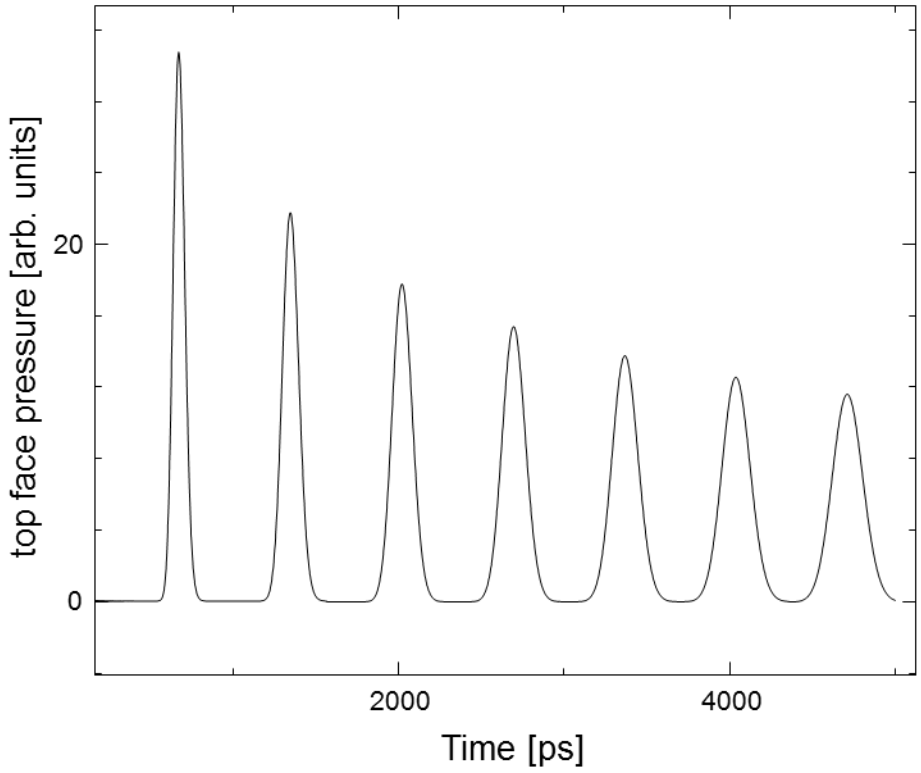

Figure 5.2: Simulation results for a water gap of 505 nm. The average pressure on the top face is shown above. The mesh size was 5 nm and the time step was 2 ps.

time steps. In the simulation, the rigid solid structure was modeled as a fluid with the same properties as water but with a density 10^6 times larger than that of water. After each time step, the average pressure on the boundary was recorded.

As a test, no solid was included in the domain, and the initial pulse was allowed to traverse the water gap several times. The mesh size was 5 nm and the time step 1 ps. All of the fluid properties used in the simulation were the same as those in Table 5.1, except the sound velocity was rounded up to 1.5 nm ps^{-1}. The period was 400 nm, and the distance from the top boundary to the bottom was 505 nm. The average pressure on the top face versus time is shown in Fig. 5.2. Based on the discussion of section 2.4, the expected solution is a series of echoes of the form

$$s(t) = \sum_n \frac{a_1}{\sqrt{n}} \exp\left[-\left(\frac{t - nt_0}{\sigma_0 \sqrt{n}} \right)^2 \right], \qquad 5.10$$

where a_1 is the amplitude of the first echo. The arrival time of the first echo is

$$t_0 = 2d / c_0, \qquad 5.11$$

and the width of the first echo, from Eqs. 2.14 and 5.8

$$\sigma_0 = \sqrt{\frac{2}{c_0^3 \rho_0} \left(\frac{4}{3}\eta + \zeta \right) (2d)} \ . \qquad 5.12$$

For the data in Fig. 5.2, a Gaussian of the form

$$a_n \exp\left[-\left(\frac{t - t_n}{\sigma_n} \right)^2 \right], \qquad 5.13$$

was fitted to each echo, and the results are shown in Table 5.2. For the parameters used, the expected value of t_0 is 673.33 ps and that of σ_0 is 48.90 ps. The simulation results agree quite well with the expected result. The above was repeated for several mesh sizes and time steps, and similar results were obtained.

Echo number (n)	(a_n / a_1)	t_n [ps]	$(t_n - t_{n-1})$ [ps]	σ_n [ps]	$\left(\frac{\sigma_n - \sqrt{n}\sigma_0}{\sqrt{n}\sigma_0} \right)$ [%]	$(a_n / a_1)^{-2}$
1	1	673.338		48.936	0.075	1
2	0.7076	1346.467	673.130	69.168	0.020	2.00
3	0.5779	2019.803	673.336	84.695	-0.001	2.99
4	0.5006	2693.138	673.335	97.789	-0.010	3.99
5	0.4477	3366.471	673.334	109.329	-0.012	4.99
6	0.4088	4039.809	673.338	119.753	-0.020	5.98
7	0.3785	4713.140	673.331	129.344	-0.024	6.98

Table 5.2: Results of fitting a Gaussian of the form Eq. 5.13 to each of the echoes.

Table 5.3 summarizes the approximate maximum time step for which the algorithm is stable for a given mesh size, as well as the time step used for simulation results presented in this work.

mesh nm	approximate maximum time step ps	time step used Ps
10	5	4
5	2	1
2	0.4	0.25
1	0.1	0.1

Table 5.3: Time steps used for mesh sizes used in this work. For time steps larger than approximate maximum time step, the algorithm became unstable.

5.3 Simulation of the propagation of sound in a channel with fixed slip length

Structures of the form shown in Fig. 5.1a can serve as sensitive test for the presence of slip between the water and the sidewalls of the channels, since as the sound pulse incident on the structure gets funneled into the channel, appreciable strain-rates at the solid-liquid boundary can be expected. The simulation program described above effectively enforces a no-slip boundary condition at the solid-liquid interfaces. One way to include slip at the boundary would be to add a layer of fluid with low viscosity at the solid-liquid interface. This model of the solid-liquid interface has at least two adjustable parameters: the thickness of the boundary layer and the factor by which the viscosities are reduced. A related problem, with only one adjustable parameter, was considered to gain some insight on the effect of slip on sound propagating down a nanoscale channel.

One way to treat slip at the solid-liquid interface is through the implementation of the boundary condition, first proposed by Navier[2], where the tangential velocity of the fluid along the interface, v_t, is proportional to the shear strain rate at the surface

$$v_t = b\left(\nabla v_t \cdot \mathbf{n}\right), \qquad 5.14$$

where $\mathbf{n}$ is a unit vector which points from the solid into the liquid and is normal to the interface. The quantity *b* has dimensions of length and is called the slip length.

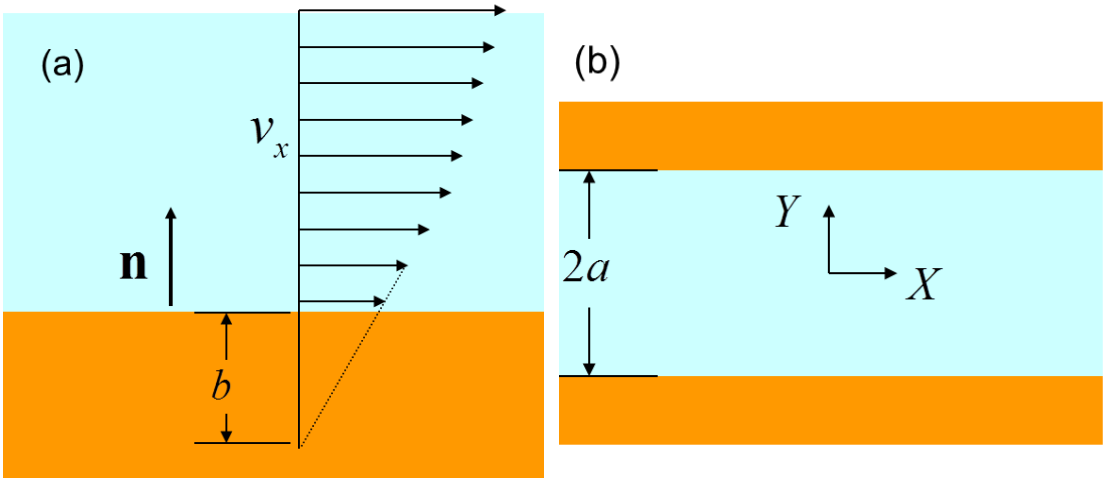

Figure 5.3: (a) Definition of the slip length. (b) The geometry of the problem considered was an infinite channel with a width of *2a*, and at the rigid walls either a no slip or a fixed slip length boundary condition was enforced.

Geometrically this is the distance into the wall at which the velocity v_t extrapolates to 0, as shown in Fig. 5.3a. At this point, no mention will be made as to proposed mechanisms of slip; in this section, the mathematical problem stated below is treated.

The geometry of the problem is shown in Fig. 5.3b. The fluid extends to infinity in the *x* and *z* directions, and is bounded by two impenetrable walls at $y = a$ and $y = -a$. Solutions of Eqs. 5.9a-c of the form $\exp\left[i\left(kx-\omega t\right)\right]$ are sought for the cases of (1) no slip and (2) slip characterized by slip length *b* at the boundaries. By considering the effect of the slip length on the phase velocity and attenuation of various frequency components as they propagate down the channel, some insight as to the magnitude of the effects of slip can be gained. The starting point is the treatment of Sorokin and

Chubinskij [3], who used velocity potentials to find the dispersion relation for the no slip case. The same method is applied to the slip boundary condition case, and the roots of the dispersion relation were found numerically.

5.3.1 Infinite channel with no-slip boundary conditions

Equations 5.9 can be written in the form

$$\frac{\partial s}{\partial t} = -\frac{\partial v_x}{\partial x} - \frac{\partial v_y}{\partial y}, \tag{5.15a}$$

$$\frac{\partial v_x}{\partial t} = -A\frac{\partial s}{\partial x} + (B+C)\frac{\partial^2 v_x}{\partial x^2} + B\frac{\partial^2 v_x}{\partial y^2} + C\frac{\partial^2 v_y}{\partial x \partial y}, \tag{5.15b}$$

$$\frac{\partial v_y}{\partial t} = -A\frac{\partial s}{\partial y} + B\frac{\partial^2 v_y}{\partial x^2} + (B+C)\frac{\partial^2 v_y}{\partial y^2} + C\frac{\partial^2 v_x}{\partial x \partial y}, \tag{5.15c}$$

where s is the fractional change in density

$$s = \frac{\rho - \rho_0}{\rho_0}. \tag{5.16}$$

The constants A, B, and C are

$$A = c_0^2,\ B = \left(\frac{\eta}{\rho_o}\right),\ \text{and}\ C = \left(\frac{\frac{1}{3}\eta + \zeta}{\rho_o}\right). \tag{5.17}$$

The fluid velocity can be expressed in terms of a scalar and vector potential

$$\mathbf{v} = \vec{\nabla}\phi + \vec{\nabla} \times \mathbf{\Psi}. \tag{5.18}$$

In this problem, the only non-zero component of the vector potential is the z component, and the vector potential can be written as

$$\mathbf{\Psi} = \psi(x, y)\hat{\mathbf{e}}_\mathbf{z}. \tag{5.19}$$

The x and y components of the velocity, in terms of the potentials, are

$$v_x = \frac{\partial \phi}{\partial x} + \frac{\partial \psi}{\partial y},\ v_y = \frac{\partial \phi}{\partial y} - \frac{\partial \psi}{\partial x}. \tag{5.20}$$

Substituting the above into Eq. 5.15 yields two equations for the two potentials

$$\frac{\partial}{\partial t}\psi = B\left(\frac{\partial^2}{\partial x^2}+\frac{\partial^2}{\partial y^2}\right)\psi, \tag{5.21a}$$

$$\frac{\partial^2\phi}{\partial t^2} = \left[(B+C)\frac{\partial}{\partial t}+A\right]\left(\frac{\partial^2\phi}{\partial x^2}+\frac{\partial^2\phi}{\partial y^2}\right). \tag{5.21b}$$

The use of velocity potentials has simplified the partial differential equations, but at the cost of complicating the boundary conditions. A no-slip boundary condition was enforced at the edges of the waveguide

$$v_x\left(x, y=\pm a\right)=0, \tag{5.22}$$

and no fluid was allowed to penetrate the wall

$$v_y\left(x, y=\pm a\right)=0. \tag{5.23}$$

Solutions for the potentials of the form

$$\phi(x,y) = g(y)\exp\left[i\left(kx-\omega t\right)\right], \tag{5.24a}$$

$$\psi(x,y) = h(y)\exp\left[i\left(kx-\omega t\right)\right]. \tag{5.24b}$$

are sought. The boundary conditions, using 5.24, become

$$ikg\left(y=\pm a\right)+h'\left(y=\pm a\right)=0, \tag{5.25a}$$

$$g'\left(y=\pm a\right)-ikh\left(y=\pm a\right)=0. \tag{5.25b}$$

Substituting Eq. 5.24 into Eq. 5.21 yields two ordinary differential equations

$$h''(y)=\left(-i\frac{\omega}{B}+k^2\right)h(y), \tag{5.26}$$

$$g''(y)=\left(-\frac{A\omega^2+i\omega^3(B+C)}{A^2+\omega^2(B+C)^2}+k^2\right)g(y). \tag{5.27}$$

Through the change of variables $\tilde{y}=y/a$ and the introduction of the dimensionless parameters for the wave number and the angular frequency $K=ka$, $\Omega=\omega a/c_o$, and the dimensionless parameters

$$\gamma = \frac{B}{c_0 a},\ \mu = \frac{(B+C)}{c_0 a}, \tag{5.28}$$

equations 5.26 and 5.27 become

$$g''(\tilde{y}) = \left(K^2 - \frac{\Omega^2 + i\mu\Omega^3}{1+\mu^2\Omega^2} \right) g(\tilde{y}), \tag{5.29}$$

$$h''(\tilde{y}) = \left(K^2 - i\frac{\Omega}{\gamma} \right) h(\tilde{y}). \tag{5.30}$$

The solutions to the above are

$$h(\tilde{y}) = A_1 \cos\beta\tilde{y} + A_2 \sin\beta\tilde{y}, \tag{5.31a}$$

$$g(\tilde{y}) = B_1 \cos\alpha\tilde{y} + B_2 \sin\alpha\tilde{y}, \tag{5.31b}$$

where

$$\beta = \sqrt{i\frac{\Omega}{\gamma} - K^2},\ \alpha = \sqrt{\frac{\Omega^2 + i\mu\Omega^3}{1+\mu^2\Omega^2} - K^2}. \tag{5.32}$$

Substituting Eq. 5.31 into the boundary conditions yields four equations

$$\begin{pmatrix} 0 & \beta\cos\beta & iK\cos\alpha & 0 \\ -\beta\sin\beta & 0 & 0 & iK\sin\alpha \\ -iK\cos\beta & 0 & 0 & \alpha\cos\alpha \\ 0 & iK\sin\beta & \alpha\sin\alpha & 0 \end{pmatrix} \begin{pmatrix} A_1 \\ A_2 \\ B_1 \\ B_2 \end{pmatrix} = 0. \tag{5.33}$$

The above is a homogenous linear system of equations for the coefficients A_1, A_2, B_1, and B_2. A sufficient and necessary condition for a solution to exist is that the determinant of the coefficient matrix vanishes. The determinant of the coefficient matrix in Eq. 5.33 can be expressed as the product of two quantities

$$\left(\alpha\beta\cos\alpha\sin\beta + K^2\sin\alpha\cos\beta\right)\left(\alpha\beta\sin\alpha\cos\beta + K^2\cos\alpha\sin\beta\right) = 0. \tag{5.34}$$

This implies that either

$$\left(\alpha\beta\cos\alpha\sin\beta + K^2\sin\alpha\cos\beta\right) = 0, \tag{5.35a}$$

or

$$\left(\alpha\beta\sin\alpha\cos\beta + K^2\cos\alpha\sin\beta\right) = 0\,. \qquad 5.35b$$

Equations 5.35a and 5.35b are dispersion equations and express the relationship between the dimensionless frequency Ω and wave number K. From Eqs. 5.33 and 5.31 it can be shown that Eq. 5.35a corresponds to $A_1 = B_2 = 0$. The first dispersion relation applies to modes where the potential ϕ has even symmetry about the center of the waveguide. Likewise, it can be shown that the second dispersion relation corresponds to modes where $A_2 = B_1 = 0$, which are modes where the potential ϕ has odd symmetry.

5.3.2 Infinite channel with slip length boundary conditions

The above analysis can be repeated using a slip boundary condition. Applying the boundary condition of Eq. 5.14 to this geometry

$$v_x(x,a) = -b\left.\frac{\partial v_x}{\partial y}\right|_{y=a}, \text{ and } v_x(x,-a) = b\left.\frac{\partial v_x}{\partial y}\right|_{y=-a}. \qquad 5.36$$

The boundary condition on the normal component (v_y) of the fluid velocity is still Eq. 5.23 for the no slip case.

By introducing the dimensionless slip parameter $\lambda = b/a$, the boundary conditions become

$$iKg(\tilde{y}=1) + h'(\tilde{y}=1) = -i\lambda K g'(\tilde{y}=1) + \lambda\beta^2 h(\tilde{y}=1), \qquad 5.37$$

$$iKg(\tilde{y}=-1) + h'(\tilde{y}=-1) = i\lambda K g'(\tilde{y}=-1) - \lambda\beta^2 h(\tilde{y}=-1), \qquad 5.38$$

$$g'(\tilde{y}=\pm 1) - iKh(\tilde{y}=\pm 1) = 0\,. \qquad 5.39$$

Proceeding in the same way as before yields four equations for the coefficients in Eq. 5.31, which now become

$$\begin{pmatrix} 0 & \beta\cos\beta-\lambda\beta^2\sin\beta & iK\cos\alpha-i\lambda K\alpha\sin\alpha & 0 \\ -\beta\sin\beta-\lambda\beta^2\cos\beta & 0 & 0 & iK\sin\alpha+i\lambda K\alpha\cos\alpha \\ -iK\cos\beta & 0 & 0 & \alpha\cos\alpha \\ 0 & iK\sin\beta & \alpha\sin\alpha & 0 \end{pmatrix}\begin{pmatrix} A_1 \\ A_2 \\ B_1 \\ B_2 \end{pmatrix}=0$$

5.40

This results in two dispersion relations, one for modes where ϕ has even symmetry

$$\left(\alpha\beta\cos\beta\sin\alpha+K^2\cos\alpha\sin\beta\right)-\lambda\alpha\left(\beta^2+K^2\right)\sin\beta\sin\alpha=0, \qquad 5.41a$$

and one where ϕ has odd symmetry

$$\left(K^2\sin\alpha\cos\beta+\beta\alpha\sin\beta\cos\alpha\right)+\lambda\alpha\left(\beta^2+K^2\right)\cos\beta\cos\alpha=0. \qquad 5.41b$$

As λ approaches 0, the no-slip dispersion relations are recovered. Using the above results, the expressions for v_x and v_y for the even symmetry modes become

$$v_x(x,y)=\frac{A_2}{a}\left[\cos\left(\alpha\frac{y}{a}\right)\left(\lambda K^2\frac{\sin\beta}{\cos\alpha}+\lambda\beta^2\frac{\sin\beta}{\cos\alpha}-\beta\frac{\cos\beta}{\cos\alpha}\right)+\beta\cos\left(\beta\frac{y}{a}\right)\right]\exp\left[i\left(kx-\omega t\right)\right]+c.c.$$

$$v_y(x,y)=\frac{A_2}{a}\left[iK\frac{\sin\beta}{\sin\alpha}\sin\left(\alpha\frac{y}{a}\right)-iK\sin\left(\beta\frac{y}{a}\right)\right]\exp\left[i\left(kx-\omega t\right)\right]+c.c.$$

5.42

5.3.3 Numerical determination of the phase velocity and attenuation

The dispersion relations in Eq. 5.41 cannot be expressed as a simple function such as $K(\Omega)$ for either the slip or no-slip case, and to make progress we must resort to a numerical approach. For a given channel width and fluid properties, Eq. 5.41 becomes a complex transcendental equation of the form $f(K,\Omega)=0$. The goal is to find the roots K of this equation for a given value of the dimensionless frequency Ω. The frequency is restricted to be real and positive. For each Ω, there will be a series of complex K that satisfy the dispersion relation. Each root K will belong to a particular mode. The search

for roots is restricted to $\mathrm{Re}(K) \geq 0$ and $\mathrm{Im}(K) \geq 0$. From Eq. 5.24, these restrictions on the real and imaginary parts of *K* correspond to damped waves traveling in the positive *x* direction.

Assuming a root *K* for a value of Ω has been found, the phase velocity is

$$c_{phase} = c_0 \frac{\Omega}{\mathrm{Re}(K)}, \tag{5.43}$$

and the amplitude attenuation is given by

$$\delta = \frac{\mathrm{Im}(K)}{a}, \tag{5.44}$$

such that after propagating a distance *D*, the wave amplitude will be diminished by a factor $\exp(-\delta D)$.

The roots *K* for a given value of Ω were found by implementing a simplified version of what is referred to as the direct Kuhn algorithm[4]. The technique is derived from the related problem of finding the roots of a complex polynomial

$$f(z) = \sum_{n=0}^{N} a_n z^n, \tag{5.45}$$

where the coefficients a_n are constant and complex. For complex polynomials of the form of Eq. 5.45, Kuhn observed that the search for the roots, *i.e.*, the *N* values of *z* such that $f(z) = 0$, can be implemented in the following way[5]. The complex plane is divided into a grid, and the function *f* is evaluated at each point. A label is then given to each point based on the rule

$$L(z) = \begin{cases} 0 & -\pi/3 < \arg\left[f(z) \right] \leq \pi/3 \\ 1 & \arg\left[f(z) \right] > \pi/3 \\ 2 & \arg\left[f(z) \right] \leq -\pi/3 \end{cases}. \tag{5.46}$$

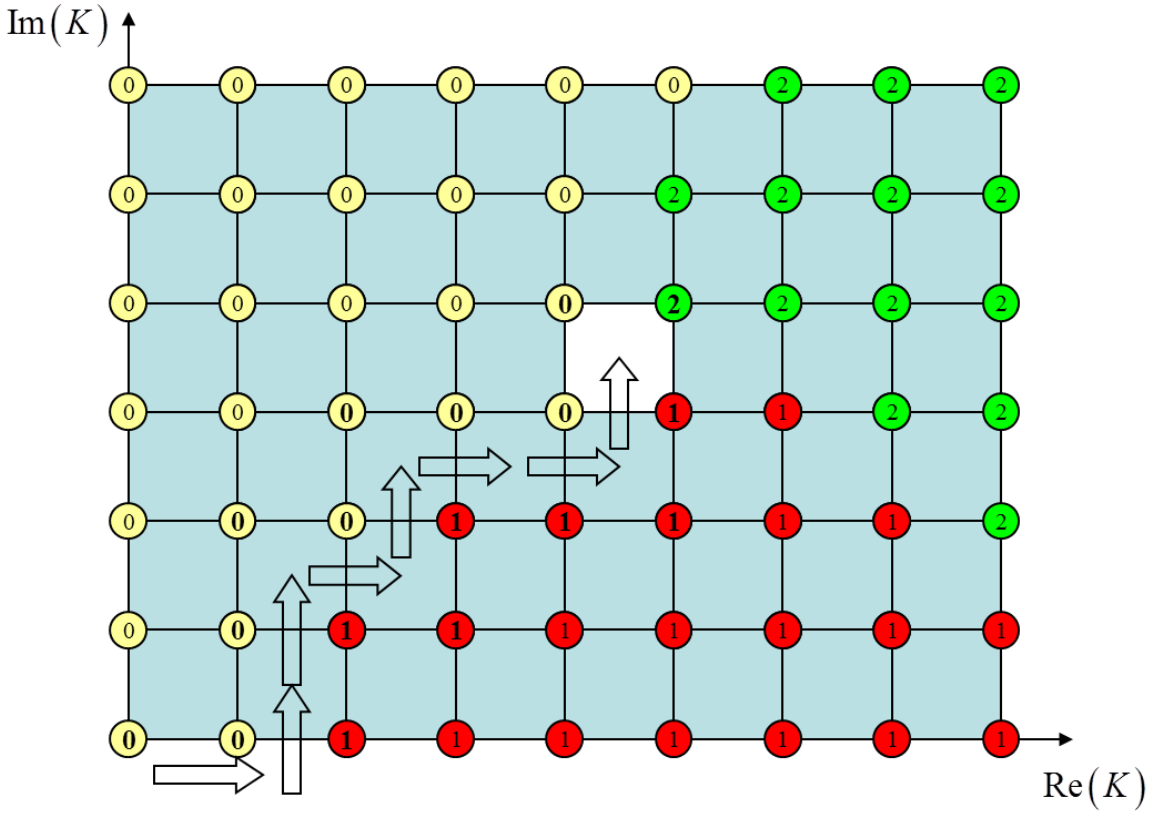

Figure 5.4: Implementation of the direct Kuhn algorithm on a square grid. The program walks along the bottom boundary of the domain being searched until it finds two adjacent points with different labels. The program then walks into the domain, progressing from square to square along the boundary between the regions with different labels, until it finds the square where at least one of each label is present. That square is then divided into a smaller grid, and the search is repeated. The bold labels are represent the points where *f(K)* is evaluated.

Kuhn was able to show that if a triangle in the complex plane formed by the points z_1, z_2, z_3 has one of each label, then at least one root is located in that triangle. Various algorithms have been written that involve searching for triangles with roots in them and then subdividing those triangles and repeating the process[5,6]. The rigorous proof that the above method will converge onto the roots of *f* is based on the assumption that the function is a polynomial. However, it has been demonstrated that the above procedure will converge onto roots of the function even if it is not a polynomial. Long and Jiang[4] showed empirically for several examples that as long as the function is not varying too rapidly in the neighborhood around a root, then the above procedure will still converge onto the root. Intuitively, if the function *f* is well behaved near its root, then it can replaced by its polynomial approximation.

case	a	b	f	Ω	M	γ	λ
1	25 nm	0 nm	1 GHz	0.10472	0.0259	0.107	0.0
2	25 nm	5 nm	1 GHz	0.10472	0.0259	0.107	0.2

Table 5.4: Parameters used for the two cases considered here.

In the implementation used in this work, the domain of K space being searched was split into a square grid. The program scanned along the boundary of the domain until it found two adjacent points with different labels, and then walked into the domain until it found a square whose four corners had all three labels; this is illustrated in Figure 5.4. That particular square was then subdivided into a smaller grid, and the procedure was repeated. The label was found using the rule in Eq. 5.46, where f is the left hand side of the dispersion relation Eq. 5.41a. Note that this method does not require the function f to be evaluated at every point in the domain.

As an illustration, consider a channel with half width a = 25 nm. Using the above procedure, the values of K that satisfy the dispersion relation Eq. 5.41a for a frequency of 1 GHz for the no slip case (b = 0 nm) and a small slip case (b = 5 nm) were found . The values of the various dimensionless parameters are summarized in Table 5.4 for the two cases considered here.

Figure 5.5a shows the label at all the points in the domain Re K < 10, Im K <10 for case 1 (no slip). This is shown for the purpose of illustrating the locations of the various roots in the domain; the above described search algorithm does not actually label all of the points in the domain being searched. From this, it appears that there are at least 4 roots in this domain, labeled S_n, $n = 0,\ldots 3$ (S stands for symmetric.) Even though the function is transcendental, the program rapidly converged on all the roots. Figure 5.6 shows a close up of the region of K space around roots S_0 and S_1 for case 1. The contours represent lines of constant $f(K)$. The algorithm has some difficulty around S_1; the circled point labeled B is not a root, even though it appears that all 3 labels are present in the circle on the plot. The point A appears to be a root, since the value of $f(K)$ can be made quite small

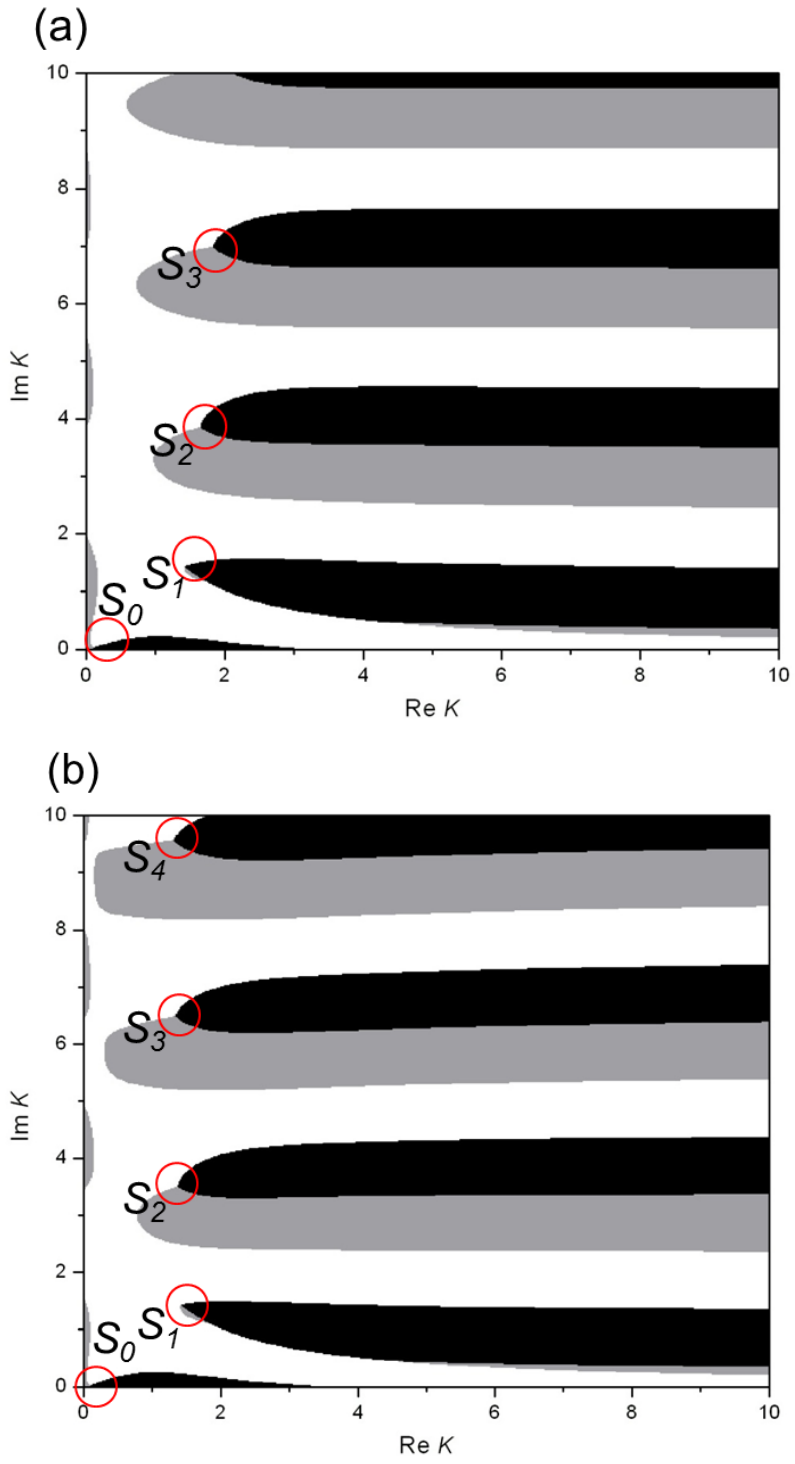

Figure 5.5: Fully labeled domain for (a) case 1 and (b) case 2. The roots of the dispersion relaxtion are at the points where the domains with labels 0, 1, and 2 intersect.

at the point. For some frequencies and values of the channel half-width a, the algorithm missed the root S_1.

Root	Re K	Im K	$\left\|f(K)\right\|$
S_0	1.19535792E-1	3.5761892E-2	1.4E-9
S_1	1.42110075649	1.42110075649	4.4E-7
S_2	1.6383275783	3.8509426084	3.5E-9
S_3	1.8195935673	6.9881904153	4.3E-9

Table 5.5: Roots converged on by the search algorithm in the domain searched for the case a = 25 nm, b = 0 nm (no slip), and f = 1 GHz.

Root	Re K	Im K	$\left\|f(K)\right\|$
S_0	1.10941325E-1	2.433995E-2	2.3E-9
S_1	1.42110075649	1.42110075649	7.2E-7
S_2	1.3722431474	3.498781262	4.7E-9
S_3	1.3378452361	6.484123250	7.2E-9
S_4	1.3166866661	9.5624272427	9.7E-9

Table 5.6: Roots converged on by the search algorithm for the case a = 25 nm, b = 5 nm, and f = 1 GHz.

Table 5.5 shows the roots that the algorithm converged on for case 1 (no slip). The fact that these values of K do indeed satisfy the dispersion relation is borne out by the fact that $\left|f(K)\right|$ can be made on the order of 10^{-9} or less.

Figure 5.5b shows the label at all the points in the domain Re K < 10, Im K <10 for case 2 (b = 5 nm). From this, it appears that there are 5 roots in this domain, and Table 5.6 shows the roots found for case 2 in this domain. In both the slip and no slip cases, all of the modes are strongly damped except for S_0.

Table 5.7 shows the relative phase velocity and the amplitude attenuation factor after propagating a distance of 100 nm for the roots for cases 1 and 2. The most noticeable

difference between the slip and no slip case is the difference in the phase velocity of almost 7% for the mode S_0.

	Case 1 (b = 0 nm)		Case 2 (b = 5 nm)	
Root	Relative phase velocity (% of c_0)	$\exp(-\delta D)$ for D = 100 nm	Relative phase velocity (% of c_0)	$\exp(-\delta D)$ for D = 100 nm
S_0	87.6	0.867	94.5	0.906
S_1	7.4	0.0034	7.4	0.0034
S_2	6.4	$<10^{-6}$	7.7	$<10^{-6}$
S_3	5.8	$<10^{-6}$	7.9	$<10^{-6}$
S_4	-	-	8.0	$<10^{-6}$

Table 5.7: Relative phase velocity and amplitude attenuation after 100 nm, computed using Eq. 5.43 and 5.44, for the roots in Tables 5.5 and 5.6. The most notable change to the mode S_0, upon the introduction of a finite slip length, is an increase in the phase velocity.

5.4 Conclusions

Two markedly different simulation tools were presented in this chapter. The FDTD program was essential in interpreting the results of POAM experiments. The wave guide problem considered in section 5.3 combined with the FDTD program and experimental results provide a means of placing an upper limit on the slip length for a fluid-solid system. The presence of slip will manifest itself as an increase in the speed at which sound propagates down the channel and returns to the transducer; this increase in speed will appear as a discrepancy between the experimental data and the results of the FDTD simulation, which has essentially no slip. From the magnitude of the time discrepancy and the results of the waveguide simulations presented in section 5.3, an estimate of the slip length can be obtained. This will be more fully explored in the next chapter.

Bibliography

1. Herzfeld, K. & Litovitz, T.A. *Absorption and dispersion of ultrasonic waves*. (Academic Press: New York, 1959).
2. Navier, C.L.M.H. Mémoires sur les lois du mouvement des fluides. *Mémoires de l'Académie des sciences de l'Institut de France* 389 (1823).
3. Sorokin, S.V. & Chubinskij, A.V. On the role of fluid viscosity in wave propagation in elastic plates under heavy fluid loading. *Journal of Sound and Vibration* 311, 1020-1038 (2008).
4. Long, Y. & Jiang, H. Rigorous Numerical Solution to Complex Transcendental Equations. *International Journal of Infrared and Millimeter Waves* 19, 785-790 (1998).
5. Kuhn, H.W. Finding roots of polynomials by pivoting. *Fixed points : algorithms and applications* 11-40 (1977).
6. Kuhn, H.W. & MacKinnon, J.G. Sandwich method for finding fixed points. *J Optim Theory Appl* 17, 189-204 (1975).

Chapter 6

Planar Opto-Acoustic Microscopy of 1D Periodic Nanostructures

6.1 Introduction

This chapter explores the use of planar opto-acoustic microscopy (POAM) with samples that were periodic in one dimension. The samples investigated had dimensions that made their non-destructive characterization either difficult or impossible by existing methods. Three different areas were explored. First, the problem of inferring the major dimensions (pitch, line width, and height) along with the profile details (sidewall angle, roundedness of the tops, etc.) was explored by comparing experimental data to a library of simulations and searching for the best fit. Second, the echo from the bottom for channels that were less than 60 nm wide was compared to simulations. Finally, since the presence of slip between the water and the channel side walls would greatly affect both the amplitude and the arrival time of the echo from the bottom of the channel, the POAM data was used to estimate how much slip was present at the water-sidewall interface.

6.2 Experimental details

6.2.1 Sample description and characterization

Figure 6.1 shows the structure of the samples used in this work. The samples were fabricated by Novellus Systems, Inc., and consisted of lithographically defined silicon dioxide lines on a silicon substrate that were covered with a conformal coating of silicon nitride that was approximately 60 nm thick. The gaps between the lines are referred to below as channels. There were two groups of structures; one with channels 400 nm deep, and the other 230 nm deep. There were a variety of patterns on each wafer, and the patterned areas were on the order of 200 μm x 200 μm.

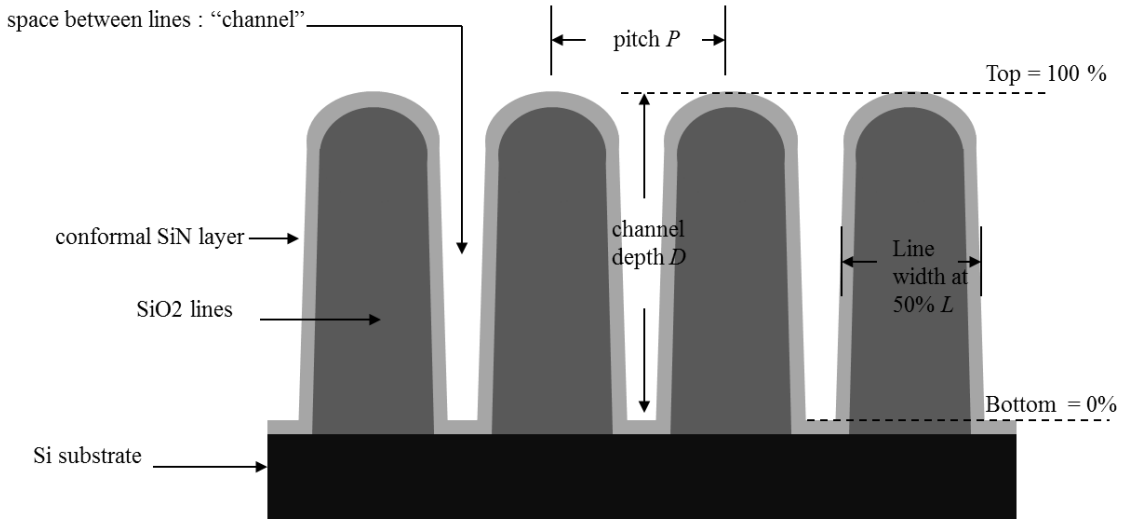

Figure 6.1: Cross sectional schematic of the samples studied showing their composition. The line profile was specified by the width of the line (or channel) at various height levels, with 100% corresponding to the tops of the lines.

The main features of the structures can be described by three critical dimensions: the repeat distance, or pitch (denoted by *P*), the height of the lines (*D*), and the width of the lines halfway down the channel (*L*). The cross sectional profile of the lines was described by measuring the width of the lines at different heights. The height levels at which the widths of the lines were measured were labeled by a percentage, where 100% corresponded to the top of the line and 0% the bottom of the channel.

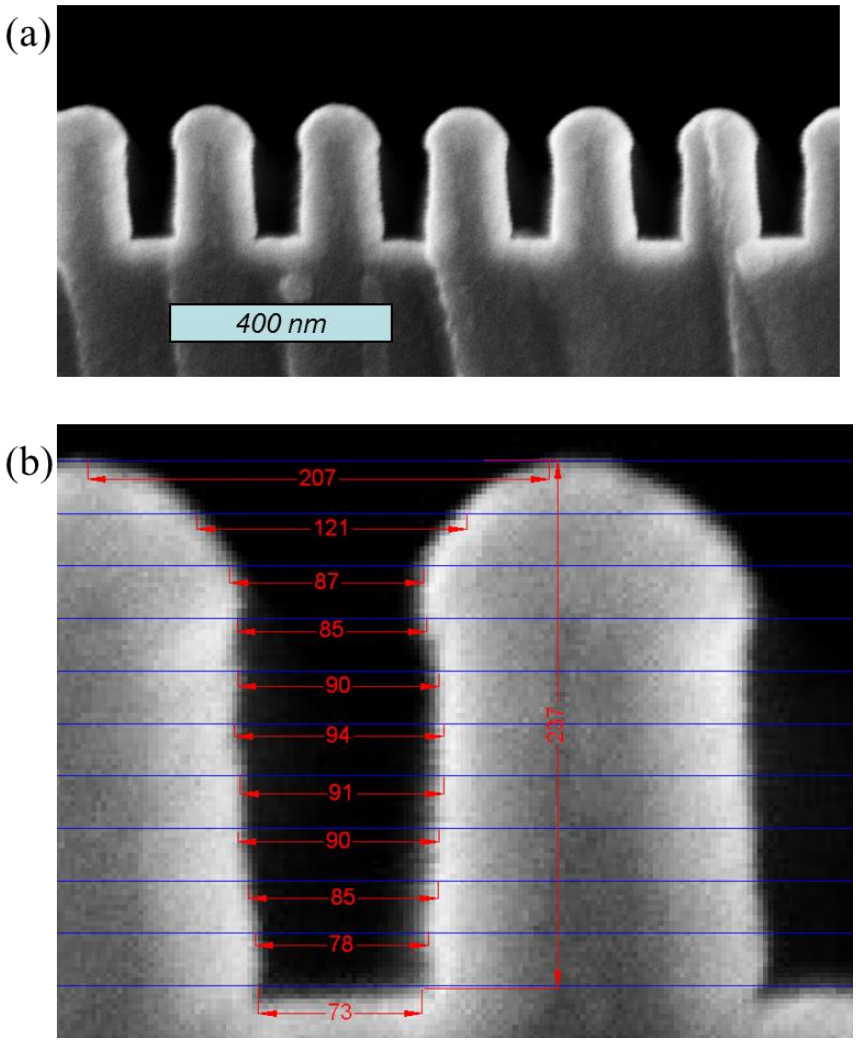

Figure 6.2: (a) An example of a cross sectional SEM. Scale bar is 400 nm. (b) A close up view showing the measured widths at 10% height levels. For this image, the uncertainty in the width measurements was +/- 8 nm.

The sample profiles were measured by destructive cross sectional scanning electron microscopy (SEM). After each set of POAM measurements, the sample piece was cleaved perpendicular to the lines. The exposed cross section was then coated with approximately 4 nm of evaporated amorphous carbon. The amorphous carbon helped to reduce the effects of surface charging during the imaging process. An example cross sectional SEM image is shown in Figure 6.2a. The pitch of the structure was 230 ± 5 nm, the channel depth was 235 ± 5 nm, and the line width at 50% was 135 ± 8 nm. A close up view of one of the channels is shown in 6.2b, with the widths measured at 10% increments of the height. For the highest resolution images, the widths of the lines were

measured at height levels of 100% to 90% in 2% increments, and then 85% to 0% in 5% increments. For each of the samples examined in this work, the profiles of 20 – 50 individual channels were measured. The widths at each height level were then averaged to form the average channel profile that was used in the simulations. In all the simulations, the profile of the line was assumed to be symmetric.

6.2.2 Major features of the POAM data

The experimental procedure used for acquiring POAM data was identical to that described in section 4.5. The sample was mounted onto the sample positioning system, one drop of distilled water was placed on the sample, and the cavity was placed on top of the sample. The pump and probe beams were focused onto the cavity transducer, and

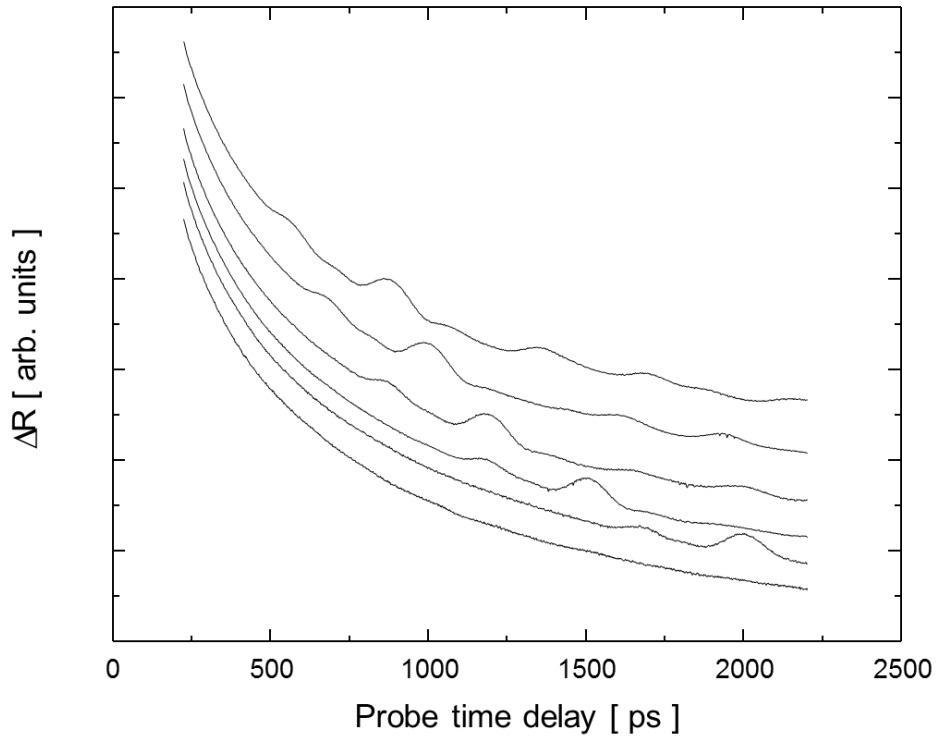

Figure 6.3 : POAM data taken at different water film thicknesses for the sample shown in Figure 6.2a

then the water film thickness was decreased until acoustic echoes were visible in the data. Figure 6.3 shows the experimental data taken at different water film thicknesses for the sample whose cross sectional image is shown in Figure 6.2a. The data has been treated

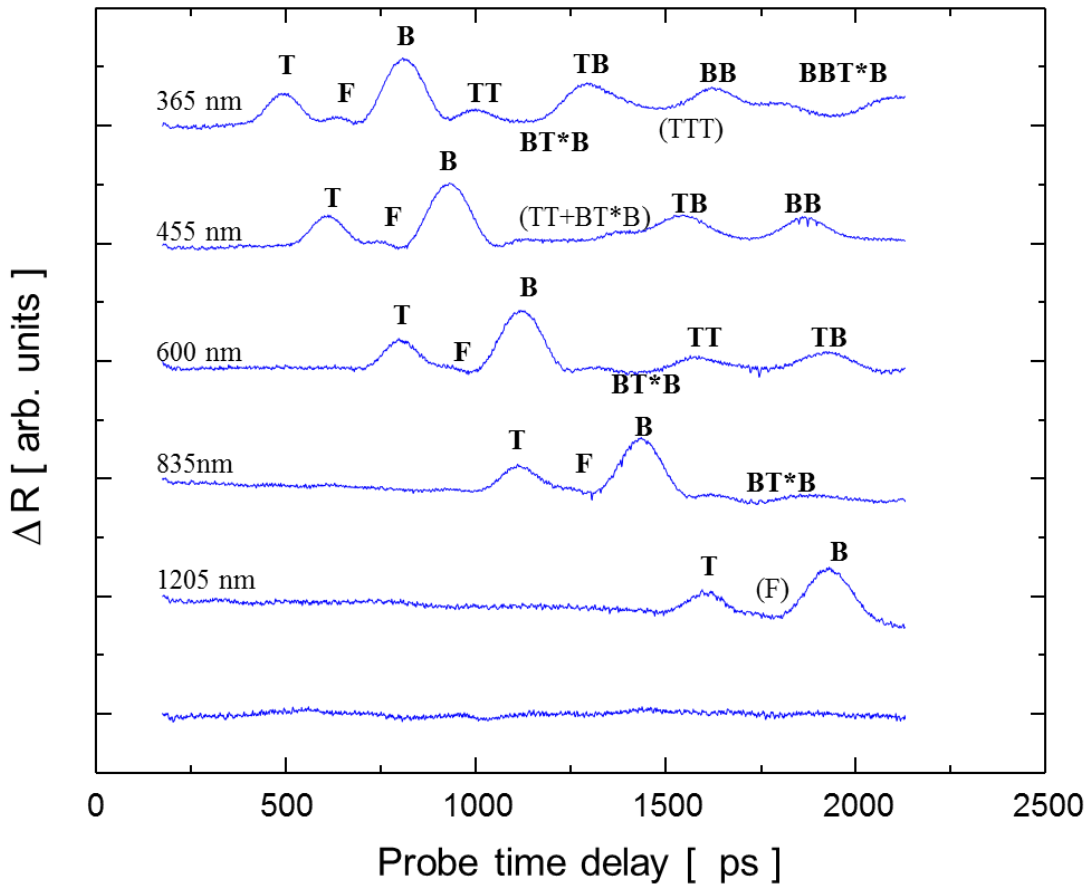

Figure 6.4 : POAM data from Figure 6.3 after the background subtraction process. The water film thickness was estimated from the arrival time of the first echo T. Each echo is labeled by a sequence of letters; each T refers to a reflection from the top of the lines and B the bottom of the channel. The feature F always occurred at the same time after T, independent of water film thickness.

as previously described in chapter 4. The lowest curve in Fig. 6.3 was taken with a water gap at least 0.5 microns larger than the curve above it. A function of the form $y(t) = y_0 + A_1 \exp(-t/\tau_1) + A_2 \exp(-t/\tau_2)$, was fitted to the lowest curve, and τ_1 and τ_2 were found to be 165.0 ps and 842.5 ps, respectively. This background was then subtracted from each data set. Finally, each data set was shifted in time by an amount t_{offset} = 75 ps. The offset time corresponds to the time it takes the sound to travel through the cavity films once and the thick aluminum and cap silicon dioxide films twice. Using the model discussed in chapter 4, the time t_{offset} should be $T_1 + 2T_2$, where T_1 is the time it takes sound to travel through the cavity spacer layer, and T_2 is the time it takes the sound

to travel through the combined thickness of the thick Al film and cap SiO_2 film. The resulting curves are shown in Figure 6.4. The first echo to arrive, denoted by T, is due to sound that has reflected from the tops of the lines and then returned to the cavity. From the arrival time *t* of the first echo, the thickness of the water gap can be estimated as *vt/2*, where *v* is the sound velocity in water. The thickness of the water gap for the curves in Fig. 6.4 is found to be, from top down, 368, 457, 597, 836, and 1207 nm. The echoes marked B are from sound that has travelled down the channels, reflected off of the bottom, and returned to the cavity. Table 6.1 lists the arrival times of the first three echoes. The quantity $(B-T)v/2$ was found to match up with the depth of the channels D, provided that the channels were wider than ~100 nm. For channels narrower than 100 nm, the data implied that the velocity of the sound pulse in the channel was up to 10% slower than that in unconfined water.

T [ps]	F [ps]	B [ps]	$Tv/2$ [nm]	$(B-T)v/2$ [nm]	$(F-T)v$ [nm]
493	637	810	368	239	218
609	753	929	457	241	216
798	943	1118	597	240	218
1114	---	1433	836	240	---
1609	---	1924	1207	236	---

Table 6.1: Arrival times of the first three features, *T*, *F*, and *B*, for the data shown in Fig. 6.4. The quantity *Tv/2* is the water film thickness and (*B* – *T*)*v/2* the depth of the channels. The quantity (*B* – *T*)*v* was comparable to the pitch of the structure for the curves where the arrival time of *F* was measurable.

There were echoes from sound that has reflected off of the sample and transducer faces multiple times; these are denoted by TT, TB, BB, TTT, etc. There was also an echo visible in many of the curves that occur after the echo B whose arrival time corresponds to an addition round trip through the channel. This echo, denoted BT*B, is from sound that, after reflecting off the bottom, reflected off of the opening of the channel, reflected

off the bottom again, and then returned to the cavity. For echoes that have reflected from either the top or the bottom multiple times, there can be multiple contributions that will occur at the same time delay, regardless of the water film thickness. For example, echo BB and TBT*B will always occur at the same time. In addition, there can also be overlap in echoes if the water film thickness has a particular value. An example of this can be seen for the water film thickness of 457 nm in Fig. 6.4. In this curve, the echoes TT and BT*B arrive at around 1250 ps, and their contributions to the signal overlap. In order to get data where the echo from the bottom was clear, the water film thickness had to be larger than the depth of the channels, otherwise the echo B will be lost among the echoes T, TT, etc. This places a limit on the depth of channel that can be measured, since the deeper the channel is, the larger the water film thickness must be, which in turn will reduce the signal amplitude due to attenuation of the pulse as it travels through the water. One way to avoid this difficulty would be to position the cavity transducer very close to the tops of the lines.

There was a feature in the data at an arrival time which could not be expressed as integer multiples of the time to traverse the water film thickness and the channel depth. This is denoted by F in Fig. 6.4. There may possibly be other such features in the data, but overwhelmed by the other echoes. For all of the samples that were studied, the difference in the arrival time of echo T and the peaks in F were independent of the water film thickness. We noticed that the quantity $(F-T)v$ was usually within 15% of the pitch of the structure, but we have not been able to provide a satisfactory explanation for this.

The finite difference time domain (FDTD) program discussed in chapter 5 was used to directly model the signals seen in the POAM experiments. The change in the optical reflectivity of the cavity was assumed to be proportional to the average excess pressure in the fluid at the transducer face. The shapes were modeled as a stack of trapezoids. Depending on the resolution of the simulations, anywhere from 4 to 21 trapezoids were used to model the shape of the structure. Figure 6.5 shows the simulated POAM data for

the structure shown in Fig 6.2a. The mesh size was 5 nm, and the time step was 2 ps. There is an excellent agreement in the arrival times of the different echoes, but there is a

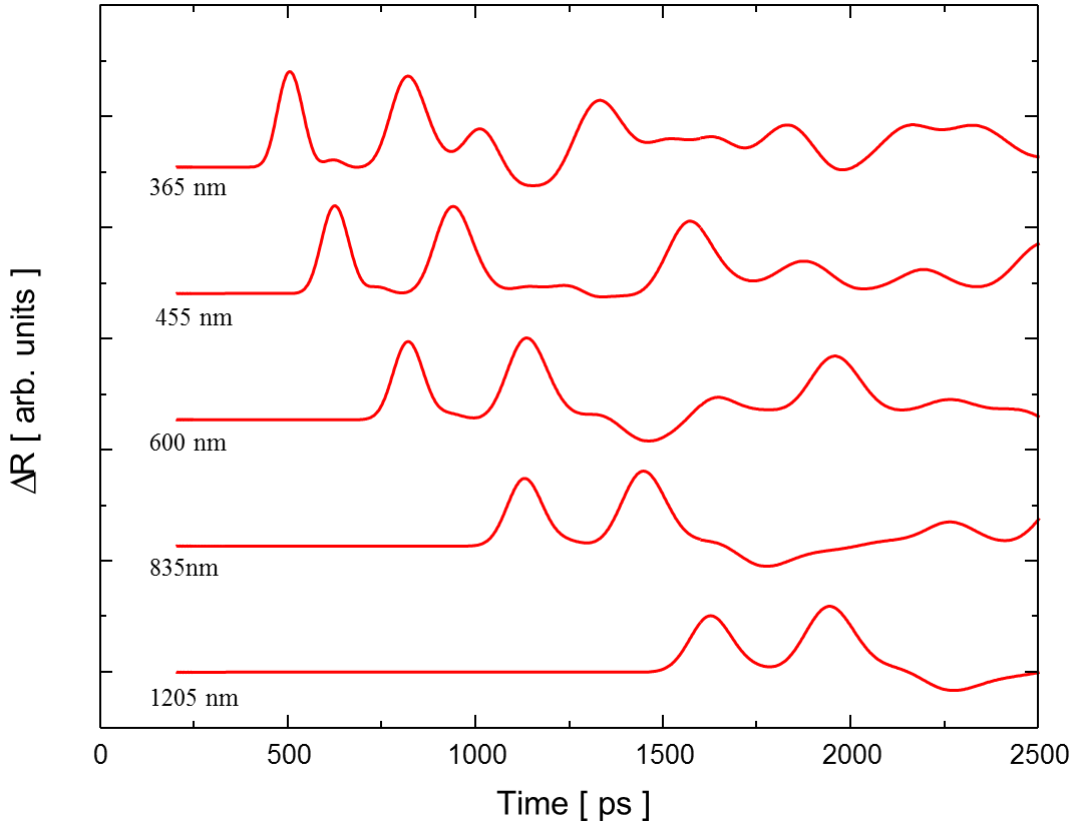

Figure 6.5 : Simulated POAM data using the FDTD program discussed in Chapter 5. The dimensions at 5% levels for the structure shown in Fig. 6.2a were rounded to the nearest 5 nm. The mesh size was 5 nm, and the time step was 2 ps. The arrival times agree with the POAM data in Fig. 6.4 qutie well, but there is a discrepancy between the relative sizes of the echoes

noticeable difference between the relative amplitudes of the various echoes. This will be more fully explored in the next section.

6.2.3 Sample catalog and outline of results

Table 6.2 lists the critical dimensions for the samples examined in this work. These are obtained from the SEM measurements.

In Section 6.3 the inverse problem of inferring information about the geometry of the sample from the POAM data is explored. In Section 6.4, the effects of channel width and depth on the amplitude and arrival time are investigated. In Section 6.5 a combination of

POAM experimental results and the numerical tools presented in chapter 5 is used to put an upper limit on the amount of slip that potentially occurs at the water – channel wall boundary.

Sample	repeat distance P	channel depth D	line width @ 50% L	section
A	360	400	290	6.3
B	200	227	135	6.3
C	230	410	165	6.4
D	230	410	200	6.4
E	230	410	180	6.5

Table 6.2: Critical dimensions for the structures studied in this work. Dimensions taken from SEM images. All uncertainties are +/- 5 nm.

6.3 Dimensional metrology of periodic nanostructures

For structures whose POAM data was sufficiently well developed (*i.e.*, the echoes *T*, *F*, and *B* were clearly visible), some information about the critical dimensions *P*, *L*, and *D*, and information about the profile shape could be extracted. For structures where the ratio of channel width to pitch was less than 0.2, the only features that were very prominent were *T*, *B*, and *TT*. The arrival time and amplitude of *B* relative to *T* was found to be quite sensitive to the width and depth of the channel.

6.3.1 Existing metrology methods

There are three main techniques for non-destructively measuring nanostructures of this general type. Optical scatterometry[1,2] is a technique based on white light interferometry. While the individual features are unresolvable, the collective effects of a group of structures will alter the signal relative to the signal from an unpatterned area. The average properties of the structures can then be estimated based on a comparison with the results of simulations. CD-SEM[3–7]refers to inferring information about the properties of nanostructures based on top down SEM images with either modeling or a look-up table of the results of previous destructive characterization of the structures being measured.

Atomic force microscopy (AFM) techniques [8–14] with special tips have been developed for the accurate measurement of structures with steep side walls. Special techniques to grow sharp tips with metals such as W were developed by Lee[8]. Much work has also gone into exploring the use of reinforced carbon nanotube (CNT) tips. These tips, while capable of high lateral resolution imaging, have their own unique artifacts, such as vibrations of the CNT structure being interpreted as ripples in the profile being measured[13,14].

It is noted that CD-SEM and AFM measure individual nanostructures whereas optical scatterometry and POAM measure average properties of an array of structures.

6.3.2 Procedure for comparing experimental and simulation data

As an example we consider the POAM data shown in Figure 6.6a. The lower curve is the signal recorded from the lock-in amplifier, and contains, in addition to the acoustic echoes of interest, a slowly decaying background and fast oscillations. The subtraction of the slowly varying background was necessary for a rigorous comparison of the experimental data to the simulation results. The following procedure was used. First, the Brillouin oscillations were filtered out using the procedure described in Chapter 4. The time offset of 75 ps was then applied to give the upper curve in Figure 6.6a. Then, points in the simulation data where the pressure on the transducer face vanished were found, as shown in Figure 6.6b. The corresponding points in the experimental data were used as a piecewise linear background function, as shown in Figure 6.7a. For some simulation results, there were large time gaps between the points where the pressure is zero. In cases where the zero points in the simulation were farther than 600 ps apart, another point was inserted at a local minimum between them; an example is marked by the arrow in Fig. 6.6b. After the piecewise linear background was subtracted from the experimental data, the experimental and simulation data were both normalized so that the height of the first echo was 1. The offset time for the experimental data was adjusted by 2 ps increments until the best overlap of the first echoes was achieved. Figure 6.7b shows the results of the background subtraction process for the example experimental data and simulation

data sets from Fig 6.6. Each time an experimental data set was compared to a different simulation result, a different background was subtracted from the experimental data. The

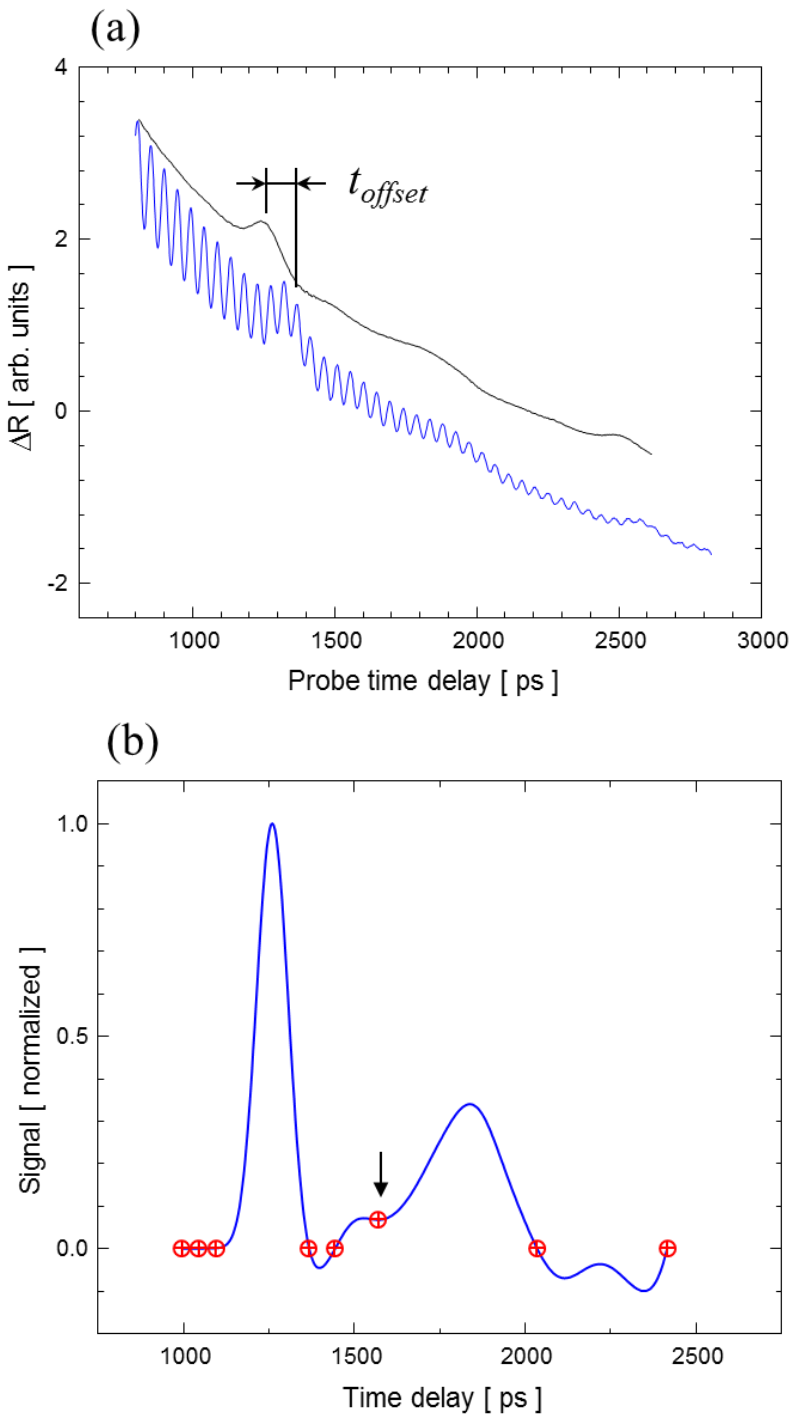

Figure 6.6: (a) The experimental data was prepared for the background subtraction process by filtering out the Brillouin oscillations and then shifting the time by t_{offset} = 75 ps. (b) The simulation data to be compared to the experimental data was normalized to the magnitude of the first returning echo. The points in the simulation where the signal is zero (shown in red) were

used to generate a piecewise linear background to subtract from the experimental data. If the space between two consecutive zero points was larger than 600 ps, then another point was inserted at a local minima between the two zero points.

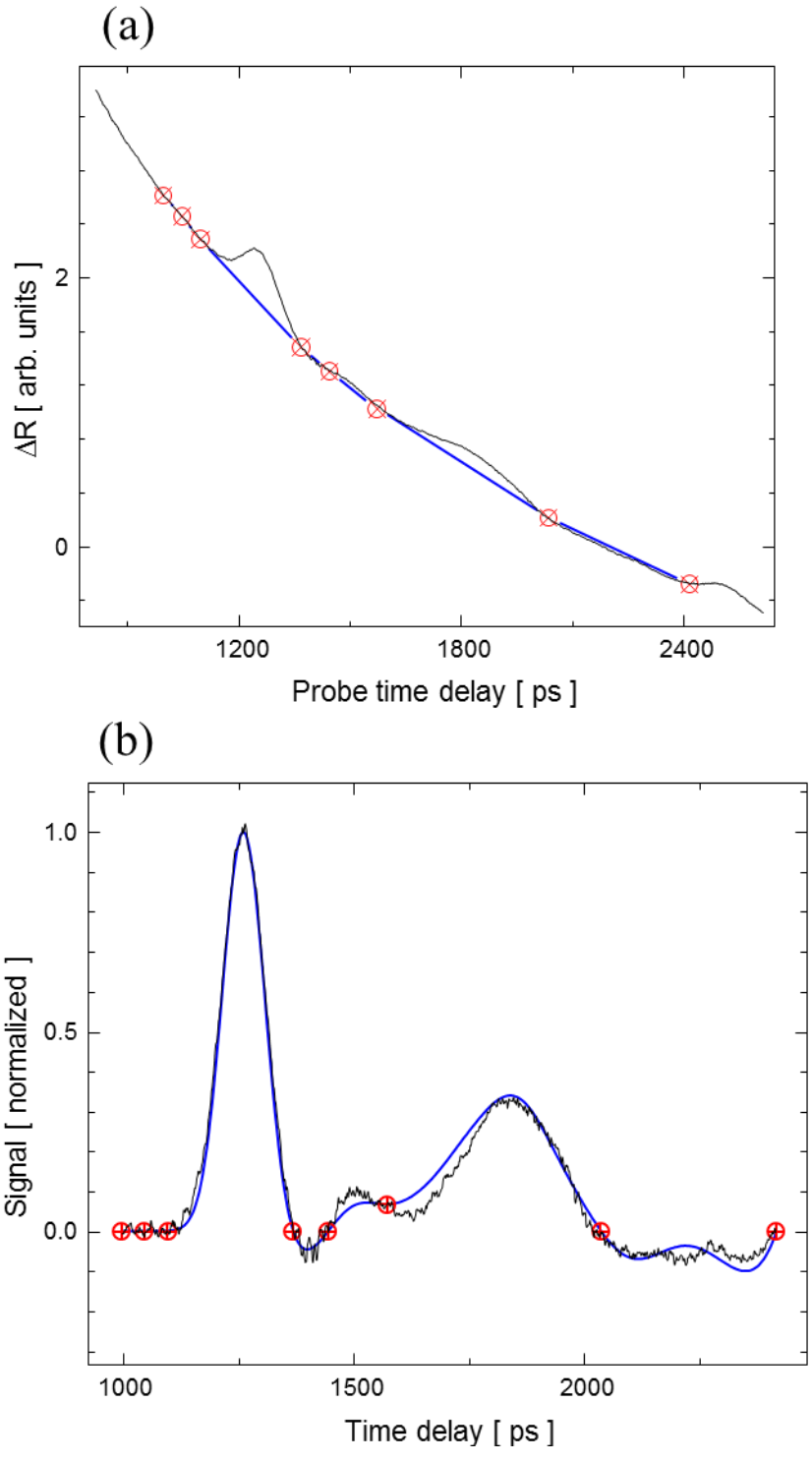

Figure 6.7: (a) Typical POAM data, along with the piecewise linear background obtained from the zero points in the simulation data. (b) After the background subtraction, the experimental data was also normalized to the magnitude of the first returning echo.

goodness of fit of the background subtracted experimental data, $s(t)$, to the normalized simulation data, $n(t)$, was quantified by

$$\chi^2 = \sum_{t=t_1}^{t_2} \left[s(t) - n_{lin}(t) \right]^2 , \qquad 6.1$$

where $n_{lin}(t)$ is the linear interpolation of the simulation data at the two time steps that straddle the time t, and (t_1, t_2) was the time delay range over which the experimental and simulation data were being compared. The time spacing for the simulations depended on the mesh size. For a mesh size of 5 nm, a 2 ps time step was used, and for a mesh size of 10 nm, 4 ps. The time interval over which the simulations were compared to the experiment was on the order of 1-2 ns.

6.3.3 Critical dimension and profile metrology of broad channel structures

A library search method was used to determine the average critical dimensions and profile of the group of structures probed during the POAM measurement. The general procedure was as follows. First, the POAM data were taken on the pattern of interest. The water film thickness was set such that the echo TT did not overlap with either echo B or echo BT*B. A library of simulations was generated for different profiles and critical dimensions *P*, *L*, and *D*. Then each simulation was compared to the experimental POAM data, and the best fit was found.

A. Sample A

As a first step we made fit to the results of the SEM measurements. Figure 6.8 illustrates the variety of structure profiles generated for the library used for Sample A. The structures were modeled as a stack of 4 trapezoids. The profile on each side was adjusted at the 0%, 75%, 90%, and 100% height levels in 20 nm increments. The profile codes ran from 0000, which corresponded to a square channel of uniform width, to 3333 which

was severely tapered. The profiles were chosen such that the width, from top to bottom, was either constant or increasing, and no overhangs or undercuts were present in this library. For each choice of pitch, line width, and channel depth, eighty different profiles

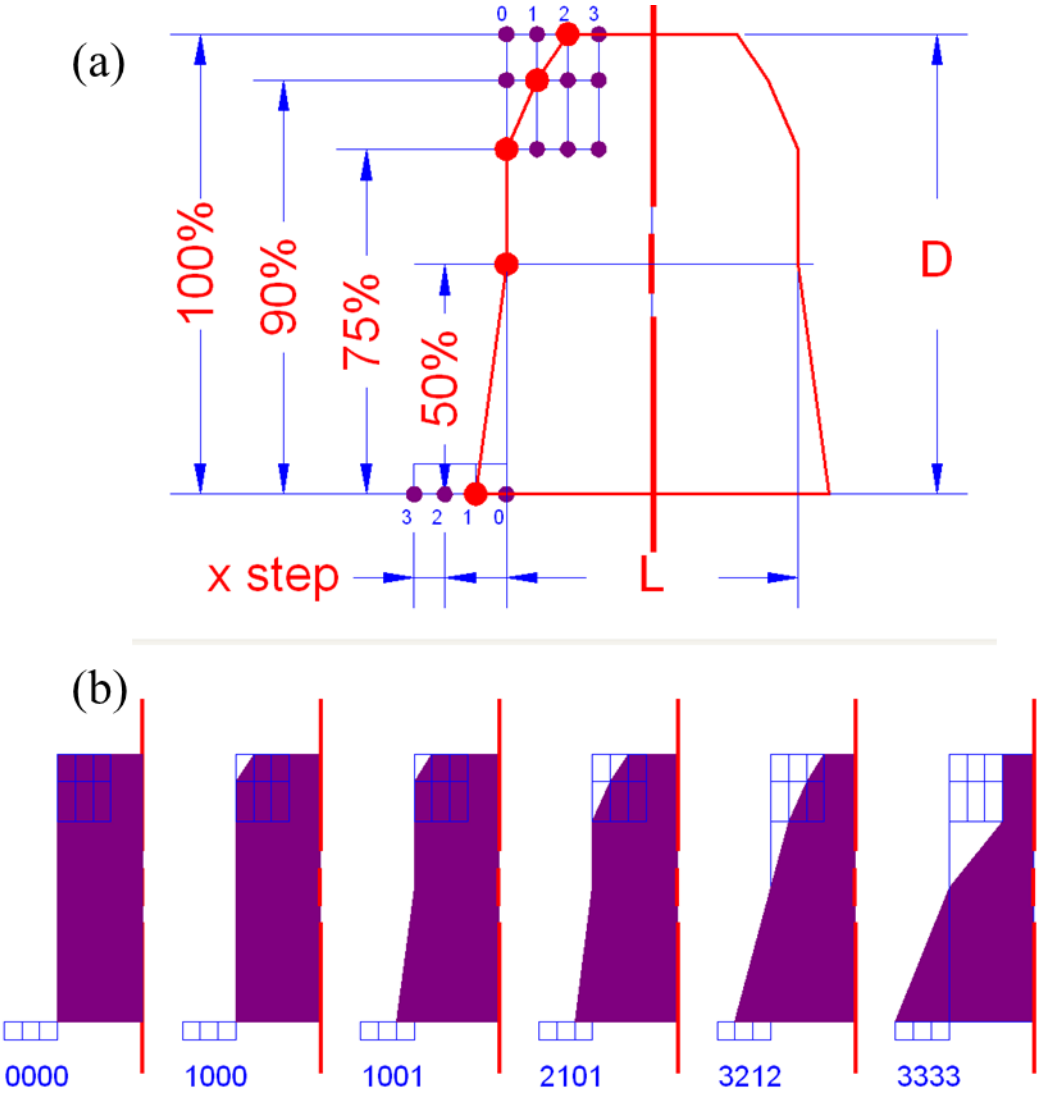

Figure 6.8: (a) For each value of P, L, and D, a family of structures with different profiles was generated and their simulations were compared to POAM data for sample A. The width of the line at 4 levels was varied in steps . Each profile had a 4 integer code. (b) Examples of some of the profiles generated. For each value of *P*, *L*, and *D* in the library, there were 80 different profiles simulated.

were simulated. Figure 6.8b shows some examples of the profiles contained in the simulation library generated for sample A.

Figure 6.9a shows a cross sectional SEM image of sample A. The sample had a pitch of 360 nm, a line width at the 50% level of 290 nm, and a height of 400 nm. The measured width of the channel at 5% height level increments is shown in Figure 6.9b. The different profiles simulated for L = 290 nm, D = 400 nm are shown as thin lines. The measured

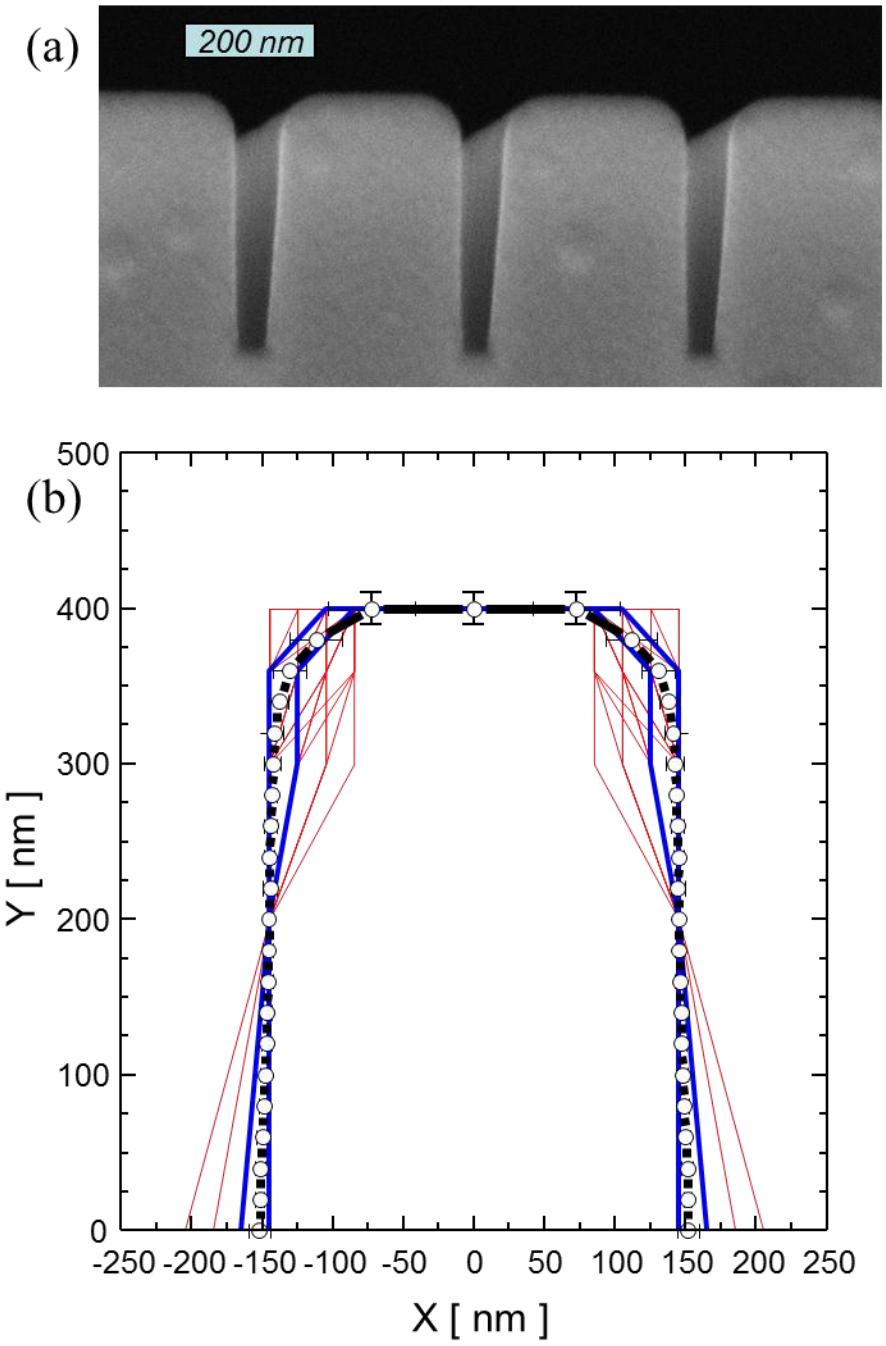

Figure 6.9: (a) Cross sectional SEM image of sample A. The pitch of the structure was measured to be 360 ± 5 nm, the channel height 400 ± 5 nm, and the width of the lines at 50% 290 nm. (b) From the SEM cross sectional images, the average profile of over 40 individual lines was

measured. The circles connected by the thick line represents the measured average profile of the structure. The thin lines are the 80 profiles generated by the for an L = 290 nm and D = 400 nm. The profile measured by SEM falls in between the two library profiles with codes 3110 and 2001 (denoted by thicker lines).

profile falls between profile codes 3110 and 2001, which are denoted by the thicker lines in Fig. 6.9b.

We now turn to the construction of a library to compare with the POAM data. In this library, the pitch P was varied from 330 to 390 nm in 10 nm steps, the line width at the 50% level L was varied from 160 to 310 nm in 10 nm increments, and the depth of the channels D was varied from 310 to 460 nm in 10 nm increments. A total of 143,360 simulations were performed.

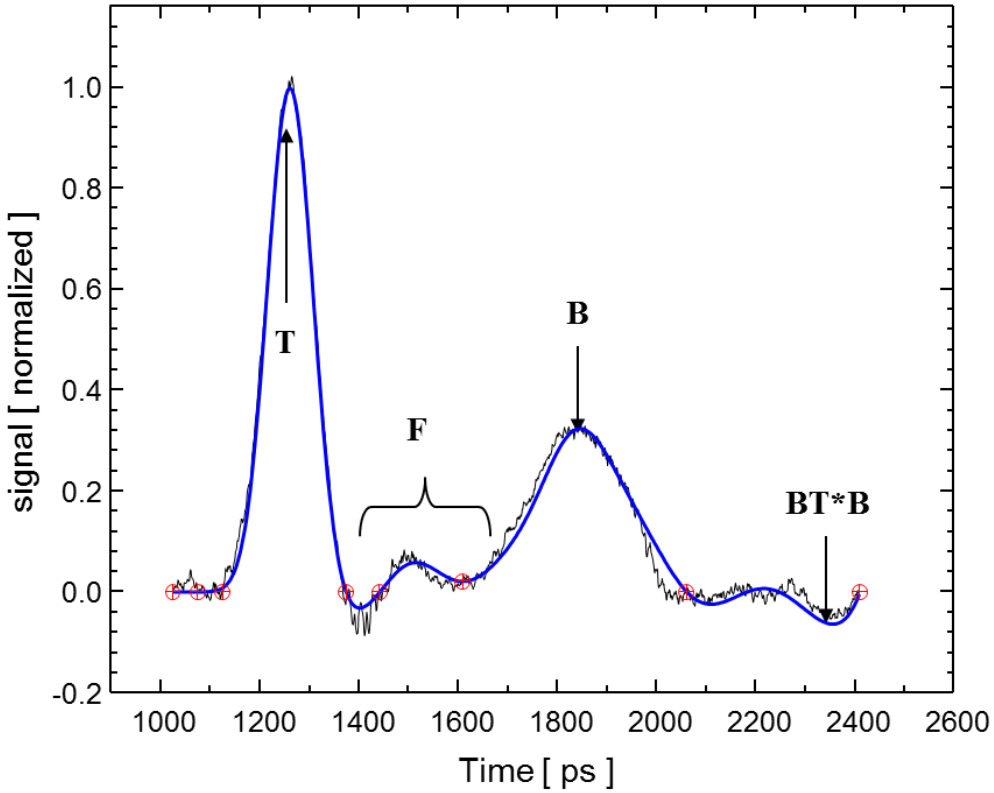

Figure 6.10: A comparison of the normalized simulation data for structure (P,L,D) = (360 nm, 270 nm, 400 nm), profile 0001, and the experimental data after background subtraction and normalization.

First, the search through the library for the best fit was restricted to structures with pitch P = 360 nm, the average value obtained from the SEM measurements. The best fit

occurred for L = 270 nm, D = 400 nm, and profile 0001 with $\chi^2_{best} = 0.65$. Figure 6.10 shows the experimental data and the simulation data for the best fit. The agreement between the simulation and the experimental data for the best fit case was quite good. In

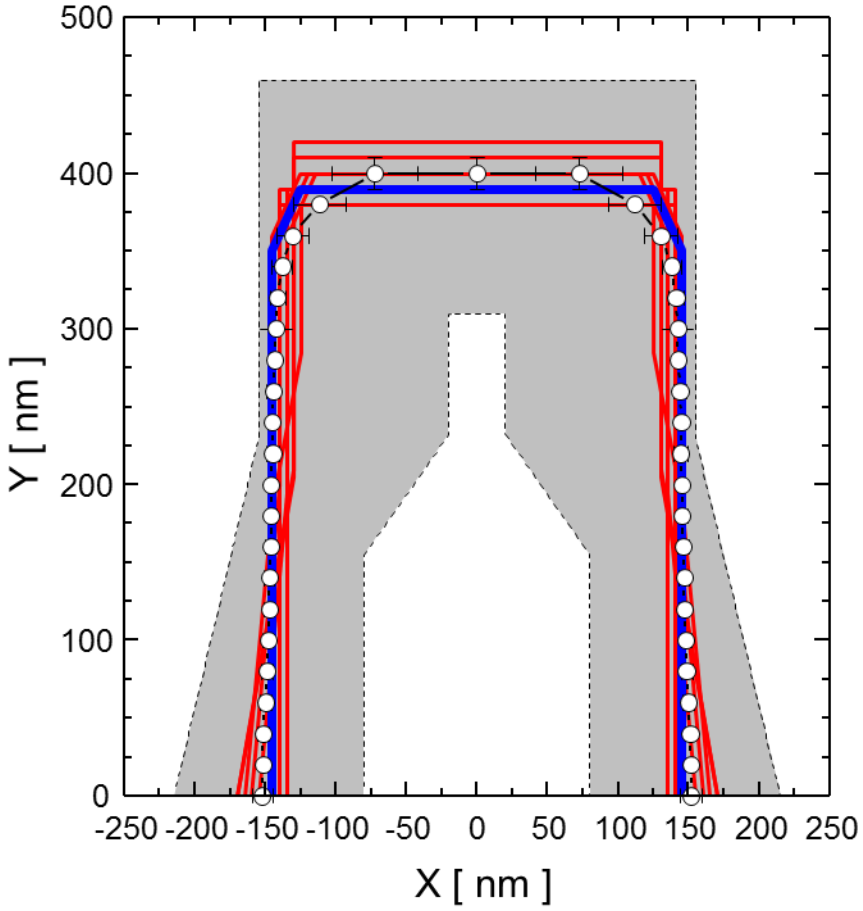

Figure 6.11: The shaded grey region represents the range of profiles generated by the library algorithm. The circles are the profile as measured by SEM, while the lines are the profiles of the top 10 best fits. For each value of the pitch, 20,480 structures were simulated and compared to the experimental data.

Figure 6.11, the range of line shapes searched is represented by the shaded grey area. The circles with the error bars are the average profile measured from the cross sectional SEM images. The thick line is the profile that had the best fit, and the thinner lines are the profiles from the best 10 fits. Figure 6.12 is a contour plot of χ^2 / χ^2_{best} in the (L, D) critical space. The best fits are located in the neighborhood of L = 270 – 290 nm and D = 380 – 410 nm.

Figure 6.13 shows an example of fitting results for (a) $\chi^2 / \chi^2_{best} = 2$, and (b) $\chi^2 / \chi^2_{best} = 5$. For these examples, and almost all of the others that were examined, the

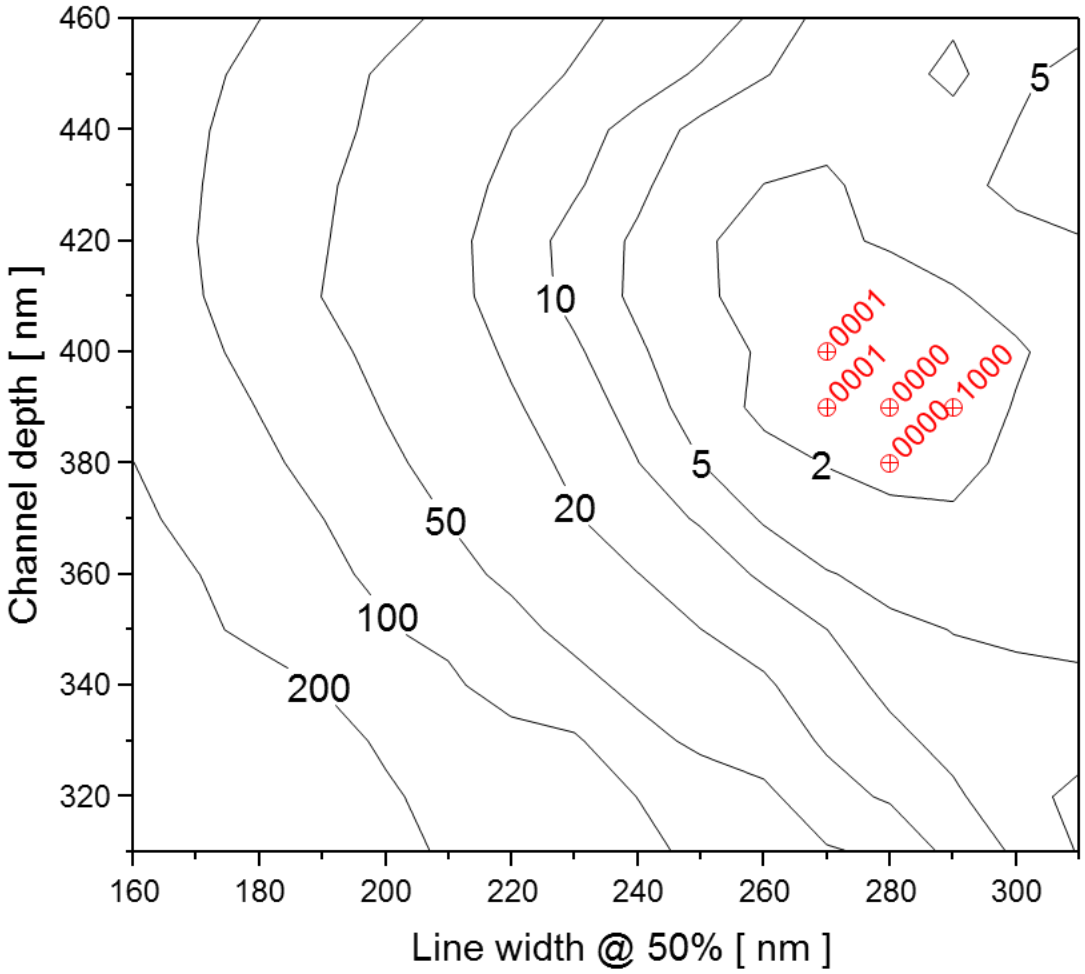

Figure 6.12: A contour plot of the best fits in the (*L*,*D*) critical space, with *P* = 360 nm. For each point, there were 80 line profiles simulated and compared to the experimental data. The best value of χ^2 was 0.65 at (*L*,*D*) = (270 nm, 400 nm), profile code 0001 (square top, slightly chamfered bottom). The contours mark levels of χ^2 normalized to the χ^2 value for the best fit. The locations of the 5 best fits, along with their profile codes, are marked on the plot.

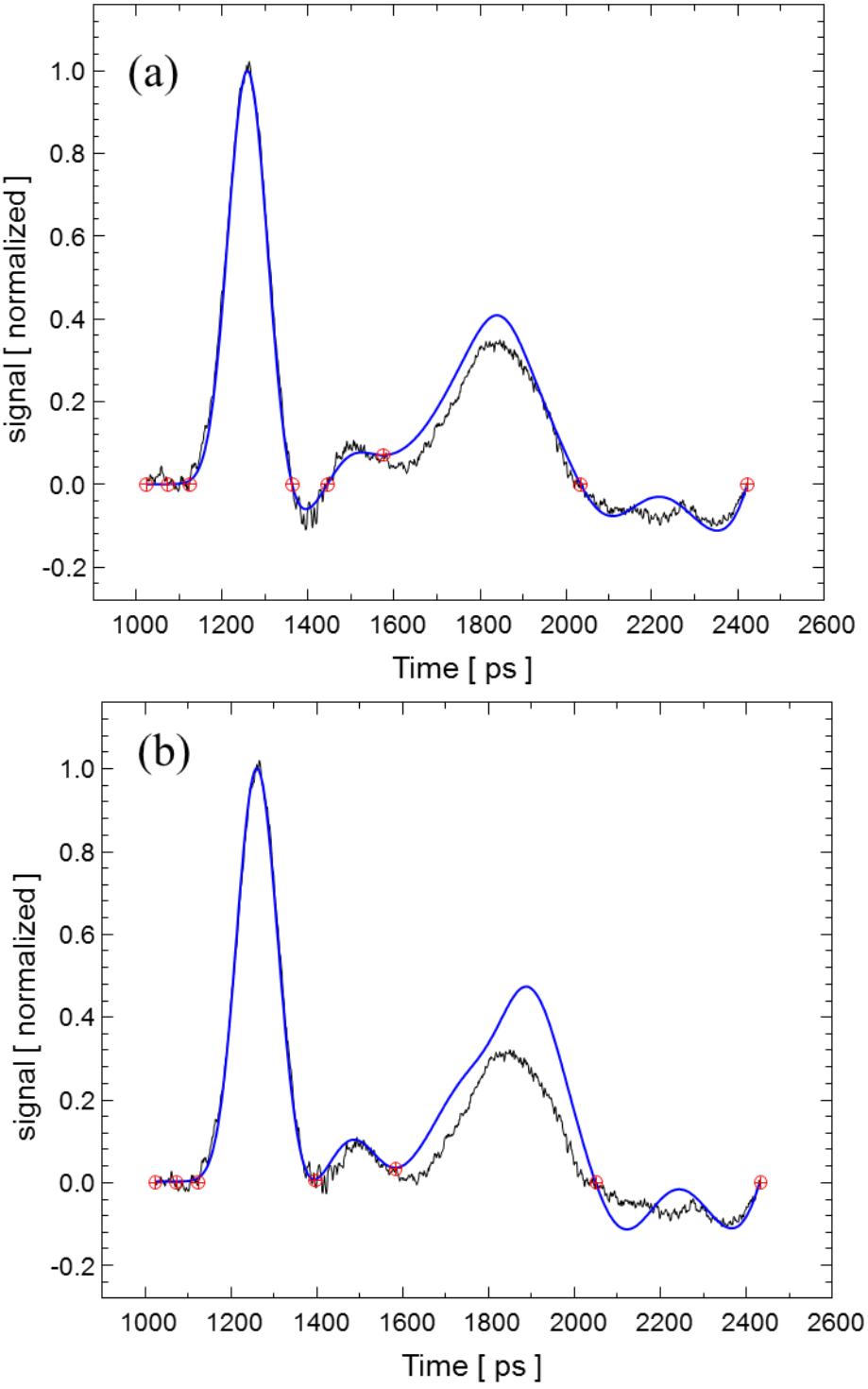

Figure 6.13: Typical fits simulated structures with $\chi^2/\chi^2_{(best)}$ values of (a) 2, and (b) 5. The goodness of the fit is dominated by how the echo from the bottom of the channel from the experimental data compares to the simulated data.

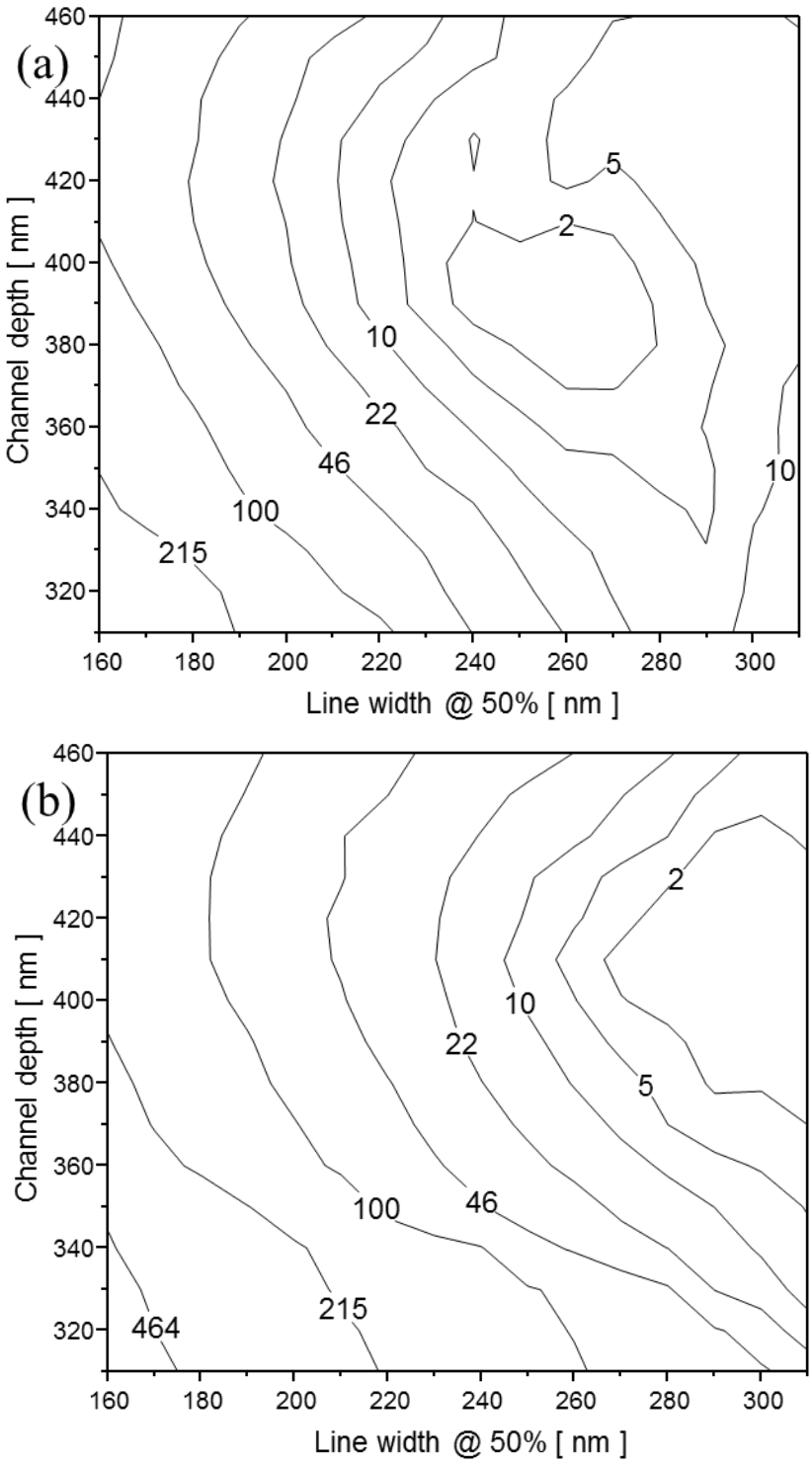

Figure 6.14: Contour plots of the critical space (*L*,*D*) for a pitch of (a) 330 nm and (b) 390 nm. When the pitch was decreased, the line width where the best fits occurred decreased by corresponding amounts. This suggests that the goodness of the fits were determined not so much by the absolute values of the pitch and line width, but their ratio.

echo from the bottom was the most important feature for determining how good the fit was, *i.e.*, how small the χ^2 value was. Figure 6.14 shows a critical space plot for (a) pitch P = 330 nm, and (b) pitch P = 390 nm. As the pitch was increased, the line widths where the best fits were located also increases. This suggested that the goodness of the fit was mostly determined by the ratio L/P.

B. Sample B

Figure 6.15a illustrates the method used to generate profiles for the library for sample B. The method was the same as for the library for sample A, except modest overhangs were allowed. The profiles were incremented in 10 nm steps, and the mesh size of the simulations was decreased to 5 nm. Figure 6.16a shows a cross sectional SEM image of sample B. These lines were measured to be 227 nm tall, with a width at the 50% level of 135 nm, and a pitch of 230 nm. The profiles of 30 different lines were measured from SEM images such as Fig. 6.16a, and the average of the widths at each height was found. The average line profile is shown by the connected circles in Figure 6.16b. For this structure, the SEM profile falls in between profile codes $41\bar{1}1$ and 4300 for L = 135 nm and D = 225 nm, which are shown as thicker lines in Fig. 6.16b. The 336 profiles that were generated for this combination of L and D are shown as the thin lines in Fig. 6.16b. A total of 75,264 structures were simulated and compared to the experimental data.

For the library of simulations that was generated for sample B, the pitch was fixed at 230 nm, the line width at the 50% level was varied from 100 to 170 nm in 5 nm increments, and the depth was varied from 180 to 260 nm in 5 nm increments. In Figure 6.17, the entire range of structures simulated is represented by the shaded grey area, and the average profile measured from the cross sectional SEM image is plotted as open circles. The 10 profiles with the best fit are shown as thin lines. While in the SEM images the profiles show a modest overhang of approximately 10 nm, not one of the top 10 fits shows any overhang. Figure 6.18 shows the best fit, which occurred for a line width at 50% of 135 nm, channel depth of 225 nm, and profile code 4311.

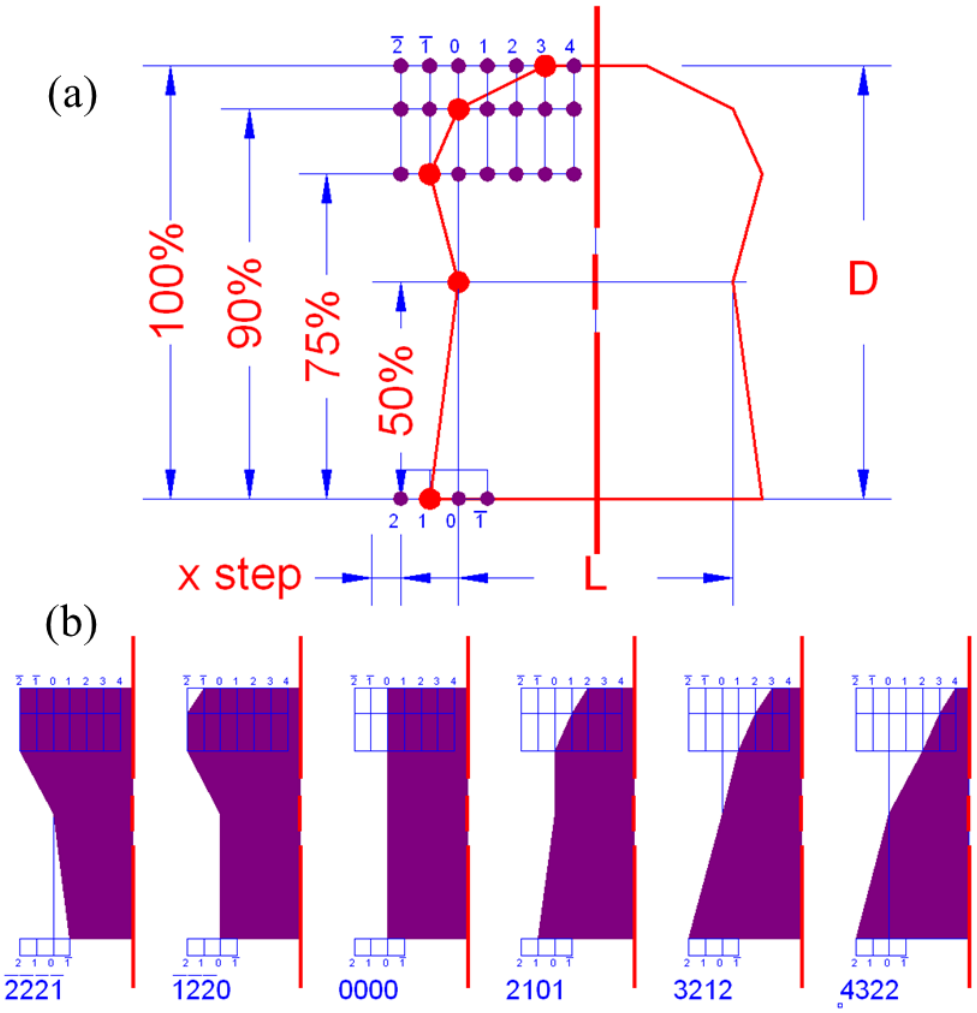

Figure 6.15: (a) For each value of *P*, *L*, and *D*, a family of structures was generated. The width of the line at 4 levels was varied in steps . Each profile had a 4 integer code. Examples of some of the profiles generated are shown in (b). For each value of *P*, *L*, and *D*, there were 336 profiles simulated. The profiles in this library were allowed to have undercuts.

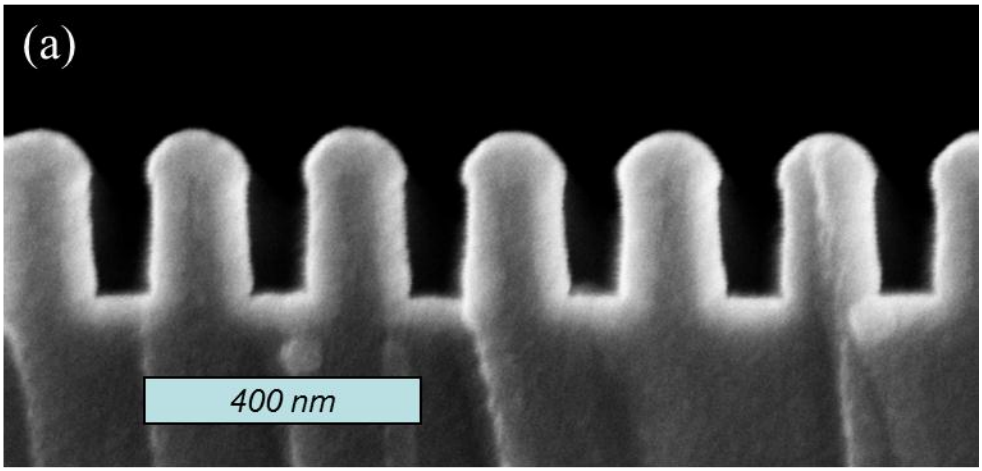

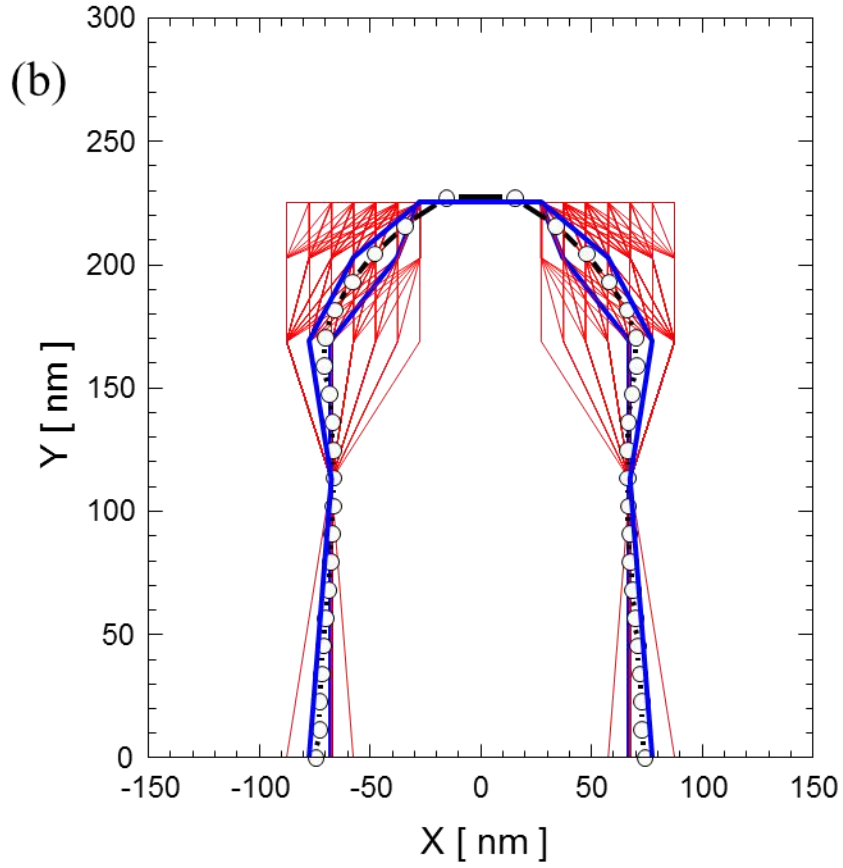

Figure 6.16: (a) Cross sectional SEM image of sample B. The pitch of the structure was measured to be 230 +/- 5 nm, the channel height 227 +/- 5 nm, and the width of the line at 50% 135 nm. (b) From the SEM cross sectional images, the average profile of over 60 individual lines was measured. The circles connected by the thick line represents the measured profile of the structure. The thin lines are the profiles generated by the profile algorithm for an *L* value of 135 nm and *D* of 225 nm. The measured profile falls in between the two library profiles with codes 4111 and 4300.

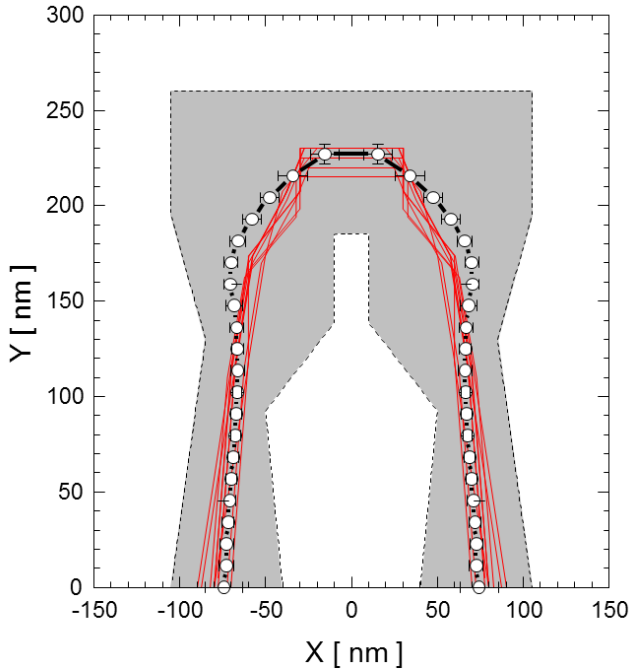

Figure 6.17: The shaded grey region represents the range of profiles generated by the library algorithm. The circles are the measured SEM profile, while the lines are the profiles of the top 10 best fits. A total of 75,264 structures were simulated and compared to the experimental data.

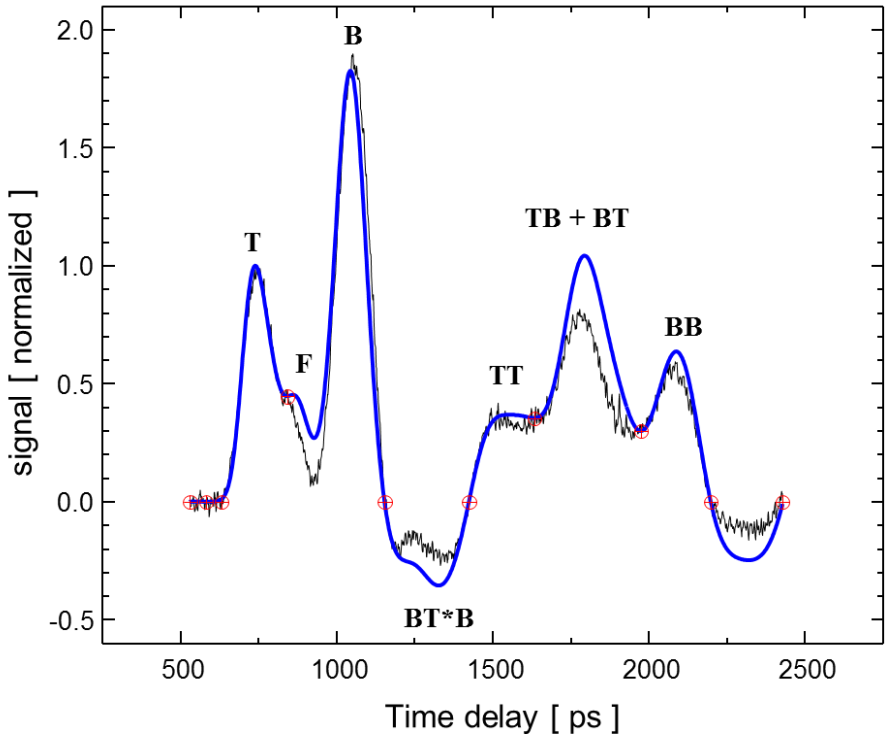

Figure 6.18: The best fit found for sample B had (P ,L, D) = (230 nm, 135 nm, 225 nm), profile 4311. Experimental data has had a background subtracted and normalized as described previously. The experimental and simulation data were compared from 530 to 2400 ps, and the best value of χ^2 was 23.75.

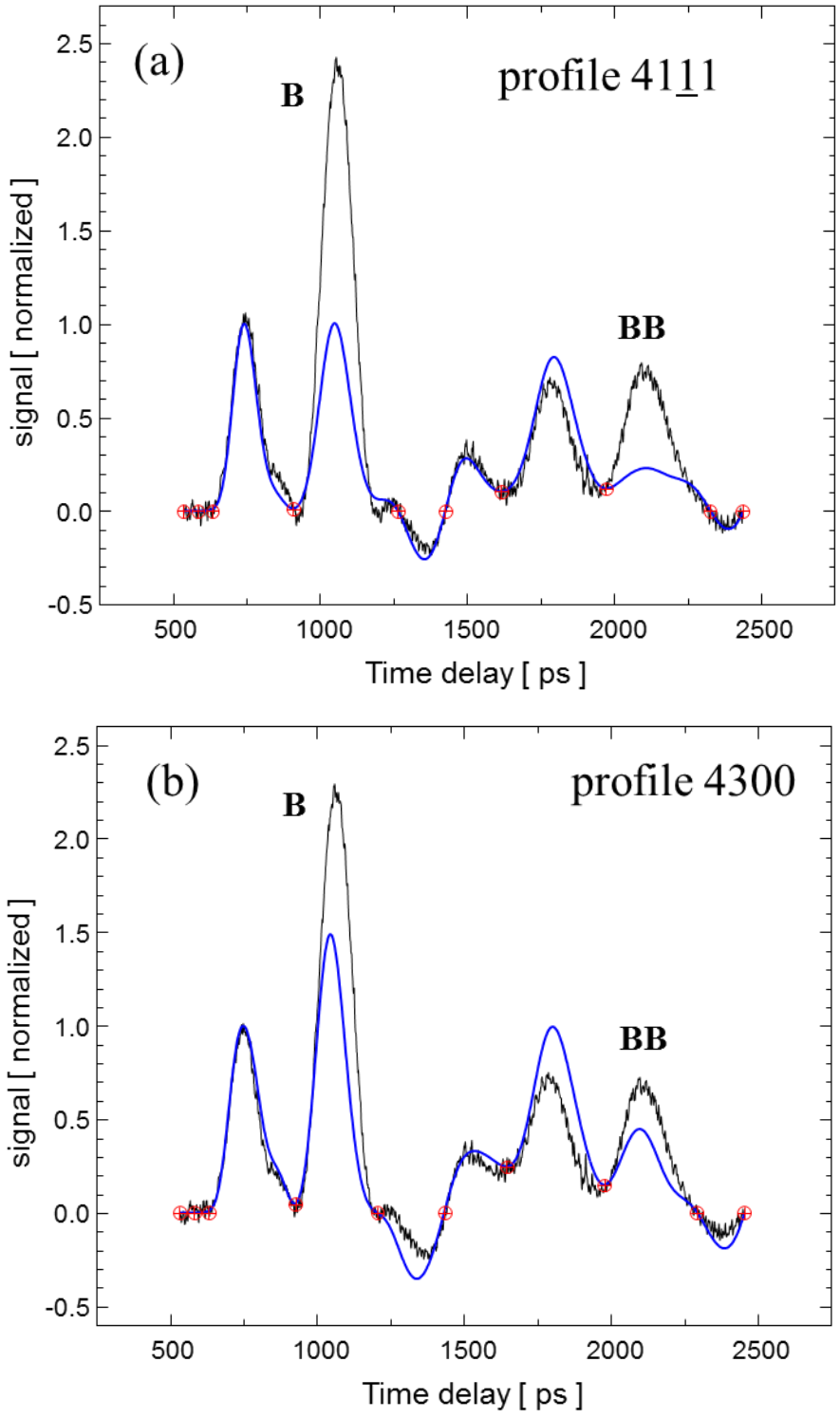

Figure 6.19: Results of the background subtraction procedure for the two profiles shown in 6.16b that bracket the profile measured in the SEM. There is a large disagreement between the experimental data and the simulation data for both (a) (*P*,*L*,*D*) = (230 nm, 135 nm, 225 nm), profile 4111, and (a) (*P*,*L*,*D*) = (230 nm, 135 nm, 225 nm), profile 4311. The disagreement is most pronounced for echoes **B** and **BB** in both cases.

Figure 6.19 shows the fitting results for the two profiles from Fig. 6.16b that bracket the measured SEM profile. For both cases, there is a pronounced disagreement for echoes B and BB. The echoes appear to be quite sensitive to even 10 nm changes in the profile, however, the best fit are not much better than the surrounding ones. Figure 6.20 is a contour plot of levels of χ^2 / χ^2_{best}. The best fits are broadly distributed, and there does

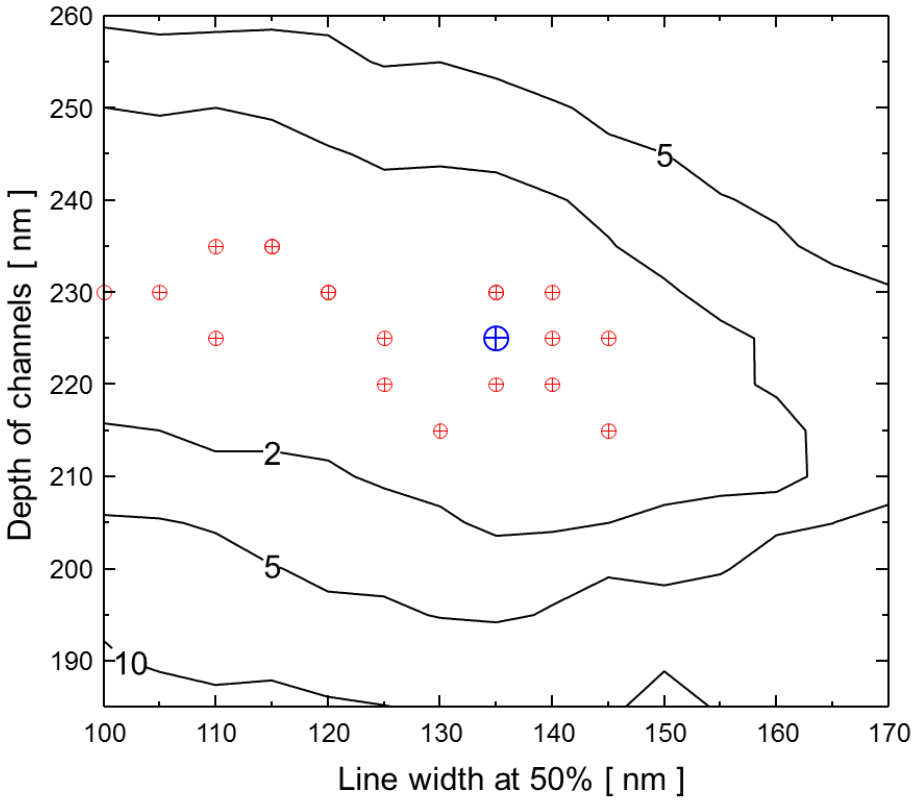

Figure 6.20: A contour plot of the best fits in the (*L*, *D*) critical space for sample B. For each point (L,D), there were 336 profiles simulated and compared to the experimental data. The best value of χ^2 was 23.75 at (*L*, *D*) = (135 nm, 225 nm), profile code 4311. The contours mark levels of χ^2 normalized to the χ^2 value for the best fit. The locations of the 20 best fits are marked by circles on the plot.

not appear to be a clear convergence onto the measured values of *L*, *D*, and profile. Some of this may be due to the longer time range over which the experimental and simulation data are compared. The experimental and simulation data were compared over a larger range of time delays than sample A, and the second set of echoes TT, TB, *etc*. were also included.

6.4 The effects of channel depth and width on echo B

For channels that were narrower than 60 nm, the magnitude and arrival time of the echo from the bottom were observed to depend on both the depth and the width of the channel. There was a series of patterns on the samples with decreasing channel widths. Below, results are presented for the narrowest channel for which an echo from the bottom was discernable, and then the next smallest channel, where the echo from the bottom was undetectable.

Figure 6.21a shows a cross sectional SEM of sample C. The white flakes are shards of material from the cleaving process. The profiles of channels 1-6 were measured, and 6 simulations were done (simulation 1 was for an infinite periodic array of channels with profile 1, etc). These are shown in Figure 6.21b by the curves labeled 1 – 6 (displaced vertically for clarity). It is clear that small variations in the widths caused significant changes in the magnitude of the echo from the bottom of the channels. The simulations were done with a mesh size of 1 nm and a time step of 0.1 ps. The two experimental data curves shown in Figure 6.21b were both derived from the same set of data, the only difference between them being how the slowly varying background was subtracted. The lowest simulation curve is for the average profile, with the set of widths as shown in Table 6.3.

Height [%]	width [nm]	Height [%]	width [nm]	Height [%]	width [nm]	Height [%]	width [nm]
100	134	92	48	75	32	50	32
98	94	90	40	70	32	25	26
96	72	85	34	65	32	10	18
94	58	80	32	60	32	0	12

Table 6.3: Channel width versus height level for the average channel of sample C.

For sample C, the echo from the bottom was visible, but it was difficult to get an accurate value for the arrival time. This was because the echo was so small that it started to blend

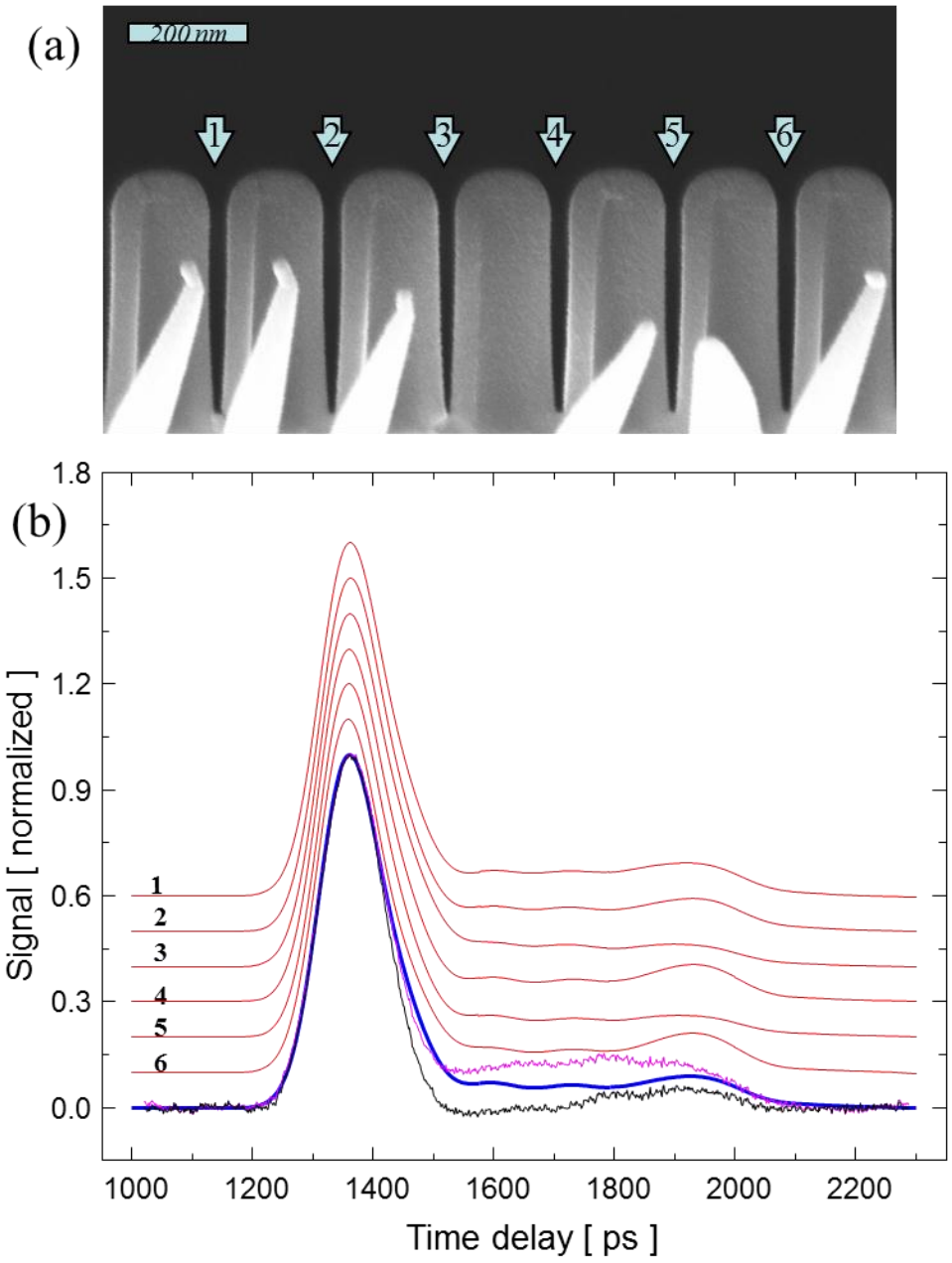

Figure 6.21: (a) Cross sectional SEM image of sample C. These were the narrowest channels from which an echo from the bottom of the channel could be detected. (b) The profiles of the channels marked 1-6 were measured and simulated, *i.e.*, the scattering of sound from an infinitely periodic array of channels with profile 1 were simulated, and then profile 2, etc. The thick line is the average of the simulations of profiles 1-6, while the two experimental curves are derived from the same experimental data set subjected to two different background subtraction procedures as described in the text.

in with the structure F that occurred after echo T. The difference in the arrival time of echo T and echo B was measured to be 582 ± 20 ps for the lower experimental curve in

Fig. 6.21b, which would be a round trip through 435 ± 15 nm of water in the bulk. The measured height from the cross sectional SEM was 410 ± 5 nm; in the channel the sound has slowed down and is only traveling at approximately 90 to 95% of the bulk sound velocity. In Figure 6.22 the experimental data on sample C is plotted alongside simulation results for the average profile. The simulation curve in the center is for the profile in Table 6.2, while for the upper curve all of the widths have been increased by 4 nm, and for the lower curve all of the widths have been decreased by 4 nm. In going from a channel width of 28 to 36 nm, the amplitude of echo B has more than doubled in magnitude.

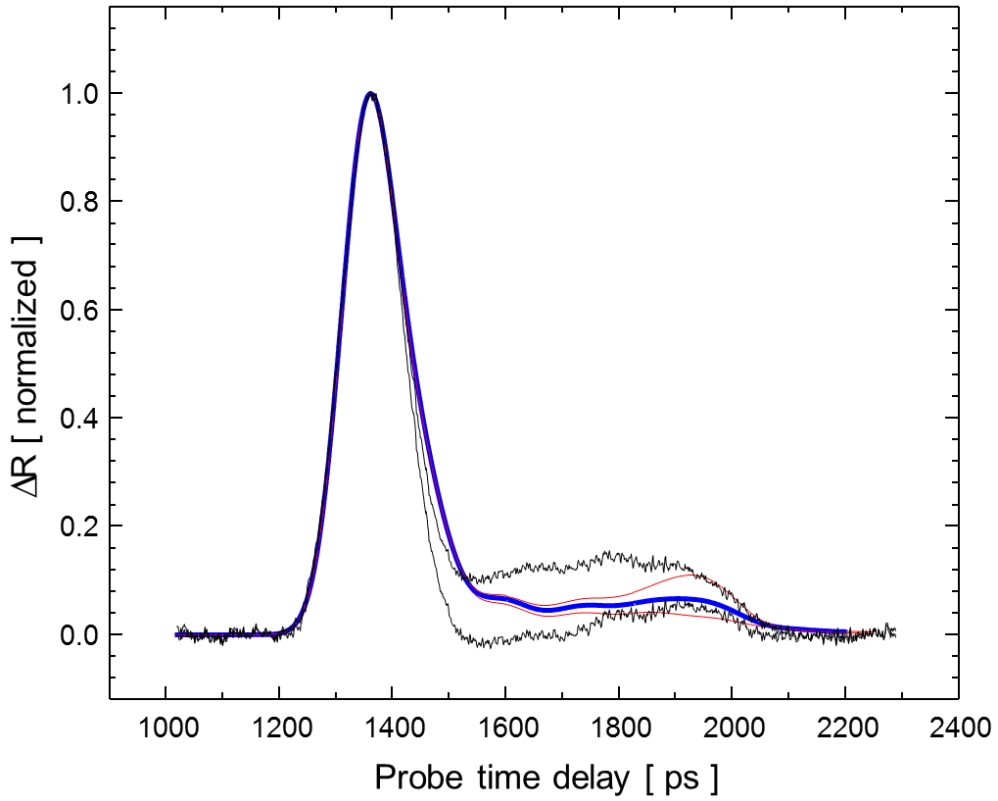

Figure 6.22: The thick curve is the simulation result for the average profile of sample C, which had a width of 32 nm halfway down the channel. The lighter curves are for channel widths of 28 and 36 nm. The experimental data shown is the same as that in the previous figure. In this range of channel widths, the magnitude of the echo from the bottom is very sensitive to the channel width.

Figure 6.23 shows a cross sectional SEM of sample D. The widths of these channels were the next size down from sample C. These channels were also significantly more tapered at the bottom. For approximately 25% of the channels in sample D whose

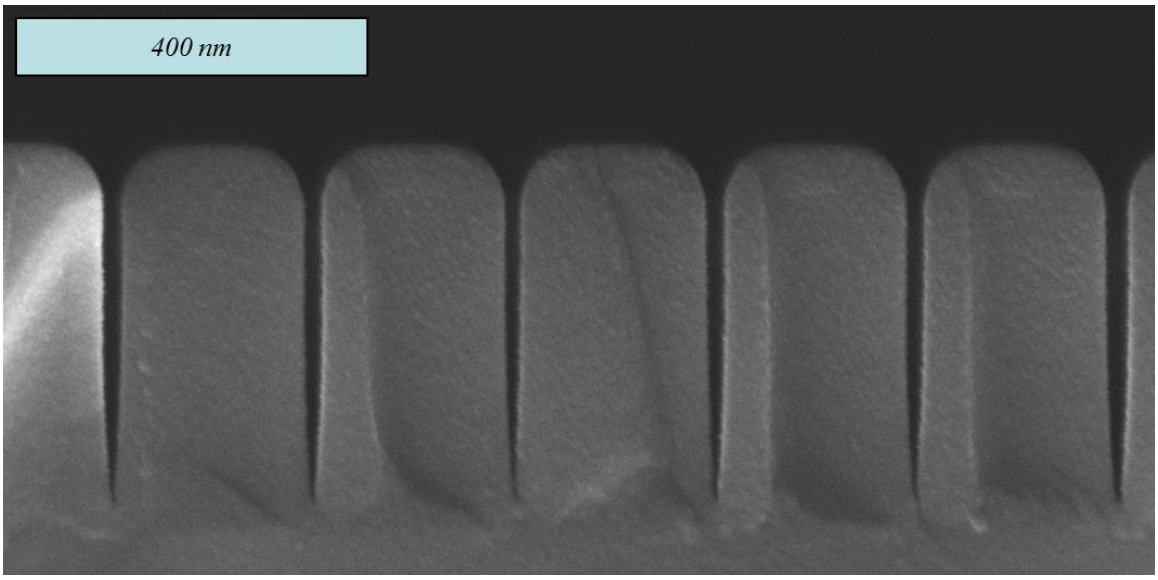

Figure 6.23: Cross sectional SEM image of sample D. The width of the channels halfway down was measured to be 24 nm on average, with a range of 20-32 nm.

profiles were measured by SEM, the width at the bottom of the channel appeared to taper right to a point. The average profile measured by cross sectional SEM imaging is shown in Table 6.4.

Height [%]	width [nm]	Height [%]	width [nm]	Height [%]	width [nm]	Height [%]	width [nm]
100	138	92	44	75	24	50	24
98	98	90	36	70	24	25	18
96	72	85	24	65	24	10	12
94	56	80	24	60	24	0	8

Table 6.4: Channel width versus height level for the average channel of sample D.

Figure 6.24 shows the POAM data taken on sample D. From the arrival time of echo T, the water film thickness was 755 nm. Moving the sample much closer to the transducer would have resulted in echo TT being superposed on where the echo B was expected to be. The lower simulation data curve is for the average profile from Table 6.4. The upper

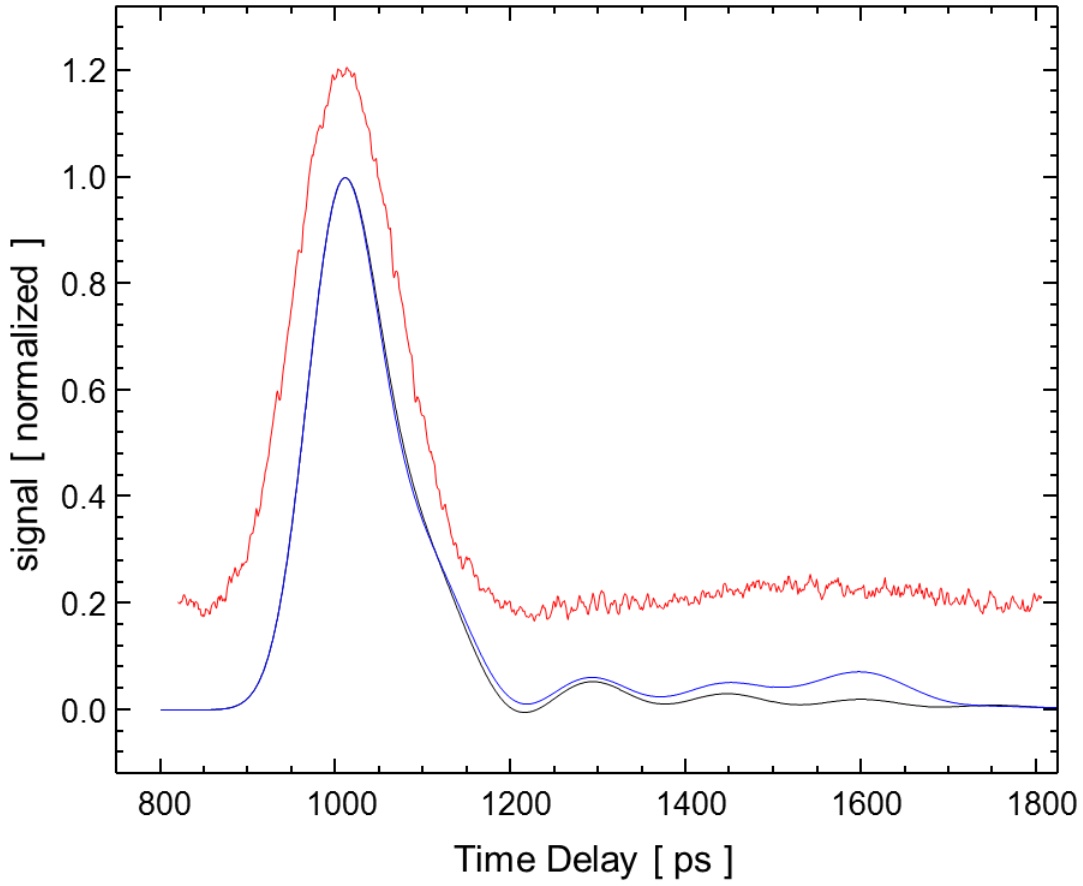

Figure 6.24: The top curve is the experimental data taken on sample D (displaced vertically for clarity) after filtering out the Brillouin oscillations and subtracting the background as described previously. Any echo from the bottom is lost in the noise. The lowest curve is the simulation data taken with the average profile measured from the SEM images with a channel width @ 50% of 24 nm. The middle curve shows a simulation for a channel with the same profile as sample C but with a channel width @50% of 32 nm.

curve is for a channel where each of the widths from Table 6.3 has been increased by 8 nm.

One very important factor that determines the visibility of the echo from the bottom is the ratio of the channel width to the pitch. Samples C and D had channels that were much narrower than the pitch, and most of the sound incident on the structures reflected off of the top. It is possible that for arrays of narrow channels with smaller pitches, the echo from the bottom will be more visible.

6.5 Estimating slip length with POAM measurements

In this section, the experimental data and the combined results of the time and frequency domain simulations are used to place an upper limit on the possible slip length at a water/silicon nitride interface. The simulation results presented below suggest that for channels with width less than 100 nm, the presence of slip will have a significant affect on the arrival time and magnitude of the echo from the bottoms of the channels. While it is difficult to measure the absolute magnitude of the echo from the bottom due to uncertainties introduced by the background subtraction process, it was possible to measure the round trip time in the channel with an uncertainty better than 10 ps. In what follows, this uncertainty in transit time is translated into an estimate on the slip length at the side walls.

6.5.1 POAM and the estimation of slip length

In the POAM estimates of slip, the time it takes the sound pulse to travel in the channel is compared to the results of the FDTD simulations. The solid in the FDTD simulations was modeled as a liquid whose properties were the same as water, except the density was taken to be a factor of 10^6 times larger than that of the water. This resulted in essentially no slip at the interface. The difference in the arrival times of echoes T and B was measured and compared to the results of the FDTD simulation, and the difference between simulation and experiment was translated into a slip length with the aid of the frequency domain numerical results discussed in section 5.3.

6.5.2 Choice of sample

Figure 6.25 shows a SEM cross sectional image of sample E. This structure was chosen for the slip experiments from consideration of two factors. For a fixed slip length, the effect of slip will be more pronounced for narrower channels than wider ones. However, of the channels that were available the profile became more tapered as the width decreased. For example, in Fig. 6.23 the average width of the channel at the 50% level was 31 nm, but at the bottom the average width of the channel was 11 nm. For the wider channels, such as those in sample A, the width from the 85% level to the bottom only

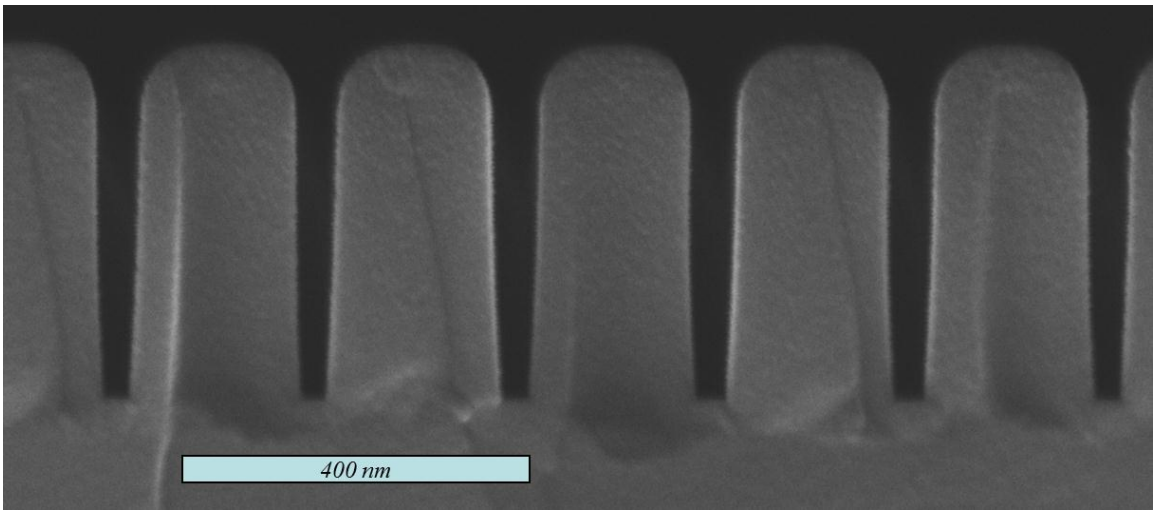

Figure 6.25: Cross sectional SEM image of sample E. The width of the channels halfway down was measured to be 52 nm on average, with a range of 48 – 54 nm.

varied by at most 10 nm, but for these broad channels the effects of a slip length of 2 – 5 nm will become less pronounced. The dimensions and profile of sample E represented a compromise between narrowness and uniformity among the available patterns.

Several SEM images like that in Fig. 6.25 were taken and the profiles of 20 channels were measured, and then the width at each height level was averaged to determine the profile of the "average" channel. This was the profile that was then used in the time domain simulations. The average widths of the channels as a function of height are listed in Table 6.5.

Height [%]	width [nm]	Height [%]	width [nm]	Height [%]	width [nm]	Height [%]	width [nm]
100	168	92	70	75	56	50	54
98	120	90	62	70	56	25	48
96	96	85	56	65	56	10	42
94	80	80	56	60	56	0	36

Table 6.5: Channel width versus height level for the average channel of sample E.

The uncertainty in the average widths was estimated by

$$\sigma = \sqrt{s^2 + 2l^2}, \qquad 6.2$$

where s is the standard deviation in the widths of the channels that were measured, and l is uncertainty in the location of the edge in the cross sectional SEM image. For the image shown in Fig. 6.25, s was around 3 nm and l ~ 4 nm, giving an uncertainty in the widths of about 6 nm.

6.5.3 POAM data and FDTD simulations

Figure 6.26a compares the experimental data and the time domain simulation data, and Figure 6.26b shows a close up of the echo from the bottom of the channel. From bottom to top, the simulation results are for channels with a width at the 50% level of 60, 62, 64, 66, 68, and 70 nm. The amplitude of the echo B for the experimental data agrees with the

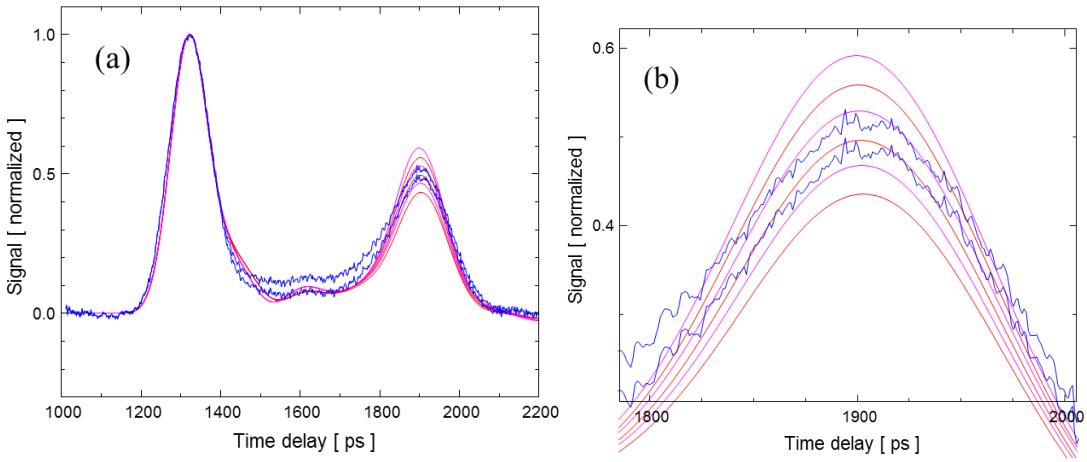

Figure 6.26: Simulation vs. experiment for sample E. The two curves with noise are the same experimental data with the background subtracted two different ways (see description for sample C). Also plotted are a series of simulations with increasing channel width, starting at 60 nm and increasing to 70 nm in 2 nm increments. (b) Close up view of the echo from the bottom from (a). The arrival time of the echo from the bottom appears to be consistent with the no slip condition enforced by the simulation program.

simulation results for a channel width between 62 and 68 nm, but the measured width was almost 10 nm less than this. The origin for the discrepancy between the simulation and experimental results was attributed to the difficulties associated with the background subtraction. The travel time in the channels for the experimental data and the simulation

results were the same to within ±12 ps, and the round trip time could be measured with an accuracy of 2%. The experimental result for the arrival time of echo B was more robust to the background subtraction process as well.

6.5.4 Frequency domain simulations for slip and no slip cases

Using the numerical method described in Section 5.3, the phase velocity as a function of frequency for several combinations of channel width and slip length was computed. The resulting curves are shown in Figure 6.27. The phase velocity has been normalized to the value of the sound velocity in water. The three lowest curves are for channels 48, 60, and 70 nm wide, respectively, with a no slip boundary condition. The dependence of the phase velocity on the channel width is demonstrated; sound travels faster down wider channels for all frequencies. The curves labeled 4, 5, and 6 are the results for a channel that is 60 nm wide with a slip length of 2, 5, and 8 nm at each boundary. The presence of slip at the boundary significantly increases the phase velocity. Figure 6.28 shows the amplitude attenuation as a function of frequency. The presence of slip significantly decreased the amplitude attenuation for waves propagating along the channel.

Let $v_{phase}(f, w, b)$ be the computed phase velocity as a function of frequency f for a channel width w and slip length b. In Figure 6.29, the expression

$$\frac{v_{phase}(f, w, b) - v_{phase}(f, w = 60\text{ nm}, b = 0\text{ nm})}{v_{phase}(f, 60\text{ nm}, 0\text{ nm})} \times 100 \qquad 6.3$$

is plotted versus frequency for each of the curves in Fig. 6.28. The upper and lower bounds of the shaded grey area are for channel widths of 48 and 70 nm with no slip, respectively. The shaded area represents possible variations in the phase velocity due to variations in the channel width from channel to channel. The solid curves are all for channels with a width of 60 nm and increasing amounts of slip (2, 5, and 8 nm). From the above results, the slip length at the side wall water interface was estimated to be less than 5 nm.

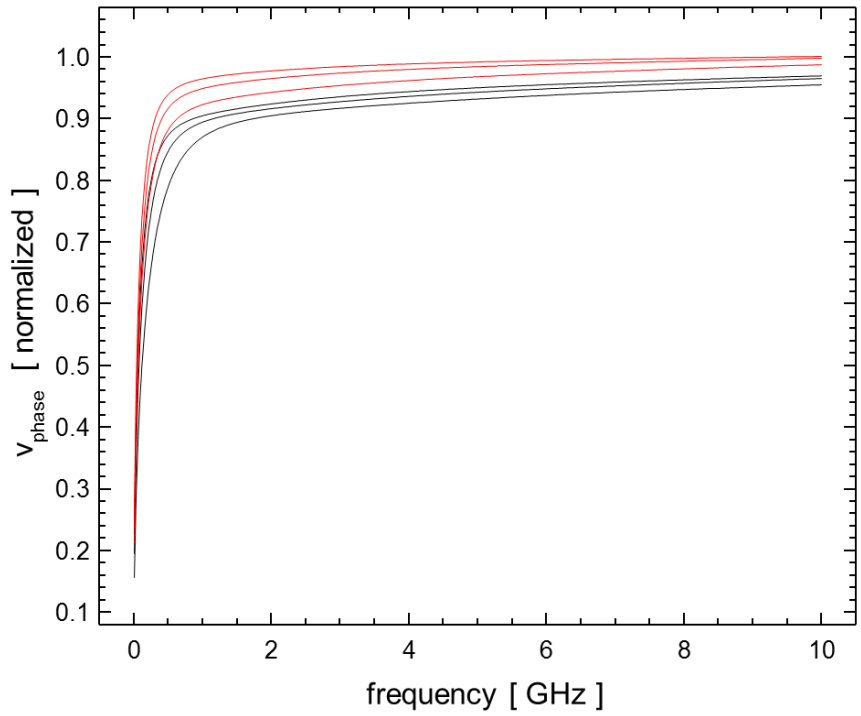

Figure 6.27: Relative phase velocity (normalized to the bulk sound velocity) versus frequency for several values of channel width and slip length. The three lower curves, starting at the lowest, have widths of 48, 60, and 70 nm, and no slip. The three upper curves all have a channel width of 60 nm, and slip lengths of 2, 5, and 8 nm.

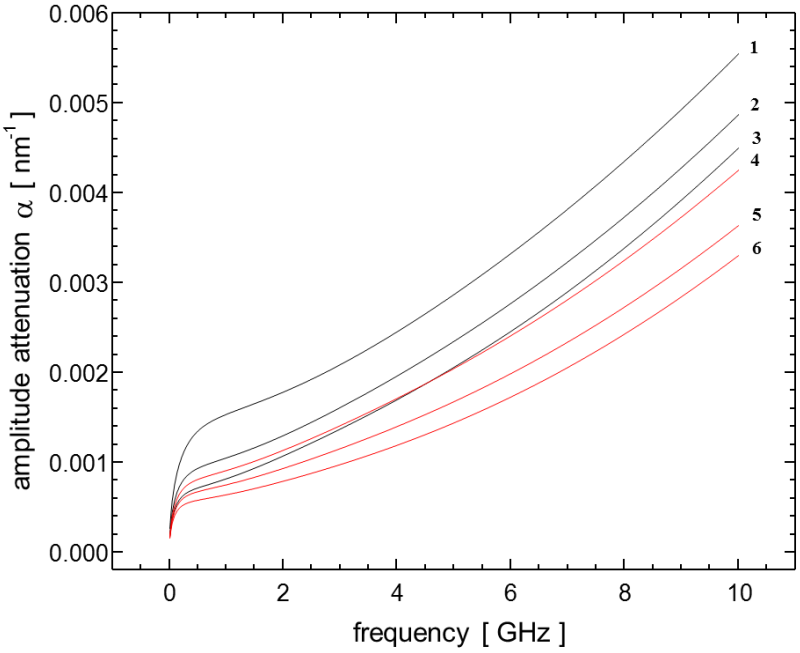

Figure 6.28: Amplitude attenuation versus frequency for several values of channel width and slip length. Curves 1-3 are for the no slip case and have widths of 48, 60, and 70 nm. Curves 4-6 are for channels with a width of 60 nm and slip lengths of 2, 5, and 8 nm.

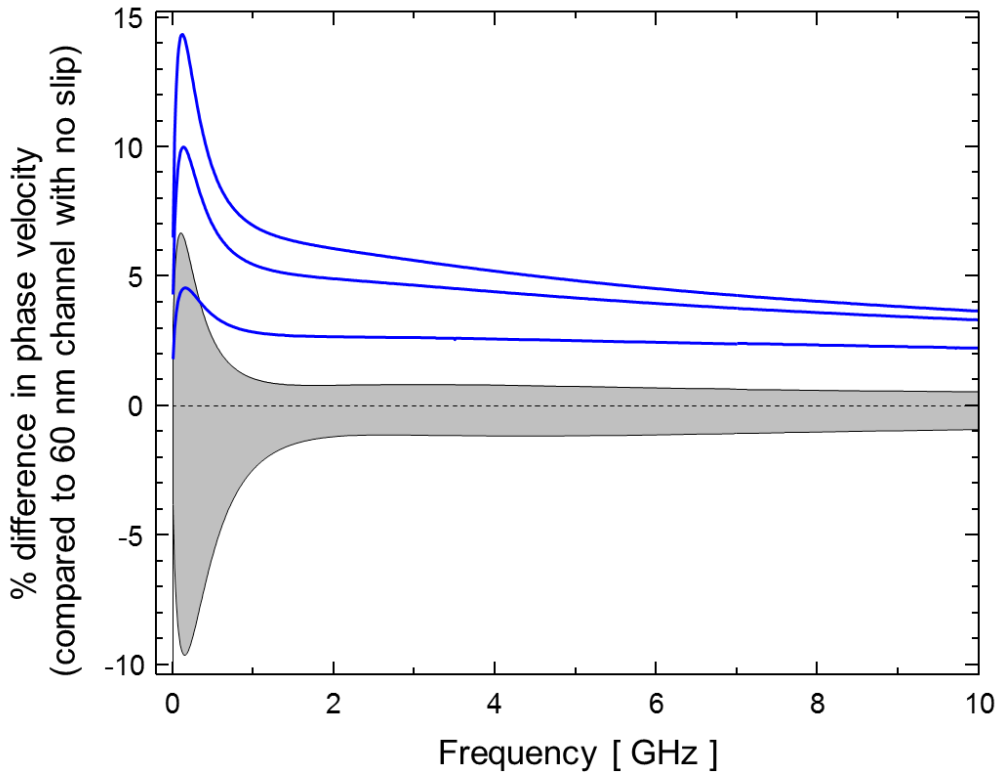

Figure 6.29: The phase velocities for various channel widths and slip lengths compared to the case of a 60 nm wide channel with no-slip conditions. The shaded grey region covers the cases from 48 – 70 nm wide channels with no slip and represents the maximum uncertainty introduced by the variation in the widths from channel to channel measured for sample E. The thick curves are 60 nm channels with increasing amounts of slip (2, 5, and 8 nm slip lengths on each wall of the channel) The introduction of a small amount of slip increased the phase velocities significantly

6.5.5 Comments on extending the technique to other fluid/solid interfaces

The above results deal with possible slip at the interface between the walls of the channels and water. In order to make a measurement, a sample with channels like that shown needs to be fabricated. This is the main disadvantage of using a POAM measurement to investigate the slip at interfaces, since slip measurements are usually done on surfaces that are treated in certain ways, either chemically or physically. If the sound was focused into the mouth of one channel with an acoustic lens, *i.e.*, if a similar measurement was performed using a scanning opto-acoustic microscopy (SOAM) technique, then the sample preparation and characterization would be less cumbersome, since only 1 channel would need to be prepared instead of an array of them.

6.6 Conclusions

Results of POAM measurements of 1D periodic nanostructures were presented. The relative sizes of the echoes in the POAM data were used to infer information about the average critical dimensions and profile of groups of structures. For structures with channels that were less than 60 nm wide, the amplitude and arrival time of the echo from the bottom of the channels were very sensitive to the channel width and depth. POAM was shown to provide a way of measuring the dimensions of these features nondestructively. For narrow channels, the presence of slip between the water-side wall interface would have a measurable effect on the echo from the bottoms of the channels. POAM data was used to place an upper limit of 5 nm on the slip length at the water-silicon nitride interfaces.

Bibliography

1. De Groot, P., Colonna de Lega, X., Liesener, J. & Darwin, M. "Metrology of optically-unresolved features using interferometric surface profiling and RCWA modeling." *Opt. Express* **16**, 3970-3975 (2008).
2. De Groot, P., Darwin, M.J., Stoner, R., Gallatin, G.M. & De Lega, X.C. United States Patent: 7948636 - Interferometer and method for measuring characteristics of optically unresolved surface features. (2011).
3. Villarrubia, J.S. "Scanning electron microscope analog of scatterometry." *Proceedings of SPIE* 304-312 (2002).
4. Bingham, P.R., Price, J.R., Tobin, K.W. & Karnowski, T.P. "Semiconductor sidewall shape estimation." *J. Electron. Imaging* **13**, 474 (2004).
5. Villarrubia, J.S., Vladár, A.E. & Postek, M.T. "Scanning electron microscope dimensional metrology using a model-based library." *Surface and Interface Analysis* **37**, 951-958 (2005).
6. Villarrubia, J.S. & Ding, Z.J. "Sensitivity of scanning electron microscope width measurements to model assumptions." *Journal of Micro/Nanolithography, MEMS and MOEMS* **8**, 033003 (2009).
7. Postek, M.T. & Vladár, A.E. "Modeling for accurate dimensional scanning electron microscope metrology: then and now." *Scanning* **33**, 111-125 (2011).
8. Lee, K.L. Submicron Si trench profiling with an electron-beam fabricated atomic force microscope tip. *J. Vac. Sci. Technol. B* **9**, 3562 (1991).
9. Hafner, J.H., Cheung, C.L. & Lieber, C.M. "Growth of nanotubes for probe microscopy tips." *Nature* **398**, 761-762 (1999).
10. Nguyen, C.V. et al. "Carbon nanotube tip probes: stability and lateral resolution in scanning probe microscopy and application to surface science in semiconductors." *Nanotechnology* **12**, 363-367 (2001).
11. Nguyen, C.V. et al. "Carbon nanotube scanning probe for profiling of deep-ultraviolet and 193 nm photoresist patterns." *Appl. Phys. Lett.* **81**, 901 (2002).
12. Oon, C.H., Thong, J.T.L., Lei, Y. & Chim, W.K. "High-resolution atomic force microscope nanotip grown by self-field emission." *Appl. Phys. Lett.* **81**, 3037 (2002).
13. Strus, M.C., Raman, A., Han, C.-S. & Nguyen, C.V. "Imaging artefacts in atomic force microscopy with carbon nanotube tips." *Nanotechnology* **16**, 2482-2492 (2005).
14. Solares, S.D. & Chawla, G. "Exploration of AFM Imaging Artifacts Occurring at Sharp Surface Features When Using Short Carbon Nanotube Probes and Possible Mitigation With Real-Time Force Spectroscopy." *J. Manuf. Sci. Eng.* **132**, 030904-14 (2010).

Chapter 7
Conclusions

This work described the development of a new mode of acoustic microscopy, POAM. Initially, POAM was conceived as a stepping stone towards a full scanning opto-acoustic microscope (SOAM), but the experimental results discussed above demonstrated that POAM has its own potential applications.

The fabrication, characterization, and testing of Fabry-Perot thin film cavities for use in picosecond ultrasonics measurements were presented. For cavities that were used in the POAM measurements, two main features were addressed; the magnitude and simplicity of the cavity's response to an incoming strain pulse. This was accomplished by using Al and SiO_2 films. These materials were sufficiently well matched acoustically such that the response function of the cavity only had a small tail. It was important to fully

characterize the response of the cavity to a returning sound pulse in order to distinguish between signals coming from different features of the sample being studied.

Results of POAM measurements of 1D periodic nanostructures were presented. The relative sizes of the echoes in the POAM data were used to infer information about the average critical dimensions and profile of groups of structures. For structures with channels that were less than 60 nm wide, the amplitude and arrival time of the echo from the bottom of the channels were very sensitive to the channel width and depth. POAM was shown to provide a way of measuring the dimensions of these features nondestructively. For narrow channels, the presence of slip between the water-side wall interface would have a measurable effect on the echo from the bottoms of the channels. POAM data was used to place an upper limit of 5 nm on the slip length at the water-silicon nitride interfaces.

Appendix A

Code for the 2D Finite difference time domain simulations of sound propagation in a Newtonian fluid

This appendix contains the code, written by Professor Humphrey J Maris, for the program discussed in Section 5.2. This program was used in conjuction with a visual basic script, not shown, to generate simulation libraries for comparison to the experimental data. The script generated a separate input file for each simulation. The program reads the name of the file with the input information in the file `xy_water.inp`.

xy_water_IG.for

```
c     Program 'xy_water_IG.for'  ***************************************
c     It is assumed that all motion is in the x-y plane.
c     Saves the positions of a grid of selected atoms in a file from
c     which a plot can be made.
c     a             = spacing of atoms.
c     t_step        = time step in simulation.
c     eta           = volume viscosity.
c     m(n_x,n_y)    = mass of atom n_x,n_y.
c     n_rect        = # of a rectangle.
c     n_rects_max   = total number of rectangles in sample.
c     n_x           = x-mesh coordinate of an atom.
c     n_x_max       = # of mesh steps in x, determines size of atoms.
c     n_y           = y-mesh coordinate of an atom
c     n_y_max       = # of mesh steps in y.
c     pitch         = repeat distance across surface of sample.
c     t             = time.
c     t_save        = time between saving displacement distribution.
c     t_stop        = time to stop simulation.
c     u_x(n_x,n_y)  = x-component of displacement of atom n_x,n_y.
c     u_y(n_x,n_y)  = y-component of displacement of atom n_x,n_y.
c     v_x(n_x,n_y)  = x-component of velocity of atom n_x,n_y.
c     v_y(n_x,n_y)  = y-component of velocity of atom n_x,n_y.
      implicit real*8 (a-h,o-z)
      real*8 u_x(0:1001,-1:2000),u_y(0:1001,-1:2000)
       real*8 v_x(0:1001,-1:2000),v_y(0:1001,-1:2000)
      real*8 x_1_curve(6),x_2_curve(6),y_1_curve(6),y_2_curve(6)
       real*8 x_quad(200,4),y_quad(200,4)
```

```
       real*8 x_left_ellipse(6),x_right_ellipse(6),
     &y_top_ellipse(6),y_center_ellipse(6)
       real*8 m(0:1001,-1:2000)
       real*8 strain(0:1000,0:2000),strain_old(0:1000,0:2000)

       character*40 signal$
       character*40 inputs$

$debug
       pi=2.0d0*dacos(0.0d0)
c      ********************************************************************
c      open xy_water.inp and read  ***********************************
c      ********************************************************************
       open(8,file='xy_water.inp',status='old')
       read(8,*) inputs$
       close(8)
c      ********************************************************************
c      Open file that has input data ***********************************
c      ********************************************************************
       open(1, file=inputs$, status='old')


c      ********************************************************************
c      Open output file for signal. ************************************
c      ********************************************************************
c      write (*,*) 'name for signal file:'
       read(1,*) signal$
       open(2,file=signal$,status='unknown')
       open(9,file='xy_water_signal.dat', status='unknown')
c      ********************************************************************
c      Read in parameters for water. ***********************************
c      ********************************************************************
       read(1,*) rho  ! density of water. ******************************
       read(1,*) c    !  sound velocity in water.  **********************
       b=rho*c**2  ! bulk modulus. *************************************
       read(1,*) eta,zeta   ! shear and bulk viscosity ******************
c      ********************************************************************
c      Read in parameters for structure. *******************************
c      ********************************************************************
       read(1,*) pitch  ! lateral repeat distance of structure. *********
       read(1,*) height  ! total height.  ******************************
c      ********************************************************************
c      Read in mesh parameters. ****************************************
c      ********************************************************************
       read(1,*) n_x_max  ! # of mesh points in x.
       a=pitch/n_x_max         ! spacing of the square mesh. *****************
       n_y_max=int(height/a) ! # of mesh points in y ********************
       write(*,*) 'n_x_max',n_x_max,'   n_y_max',n_y_max
c      ********************************************************************
c      Read in parameters for curves. **********************************
c      ********************************************************************
       read(1,*) n_curves_max ! # of curves
       do n_curve=1,n_curves_max
            read(1,*) x_1_curve(n_curve),x_2_curve(n_curve),
     &     y_1_curve(n_curve),y_2_curve(n_curve)
       end do
c      ********************************************************************
c      Read in parameters for quadrilaterals. **************************
c      ********************************************************************
       read(1,*) n_quads_max ! # of quadrilaterals
       do n_quad=1,n_quads_max
```

```
         do i=1,4
           read(1,*) x_quad(n_quad,i),y_quad(n_quad,i)
         end do
       end do
c      ********************************************************************
c      Read in parameters for semi-ellipses. ****************************
c      ********************************************************************
       read(1,*) n_ellipses_max ! # of semi-ellipses. ****************
       do n_ellipse=1,n_ellipses_max
         read(1,*) x_left_ellipse(n_ellipse),x_right_ellipse(n_ellipse),
     &   y_top_ellipse(n_ellipse),y_center_ellipse(n_ellipse)
       end do
c      ********************************************************************
c      Read in time step and stop time. *********************************
c      ********************************************************************
       read(1,*) t_step
       read(1,*) t_stop
c      ********************************************************************
c      Read in time between saves to a file. ****************************
c      ********************************************************************
       read(1,*) t_save
c      ********************************************************************
c      ********************************************************************
c      Set the value of the masses throughout the structure. ************
c      ********************************************************************
       call set_masses(n_x_max,n_y_max,a,rho,n_curves_max,x_1_curve,
        &x_2_curve,y_1_curve,y_2_curve,n_quads_max,x_quad,y_quad,
     &n_ellipses_max,
     &x_left_ellipse,x_right_ellipse,y_top_ellipse,y_center_ellipse,m)
c      ********************************************************************
c      Set an initial condition. ****************************************
c      ********************************************************************
       call set_initial(n_x_max,n_y_max,a,u_x,u_y,v_x,v_y)
c      Time develop. ****************************************************
       do t=t_step,t_stop,t_step
         if (amod(t,1.0) .lt. t_step) write(*,101) t
101      format(' Time=',f6.1)
          call time_develop(n_x_max,n_y_max,t_step,a,b,eta,zeta,m,
     &   u_x,u_y,v_x,v_y,strain,strain_old)
         call signal_calc(n_x_max,n_y_max,u_y,signal)
          write(2,100) t,signal
          write(9,100) t,signal
100       format(f8.2,es14.5)
         if (amod(t,t_save) .lt. t_step) then
           call save_all(t,n_x_max,n_y_max,a,b,u_x,u_y,v_x,v_y)
         end if
       end do
       close(2)
       close(1)
       stop
       end
c      ********************************************************************
       subroutine save_all(t,n_x_max,n_y_max,a,b,u_x,u_y,v_x,v_y)
c      ********************************************************************
       implicit real*8 (a-h,o-z)
       real*8 u_x(0:1001,-1:2000),u_y(0:1001,-1:2000)
       real*8 v_x(0:1001,-1:2000),v_y(0:1001,-1:2000)
       real*8 p(0:1000,0:2000)
       character*20 file$
       character*20 slice$
       character*20 file_vx$
```

```
       character*20 file_vy$
      character*4 dat$
c     ***********************************************************************
c     Open output file for save. ********************************************
c     ***********************************************************************
      dat$='.dat'
       i_t=int(t)
       write(file$,*) i_t,'.dat'
       write(slice$, *) i_t, 'mid.dat'
       write(file_vx$, *) i_t, '_vx.dat'
       write(file_vy$, *) i_t, '_vy.dat'
      open(3,file=file$,status='unknown')
       open(4,file=slice$,status='unknown')
       open(5,file=file_vx$,status='unknown')
       open(6,file=file_vy$,status='unknown')

c     ***********************************************************************
c     Calculate pressure distribution. **********************************
c     ***********************************************************************
       do n_x=0,n_x_max
         do n_y=0,n_y_max
          p(n_x,n_y)=(0.5*b/a)*(u_x(n_x,n_y)-u_x(n_x+1,n_y)-
     & u_x(n_x+1,n_y+1)+u_x(n_x,n_y+1)+u_y(n_x,n_y)+u_y(n_x+1,n_y)-
     & u_y(n_x+1,n_y+1)-u_y(n_x,n_y+1))
         end do
         p(n_x,n_y_max+1)=0.0d0
       end do

c       write the pressure distribution down a vertical line in the middle
       n_x=n_x_max/2
       do n_y=0,n_y_max+1
          write(4,*) n_y, p(n_x,n_y)
       end do
       close(4)

c       write the entire pressure distribution

      do n_y=0,n_y_max+1
         do n_x=0,n_x_max

c          write(3,100) n_x,n_y,u_x(n_x,n_y),u_y(n_x,n_y),v_x(n_x,n_y),
c     &       v_y(n_x,n_y),p(n_x,n_y)
           write(3,100) n_x,n_y,p(n_x,n_y)
             write(5,100) n_x,n_y,v_x(n_x,n_y)
             write(6,100) n_x,n_y,v_y(n_x,n_y)

100       format(2i5,5f13.7)
         end do
c        write(3,100)
       end do
       close(3)
       close(5)
       close(6)
       return
       end
c     ***********************************************************************
      subroutine signal_calc(n_x_max,n_y_max,u_y,signal)
c     Save integral of pressure at transducer. ************************
c     ***********************************************************************
      implicit real*8 (a-h,o-z)
      real*8 u_y(0:1001,-1:2000)
```

```
      signal=0.0d0
      do n_x=1,n_x_max
         signal=signal+u_y(n_x,n_y_max)-u_y(n_x,n_y_max+1)
       end do
       return
       end
c     ****************************************************************
      subroutine set_initial(n_x_max,n_y_max,a,u_x,u_y,v_x,v_y)
c     Initial condition is with a displacement of the top row of atoms
c     displaced by -0.1*a. ********************************************
c     ****************************************************************
      implicit real*8 (a-h,o-z)
      real*8 u_x(0:1001,-1:2000),u_y(0:1001,-1:2000)
       real*8 v_x(0:1001,-1:2000),v_y(0:1001,-1:2000)
      do n_x=0,n_x_max+1
         do n_y=-1,n_y_max+1
           u_x(n_x,n_y)=0.0d0
           u_y(n_x,n_y)=0.0d0
           v_x(n_x,n_y)=0.0d0
           v_y(n_x,n_y)=0.0d0
        end do
       end do
      do n_x=0,n_x_max+1
        u_y(n_x,n_y_max+1)=-0.1*a
       end do
       return
       end
c     ****************************************************************
      subroutine time_develop(n_x_max,n_y_max,t_step,a,b,eta,zeta,m,
     &u_x,u_y,v_x,v_y,strain,strain_old)
c     ****************************************************************
      implicit real*8 (a-h,o-z)
      real*8 u_x(0:1001,-1:2000),u_y(0:1001,-1:2000)
       real*8 v_x(0:1001,-1:2000),v_y(0:1001,-1:2000)
       real*8 a_x(0:1001,-1:2000),a_y(0:1001,-1:2000)
       real*8 strain(0:1000,0:2000),strain_old(0:1000,0:2000)
       real*8 stress(0:1000,0:2000)
      real*8 m(0:1001,-1:2000)
c     ****************************************************************
c     Calculate strain distribution. **********************************
c     Strain means dilatation. ****************************************
c     ****************************************************************
       do n_x=0,n_x_max
         do n_y=0,n_y_max
           strain(n_x,n_y)=(0.5/a)*(-u_x(n_x,n_y)+u_x(n_x+1,n_y)+
     & u_x(n_x+1,n_y+1)-u_x(n_x,n_y+1)-u_y(n_x,n_y)-u_y(n_x+1,n_y)+
     & u_y(n_x+1,n_y+1)+u_y(n_x,n_y+1))
         end do
       end do
c     ****************************************************************
c     Calculate contribution to the stress from the sum of the pressure
c     and the time dependence of the density.  ************************
c     ****************************************************************
       do n_x=0,n_x_max
         do n_y=0,n_y_max
           stress(n_x,n_y)=-b*strain(n_x,n_y)-
     & (zeta+eta/3)*(strain(n_x,n_y)-strain_old(n_x,n_y))/t_step
         end do
       end do
c     ****************************************************************
c     Calculate acceleration. *****************************************
```

```
c     ****************************************************************
c     Contribution from the sum of the pressure and the time dependence
c     of the density. ************************************************
c     ****************************************************************
      do n_x=1,n_x_max
        do n_y=1,n_y_max
         a_x(n_x,n_y)=(0.5d0*a**2/m(n_x,n_y))*
     & (stress(n_x-1,n_y-1)-stress(n_x,n_y-1)
     &    -stress(n_x,n_y)+stress(n_x-1,n_y))
         a_y(n_x,n_y)=(0.5d0*a**2/m(n_x,n_y))*
     & (stress(n_x-1,n_y-1)+stress(n_x,n_y-1)
     &    -stress(n_x,n_y)-stress(n_x-1,n_y))
       end do
      end do
c     ****************************************************************
c     Contribution from the shear viscosity term (see notes). **********
c     ****************************************************************
      do n_x=1,n_x_max
        do n_y=1,n_y_max
         a_x(n_x,n_y)=a_x(n_x,n_y)+(eta*a/m(n_x,n_y))*
     &     (v_x(n_x+1,n_y)-2*v_x(n_x,n_y)+v_x(n_x-1,n_y)+
     &      v_x(n_x,n_y+1)-2*v_x(n_x,n_y)+v_x(n_x,n_y-1))
         a_y(n_x,n_y)=a_y(n_x,n_y)+(eta*a/m(n_x,n_y))*
     &     (v_y(n_x+1,n_y)-2*v_y(n_x,n_y)+v_y(n_x-1,n_y)+
     &      v_y(n_x,n_y+1)-2*v_y(n_x,n_y)+v_y(n_x,n_y-1))
       end do
      end do
c     ****************************************************************
c     Calculate new velocities. **************************************
c     ****************************************************************
      do n_x=1,n_x_max
        do n_y=1,n_y_max
         v_x(n_x,n_y)=v_x(n_x,n_y)+a_x(n_x,n_y)*t_step
         v_y(n_x,n_y)=v_y(n_x,n_y)+a_y(n_x,n_y)*t_step
       end do
      end do
c     ****************************************************************
c     Calculate new positions. ***************************************
c     ****************************************************************
      do n_x=1,n_x_max
        do n_y=1,n_y_max
          u_x(n_x,n_y)=u_x(n_x,n_y)+v_x(n_x,n_y)*t_step
          u_y(n_x,n_y)=u_y(n_x,n_y)+v_y(n_x,n_y)*t_step
       end do
      end do
c     ****************************************************************
c     Apply periodic boundary conditions. ****************************
c     ****************************************************************
      do n_y=1,n_y_max
        u_x(0,n_y)=u_x(n_x_max,n_y)
        u_y(0,n_y)=u_y(n_x_max,n_y)
        u_x(n_x_max+1,n_y)=u_x(1,n_y)
        u_y(n_x_max+1,n_y)=u_y(1,n_y)
        v_x(0,n_y)=v_x(n_x_max,n_y)
        v_y(0,n_y)=v_y(n_x_max,n_y)
        v_x(n_x_max+1,n_y)=v_x(1,n_y)
        v_y(n_x_max+1,n_y)=v_y(1,n_y)
      end do
c     ****************************************************************
c     Update strain_old. *********************************************
c     ****************************************************************
```

```
      do n_x=0,n_x_max
         do n_y=0,n_y_max
           strain_old(n_x,n_y)=strain(n_x,n_y)
         end do
       end do

       return
       end
c     ****************************************************************
      subroutine set_masses(n_x_max,n_y_max,a,rho,n_curves_max,
     &x_1_curve,x_2_curve,y_1_curve,y_2_curve,n_quads_max,x_quad,y_quad,
     &n_ellipses_max,
     &x_left_ellipse,x_right_ellipse,y_top_ellipse,y_center_ellipse,m)
c     ****************************************************************
      implicit real*8 (a-h,o-z)
      real*8 x_1_curve(6),x_2_curve(6),y_1_curve(6),y_2_curve(6)
       real*8 x_quad(200,4),y_quad(200,4)
      real*8 x_left_ellipse(6),x_right_ellipse(6),y_top_ellipse(6),
     &y_center_ellipse(6)
      real*8 m(0:1001,-1:2000)
       real*8 m_water,m_infinity
c     ****************************************************************
c     Open file for sample shape.
c     ****************************************************************
       open(4,file='xy_water_shape.dat',status='unknown')
c     ****************************************************************
c     Write top and bottom lines of sample.
c     ****************************************************************
       do n_x=1,n_x_max
         write(4,100) n_x*a,(n_y_max+1)*a
         write(4,100) n_x*a,-a
100     format(2f12.3)
      end do
c     ****************************************************************
c     Set all masses equal to mass in water. ***************************
c     ****************************************************************
      m_water=rho*a**3
      do n_x=0,n_x_max+1
         do n_y=0,n_y_max+1
           m(n_x,n_y)=m_water
        end do
       end do
c     ****************************************************************
c     Set masses in solid to a large value. ****************************
c     ****************************************************************
      m_infinity=1.0d6*m_water
      do n_x=0,n_x_max+1
         x=n_x*a
         do n_y=-1,n_y_max+1
           y=n_y*a
c     ****************************************************************
c         Curves. ******************************************************
c     ****************************************************************
           do n_curve=1,n_curves_max
             y_curve=y_1_curve(n_curve)+
     &   (y_2_curve(n_curve)-y_1_curve(n_curve))*
     &      (x-x_1_curve(n_curve))**2/
     &      (x_2_curve(n_curve)-x_1_curve(n_curve))**2
             if ((y .lt. y_curve) .and. (x .gt. x_1_curve(n_curve))
     &      .and. (x .lt. x_2_curve(n_curve))) then
               m(n_x,n_y)=m_infinity
```

```
              write(4,100) n_x*a,n_y*a
              goto 10
            end if
            if ((y .lt. y_curve) .and. (x .lt. x_1_curve(n_curve))
     &      .and. (x .gt. x_2_curve(n_curve))) then
               m(n_x,n_y)=m_infinity
              write(4,100) n_x*a,n_y*a
              goto 10
            end if
          end do
c     ****************************************************************
c         Quadrilaterals. ************************************************
c     ****************************************************************
          do n_quad=1,n_quads_max
             do i=1,4
               if (i .eq. 1) then
                 x_edge=x_quad(n_quad,1)-x_quad(n_quad,4)
                 y_edge=y_quad(n_quad,1)-y_quad(n_quad,4)
                     else
                 x_edge=x_quad(n_quad,i)-x_quad(n_quad,i-1)
                 y_edge=y_quad(n_quad,i)-y_quad(n_quad,i-1)
               end if
               x_0=x-x_quad(n_quad,i)
               y_0=y-y_quad(n_quad,i)
               if (x_edge*y_0-y_edge*x_0 .gt. 0) goto 11
             end do
             m(n_x,n_y)=m_infinity
            write(4,100) n_x*a,n_y*a
            goto 10
11          continue
          end do
c     ****************************************************************
c         Ellipses. ******************************************************
c     ****************************************************************
           do n_ellipse=1,n_ellipses_max
             x_center=
     &   (x_left_ellipse(n_ellipse)+x_right_ellipse(n_ellipse))/2
            y_center=y_center_ellipse(n_ellipse)
             a_ellipse=
     &   (x_right_ellipse(n_ellipse)-x_left_ellipse(n_ellipse))/2
             b_ellipse=
     &   y_top_ellipse(n_ellipse)-y_center_ellipse(n_ellipse)
             if ((x-x_center)**2/a_ellipse**2+
     &   (y-y_center)**2/b_ellipse**2 .lt. 1) then
               m(n_x,n_y)=m_infinity
              write(4,100) n_x*a,n_y*a
                    goto 10
              endif
          end do
10        continue
        end do
       end do
      close(4)
       return
       end
```

Appendix B

Numerical solution of complex dispersion relationships

Below is the code for the program discussed in Section 5.3. The dispersion relation is contained in the subroutine `disp`. As discussed in Section 5.3, the program searches for a square in complex K space such that the four corners have all three possible labels. The rule for labeling a point is contained in the subroutine `label`.

The program will terminate if

1.) The result of feeding `K1` into the dispersion relation is less than the specified error `dispERR`.

2.) The algorithm wanders too far and goes `size` number of steps in one direction without finding a square whose four corners are completely labeled. In this case, `size` is 2500 steps.

VWG_freq.f90

```
!Viscous Wave Guide
 PROGRAM VWG_freq
       complex(8)          K1, K2 ! complex wavevectors
       ! note - K1 is used as a trial, and K2 contains the result of feeding
       ! K1 into the dispersion relation.  If K1 is a root, then K2 should be
       ! zero.
       complex(8)    omega        ! dimensionless angular frequency
       complex(8)    Kstart       ! place to start search for root
       complex(8)    I            ! i
       real*8        nu,mu        ! dimensionless parameters for the shear
                                        ! and bulk viscosity
       real*8        inc          ! step size
       integer       size         ! maximum number of steps to take in one
                                  ! direction
       real*8        PI
       real*8        realK, imagK
       logical       stepFlag
       logical       contLook     ! true = keeps looking, false =
                                  ! completely labeled square found
       logical       gateFound    ! true = edge found with two different
                                  ! labels
```

```
real*8        dispERR       ! look for a root K until
                            ! ABS(Disp(K)).LT.dispError
real*8        freq          ! frequency in GHz
real*8        a             ! channel half width in nm
real*8        b             ! slip length in nm
real*8        lambda

!search variables
integer             curX, curY
integer             lab1, lab2
integer             indX, indY

integer             nextStep
character*50  strFileOut$
character*50  strFileDim$

!constants
PI            =      2.0d0*DACOS0.0d0)
I             =      (0.0, 1.0)

!read inputs from file VWG.inp
open(2, file='VWG.inp', status='old')
read(2,*) strFileOut$
read(2,*) strFileDim$
read(2,*) freq
read(2,*) a
read(2,*) b
close(2)

! read starting point from VWG_kstart.inp
open(2, file='VWG_kstart.inp', status='old')
read(2,*) realK
read(2,*) imagK
close(2)

! read the increment size
open(2, file='VWG_inc.inp', status='old')
read(2,*) inc
close(2)

! read the in the quantity dispErr
open(2, file='VWG_dispErr.inp', status='old')
read(2,*) dispErr
close(2)

! set the values of the dimensionless paramters
! see notes - these values correspond to 22Celcius
omega = DCMPLX(freq*2*PI*0.001*a/1.4876)
nu = 0.64817/a
mu = 2.68341/a      ! see notes - these values correspond to 22Celcius
lambda = b/a

Kstart = DCMPLX(realK, imagK)
size = 2500

!initialize flags
contLook = .TRUE.
gateFound = .FALSE.

DO WHILE(contLook)
```

```
!*******search the bottom (leg 1) of the zone for a gate
indX = 0
indY = 0
nextStep = 0

lab1 = 0
lab2 = 0

do while (lab1.EQ.lab2.AND.indX.LT.size)
       curX = indX
       curY = indY
       !~~~Set label 1
       K1 = Kstart + DCMPLX(curX*inc, curY*inc)
       call disp(K1,omega,nu,mu,lambda,K2)
       call label(K2, lab1)
       !~~~Set label 2
       K1 = Kstart + DCMPLX((curX+1)*inc, curY*inc)
       call disp(K1,omega,nu,mu,lambda,K2)
       call label(K2, lab2)

       write(*,*) lab1, lab2

       indX = indX + 1
       IF(lab1.NE.lab2) THEN
              gateFound = .TRUE.
       END IF
end do
!after scanning the bottom leg, if a gate was found, program
!proceeds
IF(gateFound) THEN
       write(*,*) Kstart + DCMPLX(curX*inc, curY*inc)
       !at this point, curX,curY is at a gate

       !~~~Set label 3
       K1 = Kstart + DCMPLX((curX+1)*inc, (curY+1)*inc)
       call disp(K1,omega,nu,mu,lambda,K2)
       call label(K2, lab3)
       !~~~Set label 4
       K1 = Kstart + DCMPLX((curX)*inc, (curY+1)*inc)
       call disp(K1,omega,nu,mu,lambda,K2)
       call label(K2, lab4)

       !~~~ Check the labels and determine the direction for the
       !next step
       call afterStepUP(lab1, lab2, lab3, lab4, nextStep)
ENDIF

!If gate wasn't found, then scan up leg 2
IF(.NOT.gateFound) THEN
       lab2 = 0
       lab3 = 0

       do while(lab2.EQ.lab3.AND.indY.LT.size)
              curX = indX
              curY = indY

              !~~~Set label 2
              K1 = Kstart + DCMPLX((curX+1)*inc, curY*inc)
              call disp(K1,omega,nu,mu,lambda,K2)
              call label(K2, lab2)
              !~~~Set label 3
```

```
                        K1 = Kstart + DCMPLX((curX+1)*inc, (curY+1)*inc)
                        call disp(K1,omega,nu,mu,lambda,K2)
                        call label(K2, lab3)

                        write(*,*) lab1, lab2

                        indY = indY + 1
                        IF(lab2.NE.lab3) THEN
                               gateFound = .TRUE.
                        END IF

                enddo

                !~~~Set label 1
                K1 = Kstart + DCMPLX((curX)*inc, (curY)*inc)
                call disp(K1,omega,nu,mu,lambda,K2)
                call label(K2, lab1)
                !~~~Set label 4
                K1 = Kstart + DCMPLX((curX)*inc, (curY+1)*inc)
                call disp(K1,omega,nu,mu,lambda,K2)
                call label(K2, lab4)

                call afterStepLEFT(lab1, lab2, lab3, lab4, nextStep)


        END IF

        write(*,*) lab1, lab2, lab3, lab4
        write(*,*) curX, curY
        write(*,*) nextStep

!=================================================================
!|   MAIN LOOP FOR SEARCHING for a square that is completely labeled
!|           nextStep = 0 - there has been an error
!|                        = 1 - UP
!|                        = 2 - RIGHT
!|                        = 3 - DOWN
!|                        = 4 - LEFT
!|                        = 5 - The end has been reached
!=================================================================

        do while (nextStep.NE.5.AND.nextStep.NE.0)
                !Take the NEXT STEP
                IF(nextStep.EQ.1) THEN
                   curY = curY + 1 !UP
                ELSE IF(nextStep.EQ.2) THEN
                   curX = curX + 1 !RIGHT
                ELSE IF(nextStep.EQ.3) THEN
                   curY = curY - 1 !DOWN
                ELSE IF(nextStep.EQ.4) THEN
                   curX = curX - 1 !LEFT
                ELSE IF(nextStep.EQ.5) THEN
                   curX = curX
                   curY = curY

                ELSE
                        nextStep = 0
                ENDIF

                !set the labels for the current square
                !~~~Set label 1
```

```
                K1 = Kstart + DCMPLX((curX)*inc, (curY)*inc)
                call disp(K1,omega,nu,mu,lambda,K2)
                call label(K2, lab1)
                !~~~Set label 2
                K1 = Kstart + DCMPLX((curX+1)*inc, (curY)*inc)
                call disp(K1,omega,nu,mu,lambda,K2)
                call label(K2, lab2)
                !~~~Set label 3
                K1 = Kstart + DCMPLX((curX+1)*inc, (curY+1)*inc)
                call disp(K1,omega,nu,mu,lambda,K2)
                call label(K2, lab3)
                !~~~Set label 4
                K1 = Kstart + DCMPLX((curX)*inc, (curY+1)*inc)
                call disp(K1,omega,nu,mu,lambda,K2)
                call label(K2, lab4)

                stepFlag = .TRUE.   !true = has not set the new next step

                !call the appropriate after step function
                IF(nextStep.EQ.1.AND.stepFlag) THEN
                       call afterStepUP(lab1, lab2, lab3, lab4, nextStep)
                       stepFlag = .FALSE.
                ELSE IF(nextStep.EQ.2.AND.stepFlag) THEN
                       call afterStepRIGHT(lab1, lab2, lab3, lab4, nextStep)
                       stepFlag = .FALSE.
                ELSE IF(nextStep.EQ.3.AND.stepFlag) THEN
                       call afterStepDOWN(lab1, lab2, lab3, lab4, nextStep)
                       stepFlag = .FALSE.
                ELSE IF(nextStep.EQ.4.AND.stepFlag) THEN
                       call afterStepLEFT(lab1, lab2, lab3, lab4, nextStep)
                       stepFlag = .FALSE.
                ELSE IF(nextStep.EQ.5) THEN
                       nextStep = 5
                ELSE
                       nextStep = 0
                ENDIF

                       ! if algorithm wanders too far, break the loop
                IF (abs(curX).GT.size.OR.abs(curY).GT.size) THEN
                       write(*,*) 'Algorithm went OUT of BOUNDS!!'
                       contLook = .FALSE.
                       nextStep = 0
                END IF
        enddo

        write(*,*) curX, curY

        K1 = Kstart + DCMPLX((curX-1)*inc, (curY-1)*inc)
        write(*,*) 'END:', K1
        call disp(K1,omega,nu,mu,lambda,K2)
        write(*,*) 'error:', K2

        !preparations for next loop.  Set lower left corner of search
        !domain to K1 and decrease step size by a factor of 10
        inc = inc/10
        Kstart = K1

        !loop test statements
        !if K2 is smaller than dispErr, then the program is done
        IF (abs(K2).LT.dispERR) THEN
                contLook = .FALSE.
```

```
              END IF

              write(*,*) DREAL(omega), DREAL(K1), DIMAG(K1)
       END DO

       open(1,file=strFileOut$,access ='append',status='unknown')
       open(2,file=strFileDim$,access ='append',status='unknown')
       open(3,file='error.dat',access ='append',status='unknown')
       open(4,file='VWG_kstart.inp', status='old')

       write(1,*) DREAL(omega), DREAL(K1), DIMAG(K1)
       write(2,*) freq, DREAL(omega)/DREAL(K1), DIMAG(K1)/a
       write(3,*) DREAL(omega), ABS(K2)
       write(4,*) DREAL(K1)
       write(4,*) DIMAG(K1)
       close(1)
       close(2)
       close(3)
       close(4)


END PROGRAM

!~~~~~~~~~~~~~~~ Sub-routines ~~~~~~~~~~~~~~~~~~~~
!*********************************************
subroutine afterStepUP(lab1, lab2, lab3, lab4, nextStep)
!*********************************************
integer lab1,lab2,lab3,lab4, nextStep

       IF (lab4.NE.lab1.AND.lab4.NE.lab2) THEN
              nextStep = 5 !done
       ELSE IF (lab3.NE.lab1.AND.lab3.NE.lab2) THEN
              nextStep = 5 !done
       ELSE IF (lab4.EQ.lab3.AND.lab4.EQ.lab1) THEN
              nextStep = 2 !RIGHT

       ELSE IF (lab4.EQ.lab3.AND.lab4.EQ.lab2) THEN
              nextStep = 4 !LEFT
       ELSE IF (lab4.EQ.lab1.AND.lab3.EQ.lab2) THEN
              nextStep = 1 !UP
       ELSE
              nextStep = 0
       END IF

return
end

!*********************************************
subroutine afterStepRIGHT(lab1, lab2, lab3, lab4, nextStep)
!*********************************************
integer lab1,lab2,lab3,lab4, nextStep

       IF (lab3.NE.lab4.AND.lab3.NE.lab1) THEN
              nextStep = 5 !done
       ELSE IF (lab2.NE.lab4.AND.lab2.NE.lab1) THEN
              nextStep = 5 !done
       ELSE IF (lab1.EQ.lab2.AND.lab3.EQ.lab4) THEN
              nextStep = 2 !RIGHT
       ELSE IF (lab4.EQ.lab3.AND.lab4.EQ.lab2) THEN
              nextStep = 3 !DOWN
       ELSE IF (lab1.EQ.lab3.AND.lab3.EQ.lab2) THEN
```

```
              nextStep = 1 !UP
       ELSE
              nextStep = 0
       END IF

return
end

!***********************************************
subroutine afterStepLEFT(lab1, lab2, lab3, lab4, nextStep)
!***********************************************
integer lab1,lab2,lab3,lab4, nextStep

       IF (lab4.NE.lab3.AND.lab4.NE.lab2) THEN
              nextStep = 5 !done
       ELSE IF (lab1.NE.lab3.AND.lab1.NE.lab2) THEN
              nextStep = 5 !done
       ELSE IF (lab4.EQ.lab1.AND.lab4.EQ.lab2) THEN
              nextStep = 1 !UP
       ELSE IF (lab4.EQ.lab1.AND.lab4.EQ.lab3) THEN
              nextStep = 3 !DOWN
       ELSE IF (lab1.EQ.lab2.AND.lab3.EQ.lab4) THEN
              nextStep = 4 !LEFT
       ELSE
              nextStep = 0
       END IF

return
end

!***********************************************
subroutine afterStepDOWN(lab1, lab2, lab3, lab4, nextStep)
!***********************************************
integer lab1,lab2,lab3,lab4, nextStep

       IF (lab1.NE.lab3.AND.lab1.NE.lab4) THEN
              nextStep = 5 !done
       ELSE IF (lab2.NE.lab3.AND.lab2.NE.lab4) THEN
              nextStep = 5 !done
       ELSE IF (lab1.EQ.lab2.AND.lab1.EQ.lab4) THEN
              nextStep = 2 !RIGHT
       ELSE IF (lab1.EQ.lab2.AND.lab1.EQ.lab3) THEN
              nextStep = 4 !LEFT
       ELSE IF (lab3.EQ.lab2.AND.lab1.EQ.lab4) THEN
              nextStep = 3 !DOWN
       ELSE
              nextStep = 0
       END IF

return
end


!***********************************************
subroutine disp(K,omega,nu,mu,lambda,result)
!*  plugs K, omega, mu and nu into the dispersion relation and puts
!*  the result into result.  If K is a bonafide root, the result
!*  should be 0.
!***********************************************
       complex(8) K,omega, result
       real*8 nu,mu,lambda
```

```
      complex(8) alpha, beta
      complex(8) I
      I = (0.0, 1.0)

      alpha = CDSQRT(((omega**2+I*omega**3*mu)/(1+mu**2*omega**2) - K**2))
      beta = CDSQRT((I*omega/nu - K**2))

      result = alpha*CDSIN(alpha)*beta*CDCOS(beta) +
                           K*K*CDCOS(alpha)*CDSIN(beta)
      result = result - lambda*alpha*(beta*beta+K*K)*CDSIN(beta)*CDSIN(alpha)
                                !^-- lambda term = slip length contribution
return
end
!*********************************************
subroutine label(dispResult, lbl)
!*      Takes complex number dispResult and applies the label
!*      0, 1, or 2 depending on Arg(dispResult)
!*********************************************
      complex(8) dispResult
      integer lbl

      real*8 temp
      real*8 PI
      real*8 limit

      PI = 2.0d0*DACOS(0.0d0)
      limit = PI/3.0

      temp = DATAN2(DREAL(dispResult), DIMAG(dispResult))

      IF (temp.LT.limit.AND.temp.GT.-1*limit) THEN
            lbl = 0
      ELSE IF (temp.GE.limit) THEN
            lbl = 1
      ELSE
            lbl = 2
      END IF

return
end
```

Below are some typical inputs.

VWG.inp

```
test.dat
test_dim.dat
1
25
0
```

VWG_dispErr.inp

```
1.0d-10
```

VWG_inc.inp

```
1.0d-5
```

VWG_Kstart.inp

```
0.1
0.003
```

The following visual basic script can be used in conjunction with the above program to loop through a series of frequencies. The solution used at a previous frequency is used as the starting point for the next frequency.

VWG_freq.vbs

```
Const startFreq = 0.01
Const incFreq = 0.01

strInFile = "VWG.inp"
strOutFile = "a50b00.dat"
strDimFile = "a50b00_dim.dat"

Dim i

Wscript.echo "VWG Frequency looping Script"

Set WshShell = CreateObject("WScript.Shell")

For i=0 to 999
       'set the frequency
       strFreq = startFreq+i*incFreq

       'open the input file and read in contents line by line
       Set objFSO = CreateObject("Scripting.FileSystemObject")
       Set objFile = objFSO.OpenTextFile(strInFile, 1)

       strLine = objFile.ReadLine
       strContents = strOutFile & vbCrLf

       strLine = objFile.ReadLine
       strContents = strContents & strDimFile & vbCrLf

       strLine = objFile.ReadLine
       strLine = strFreq                'change frequency
       strContents = strContents & strLine & vbCrLf

       'read in rest of input file
       Do Until objFile.AtEndOfStream
           strLine = objFile.ReadLine
           strContents = strContents & strLine & vbCrLf
       Loop

       objFile.Close

       'open input file and write contents to it
       Set objFile = objFSO.OpenTextFile(strInFile, 2)
```

```
        objFile.Write(strContents)
        objFile.Close

        'run the fortran program
        wshShell.Run "VWG_freq.exe",1,true

        'clear the contents string for the next iteration
        strContents = ""

Next
```

Appendix C

Comparing POAM experimental data to simulation data

Below is the code for the program, `fitter3.f90`, used to carry out the procedure to subtract the background from the POAM data and compare it to a simulation result, as described in Section 6.3.2.

fitter3.f90

```
PROGRAM fitter3
real   simData(5000,2)      !Simulation data 1- time 2- signal
real   simData_T(5000,2)    ! transformed simulation data

real   expData(5000,2)      !Experimental data (funny oscillations subtracted)
real   zeroPoints(20,2)     !times where the simulation data is zero
integer nZeros              !# of zero points
integer nExpP               !# of experimental data points

real   expT                 !Experimental time step
real   simT                 !Simulation time step
real   expOffset            !Offset time in experimental data
real   expNorm              !height of the first echo after backround subtraction
real   m34slope             !slope of the background to be subtracted between
                                  !zeropoints 3 and 4

real   err                  !chi square between sim and exp data
integer maxInd              !index for the maximum

real   Tstart               !Time to start comparing the datas
real   Tstop                !Time to stop comparing the datas
real   lowerT               !Time to start looking for first peak in sim data
real   upperT               !Time to stop looking for the first peak in sim data

character*40 fOut$          !Output file name
character*40 simFName$      !simulation data file name
character*40 expFName$      !experimental data file name
character*70 line$
logical      reportErr      !flag for writing error or not

!read in fitter parameters from fitter.inp
open(1, file='fitter3.inp', status='old')
read(1,*) simFName$
read(1,*) expFName$
read(1,*) fOut$
read(1,*) lowerT, upperT
read(1,*) Tstart, Tstop
close(1)
```

```
!read in simulation data
open(1, file=simFName$, status='unknown')
i=1
do while (.NOT.EOF(1))
       read(1, '(A)') line$
       read(line$,*) simData(i,1), simData(i,2)
       i=i+1
enddo
close(1)

!read in the experimental data
i=1
open(2, file=expFName$, status='unknown')
do while (.NOT.EOF(2))
       read(2, '(A)') line$
       read(line$,*) expData(i,1), expData(i, 2)
       i=i+1
enddo
nExpP = i


close(2)

! deduce the time steps in the data sets
expT = expData(100,1) - expData(99,1)
simT = simData(100,1) - simData(99,1)

! Normalize the simulation data
call NormalizeSimData(simData_T, maxInd, lowerT, upperT)

! Find the zero points in in the simulation data
call FindZeroPoints(simData_T, maxInd, zeroPoints, nZeros, Tstop)


! write normalized sim data to a file for inspection etc.
open ( 7 , file = 'normSIM.dat', status = 'unknown')
i = 0
do while (simData_T(i,1).LT.zeroPoints(1,1))
       i = i+1
end do

do while (simData_T(i,1).LT.zeroPoints(nZeros,1) )
       write(7,*) simData_T(i,1), simData_T(i,2)
       i = i+1
end do
close(7)

! find the best offset time for the experimental data
call OffSetExpData(expData, simData_T, maxInd, zeroPoints, expOffset, expNorm,
nExpP)

call CalcExpNorm(expData, simData_T, maxInd, zeroPoints, expNorm, m34slope)

call SubtractBackRound(expData, expNorm, zeroPoints, nZeros, nExpP)

call CompareExpSim(expData, simData_T, err, zeroPoints(1,1),
zeroPoints(nZeros,1))

reportErr = .TRUE.
```

```
if (reportErr) then
       write(*,*) err
       open(9, file = fOut$, status = 'unknown')
       write(9,*) err, nZeros, zeroPoints(nZeros,1)
       close(9)
endif

END PROGRAM

!************************************************************
SUBROUTINE SubtractBackRound(expData, expNorm, zeroPoints, nZeros, nExpP)
!************************************************************
! Find lines that correspond to the zeropoints in the experimental data and
! then subtracts them from the experimental data (after applying the time
! offset.  Then normalizes the data by the factor expNorm.
real   expData(5000,2)     !Experimental data
real   expNorm             !Height of the first maximum
real   zeroPoints(20,2)    !list of the times where sim is zero
integer nZeros             !# of zeroPoints used/found
integer nExpP              !# of experimental points

real   bR(20,2)            !Points of the lines of the background
real   x1, y1              !temporary points used to find the background lines
real   x2, y2
integer ind, i
real   temp

!1. Find the backround points from the zeroPoints
open(6, file='BR.dat', status = 'unknown')
ind = 1
do i=1, nZeros
       do while (expData(ind,1).LT.zeroPoints(i,1))
              ind = ind + 1
       end do

       x1 = expData(ind-1,1)
       y1 = expData(ind-1,2)
       x2 = expData(ind,1)
       y2 = expData(ind,2)

       bR(i,1) =     zeroPoints(i,1)
       bR(i,2) =     (((y2-y1)/(x2-x1))*(zeroPoints(i,1)-x1)+y1 ) -
                            zeroPoints(i,2)*expNorm

       write(6,*) bR(i,1), bR(i,2)
enddo
close(6)

!2. Subtract the lines from the experimental data and normalize
ind=1
do while (expData(ind,1).LT.bR(1,1))
              ind = ind+1
enddo
       !index ind is now just after br point i

do i=1, nZeros-1
       do while (expData(ind,1).LT.bR(i+1,1))
              temp = ((bR(i+1,2)-bR(i,2))/(bR(i+1,1)-bR(i,1)))*(expData(ind,1)-
                            bR(i,1))+bR(i,2)
              expData(ind,2) = (expData(ind,2) - temp)/expNorm
```

```
            ind = ind+1
      enddo
enddo

!3.  write expData to a file for reference
open(7, file='expDataBS.dat', status='unknown')
do i=1,nExpP
      if(expData(i,1).GT.bR(1,1).AND.expData(i,1).LT.bR(nZeros,1)) then
            write(7,*) expData(i, 1), expData(i, 2)
      endif
enddo
close(7)

return
END

!*************************************************************
SUBROUTINE OffSetExpData(expData, simData, maxInd, zeroPoints, expOffset,
expNorm, nExpP)
!*************************************************************
!background subtracted from experimental data is the line between zero
!points 3&4

real   expData(5000,2)     !Experimental data
real   simData(5000,2)     !Simulation data
real   zeroPoints(20,2)    !Times of the zeros in simData
real   expOffset    !Offset time between exp and sim data
real   tempOffset
real   TOStart      !starting offset time (80 ps)
real   tStep        !Time to change offset time by (1ps)

integer nExpP       !number of experimental points

real   tempNorm
real   expNorm      !Height of the first echo in the exp data after subtraction

real   lT           !Times bracketing the first maximum
real   uT

integer maxInd      !index of the first maximum in simData

real   tempData(5000,2)    !temporary container for experimental datas
real   tempSim(5000, 2)    !temporary container for simulation data
integer ind, i, j
integer t           ! index for offset time loop

real   err          !difference between the sim and shifted exp data
real   bestErr      !best error found for finding the ideal offset time

real   x1, x2       !points 1 and 2 - temporary values that bracket the
zeropoints
real   y1, y2
real   x3, x4       !point corresponding to zeroPoint 3
real   y3, y4       !point corresponding to zeroPoint 4
real   z3, z4       !shorthand for zeroPoint(3/4, 2)

tStep        = 2.0        !increment offset times by 3 ps
TOStart      = -20.0
bestErr      = 100000.0

lT = simData(maxInd,1) - 40.0
```

```
uT = simData(maxInd,1) + 40.0

do t=0, 20
! 1.  offset the data
tempOffset = TOStart + t*tStep
!Fill up the tempData array and offset the times
do i=1, 5000
       tempData(i,1) = expData(i,1) - tempOffset
       tempData(i,2) = expData(i,2)

       tempSim(i,1) = simData(i,1)
       tempSim(i,2) = simData(i,2)

enddo

! 2.  find the points in the experimental data that corresponds to zeropoints
3&4
ind = 1
do while(tempData(ind, 1).LT.zeroPoints(3,1))
       ind = ind + 1
enddo
x1 = tempData(ind-1,1)
y1 = tempData(ind-1,2)
x2 = tempData(ind,1)
y2 = tempData(ind,2)

x3 = zeroPoints(3,1)
y3 = ((y2-y1)/(x2-x1))*(x3-x1)+y1
z3 = zeroPoints(3,2)

do while(tempData(ind,1).LT.zeroPoints(4,1))
       ind = ind + 1
enddo
x1 = tempData(ind-1,1)
y1 = tempData(ind-1,2)
x2 = tempData(ind,1)
y2 = tempData(ind,2)

x4 = zeroPoints(4,1)
y4 = ((y2-y1)/(x2-x1))*(x4-x1)+y1
z4 = zeroPoints(4,2)

!3. subtract the line from x3,y3 to x4,y4 from the temp data, and the line
x3,z3 to
! x4,z4 from the temp sim
       ind = 1
       do while(tempData(ind,1).LT.x3)
              ind = ind+1
       enddo

       do while(tempData(ind,1).LT.x4)
              tempData(ind,2) = tempData(ind,2) - (((y4-y3)/(x4-
                     x3))*(tempData(ind,1)-x3)+y3)
              tempSim(ind,2) = tempSim(ind,2) - (((z4-z3)/(x4-
                     x3))*(tempSim(ind,1)-x3)+z3)

              ind=ind+1
       enddo

!4a. find the max in the tempSim data
```

```
       ind = 1
       do while(tempSim(ind,1).LT.x3)
              ind = ind+1
       enddo

       tempNorm = -10000000

       do while(tempSim(ind,1).LT.x4)
              if(tempSim(ind,2).GT.tempNorm) then
                     tempNorm = tempSim(ind,2)
                     j = ind       !mark the index of the maximum

              endif
              ind=ind+1
       enddo

!4b normalize the temp sim data
       ind = 1
       do while(tempSim(ind,1).LT.x3)
              ind = ind+1
       enddo

       do while(tempSim(ind,1).LT.x4)
              tempSim(ind,2) = tempSim(ind,2)/tempNorm
              ind=ind+1
       enddo


!4c. find the max in the temp data
       ind = 1
       do while(tempData(ind,1).LT.x3)
              ind = ind+1
       enddo

       tempNorm = -10000000

       do while(tempData(ind,1).LT.x4)
              if(tempData(ind,2).GT.tempNorm) then
                     tempNorm = tempData(ind,2)
                     j = ind       !mark the index of the maximum

              endif
              ind=ind+1
       enddo

!4d - normalize the tempData
       ind = 1
       do while(tempData(ind,1).LT.x3)
              ind = ind+1
       enddo

       do while(tempData(ind,1).LT.x4)
              tempData(ind,2) = tempData(ind,2)/tempNorm
              ind=ind+1
       enddo

! 5. Compare sim and temp (exp) data between x3 and x4

       call CompareExpSim(tempData, tempSim, err, lT, uT)

       write(*,*) tempOffset, err
```

```
      if (err.LT.bestErr) then
            expOffset = tempOffset
            expNorm = tempNorm
            bestErr = err
      endif


enddo

write(*,*) expOffset,bestErr

!Finally, Offset the experimental data with expOffset
open(5, file = 'expDataOffset.dat', status = 'unknown')
do i=1, nExpP-50
      expData(i, 1) = expData(i,1) - expOffset
      write(5,*) expData(i, 1), expData(i, 2)
enddo
close(5)


return
END

!*************************************************************
SUBROUTINE CalcExpNorm(expData, simData, maxInd, zeroPoints, expNorm, m34slope)
!*************************************************************
!background subtracted from experimental data is the line between zero
!points 3&4
real   expData(5000,2)     !Experimental data
real   simData(5000,2)     !Simulation data
real   zeroPoints(20,2)    !Times of the zeros in simData

real   expNorm             !Height of the first echo in the exp data after
                           ! subtraction

integer maxInd             !index of the first maximum in simData

integer ind


real   x1, x2  ! points 1 and 2 - temporary values that bracket the zeropoints
real   y1, y2

real   xm, ym  !point in exp data that is the first maximum
real   x3, x4  !point corresponding to zeroPoint 3
real   y3, y4  !point corresponding to zeroPoint 4

real   z3, z4  !shorthand for zeroPoint(3/4, 2)

real   det, m34slope ! shorthand - see notes


! 0.  find the point in the exp data that corresponds to the peak in the sim
! data
      ind = 1
      do while(expData(ind, 1).LT.simData(maxInd,1))
            ind = ind + 1
      enddo

      xm = expData(ind,1)
```

```
       ym = expData(ind,2)

! 1.  find the points in the experimental data that corresponds to zeropoints
! 3&4
       ind = 1
       do while(expData(ind, 1).LT.zeroPoints(3,1))
              ind = ind + 1
       enddo
       x1 = expData(ind-1,1)
       y1 = expData(ind-1,2)
       x2 = expData(ind,1)
       y2 = expData(ind,2)

       x3 = zeroPoints(3,1)
       y3 = ((y2-y1)/(x2-x1))*(x3-x1)+y1
       z3 = zeroPoints(3,2)

       do while(expData(ind,1).LT.zeroPoints(4,1))
              ind = ind + 1
       enddo
       x1 = expData(ind-1,1)
       y1 = expData(ind-1,2)
       x2 = expData(ind,1)
       y2 = expData(ind,2)

       x4 = zeroPoints(4,1)
       y4 = ((y2-y1)/(x2-x1))*(x4-x1)+y1
       z4 = zeroPoints(4,2)


 !2. caluclate Det, expNorm, and mslope
       det = (x4 - x3) - z4*(xm - x3)

       m34slope = (y4 - y3) - z4*(ym - y3)
       m34slope = m34slope/det

       expNorm = (ym - y3)*(x4 - x3) - (y4 - y3)*(xm - x3)
       expNorm = expNorm/det

return
END


!************************************************************
SUBROUTINE CompareExpSim(expData, simData, err, Tstart, Tstop)
!************************************************************
real   expData(5000,2)            !Experimental data
real   simData(5000,2)            !Simulation data
real   err                               !Difference between the exp and sim
data
real   Tstart                     !Time to start the comparison
real   Tstop                      !Time to stop the comparison

real   diff                       !difference between exp and sim data
integer ind, i
integer counter

ind = 1
err = 0.00

do while (expData(ind,1).LT.Tstart)
```

```
       ind = ind+1
enddo

counter = 0
do while (expData(ind,1).LE.Tstop)
       i=1
       do while(simData(i,1).LT.expData(ind,1) )
              i=i+1
       enddo

       x1 = simData(i-1,1)
       y1 = simData(i-1,2)
       x2 = simData(i,1)
       y2 = simData(i,2)

       diff = ((y2-y1)/(x2-x1))*(expData(ind,1)-x1)+y1-expData(ind,2)
       err = err + diff*diff
       ind = ind+1
       counter = counter + 1

enddo

return
END

!************************************************************
SUBROUTINE FindZeroPoints(simData, maxInd, zeroPoints, nZeros, Tstop)
!************************************************************
! Searches between time Tstart and time Tstop and finds the points
! where the simulation signal is zero
! First 3 zeropoints are before the first maximum and are just
! evenly spaced     every 50 picoseconds

real   simData(5000,2)     !simulation data passed in (normalized)
real   zeroPoints(20,2)    !zeropoints array to be filled
integer      maxInd !index of the first maximum in the simulation data
integer mInd        !index of a local extrema (if needed)
integer nZeros             !# of zeros found
real   Tstop               !time to stop looking for zeros

real   maxSpace            ! maximum distance between the zeropoints in time

integer ind, i, j
integer nn
real   small
real   zero
real   weight

logical zeroFound
logical p3NotFound
logical minNotFound

real   x1, y1
real   x2, y2

weight = 0.3

zero = 0.000
small = 1E-3
maxSpace = 600.0
```

```
! 1. Find three zero points before the arrival of the first echo
ind = 1
p3NotFound = .TRUE.
do while (ind.LT.maxInd.AND.p3NotFound)
       if(simData(ind,2).LT.small.AND.simData(ind+1,2).GE.small) then
              zeroPoints(3,1) = simData(ind,1)
       endif
       ind = ind + 1
enddo

zeroPoints(2,1) = zeroPoints(3,1) - 50.0
zeroPoints(1,1) = zeroPoints(2,1) - 50.0

! 2. Now found the zero points after the first maximum
nZeros = 3
ind = maxInd
zeroFound = .FALSE.

do while (simData(ind,1).LT.TStop)
       if(simData(ind,2).LT.zero.AND.sign(simData(ind,2),simData(ind+1,2)).GT.
       zero) then
              zeroFound = .TRUE.
       endif

       if(simData(ind,2).GT.zero.AND.sign(simData(ind,2),simData(ind+1,2)).LT.
       zero) then
              zeroFound = .TRUE.
       endif

       if(zeroFound) then
              x1 = simData(ind,1)
              y1 = simData(ind,2)
              x2 = simData(ind+1,1)
              y2 = simData(ind+1,2)
              nZeros = nZeros + 1
              zeroPoints(nZeros,1) = x1 -  ((x2-x1)/(y2-y1))*y1

       endif

       ind = ind+1
       zeroFound = .FALSE.
enddo


! 3. Check the spaces between the zeroes
i = 3
do while (i.LT.nZeros)
       temp = zeroPoints(i+1,1)-zeroPoints(i,1)
       if(temp.GT.maxSpace) then

              nn = nZeros - i - 1
              do j = 0, nn
                     zeroPoints(nZeros - j + 1, 1) = zeroPoints(nZeros - j, 1)
                     zeroPoints(nZeros - j + 1, 2) = zeroPoints(nZeros - j, 2)

              enddo

              minNotFound = .TRUE.
              call FindMinima(simData, mInd, zeroPoints(i,1)+10,
                     zeroPoints(i+1,1), minNotFound)
```

```
              nZeros = nZeros + 1

              if (minNotFound) then
                     write(*,*) simData(mInd,1), simData(mInd,2)
                     zeroPoints(i+1,1) = simData(mInd+50,1)
                     zeroPoints(i+1,2) = simData(mInd+50,2)
              else
                     write(*,*) simData(mInd,1), simData(mInd,2)
                     zeroPoints(i+1,1) = simData(mInd,1)
                     zeroPoints(i+1,2) = simData(mInd,2)
              endif
       endif
       i = i+1
enddo

! record zeroPoints in external file
open(8, file = 'zeroPoints.dat', status='unknown')
ind = 1
do ind = 1, nZeros
       write(8,*) zeroPoints(ind,1), zeroPoints(ind,2)
enddo
close(8)

return
END

!************************************************************
SUBROUTINE NormalizeSimData(simData, maxInd, lowerT, upperT)
!************************************************************
!Searches around the first peak, find the maximum value, and
!normalizes the simulation data so that the height of the first
!echo is 1.0000.

!Index in sim data where the first maximunm occurs is placed into
! maxInd

real   simData(5000,2)      !simulation data passed in
integer       maxInd !index for the maximum

real   maxT                 !Time at which maximum occurs
real   max                  !the maximum of the first peak (echo from the Top)
real   lowerT        !Times to search for maximum value between
real   upperT
integer ind,i

max = 0.0001

ind=1
do while(simData(ind,1).LT.lowerT)
       ind=ind+1
enddo

do while(simData(ind,1).LE.upperT)
       if(simData(ind,2).GT.max) then
              maxT = simData(ind,1)
              max  = simData(ind,2)
              maxInd = ind
       endif

       ind=ind+1
enddo
```

```
do i=1,5000
       simData(i, 2) = simData(i, 2)/max
enddo

return
END


!************************************************************
SUBROUTINE FindMinima(simData, minInd, T1, T2, minNotFound)
!************************************************************
! Finds the first local minima between T1 and T2.
! Does not handle the case of no minima

real   simData(5000,2)     !simulation data passed in
integer      minInd !index for the minimum
real   minT                !Time at which maximum occurs
real   T1, T2        !Times to search for maximum value between
real   m1, m2        !local slopes

logical minNotFound
integer ind

minNotFound = .TRUE.

ind=1
do while(simData(ind,1).LT.T1)
       ind=ind+1
enddo

do while(simData(ind,1).LT.T2.AND.minNotFound)

       m1 = (simData(ind,2)-simData(ind-1,2))/(simData(ind,1)-simData(ind-1,1))
       m2 = (simData(ind+1,2)-simData(ind,2))/(simData(ind+1,1)-simData(ind,1))

       if(m1.LT.0.0d0.AND.m2.GE.0.0d0) then
              minT = simData(ind,1)
              minInd = ind
              minNotFound = .FALSE.
       endif

       ind=ind+1
enddo

return
END

!************************************************************
SUBROUTINE FindMaxima(simData, mInd, T1, T2)
!************************************************************
! Finds the first local minima between T1 and T2.
! Does not handle the case of no minima

real   simData(5000,2)     !simulation data passed in
integer      mInd          !index for the minimum

real   maxT                !Time at which maximum occurs
real   T1, T2        !Times to search for maximum value between

real   m1, m2        ! local slopes
```

```
logical maxNotFound
integer ind

maxNotFound = .TRUE.

ind=1
do while(simData(ind,1).LT.T1)
       ind=ind+1
enddo

do while(simData(ind,1).LT.T2.AND.maxNotFound)

       m1 = (simData(ind,2)-simData(ind-1,2))/(simData(ind,1)-simData(ind-
              1,1))
       m2 = (simData(ind+1,2)-simData(ind,2))/(simData(ind+1,1)-
              simData(ind,1))

       if(m1.GT.0.0d0.AND.m2.LE.0.0d0) then
              maxT = simData(ind,1)
              mInd = ind
              maxNotFound = .FALSE.
       endif

       ind=ind+1
enddo

return
END
```